THE UNIVERSITY *of* EDINBURGH

Optical Wireless Energy Transfer for Self-Sufficient Small Cells

Ioannis (John) Fakidis

THE UNIVERSITY
of EDINBURGH

A thesis submitted for the degree of Doctor of Philosophy.
The University of Edinburgh.
May 2017

Abstract

Wireless backhaul communication and power transfer can make the deployment of outdoor small cells (SCs) more cost effective; thus, their rapid densification can be enabled. For the first time, solar cells can be leveraged for the two-fold function of energy harvesting (EH) and high speed optical wireless communication. In this thesis, two complementary concepts for power provision to SCs are researched using solar cells – the optical wireless power transfer (OWPT) in the nighttime and solar EH during daytime. A harvested power of 1 W is considered to be required for an autonomous SC operation. The conditions of darkness – worst case scenario – are initially selected, because the SC needs to harvest power in the absence of ambient light. The best case scenario of daytime SC EH from sunlight is then explored to determine the required battery size and the additional power from optical sources.

As a first approach, an indoor 5 m experimental link is created using a white light-emitting diode for OWPT to an amorphous silicon (Si) solar panel. Despite the use of a large mirror for collimation, the harvested power and energy efficiency of the link are measured to be only 18.3 mW and 0.1%, respectively. Up to five red laser diodes (LDs) with lenses and crystalline Si (c-Si) cells are used in a follow-up study to increase the link efficiency. A maximum power efficiency of 3.2% is measured for a link comprising two LDs and a mono-c-Si cell, and the efficiency of all of its components is determined. Also, the laser system is shown to achieve an improvement of the energy efficiency by 2.7 times compared with a state-of-the-art inductive power transfer system with dipole coils. Since the harvested power is only 25.7 mW, an analytical model for an elliptical Gaussian beam is developed to determine the required number of LDs for harvesting 1 W; this shows an estimated number of 61 red LDs with 50 mW of output optical power per device. However, a beam enclosure of the developed Class 3B laser system of up to a 3.6 m distance is required for eye safety. A simulation study is conducted in Zemax for the design of an outdoor 100 m infrared wireless link able to harvest 1 W under clear weather conditions. Harvesting 1.2 W and meeting eye safety regulations for Class 1 are shown to be feasible by a 1550 nm laser link. The required number of laser power converters is estimated to be 47 with an area of $5 \times 5\,\text{mm}^2$ per device. Also, the dimensions of the transmitter and receiver are considered to be acceptable for the practical application of SC EH.

In the last part of this thesis, two multi-c-Si solar panels are initially used for EH in an outdoor environment during daytime. The power supply of at least 1 W is shown to be achievable during hour periods under sunny and cloudy conditions. A maximum average power of 4.1 W is measured in the partial presence of clouds using a 10 W solar panel. Since the variability of weather conditions induces the harvested power to fluctuate with values of mW, the use of optical sources is required in periods of insufficient solar EH for SCs. Therefore, a hybrid solar/laser based EH design is proposed for a continuous annual SC provision of 1 W in 'darker' places on earth such as Edinburgh, UK. The 10 W multi-c-Si solar panel and the 1550 nm laser link are considered; thus, the feasibility of supplying the SC with at least 1 W per hour monthly using a battery with energy content of only 60 Wh is shown through simulations. A maximum monthly average harvested power of 824 mW is shown to be required by the 1550 nm laser system that has already been overachieved through simulations in Zemax.

Lay summary

Small cells (SCs) are low powered radio access points, which allow data communication to users within areas ranging from a few metres (m) to two kilometres. They have been widely acknowledged for their benefits to the energy consumption of wireless networks. A wide outdoor deployment of SCs could potentially be enabled, if the respective cost was reduced and there was no need for a mains power supply. Hence, alternative cost effective sources of power provision to SCs are explored in this thesis; these are based on the complementary concepts of nighttime optical wireless power transfer or charging and daytime solar energy harvesting (EH). The required electrical power for an autonomous SC operation is determined to be 1 Watt (W).

The key elements to transmit optical power without wires are light-emitting diodes (LEDs) and laser diodes (LDs). Also, optical devices, such as mirrors and lenses, are used to collimate, i.e. make rays parallel, and focus the light beams. While photovoltaic (PV) panels are mostly used to harvest electrical energy from sunlight, they are also able to convert optical power from laser sources and LEDs to electricity. Experimental results in this thesis show that the use of red laser beams offer more efficient power transfer compared with white LEDs. This is because LEDs radiate in a spherical form complicating light collimation, while the radiation of LDs is inherently more directive. The eye safety regulations and the system dimensions are shown to be the main restrictive factors for laser charging of SCs. Eye safety parameters depend on the transmitted optical power and the wavelength of the laser transmitter. Also, the system dimensions are mostly limited by cost. Most importantly, an eye safe infrared (IR) laser system of suitable dimensions is designed to transfer power at 100 m and is shown to be capable of harvesting 1.2 W through simulations.

In the last part of this thesis, two PV panels are used for daytime solar EH in an outdoor environment. The required power of 1 W is shown to be generated by each solar panel for periods of hours under sunny and partly cloudy weather conditions. However, the presence of high density clouds is shown to decrease the harvested power significantly; hence, additional charging from laser sources and a battery are needed. Therefore, a hybrid solar/laser based EH system is simulated to investigate the feasibility of an annual autonomous SC operation in 'darker' places on earth such as Edinburgh in the UK. The results show the possibility of supplying a SC with 1 W per hour using the solar panel from the experiments, the 100 m IR laser link and a small battery.

Declaration of originality

I hereby declare that the research recorded in this thesis, all of the included publications and the thesis itself were composed and originated entirely by myself in the Light-Fidelity (Li-Fi) Research and Development (R&D) Centre, Institute for Digital Communications, School of Engineering, University of Edinburgh.

The exceptions to the above are listed below:

- Concepts that are presented in Chapter 3, Chapter 4 and Chapter 5 have originated from discussions with Dr. Stepan Kucera and Dr. Holger Claussen from Nokia, Bell Labs in Ireland as part of the project titled 'Free-space optical backhaul communication and power transfer for autonomous small cells'.
- The light-emitting diode driver, used in the experiments of Chapter 3, has been built by Dr. Zixiong Wang in the Li-Fi R&D Centre.
- Measurements in the experiments of Chapter 3 and Chapter 4 have been obtained in collaboration with Dr. Muhammad Ijaz and Dr. Stefan Videv, respectively, in the Li-Fi R&D Centre.

Ioannis (John) Fakidis

Acknowledgements

First of all, I would like to thank my supervisor, Professor Harald Haas, who gave me the opportunity to pursue the Ph.D. degree on a novel research area of practical interest. His continuous support and encouragement for hard work contributed to the completion of my studies. His high standards, attention to detail and 'out-of-the-box' thinking for the solution of difficult real-world problems contributed to the shape of my research profile.

The work of Professor Haas was supported by the Engineering and Physical Sciences Research Council under the Established Career Fellowship Grant EP/K008757/1. This work was supported in part by the Bell Labs, Nokia Ireland. In particular, I would like to thank Dr. Holger Claussen and Dr. Stepan Kucera for the fruitful collaboration on our joint project. I would also like to thank them for our excellent discussions on technical aspects of the same project and their appropriate research guidelines.

I would like to thank Dr. Majid Safari for our constructive discussions on the area of free-space optics and his important advice during my studies. I would like to express my sincere thanks to Dr. Athanasios Stavridis and Dr. Dobroslav Tsonev for their help with the beginning of my studies and our useful discussions on topics of common research interest. I would also like to thank Dr. Stefan Videv for our substantial collaboration on practical aspects of my work.

I would like to express my gratitude to Ms. Adean Lutton for her continuous support and assistance throughout my studies. Her valuable contribution to research paper proofreading is highly appreciated. Also, I would like to thank Fr. Luke Jeffery for proofreading parts of this thesis.

My four-year research trip would not have been possible without the support of my close friends. Thus, I would like to thank Vasilis and Loukas for standing by me whenever I needed their help and advice. I would also like to thank Dimitris, Sakis, Tasos, Zafeiris and Giorgos and our newer friends Miryam, Alexis, Isidora, Stefanos, Gökçen, Tezcan, Elham and Hossein for sharing enjoyable moments in Edinburgh.

I would like to express my wholehearted gratitude to my partner, Danai, for her selfless love and encouragement during my studies. I will never forget her care and patience in addition to my family's courage and determining contribution to our needs through thick and thin. Also, I would like to express my love to my mother, my father and my sister for their love and support throughout my life and the values they passed on to me. The least I can do is to dedicate this thesis to Danai and my family.

Last but not least, let me thank God for keeping me strong until the end of my studies in Edinburgh.

Contents

List of figures

List of tables

Acronyms and abbreviations

AEL	Accessible emission limit
AM	Air mass
Al	Aluminium
a-Si	Amorphous silicon
am	Ante meridiem
ARC	Anti-reflection coating
CW	Continuous wave
CMRS	Coupled magnetic resonance system
c-Si	Crystalline silicon
CF	Curve factor
DC	Direct current
EM	Electromagnetic
EH	Energy harvesting
FF	Fill factor
FSO	Free space optical
FWHM	Full width at half maximum
GaAs	Gallium arsenide
HWHM	Half width at half maximum
InGaAsP	Indium gallium arsenide phosphide
IPTS	Inductive power transfer system
IR	Infrared
LD	Laser diode
LPC	Laser power converter
Laser	Light amplification by stimulated emission of radiation
LED	Light-emitting diode
LoS	Line-of-sight
MPE	Maximum permissible exposure
MPP	Maximum power point
MSE	Mean squared error

MPT	Microwave power transfer
mono-c-Si	Mono-crystalline silicon
multi-c-Si	Multi-crystalline silicon
MJ	Multi-junction
MQW	Multi-quantum well
NIR	Near infrared
NOHD	Nominal ocular hazard distance
NSC	Non-sequential components
N	North
OAP	Off-axis parabolic
OW	Optical wireless
OWC	Optical wireless communications
OWPT	Optical wireless power transfer
PM	Parabolic mirror
PD	Photodiode
PV	Photovoltaic
PCX	Plano-convex
pm	Post meridiem
PH	Power harvesting
PSD	Power spectral distribution
RF	Radio frequency
Si	Silicon
SC	Small cell
SPS	Solar power satellite
STC	Standard test conditions
SoC	State of charge
SotA	State-of-the-art
VL	Visible light
VLC	Visible light communications
WLED	White light-emitting diode
WET	Wireless energy transfer
WPT	Wireless power transfer

Nomenclature

Constants (mathematical and physical)

e	2.718281828	Base of the natural logarithm (Euler's number)
j	$\sqrt{-1}$	Imaginary unit
π	3.141592654	Ratio of the circumference over the diameter of a circle
k_{B}	8.617×10^{-5} eV/K	Boltzmann constant
q_{e}	1.602×10^{-19} C	Electron charge
h	4.136×10^{-15} eV·s	Planck constant
c	3×10^{8} m/s	Speed of light

Mathematical functions

$\mathrm{erf}\,(.)$	Error function
$\exp(.)$	Natural exponential function

Mathematical matrices

$\mathbf{M}_{\mathrm{lens}}$	$ABCD$ matrix of a thick lens
$\mathbf{M}_1$	$ABCD$ matrix of free space between a LD and the input surface of a lens
$\mathbf{M}_2$	$ABCD$ matrix of free space between the output surface of a lens and the input surface of a solar receiver
$\mathbf{M}$	Total $ABCD$ matrix of a LD and lens based optical system

Mathematical operators

$\det[.]$	Determinant of a matrix
$\mathrm{Im}\{.\}$	Imaginary part of a complex number
$\mathrm{Re}\{.\}$	Real part of a complex number

Mathematical variables

(x, y, z)	Cartesian coordinates

z'	Substituted variable for z
z''	Substituted variable for z

Physical functions

$\eta_{\mathrm{c}}(z)$	Collection efficiency of a solar receiver as a function of z in the case of a single optical link
$V_{\mathrm{es}}(\lambda)$	Eye sensitivity as a function of wavelength
$G(x,y,z)$ [W/m^2]	Gaussian beam intensity generated by a LD as a function of Cartesian coordinates
$G'(x,y,z)$ [W/m^2]	Gaussian beam intensity of a LD reshaped by a lens as a function of Cartesian coordinates
$W_{\mathrm{x}}(z)$ [m]	Gaussian beam radius along x- axis as a function of z
$W_{\mathrm{y}}(z)$ [m]	Gaussian beam radius along y- axis as a function of z
$G_{\mathrm{Rx}}(z)$ [W/m^2]	Irradiance of LD measured from a square aperture stop with side length $2x_0$ at a distance z
$G'_{\mathrm{Rx}}(z)$ [W/m^2]	Irradiance of LD with lens measured from a square aperture stop with side length $2x_0$ at a distance z
$P_{\mathrm{Rx,o}}(z)$ [W]	Optical power collected by a solar receiver as a function of z
$\eta_{\mathrm{sr}}(z)$	Power conversion efficiency of a solar receiver as a function of z
$p(\lambda)$ [W/m]	Power spectral distribution of a WLED as a function of wavelength
$b(\lambda)$ [m^{-1}]	Relative power spectral density of a WLED as a function of wavelength
$W'_{\mathrm{x}}(z')$ [m]	Reshaped Gaussian beam radius along x- axis as a function of z'
$W'_{\mathrm{y}}(z'')$ [m]	Reshaped Gaussian beam radius along y- axis as a function of z''
$\rho(z)$[A/W]	Responsivity of a solar receiver as a function of z
$G_{\mathrm{sim}}(\theta_{\mathrm{x}},\theta_{\mathrm{y}})$ [W/m^2]	Simulated beam intensity generated from a rectangular source as a function of θ_{x} and θ_{y}

Physical variables

κ [W]/[W/m^2]	Accessible emission limit of a laser product
a_{m}	Air mass
N_{anr}	Analysis rays in the simulation model
ϑ [deg]/[rad]	Angle between a ray and the optical axis of a point source in paraxial optics

θ [deg]/[rad]	Angle of incidence of parallel solar rays on the earth's surface
a_{x} [deg]/[rad]	Angular divergence along x- axis in the simulation model
a_{y} [deg]/[rad]	Angular divergence along y- axis in the simulation model
α [deg]/[rad]	Angular subtense of an optical rectangular source defined in BS EN 60825-1:2014
τ [m]	Astigmatism of the beam generated from a LD
β [m]	Back focal length of a thick lens
E_{g} [eV]	Bandgap energy of a semiconductor
N_{c}	Cells number of a solar panel connected in series
R_{ch} [Ω]	Characteristic resistance of a solar receiver
$q_{0\mathrm{x}}$	Complex parameter of a Gaussian beam along x- axis at the emission point of a LD
$q_{4\mathrm{x}}$	Complex parameter of a Gaussian beam along x- axis at the input plane of a solar receiver
$q_{1\mathrm{x}}$	Complex parameter of a Gaussian beam along x- axis at the tangent plane to the input surface of a lens
$q_{2\mathrm{x}}$	Complex parameter of a Gaussian beam along x- axis at the tangent plane to the output surface of a lens
$q_{0\mathrm{y}}$	Complex parameter of a Gaussian beam along y- axis at the emission point of a LD
$q_{4\mathrm{y}}$	Complex parameter of a Gaussian beam along y- axis at the input plane of a solar receiver
$q_{1\mathrm{y}}$	Complex parameter of a Gaussian beam along y- axis at the tangent plane to the input surface of a lens
$q_{2\mathrm{y}}$	Complex parameter of a Gaussian beam along y- axis at the tangent plane to the output surface of a lens
q	Complex parameter of Gaussian beams
C_6	Correction factor used in BS EN 60825-1:2014
λ_{c} [m]	Cut-off wavelength of a semiconductor
D_{ap} [m]	Diameter of a circular aperture
Δ_{s} [m]	Diameter of a WLED source
Δ_{opt} [m]	Diameter of collimation optics
D_{im} [m]	Diameter of the circular image of a laser beam

H_{LoS}	Direct current gain of the LoS optical channel for a generalised Lambertian source
H'_{LoS}	Direct current gain of the LoS optical channel for a generalised Lambertian source with collimation optics
P_{in} [W]	Direct current input electrical power to an optical source (either a LED or a LD)
d_1 [m], d_2 [m]	Distance between a lens and a laser screen defined for the measurement of circular image diameter of a diverging laser beam
d' [m]	Distance between a LED and the planar surface of a PCX lens
d'' [m]	Distance between a LED and the vertex of a PM
d_0 [m]	Distance between the emission point of a LD and the vertex of the input surface of a lens
$d_{1\text{x}}$ [m]	Distance of the Gaussian beam waist along x- axis reshaped by a lens and the vertex of the output lens surface
$d_{1\text{y}}$ [m]	Distance of the Gaussian beam waist along y- axis reshaped by a lens and the vertex of the output lens surface
S_{eff} [m^2]	Effective area of a solar receiver (either cell or panel)
$I_{0,\text{eff}}$ [A]	Effective dark saturation current of diode of a single diode based solar panel model
A_{eff}	Effective diode ideality factor of a single diode based solar panel model
f'' [m]	Effective focal length of a PM
f [m]	Effective focal length of a thick lens
$I_{\text{Ph,eff}}$ [A]	Effective generated photo-current of a single diode based solar panel model
γ [m]	Effective reflected focal length of the OAP mirror used in simulation
$R_{\text{S,eff}}$ [Ω]	Effective series resistance of a single diode based solar panel model
$R_{\text{P,eff}}$ [Ω]	Effective shunt resistance of a single diode based solar panel model
I_{m} [A]	Electrical current at the MPP of a solar receiver
I_{L} [A]	Electrical current of a resistance load connected to the output of a solar receiver
P_{L} [W]	Electrical power harvested by the load resistor of a solar panel
V_{m} [V]	Electrical voltage at the MPP of a solar receiver

V_{L} [V]	Electrical voltage of a resistance load connected to the output of a solar receiver
ϵ_{eff}	Error between the theoretical and experimental value of power efficiency for a LD
Δ_{r} [m]	External diameter of a reflector
η_{LD}	External power efficiency of a LD
f'_{sr}	Fill factor of a solar panel for a LED based link with collimation optics
f_{sr}	Fill factor of a solar receiver
A'	First element of a total $ABCD$ matrix for a LD and lens based optical system
A	First element of an $ABCD$ matrix for a thick lens with spherical surfaces
I_{D} [A]	Forward current of diode of a single diode based solar panel model
D'	Fourth element of a total $ABCD$ matrix for a LD and lens based optical system
D	Fourth element of an $ABCD$ matrix for a thick lens with spherical surfaces
$W_{4\mathrm{x}}$ [m]	Gaussian beam radius along x- axis at the input plane of a solar receiver
$W_{1\mathrm{x}}$ [m]	Gaussian beam radius along x- axis at the tangent plane to the input surface of a lens
$W_{2\mathrm{x}}$ [m]	Gaussian beam radius along x- axis at the tangent plane to the output surface of a lens
$W_{4\mathrm{y}}$ [m]	Gaussian beam radius along y- axis at the input plane of a solar receiver
$W_{1\mathrm{y}}$ [m]	Gaussian beam radius along y- axis at the tangent plane to the input surface of a lens
$W_{2\mathrm{y}}$ [m]	Gaussian beam radius along y- axis at the tangent plane to the output surface of a lens
$W_{0\mathrm{x}}$ [m]	Gaussian beam waist along x- axis at the rectangular emission cross section of a LD
$W_{3\mathrm{x}}$ [m]	Gaussian beam waist along x- axis reshaped by a lens

W_{0y} [m]	Gaussian beam waist along y- axis at the rectangular emission cross section of a LD
W_{3y} [m]	Gaussian beam waist along y- axis reshaped by a lens
x_s [m]	Half length of a rectangular optical power sensor
x_0 [m]	Half length of a rectangular solar receiver
y_s [m]	Half width of a rectangular optical power sensor
y_0 [m]	Half width of a rectangular solar receiver
h_m [m]	Height of the OAP mirror used in the simulation
P_{id} [W]	Ideal electrical power harvested by a PV receiver
P'_{id} [W]	Ideal electrical power harvested by a solar receiver of a LED based link with collimation optics
ω [deg]/[rad]	Inclination angle between the z- axis and the surface of a PV panel
I_{in} [A]	Input current to a driver of LEDs
$P_{in,d}$ [W]	Input electrical power to a driver of LEDs
V_{in} [V]	Input voltage to a driver of LEDs
N_{lr}	Layout rays in the simulation model
l_m [m]	Length of the OAP mirror used in the simulation
Δ_l [m]	Lens diameter
r	Lens reflectance
n	Lens refractive index
t_c [m]	Lens thickness
E_1 [eV]	Lower energy level of an atom in a band diagram
η_{LED} [lm/W]	Luminous efficiency or efficacy of a LED
Φ [lm]	Luminous flux of a WLED
$\Delta_{PM,max}$ [m]	Maximum aperture diameter of a PM
$I_{0,eff,max}$ [A]	Maximum effective dark saturation current of diode of the discrete space of an exhaustive search algorithm
$I_{Ph,eff,max}$ [A]	Maximum effective generated photo-current of the discrete space of an exhaustive search algorithm
$A_{eff,max}$	Maximum effective ideality factor of diode of the discrete space of an exhaustive search algorithm
$R_{S,eff,max}$ [Ω]	Maximum effective series resistance of the discrete space of an exhaustive search algorithm

$R_{\text{P,eff,max}}$ [Ω]	Maximum effective shunt resistance of the discrete space of an exhaustive search algorithm
$P_{\text{Tx,o,m}}$ [W]	Maximum optical power of a LD
$P_{\text{LED,o,m}}(\lambda_{\text{m}})$ [W]	Maximum optical power of a WLED at a specific wavelength λ_{m}
ν [W]/[W/m^2]	Maximum permissible exposure of a laser product
P_{m} [W]	Maximum power harvested by a resistance load of a PV receiver
η'_{max}	Maximum total electrical efficiency of a LED based link with collimation optics
η_{max}	Maximum total electrical efficiency of an OW link
α_{min} [deg]/[rad]	Minimum angular subtense of an optical source defined in BS EN 60825-1:2014
$\Delta_{\text{PM,min}}$ [m]	Minimum aperture diameter of a PM
$I_{0,\text{eff,min}}$ [A]	Minimum effective dark saturation current of diode of the discrete space of an exhaustive search algorithm
$I_{\text{Ph,eff,min}}$ [A]	Minimum effective generated photo-current of the discrete space of an exhaustive search algorithm
$A_{\text{eff,min}}$	Minimum effective ideality factor of diode of the discrete space of an exhaustive search algorithm
$R_{\text{S,eff,min}}$ [Ω]	Minimum effective series resistance of the discrete space of an exhaustive search algorithm
$R_{\text{P,eff,min}}$ [Ω]	Minimum effective shunt resistance of the discrete space of an exhaustive search algorithm
d_{NOHD} [m]	Nominal ocular hazard distance of a laser product
N_{Tx}	Number of optical transmitters, i.e. pairs of a LD and a lens
V_{oc} [V]	Open-circuit voltage of a solar receiver
λ_0 [m]	Operating wavelength of a LD
η_{opt}	Optical efficiency of collimation optics
$P_{\text{Rx,o,l}}$ [W]	Optical power collected by a lens at its planar input surface
$P_{\text{Rx,o}}$ [W]	Optical power collected by a solar receiver
P_{s} [W]	Optical power measured by the S121B sensor
$P_{\text{Rx,o,t}}$ [W]	Optical power transmitted by a lens at its spherical output surface
η'_{sr}	Optical-to-electrical conversion efficiency of a solar panel of a LED based link with collimation optics

η_{sr}	Optical-to-electrical conversion efficiency of a solar receiver
d_{lpc} [m]	Optimised distance along the y- axis of the LPC from the mirror
m	Order of a generalised Lambertian optical source
I_{P} [A]	Parallel current to the source of a single diode based solar panel model
ϑ_{x} [deg]/[rad]	Parallel to the junction beam divergence of a LD
G_0 [W/m^2]	Peak optical intensity of a Gaussian beam at the emission point of a LD
ϑ_{y} [deg]/[rad]	Perpendicular to the junction beam divergence of a LD
ψ_{x} [deg]/[rad]	Plane angle along x- axis of a truncated cone created by the full laser beam widths at 36.8% of peak intensity at d_1 and d_2
ψ_{y} [deg]/[rad]	Plane angle along y- axis of a truncated cone created by the full laser beam widths at 36.8% of peak intensity at d_1 and d_2
ψ [deg]/[rad]	Plane angle of a truncated cone created by the laser beam circular images at two link distances d_1 and d_2
η_{d}	Power efficiency of a driver of LEDs
$R_{4\text{x}}$ [m]	Radius of curvature of a Gaussian beam along x- axis at the input plane of a solar receiver
$R_{1\text{x}}$ [m]	Radius of curvature of a Gaussian beam along x- axis at the tangent plane to the input surface of a lens
$R_{2\text{x}}$ [m]	Radius of curvature of a Gaussian beam along x- axis at the tangent plane to the output surface of a lens
$R_{4\text{y}}$ [m]	Radius of curvature of a Gaussian beam along y- axis at the input plane of a solar receiver
$R_{1\text{y}}$ [m]	Radius of curvature of a Gaussian beam along y- axis at the tangent plane to the input surface of a lens
$R_{2\text{y}}$ [m]	Radius of curvature of a Gaussian beam along y- axis at the tangent plane to the output surface of a lens
R_1 [m]	Radius of the input surface of a lens
R_2 [m]	Radius of the output surface of a lens
k	Ratio of the power conversion efficiency over the FF of a solar panel of a LED based link
k'	Ratio of the power conversion efficiency over the FF of a solar panel

	of a LED based link with collimation optics
z_{0x} [m]	Rayleigh range of a Gaussian beam generated by a LD along x- axis
z_{0y} [m]	Rayleigh range of a Gaussian beam generated by a LD along y- axis
z_{3x} [m]	Rayleigh range of a Gaussian beam of a LD reshaped by a lens along x- axis
z_{3y} [m]	Rayleigh range of a Gaussian beam of a LD reshaped by a lens along y- axis
G_{solar} [W/m^2]	Received solar irradiance by a PV panel
η_{ref}	Reference efficiency of a solar panel
T_{ref} [°C]	Reference temperature of a solar panel
h_{r} [m]	Reflector height
r'	Reflector reflectance
R_{L} [Ω]	Resistance load connected to the output of a solar receiver
B' [m]	Second element of a total $ABCD$ matrix for a LD and lens based optical system
B [m]	Second element of an $ABCD$ matrix for a thick lens with spherical surfaces
$\phi_{1/2}$ [deg]/[rad]	Semi-angle of half power of a WLED
$\phi'_{1/2}$ [deg]/[rad]	Semi-angle of half power of an extended optical source with a WLED and collimation optics
I_{sc} [A]	Short-circuit current of a solar receiver
$G_{\text{sim},0}$ [W/m^2]	Simulated overall peak intensity of the beam
γ_0	Solar irradiance coefficient of a PV panel
S_{x}	Super-Gaussian factor along the x- axis in simulation
S_{y}	Super-Gaussian factor along the y- axis in simulation
β_0 [°C^{-1}]	Temperature coefficient of a solar panel
T [°C]/[K]	Temperature of a PV panel
C' [m^{-1}]	Third element of a total $ABCD$ matrix for a LD and lens based optical system
C [m^{-1}]	Third element of an $ABCD$ matrix for a thick lens with spherical surfaces
T_2 [s]	Time parameter used in BS EN 60825-1:2014
d [m]	Total distance of an OW link

η_{Tx}	Total efficiency of a transmitter
η'_{Tx}	Total efficiency of a transmitter with a LED and collimation optics
$P_{\text{Tx,o}}$ [W]	Total optical power of an elliptical Gaussian beam generated by a LD
$P_{\text{LED,o}}$ [W]	Total output optical power of a WLED
D_{c} [m]	Transverse coherence length of a laser beam
E_2 [eV]	Upper energy level of an atom in a band diagram
V_{D} [V]	Voltage across the diode of a single diode based solar panel model
λ [m]	Wavelength of a WLED in the VL spectrum
w_{m} [m]	Width of the OAP mirror used in the simulation

Chapter 1
Introduction

1.1 Motivation

Optical wireless communications (OWC) have been proposed as a complementary technology to radio frequency (RF) data communication and as a potential solution to the exponential increase in demand for wireless data transmission [1]. The broad research field of OWC can be separated into two parts: free space optical (FSO) communications and visible light communications. Free space optical systems mostly comprise coherent data transmission using sources of light amplification by stimulated emission of radiation (laser) at the transmitter and photodiodes (PDs) at the receiver. Also, FSO systems are usually deployed outdoors covering distances of several kilometres. Visible light communications facilitate the use of light-emitting diodes (LEDs) and PDs and are mainly applied to indoor public places such as offices, conference venues, museums, hotels and hospitals.

The technology of small cells (SCs) is widely accepted as one of the solutions with most potential to the exponential increase in capacity demand of heterogeneous mobile networks [2]. Despite the fact that a large scale outdoor deployment of SCs offers advantages such as high network capacity [3] and reduced power consumption [4], the high installation cost is the most restrictive factor. The technology of optical fibres is considered to be one of the potential solutions to the provision of high speed backhaul communication to SCs [5]. However, its main disadvantages are the installation cost and the requirement for a mains power supply. Therefore, alternative sources of power supply and wireless backhaul communication are needed in order to make the deployment of SCs more cost effective.

A dense and irregular outdoor installation of SCs might not allow for a mains power supply due to the remoteness and inaccessibility of their location. Energy harvesting (EH) or power harvesting (PH) from renewable resources has been proposed as a potential solution to the problem of designing self-sustainable and energy autonomous communication networks [6]. The application of EH from natural sources such as sun and wind is considered to be more feasible for SCs due to the lower energy demand and cost compared with typical macro-cells [7]. How-

ever, the variability of weather conditions results in unpredictability in the levels of harvested power and unreliability for communication applications requiring high quality of service. As a result, the concept of wireless power transfer (WPT) or wireless energy transfer, based on artificial electromagnetic (EM) radiation, is considered to be a more reliable complementary solution.

The concept of WPT was inspired and demonstrated for the first time by Nikola Tesla in the late 19^{th} century using a RF resonant transformer, termed a Tesla coil [8]. The application of WPT is also feasible using devices operating at the visible light and infrared (IR) part of the EM spectrum, such as laser diodes (LDs) or LEDs and solar cells. This concept applied to the optical domain is termed optical wireless power transfer (OWPT).

1.2 Objectives

In practice, the structure of a SC base station has to be uncomplicated. Current types of SCs include femtocells, picocells and microcells. Microcells have the largest size and power requirements with femtocells having the smallest. Typical values of power consumption of $6\,\text{W}-10\,\text{W}$ are currently reported for SCs; these are expected to decrease to $5\,\text{W}$ by 2020 [9]. Also, $5.2\,\text{W}$ of power consumption have already been reported for femtocells [7, 10]. The overall power consumption of a state-of-the-art transceiver phased array chip-set is reported to be $2\,\text{W}$ operating at millimetre waves [11]. However, the use of variable gain and low noise amplifiers inevitably increases the total required electrical power of the device [11]. In this thesis, the use of exclusively passive components is considered to reduce power consumption more than the minimum reported value of $2\,\text{W}$. For the same reason, all the signal processing functions are assumed to be moved to a central unit. Under these main assumptions, electrical power supply of $1\,\text{W}$ is considered to be required for an autonomous SC operation.

Therefore, the first objective is to investigate the simultaneous application of OWPT for the provision of $1\,\text{W}$ and high speed FSO backhaul communication to outdoor SCs. However, the research in this thesis is focused on the concept of OWPT to SCs during nighttime. The condition of darkness is selected, because the SC needs to harvest power even in the absence of ambient light. Hence, the optical wireless (OW) links must be able to transfer power of some units of W. Also, to ensure eye safety along the entire wireless link, the optical beam needs to be shaped accordingly. The installation of SCs is considered within the infrastructure of urban

areas, such as on lamp posts or bus stations. Thus, the power transfer links need to operate at relatively long distances in the order of $100\,\mathrm{m}-300\,\mathrm{m}$. In addition, the potential large scale outdoor deployment of SCs requires the transmitter and receiver to be compact, i.e. in the order of cm^3. Since light can provide high speed data communication and EH at the same time [12], intelligent sleep mode concepts can be applied to the SC. When the light is turned off, there is no need for a backhaul communication link; thus, the SC goes into sleep mode. So long as light is shed on a PV cell, energy is transferred along with high speed data; this is a unique two-fold objective that is achievable using solar cells. The final objective is to explore the concept of solar PH for the daytime provision of $1\,\mathrm{W}$ to SCs. This is to determine if the additional use of electrochemical storage and optical sources for power transfer is required.

1.3 Contribution

For the first time in this thesis, a $5\,\mathrm{m}$ indoor OW link is created to harvest electrical power of $1\,\mathrm{W}$ during darkness hours. A white light-emitting diode (WLED) is used to transmit $5\,\mathrm{W}$ of optical power to an amorphous Si PV panel. Three different optical devices are used for light collimation at the transmitter. Also, an analytical model is developed for the end-to-end link and simple electrical measurements are taken to determine unknown parameters of the model. Despite the use of a large mirror at the optical source, the maximum harvested power and power efficiency of the link are reported to be only $18.3\,\mathrm{mW}$ and 0.1%, respectively. Thus, an increase in the energy efficiency of the link and, therefore, in the efficiency of each component is targeted for a follow-up study. Hence, up to five red LDs with collimation lenses are used for OWPT in the order of mW to a crystalline silicon (c-Si) solar receiver. In addition to the link implementation, a theoretical framework is developed for the end-to-end laser based WPT system; the propagation model of an elliptical Gaussian beam and a single diode based physical model of a solar panel are used. These models are used for curve fitting of the collected data, determination of parameters for eye safety and, most importantly, an estimation of the required number of LDs for harvesting $1\,\mathrm{W}$. The highest power efficiency of 3.2% is attained for the link that comprises two LDs and a mono-crystalline silicon (mono-c-Si) PV cell; this corresponds to an increase by 32 times compared with the WLED based system. Also, the components efficiency is determined, and a power efficiency of 13.3% is reported for the mono-c-Si cell. Most importantly, the implemented laser system is compared in terms of energy efficiency with an inductive power transfer system with optimally shaped dipole coils; a 2.7 times improve-

ment is shown to be provided by the red laser based WPT system. The main drawback is the requirement for beam shielding up to a distance of $3.6\,\mathrm{m}$ for the developed Class 3B system. Since the realised EH links operate at a distance of $5.2\,\mathrm{m}$, another experimental study is undertaken to show that practical links of $100\,\mathrm{m}-300\,\mathrm{m}$ are feasible. Hence, the divergence of a collimated beam created using the red LD and a large diameter lens is determined with a targeted value of $1\,\mathrm{mrad}$. An average elliptical beam divergence of $4.4\,\mathrm{mrad}$ of full width at 36.8% of peak intensity is reported at 4.4 times the required value. Therefore, the OW link can be characterised as highly directive, and the geometrical losses can be counterbalanced using a large solar panel or collection mirror at the receiver.

The required number of red LDs for harvesting $1\,\mathrm{W}$ from the mono-c-Si PV cell is shown to be 61. Each red LD has a typical output optical power of $50\,\mathrm{mW}$ and a typical power efficiency of 22%. This offers the basis for the next simulation design of a laser array comprising 42 LDs and collimation lenses operating at $785\,\mathrm{nm}$ in Zemax. The smaller number of $785\,\mathrm{nm}$ laser sources compared with the 61 red LDs is used because of their higher output optical power and efficiency, i.e. $171\,\mathrm{mW}$ and 27%, respectively, per device. An average full width at half maximum beam divergence of $1.4\,\mathrm{mrad}$ is calculated for the $785\,\mathrm{nm}$ laser link according to the analytical model. Optical power of $7\,\mathrm{W}$ is shown to be received by the solar cell up to a distance of $30\,\mathrm{m}$ through simulations and theory. This high amount of power is expected to increase the solar cell's efficiency above 13.3%, so that the harvested electrical power of $1\,\mathrm{W}$ would be affirmed. This is because an increase in the incident optical power on the solar cell results in a decrease of its series resistance. This is attributed to the increase in the conductivity of the active layer [13]. Also, it is assumed that the received optical power of $7\,\mathrm{W}$ is lower than the level of maximum efficiency point of the solar cell [14]. Yet beam enclosure of the designed Class 3B system will be needed for eye safety. A significant increase in the LD power efficiency and size of optics used at the transmitter and receiver is considered in the next simulation study for the creation of a Class 1 laser system. Thus, a $100\,\mathrm{m}$ WPT link is designed using a high power $975\,\mathrm{nm}$ LD, the mono-c-Si solar cell and two large mirrors at the transmitter and receiver for collimation and collection, respectively. The transfer of optical power of $8.7\,\mathrm{W}$ to the solar cell is regarded to be sufficient for PH of $1\,\mathrm{W}$. However, the mirror volume is considered to be unacceptable for a practical application of SC EH, since it is in the order of m^3. To affirm practical dimensions of an OWPT system for SCs, an increased maximum permissible exposure (MPE) limit for eye safety is required. Hence, the wavelength of $1550\,\mathrm{nm}$ is selected for the last simulation design, since it offers a MPE of $100\,\mathrm{mW/cm}^2$.

Thus, a highly directive link is created using two mirrors with dimensions of cm^3, and the beam convergence is in the order of μrad. Harvesting $1.2\,W$ of electrical power at $100\,m$ is shown to be feasible using 47 small laser power converters (LPCs); this is the major contribution of the simulations. Each LPC has a size of $5 \times 5\,mm^2$ and achieves 42% of power efficiency for $237.5\,mW/cm^2$ of received irradiance [15]. However, this laser system is expected to be highly sensitive to pointing errors and to have stringent requirements for beam tracking. Hence, the use of a reception mirror of larger dimensions will be needed to counterbalance misalignment losses.

The final contribution is given with an experimental study, where two multi-crystalline silicon (multi-c-Si) PV panels are used for daytime solar EH in an outdoor environment. The solar panels are capable of harvesting maximum power of $5\,W$ and $10\,W$ under standard test conditions. The variability of weather conditions is shown to cause fluctuations in the harvested electrical power. Despite the unfavourable presence of high-density clouds, the constant power supply of at least $1\,W$ is shown to be possible using the $10\,W$ PV panel for three hours in total. Also, a maximum average harvested power of $4.1\,W$ is reported using the $10\,W$ solar panel for a two-hour period. However, there are time periods of solar PH in the order of mW, during which the additional use of optical sources for WPT is required. This unique potential of simultaneous EH from a natural resource and man-made radiation sources is offered in the optical region of the EM spectrum using solar panels, while it is absent from the RF part of the EM spectrum using rectennas. Therefore, a follow-up simulation study is provided to determine the required battery size for the SC powered through solar EH on an annual basis. The $5\,W$ and $10\,W$ PV panels from the experiments are considered, and the feasibility of an energy autonomous SC operation is shown. However, the dimensions and the weight of the batteries are considered to be unacceptable for the practical application of SC EH. Hence, a hybrid power provisioning system is proposed assuming the use of the $10\,W$ panel for solar PH and the $1550\,nm$ laser based WPT link. The required electrical load of $1\,W$ per hour is shown to be met using the LPC with a maximum harvested power of $2\,W$ and the multi-c-Si solar panel without the need for electrochemical storage. The use of a battery is important though, since it will provide the SC with the required power during unfavourable weather conditions, such as fog and rain. Thus, a battery of suitable dimensions is shown to keep a full state of charge during the whole year.

1.4 Layout

The rest of this thesis is organised as follows: Chapter 2 provides the relevant background to research in Chapters 4 and 5. In particular, a literature review of experimental RF based and OWPT systems is given. Also, practical values of features of the components available for OWPT and EH from sunlight are reported. References of practical OW systems for simultaneous communication and power transfer are given with the limitations imposed by an atmospheric channel and potential solutions to them. In addition, the physical models of the components of a LD based WPT system are presented along with metrics of the energy efficiency of the link and its components. In Chapter 3, an analytical framework of a WLED based link is provided for the scenarios of uncollimated and collimated WPT. Also, the experimental WLED based WPT system is given. The components, setup and methodology of each experiment are provided. The experimental and analytical results are given. In Chapter 4, two studies are given for an experimental red LD based WPT system; the total link and components power efficiency and the laser beam collimation are investigated. Details of the components, setup and method of each experiment are provided. Also, the eye safety regulations are examined for the laser system with the highest link efficiency using the analytical model that is developed in Chapter 2. The measured data are given and are verified by the analytical framework of Chapter 2. The experimental system created for the measurement of beam divergence is given with a respective discussion of the experimental and theoretical results. In Chapter 5, three designs of a $100\,\mathrm{m}$ IR wireless link for harvesting $1\,\mathrm{W}$ are given in Zemax. The simulation model and eye safety regulations of the link comprising multiple $785\,\mathrm{nm}$ LDs and the mono-c-Si cell are provided. Also, the simulation results, supported by the physical model of the laser system of Chapter 2, are discussed. The two scenarios of the single link consisting of a $975\,\mathrm{nm}$ LD and the mono-c-Si cell are presented. In particular, the motivation, concept, simulation model, eye safety issues and the results of each scenario are given. The motivation, simulation model and the results of the third design including a single $1550\,\mathrm{nm}$ LD and a LPC are provided. In Chapter 6, the concept of solar EH with electrochemical storage for SCs is investigated. The components and setup of the two outdoor scenarios using the $5\,\mathrm{W}$ and $10\,\mathrm{W}$ PV panels are given. Also, the respective experimental results are discussed. The follow-up simulation study for the determination of the required battery for an autonomous year-round SC operation is given. In Chapter 7, the key findings of this thesis are summarised, and concluding comments are provided. Finally, the limitations of the concept of OWPT to SCs are discussed along with possible future directions.

Chapter 2
Background

2.1 Introduction

This chapter provides the relevant background to research in Chapters 4 and 5. In particular, measured data of practical state-of-the-art (SotA) systems for wireless power transfer (WPT) operating in the radio frequency (RF) region of the electromagnetic (EM) spectrum are reported from literature. The harvested power and components efficiency of experimental optical wireless power transfer (OWPT) systems and different technologies of solar cells are referred. The fundamental operation principles of light-emitting diodes (LEDs) and sources of light amplification by stimulated emission of radiation (laser) are reviewed. More importantly, an overview of the optimum wavelengths for optical energy harvesting (EH) is given. Since one of the research objectives is to achieve high speed free space optical (FSO) backhaul communication and power transfer to outdoor small cells (SCs), the constraints imposed by an atmospheric channel and the potential solutions are discussed.

In addition to the literature review, an essential analytical framework is provided for laser based WPT systems with the physical models of each component used. An elliptical Gaussian propagation model is considered for the beam transmitted from a laser diode (LD). The framework developed for a LD based WPT link is used in Chapter 4 for curve fitting of the experimental measurements, the calculation of eye safety parameters and an estimation of the number of LDs required to harvest 1 W from a solar receiver. Also, these models are used to support the simulation results of the first design of Chapter 5.

The rest of this chapter is organised as follows. The literature review is given in Section 2.2. In Section 2.3, the system model is given for LD based WPT.

2.2 Prior work

Previous work on RF based and OWPT systems; the available cells for solar EH; the fundamental properties of LEDs and LDs; the optimal wavelengths for optical EH; simultaneous

optical wireless communications (OWC) and power transfer; and challenges of an atmospheric communication channel and potential techniques to overcome them is given below.

2.2.1 Radio frequency based WPT

Tesla's pioneering work remains the research focus mostly in the RF and more particularly in the microwave region of the EM spectrum [16, 17]. The main techniques of WPT are near field magnetic resonance coupling [18, 19]; inductive coupling [20, 21]; far field RF or microwave power transfer (MPT) [22, 23]; and power transmission from laser sources [24, 25].

A strongly coupled magnetic resonance system (CMRS) was created in [18] and was able to transfer an amount of 60 W to a distance of 2 m with an overall wall-to-load efficiency of 15%. In [19], a CMRS with two lumped impedance transformers was developed with the capability of delivering 10 W at a distance of 13 cm with a total efficiency of 34.5%. Also, the delivery of 105 W at a distance of 30 cm was shown in [20] by the implementation of an inductive power transfer system with a direct current (DC)-to-load efficiency of 77%. However, so long as the outdoor installation of SCs requires a harvested amount of electrical power of 1 W at relatively long link distances in the order of $100\,\text{m} - 300\,\text{m}$, the only potential solutions are considered to be the techniques of wireless power transmission from RF or microwave antennas and laser sources [16].

The EH functionality of RF or microwave radiation is executed by a diode based circuit, termed as rectenna [16, 26]. The rectenna consists of a rectifying circuit and a receiving antenna for the conversion of the input RF or microwave power to DC power. In [16], an overview of the SotA measured values of rectenna efficiency ranging from 1.2% to 90.6% was presented. However, the results of total link efficiency and distance were not reported. Note that rectennas are exclusively designed to harvest either ambient RF power in the order of a few μW [27] or RF power from 'dedicated' antennas [28]. Thus, they do not have the ability to harvest power from a natural resource.

2.2.2 Optical wireless power transfer and solar EH

The concept of OWPT based on laser sources was first introduced for the application of solar power satellite (SPS) [24, 29]. A SPS is a large structure of photovoltaic (PV) cells that is used for EH from sunlight in space. The generated electrical power is transmitted without

wires to receiver stations at distant locations such as the earth's surface, high altitude platforms, satellites, moon and other planets [30]. The techniques of RF and laser based WPT from the SPS to earth have been mostly considered [24]. Wireless power transmission from SPSs to earth can last continuous periods of time compared with the use of solar panels on earth. This is attributed to the absence of nighttime in space [30]. Also, higher amounts of power can be generated using microwave or laser sources to transfer power to earth because of the lack of a diffusing atmosphere. The harvested electrical power by rectennas on earth from a SPS is expected to be two to three times the generated power from sun by terrestrial PV modules of the same area as rectennas [30]. The low end-to-end power efficiencies achieved by MPT systems remain a great challenge for the technology of SPSs; hence, these values are not usually reported in relevant literature [31]. However, a maximum overall link efficiency of 54% was reported for the SPS application with MPT at $2.45\,\text{GHz}$ in 1965; efficiencies of 69%, 95% and 82% were demonstrated for the microwave generator, transmitted beam and the overall capture and rectification of the rectenna, respectively [32].

Current research developments in the technology of high power LDs report levels of output optical power greater than $10\,\text{W}$ with a respective conversion efficiency of more than 65% in the wavelength region of $940\,\text{nm}-980\,\text{nm}$ [33]. Also, the use of passive optical elements for light collimation, such as lenses and mirrors, creates uncomplicated laser systems of very high directivity. In addition to this important characteristic, the wide availability of outdoor solar panels presents the unique potential of power harvesting (PH) both from ambient light, where sunlight is included, and from dedicated laser sources establishing the principle of hybrid solar EH and OWPT. Moreover, high levels of irradiance of $100\,\text{mW/cm}^2$ are considered to be received from sunlight under standard test conditions (STC) [34]. The STC refer to a radiation spectrum of air mass (AM) of 1.5 and a solar receiver temperature of $25\,^\circ\text{C}$. The AM measures how much the atmospheric absorption modifies the intensity and spectral content of solar radiation reaching the earth's surface [34]. This factor is computed by $a_\text{m} = 1/\cos(\theta)$, where θ represents the angle of incidence to the earth's surface. The STC value of $a_\text{m} = 1.5$ is achieved for $\theta = 48.2^\circ$.

Apart from lasers, other available optical sources for wireless energy transfer are LEDs, widely used for the illumination purpose. In general, the main benefits of a LED compared to a LD source are: significantly lower manufacturing cost, high reliability and low dependence of the current-optical power characteristic on temperature variations. On the other hand, the beams generated from LDs generally provide higher directivity or collimation than the diffuse light

from LEDs. However, eye and skin safety becomes an important issue in laser applications where high amounts of optical power need to be transferred to a solar receiver.

In [35], consolidated tables with reported efficiency values of solar cells and modules measured at STC are given. In particular, the modules of amorphous silicon (Si) have an efficiency of 12.3%. Also, the inexpensive technologies of mono-crystalline Si cells and multi-crystalline Si modules have an efficiency in the order of 25.6% and 18.5%, respectively. The use of Si cells is common because of the convenient absorption characteristics matching the solar spectrum [34]. The best efficiency values are reported for the technology of concentrator photovoltaics that is based on multi-junction (MJ) cells [36]. A maximum efficiency of 45.7% of a MJ cell with a concentrator is reported in [35]. In a single junction solar cell, incident photons with energy higher than the cell's bandgap lose their redundant energy as heat, while photons with energy lower than the cell's bandgap are not absorbed and their energy gets lost. Therefore, the principle of MJ cells is based on the use of multiple junctions – made of different semiconductor materials and connected in series – for harvesting energy from different wavelengths of the solar spectrum [37].

The optical illumination incident on the cells of a solar panel is desired to be uniform [38]. Thus, the electrical power harvested by the PV panel is maximised and any mismatch losses between the cells are mitigated. In a typical in-series connection of the cells of a solar panel, the cell that receives the lowest irradiance determines the electrical output of the whole panel. To minimise these mismatch losses, either the cells should be connected in parallel [38] or by-pass diodes along with a blocking diode should be added to the PV system [39]. Also, partial or non-uniform illumination on a single solar cell creates 'hot-spots'. These inhomogeneities need to be avoided, since the power efficiency and spectral response of the PV cell are negatively affected [40].

Laser power converters (LPCs) are a particular type of single junction PV cells that has attracted intense research interest. This is because LPCs achieve maximum values of power efficiency under monochromatic illumination conditions [15, 41]. This is explained by the fact that photons with energy marginally higher than the bandgap of the solar cell contribute to the creation of electron-hole pairs with almost negligible heat losses [34].

Multiple gallium arsenide (GaAs) LPCs were developed in [42] with an output voltage of $4\,\mathrm{V}$. Their conversion efficiency was 50.1% at $810\,\mathrm{nm}$ for an irradiance of $51.6\,\mathrm{W/cm^2}$, but the

distance of the optical wireless link was not reported. Also, an indium GaAs phosphide LPC was developed in [15] with an efficiency of 45% under the illumination conditions of 1550 nm and 100 mW/cm^2. However, a decreased efficiency of 13.3% was reported at STC. An OWPT system was created in [25] consisting of ten high power LDs at 1.4 μm with collimation lenses and 16 gallium antimonide diodes. The reported maximum power harvested by the LPCs at 4 m was 590 mW, while the total link efficiency was not given.

2.2.3 Fundamental properties of LEDs and LDs

To understand the operation differences between LEDs and LDs, the fundamental three ways of light interaction with an atom, i.e. absorption, spontaneous emission and stimulated emission, must be explained [43]. In absorption, an atom is raised from the ground state or a lower energy level, E_1, to a higher energy level or excited state, E_2, absorbing the incident photon. The inverse mechanism of absorption is spontaneous emission; here an atom transits from an upper energy level to a lower energy level releasing a photon; this is a random process. In stimulated emission, a photon of energy $E_2 - E_1$ interacts with an atom placed at an upper energy level. This atom transits to a lower energy level emitting a second photon with identical characteristics of the first one. The operation principle of LEDs is based on spontaneous emission, where light is generated by the radiative recombination of electrons and holes [44]. When LDs are biased below the threshold current, they produce light spontaneously in the same manner with LEDs. However, LDs typically operate above the threshold current in an approximately linear region of output power; this region is characterised by stimulated emission [44].

Stimulated emission acts as an internal mechanism of optical amplification in laser sources and results in an important property, i.e. the optical coherence. This means that all of the photons created by stimulated emission have the same phase, and add constructively to produce a wave of larger amplitude with well defined frequency and phase [44]. The partial coherence of a wave can be analysed along the perpendicular and parallel directions to the wavefront. The degree of coherence along the propagation axis is known as longitudinal or temporal coherence. In the ideal case of perfect temporal coherence, the planes of constant phase are uniformly positioned without any interruption. In practice, however, the degree of coherence of optical sources is limited either by the finite light duration or by interruptions in the wave phase. The average time between phase interruptions of the electric field is termed coherence time [44]. Also, the average distance between two consecutive phase interruptions in a wave is called longitudinal

coherence length [44]. The spectral width or linewidth of an optical source can be defined by the wavelength interval over which the optical intensity is reduced by a fraction of its maximum value; it is typically expressed using the full width at half the maximum intensity [45]. Note that the spectral width is inversely proportional to the coherence time; thus, the linewidth is narrow when the coherence time is long [43]. Laser is considered to be highly coherent and monochromatic in contrast to LED based radiation that is highly incoherent. Typical values of linewidth for LDs and LEDs are of the order of $2\,\text{nm}$ and $50\,\text{nm}$, respectively [44].

The degree of coherence along a wavefront is termed transverse or spatial coherence. In the ideal case of perfect spatial coherence, the wavefronts are continuous and the phase of the optical wave has no interruptions. Spatial coherence has a major impact on the divergence of laser beams. The divergence of a perfectly coherent laser beam passing through a circular aperture of diameter, D_{ap}, can be expressed using the half angle $\theta \simeq \lambda_0/D_{\text{ap}}$ for distances $z \gg D_{\text{ap}}$, where λ_0 denotes the operating wavelength of the LD [43]. In the case of a partially coherent beam, the transverse coherence length, $D_{\text{c}} < D_{\text{ap}}$, is defined to be the maximum separation of two points along the wavefront at which the electric fields are correlated [43]. The diffraction pattern of a partially coherent laser beam is analogous to that of a coherent beam transmitted through an aperture of diameter D_{c}; the half-angular beam divergence is given by $\theta \simeq \lambda_0/D_{\text{c}}$ [43]. Incoherent light beams such as these produced by LEDs have typically very small transverse coherence length; thus, they have very large divergence. A partially coherent light beam is called diffraction limited when the transverse coherence length increases and becomes equal to the aperture diameter.

2.2.4 Overview of optimum wavelengths for optical EH

The selection of an appropriate wavelength is of major importance for the application of OWPT to outdoor SCs at practical distances which are between $100\,\text{m}$ and $300\,\text{m}$. This is because modifying the transmission wavelength affects the maximum allowable limits for eye safety which in turn have a significant impact on the suitability of the system dimensions. Also, each optical wavelength experiences different atmospheric absorption. In addition, the responsivity of the selected solar cell technology takes different values over the wavelength spectrum because of the quantum mechanisms of photon absorption and electron-hole pair generation.

The maximum permissible exposure (MPE) for point laser sources is given as a function of wavelength in Figure 2.1 according to Table A.1 and Table 9 of [46]. Ultra-violet wave-

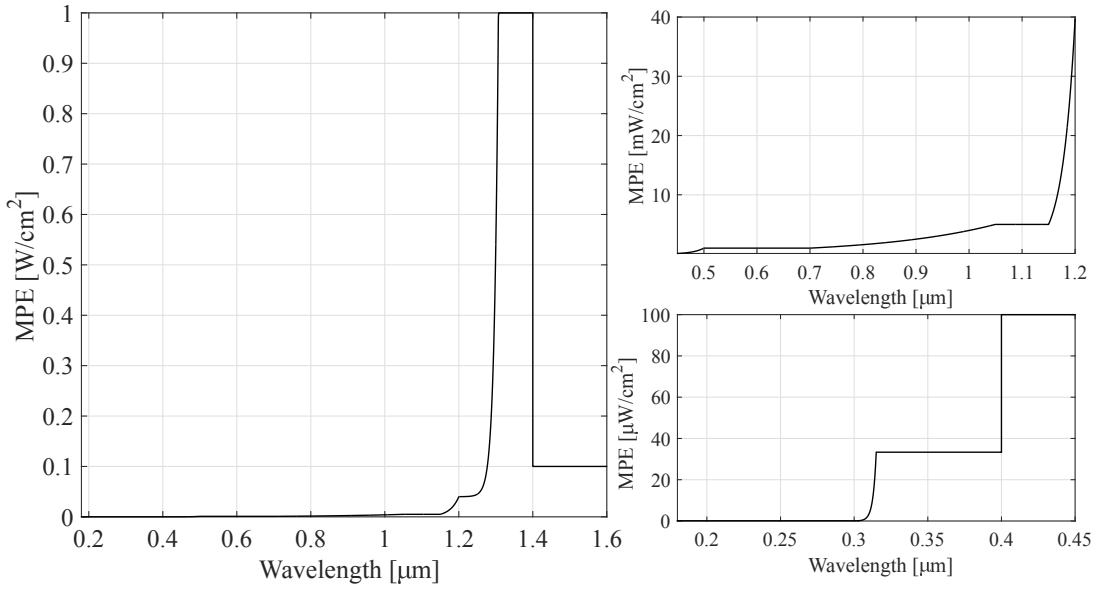

Figure 2.1: *Maximum permissible exposure of point sources of laser as a function of wavelength [46].*

lengths are shown to have very low MPE values which increase gradually from $0.1\,\mu$W/cm^2 to $0.1\,$mW/cm^2 at $400\,$nm. In the visible part of the wavelength spectrum, the MPE keeps increasing from $0.1\,$mW/cm^2 to $1\,$mW/cm^2 at $700\,$nm. The MPE increases exponentially from $1\,$mW/cm^2 to $5\,$mW/cm^2 in the infrared wavelength region between $0.7\,\mu$m and $1.05\,\mu$m. While the maximum exposure limit remains equal to $5\,$mW/cm^2 up to $1150\,$nm, it increases exponentially up to $40\,$mW/cm^2 at $1.2\,\mu$m. There is a huge exponential increase in the MPE for the wavelengths between $1.2\,\mu$m and $1.4\,\mu$m that is attributed to the use of the correction factor $C_7 = 8 + 10^{0.04(\lambda_0 - 1250)}$ of Table 9 [46]. Note that a lower correction factor $C_7 = 8$ and, thus, MPE of $40\,$mW/cm^2 is given for wavelengths between $1.2\,\mu$m and $1.4\,\mu$m in the previous British Standard BS EN 60825-1:2007 [47]. The highest MPE of $1\,$W/cm^2 along the whole laser spectrum is achieved for wavelengths between $1.31\,\mu$m and $1.4\,\mu$m. Note that a dual limit of MPE is applied in the wavelength range between $1250\,$nm and $1400\,$nm for the cornea and the skin; thus, the MPE is limited by the skin safety according to Table A.5 [46]. Wavelengths of more than $1.4\,\mu$m and less than $1\,$mm have a MPE of $100\,$mW/cm^2.

Atmosphere is considered to be highly transparent in the visible part of the spectrum [48]. The atmospheric attenuation is given as a function of the wavelength in Figure 2.2 assuming clear weather conditions. This graph was derived in [48] using the MODTRAN (MODerate resolution atmospheric TRANsmission) software [49]. There are 'windows' around the central

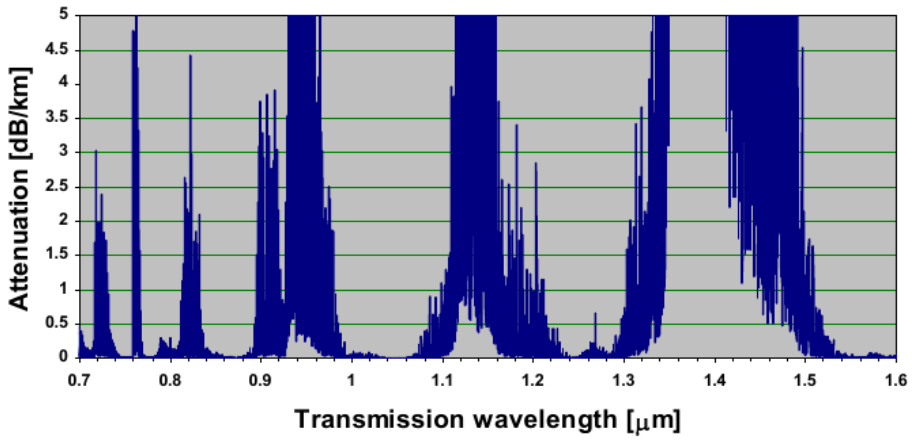

Figure 2.2: *Atmospheric attenuation as a function of the transmission wavelength [48].*

wavelengths of 780 nm, 850 nm, 1050 nm, 1250 nm and 1550 nm which experience very low atmospheric attenuation of less than 0.2 dB/km.

Since typical c-Si solar cells are used in the experiments of Chapter 4, their spectral response measured in A/W is given in Figure 2.3 as a function of the wavelength [50]. The red curve

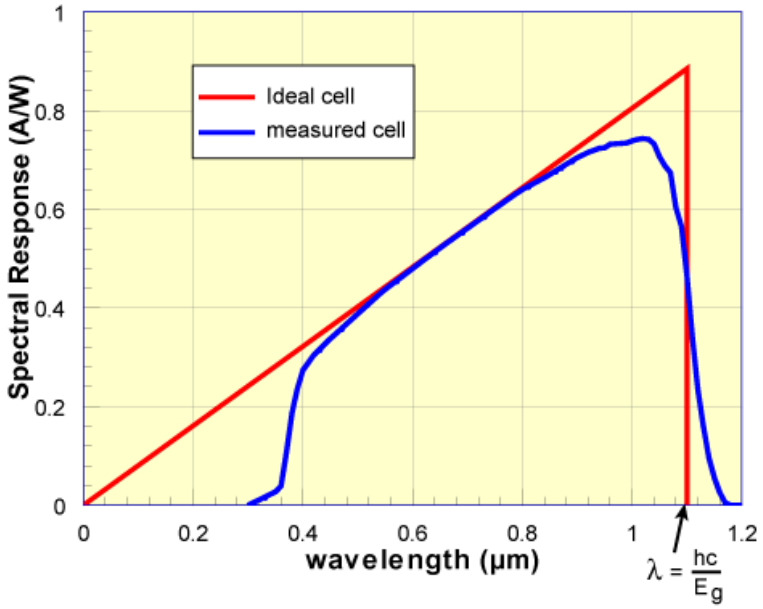

Figure 2.3: *Spectral response of typical c-Si solar cells as a function of wavelength [50].*

corresponds to the theoretical spectral response of an ideal solar cell, while the blue curve refers to the measured spectral response of a c-Si cell used with glass on top of it. Spectral response is a similar parameter of solar cells with quantum efficiency. While quantum efficiency is defined

by the ratio of the number of generated electrons by the solar cell over the number of incident photons, spectral response is given by the ratio of the output current over the received optical power of the cell [50]. Since the bandgap energy of c-Si is $E_{\mathrm{g}} = 1.12\,\mathrm{eV}$ [34], its cut-off wavelength is determined to be $\lambda_{\mathrm{c}} = 1.11\,\mu\mathrm{m}$ using the formula $\lambda_{\mathrm{c}} = hc/E_{\mathrm{g}}$. Parameters h and c denote Planck's constant and the speed of light, respectively. The ideal spectral response is shown to transit sharply from 0.88 A/W to zero at the cut-off wavelength; this is because photons of longer wavelengths have lower energy than that of the bandgap of c-Si and, therefore, cannot be absorbed. Also, shorter wavelengths than λ_{c} have higher energy than E_{g}; thus, the decrease in photons wavelength results in a decreased spectral response because their increased redundant energy is lost as heat in the semiconductor. Note that the optimum wavelength region for EH using c-Si PV cells is shown to be from about $960\,\mathrm{nm}$ to $1040\,\mathrm{nm}$, since the spectral response takes its highest values.

Overall, the use of visible light wavelengths is mostly constrained by the relatively low MPE values. On the other hand, visible light has low atmospheric losses due to absorption and can contribute to EH using off-the-shelf c-Si solar cells with responsivity values ranging from 0.28 A/W to 0.56 A/W, i.e. from 36.8% to 73.7% of the maximum responsivity. Hence, red LDs are initially selected to be used in the experiments of Chapter 4. As a next step, the wavelength of $785\,\mathrm{nm}$ is selected for the operation of LDs in Chapter 5. The $785\,\mathrm{nm}$ diodes have – higher efficiency in the particular study and – larger MPE compared with $660\,\mathrm{nm}$ laser sources, and c-Si PV cells harvest more power from wavelengths of $785\,\mathrm{nm}$ rather than $660\,\mathrm{nm}$. Also, the $785\,\mathrm{nm}$ wavelength is considered to be highly transparent in atmosphere as well as the red one. The wavelength selection of $975\,\mathrm{nm}$ in Chapter 5 is explained by the high power efficiency of the diode (54%) and the higher responsivity of the c-Si solar cell, i.e. 0.73 A/W or 96.1% of the maximum spectral response. The MPE at $975\,\mathrm{nm}$ is higher than that of lower wavelengths, but it is still low compared with that of higher wavelengths such as those of more than $1.3\,\mu\mathrm{m}$. The atmospheric losses for the $975\,\mathrm{nm}$ wavelength are of the order of $2\,\mathrm{dB/km}$ which are tolerable for the link distances between $100\,\mathrm{m}$ and $300\,\mathrm{m}$. The huge MPE of $1\,\mathrm{W/cm^2}$ could be exploited in combination with a low value of atmospheric attenuation, e.g. $2\,\mathrm{dB/km}$, using the $1310\,\mathrm{nm}$ wavelength. However, wavelengths of more than $1.2\,\mu\mathrm{m}$ cannot contribute to power generation in c-Si PV cells; thus, the use of single-junction solar cells needs to be considered for LDs operating at $1310\,\mathrm{nm}$. Since the MPE values for $1.2\,\mu\mathrm{m} \leq \lambda_0 \leq 1.4\,\mu\mathrm{m}$ are quite different in the two British standards, more research is required for the eye safety of these wavelengths. Therefore, the use of $\lambda_0 = 1550\,\mathrm{nm}$ is considered in the last study of Chapter 5 because of the

high MPE of $100\,\mathrm{mW/cm^2}$; and the almost negligible atmospheric attenuation.

2.2.5 Simultaneous OWC and power transfer

The data transfer using visible light communications systems has been investigated broadly [51, 52] and the feasibility of a data rate of 3 Gb/s by a LED source was demonstrated in [53]. Most importantly, the simultaneous use of a solar panel both for PH in the order of mW and high speed OWC with a data rate of 12 Mb/s was demonstrated in [12] for link distances of up to 95 cm. Also, the same concept was realised in [54], but with the use of a small solar cell capable of harvesting 1 mW of power and receiving data with a rate of only 3 kb/s.

2.2.6 Impact of the atmospheric channel to the communication signal and potential solutions

Laser beam propagation through an atmospheric channel is constrained by factors such as atmospheric attenuation, scintillation, misalignment and ambient light noise [48]. Atmospheric attenuation causes power reduction of the optical waves. It is presented in the form of absorption by gas molecules and Rayleigh and Mie scattering by gas molecules or aerosol particles that are suspended in the air and exist in fog, rain, clouds, smoke and dust [55]. Rayleigh scattering is the elastic scattering – a process where the total kinetic energy of the system is conserved – of optical or other form of EM radiation by particles of much smaller size than the wavelength of radiation [55]. It is caused by the relative tendency of a charge distribution, like the electron cloud of an atom or molecule, and therefore of any material body to have its charges displaced by any external electric field, i.e. electric polarizability. The blue colour of the sky and the setting of red rising sun are attributed to Rayleigh scattering. Mie scattering is similar to Rayleigh scattering, but the size of the particles is of the same order of magnitude as the wavelength of incident light [55]. The scattered and incident optical radiation have the same wavelength. Mie scattered radiation has a more complex functional dependence on the interaction between the optical wavelength and particle size distribution than that in Rayleigh scattering [55]. The term scintillation is used to describe the random changes in light intensity caused by variations in the refractive index of the atmosphere [55]. These changes of the refraction index are caused by inhomogeneities in the temperature and the pressure of the atmosphere, i.e. atmospheric turbulence, due to solar heating and wind [56]. Since highly directive laser beams are applied in FSO systems, precise alignment between the transmitter and receiver

is required for the maximum possible collection of optical power by the detector. Finally, ambient light, where sunlight is included, can affect the signal-to-noise ratio at the receiver, as it is detected in the form of shot noise.

Atmospheric losses under clear weather conditions are considered to be negligible and, in this case, only geometrical losses are dominant [57]. Note that a FSO link may become unavailable under heavy fog conditions, but these conditions occur rarely and depend on the local topography and wind conditions. In addition, even under such worst-case weather conditions, multiple FSO links can be created by a number of transmitters and receivers applying the maximal ratio combining technique for the selection of the best channel. The scintillation effect results in fading, i.e. temporal and spatial fluctuations of the optical and therefore electrical power of the received signal. The negative effects of scintillation can be alleviated using the method of aperture averaging [58]. Also, the use of a multi-element receiver, such as a solar panel, and relatively large optical devices, such as mirrors, for light collimation and reception are the most efficient ways to address misalignment problems. Therefore, the use of a large aperture at the receiver is considered to be an effective mitigation technique of the effects of scintillation and misalignment. In data communication, while a typical photodetector can be driven to saturation from excessive amounts of ambient light, a solar receiver is more resilient to large amounts of received optical power. Also, since ambient light presents slow variations in time, it can be totally removed either by the use of optical filters or other advanced detection techniques. Finally, the presence of ambient light is an important advantage for EH, as the solar receiver is able to harvest energy not only from dedicated laser sources, but also from a natural resource, i.e. sunlight.

2.3 Analytical framework for a LD based WPT system

An elliptical Gaussian model is considered for the laser beam generated from a diode and the reasoning for this is given in Section 2.3.1. The analytical model of the laser beam transmitted through a lens to free space is given in Section 2.3.2. The physical model of a solar panel is given in Section 2.3.3. Metrics for the power efficiency of a laser based link and its components are given in Section 2.3.4.

2.3.1 Motivation for a Gaussian beam model and paraxial approximation

The manufacturers' data sheets for LDs give a graph of the far field relative intensity versus the parallel and perpendicular to the junction angular divergence of the beam. These angular divergence graphs can be approximated by Gaussian curves of different widths for the LDs reported in Chapter 4 and in the first design of Chapter 5. Since the selected LDs operate at the fundamental transverse electrical mode, an elliptical Gaussian beam propagation model is considered for the generated laser beam [59].

Ray optics, also known as geometrical optics, is the simplest theory that describes light propagation [60]. According to this theory, light consists of optical rays travelling from one medium to another under defined geometrical rules. Optical rays are described by their position in space and inclination. In paraxial optics, a subset of ray optics, rays propagate at small angles from an optical axis, which the optical components are aligned with. Also, in wave optics, waves with wavefront normals forming small angles with the propagation z- axis are called paraxial. These waves satisfy the paraxial Helmholtz equation [61]. A well known and useful solution of this equation is the Gaussian beam. Paraxial optics is used in first-order ray tracing and Gaussian optics. In particular, the paraxial approximation is used and is described by the properties: $\sin(\vartheta) \approx \vartheta$, $\tan(\vartheta) \approx \vartheta$ and $\cos(\vartheta) \approx 1$, where ϑ [rad] is the angle between the optical axis and the ray.

2.3.2 Elliptical Gaussian beam propagation through a thick lens

A geometrical illustration of a Gaussian beam passing through a lens is shown in Figure 2.4 on the x-z and y-z planes, respectively. Perfect alignment of the LD, the lens and the solar panel or cell is assumed, even if misalignment of the optical axes of these components exists in practice. When a Gaussian beam passes through any circularly symmetric optical component aligned with the optical beam axis, the Gaussian beam remains Gaussian so long as the paraxial approximation holds for the system [59]. The geometrical parameters and the intensity characteristics of the Gaussian beam emitted from the LD are modified by the geometrical and optical properties of the lens. Therefore, the beam parameters are calculated at four different transverse planes, namely, the emission rectangular area of the LD; the vertices of the input and output surfaces of the aspheric lens; and the positions of the new beam waists along the x- and y- axes, respectively.

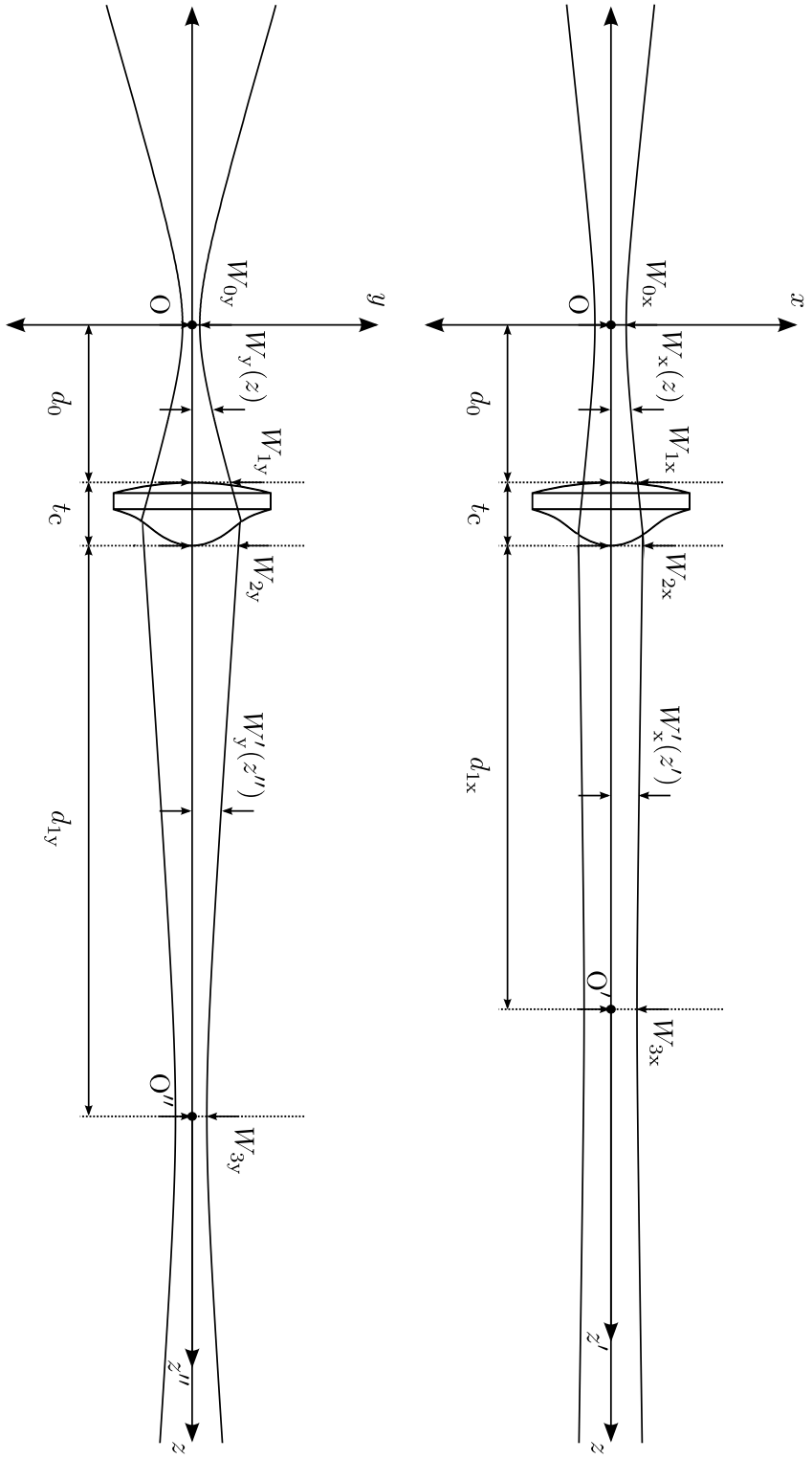

Figure 2.4: *Geometrical representation of the elliptical Gaussian beam transmitted through a thick lens along the x- and y- axes.*

2.3.2.1 Generated beam from the LD

The LDs used in the experimental studies have a multi-quantum well (MQW) structure. The emission rectangular layers of the junction placed inside the packages of the LDs have an area of $(2W_{0\mathrm{x}}) \times (2W_{0\mathrm{y}})$ [62]. Parameters $W_{0\mathrm{x}}$ and $W_{0\mathrm{y}}$ denote the beam waists along the x- and y- axes, respectively. They are calculated from the far field relative intensity patterns as a function of the angular divergences [63, 64]. In particular, the beam waists generated from the LD ($z = 0$) are given by [59]:

$$W_{0\mathrm{x}} = \frac{\lambda_0}{\pi \tan(\vartheta_{\mathrm{x}})} \approx \frac{\lambda_0}{\pi \vartheta_{\mathrm{x}}} \tag{2.1}$$

and

$$W_{0\mathrm{y}} = \frac{\lambda_0}{\pi \tan(\vartheta_{\mathrm{y}})} \approx \frac{\lambda_0}{\pi \vartheta_{\mathrm{y}}}. \tag{2.2}$$

The symbols ϑ_{x} [rad] and ϑ_{y} [rad] represent the parallel and perpendicular to the junction beam divergences. The values of ϑ_{x} and ϑ_{y} correspond to the half width at half maximum (HWHM) intensity points of the Gaussian graphs [63, 64]. The selection of the HWHM beam divergence values is made for the applicability of the paraxial approximation. However, note that the beam divergence of a Gaussian beam can also be defined according to the $1/e \simeq 0.368$ and $1/e^2 \simeq 0.135$ of peak intensity points [48, 65], where e denotes the base of the natural logarithm.

It is considered that the optical beam passes from the package aperture of the LD without any optical losses. Also, it is assumed that the protective glass window placed at the front surface of the LD package does not affect the intensity characteristics of the optical beam generated from the MQW source [63, 64]. Therefore, diffraction effects from the circular aperture of the LD are not considered here. This is explained by the Gaussian form of beam intensity shown in the respective LD data sheets [63, 64] instead of the form of a Bessel beam characterised by side lobes [59].

The temperature of the LD is an important parameter which has an impact on its power efficiency, lifetime, wavelength, linewidth and threshold current [63]. In particular, an increase in the case temperature results in a decrease in the diode's efficiency and lifetime; and an increase in the lasing wavelength and threshold current. In the experiments, a Si transfer heat compound is used as the interface between the LD's case and a small aluminium tube which acts as a passive heat sink. However, no active temperature control is used for the LDs in the experimental work of this thesis. The lack of thermoelectric cooling is considered to be an important advantage

for the overall power efficiency of the laser based power transfer systems. This is because thermoelectric coolers have high cost and quite low power efficiency with values of less than 8% [66].

The rectangular shape of the active layer and the varying gain profile across the active layer along the 'slow' beam axis induces the effect of 'astigmatism' to a LD [67]. Therefore, the beam waist of the LD along x- axis is located at a different point than the LD beam waist along y- axis, and the distance between these two points is termed astigmatism.

The beam radii along the x- and y- axes can be expressed as a function of distance from the emission area of the LD by [59]:

$$W_{\mathrm{x}}(z) = W_{0\mathrm{x}}\sqrt{1+\left(\frac{z}{z_{0\mathrm{x}}}\right)^2} \tag{2.3}$$

and

$$W_{\mathrm{y}}(z) = W_{0\mathrm{y}}\sqrt{1+\left(\frac{z}{z_{0\mathrm{y}}}\right)^2}, \tag{2.4}$$

where $0 \leq z \leq d_0$; and d_0 denotes the distance between the emission point of the LD and the vertex of the input surface of the lens. Also, $z_{0\mathrm{x}}$ and $z_{0\mathrm{y}}$ represent the Rayleigh range of the LD beam along the x- and y- directions, respectively. The Rayleigh range is defined as the axial distance between the beam waist and the point where the beam radius is increased by a multiplication factor of $\sqrt{2}$ from its minimum value. These parameters are given by $z_{0\mathrm{x}} = \pi W_{0\mathrm{x}}^2/\lambda_0$ and $z_{0\mathrm{y}} = \pi W_{0\mathrm{y}}^2/\lambda_0$ [59].

The beam radii at the tangent plane to the input surface of the lens ($z = d_0$) along the x- and y- axes are calculated by:

$$W_{1\mathrm{x}} = W_{\mathrm{x}}(d_0) \overset{(2.3)}{=} W_{0\mathrm{x}}\sqrt{1+\left(\frac{d_0}{z_{0\mathrm{x}}}\right)^2} \tag{2.5}$$

and

$$W_{1\mathrm{y}} = W_{\mathrm{y}}(d_0) \overset{(2.4)}{=} W_{0\mathrm{y}}\sqrt{1+\left(\frac{d_0}{z_{0\mathrm{y}}}\right)^2}. \tag{2.6}$$

The radii of curvature at $z = d_0$, of the Gaussian beam generated from the LD along the x- and

y- axes are given by [59]:

$$R_{1x} = d_0 \left[1 + \left(\frac{z_{0x}}{d_0} \right)^2 \right] \tag{2.7}$$

and

$$R_{1y} = d_0 \left[1 + \left(\frac{z_{0y}}{d_0} \right)^2 \right]. \tag{2.8}$$

The q- parameters of the Gaussian beam at $z = d_0$ in the x- and y- directions are described by [59]:

$$\frac{1}{q_{1x}} = \frac{1}{R_{1x}} - j \frac{\lambda_0}{\pi W_{1x}^2} \tag{2.9}$$

and

$$\frac{1}{q_{1y}} = \frac{1}{R_{1y}} - j \frac{\lambda_0}{\pi W_{1y}^2}, \tag{2.10}$$

where $j = \sqrt{-1}$ is the imaginary unit.

The optical intensity or irradiance, G, of the generated elliptical Gaussian beam in the Cartesian coordinate system, (x, y, z), is expressed as follows [59]:

$$G(x, y, z) = G_0 \frac{W_{0x} W_{0y}}{W_x(z) W_y(z)} \exp \left\{ -2 \left[\frac{x^2}{W_x^2(z)} + \frac{y^2}{W_y^2(z)} \right] \right\}, \tag{2.11}$$

where $0 \leq z \leq d_0$; $G_0 = G(0, 0, 0)$ is the overall peak intensity; and $\exp(.)$ denotes the natural exponential function.

The total optical power, $P_{\text{Tx,o}}$, of the generated beam is computed at a distance of $0 \leq z \leq d_0$ by [59]:

$$P_{\text{Tx,o}} = \frac{\pi}{2} G_0 W_{0x} W_{0y}. \tag{2.12}$$

The proof of (2.12) is presented in Appendix A. Combining (2.11) and (2.12), the laser beam intensity can be described as a function of $P_{\text{Tx,o}}$ by:

$$G(x, y, z) = \frac{2 P_{\text{Tx,o}}}{\pi W_x(z) W_y(z)} \exp \left\{ -2 \left[\frac{x^2}{W_x^2(z)} + \frac{y^2}{W_y^2(z)} \right] \right\}. \tag{2.13}$$

2.3.2.2 Thick lens

A method to relate the input and output of an optical system is the use of ray transfer or $ABCD$ matrices [60]. The method of $ABCD$ matrices is also widely used in microwave

communications [68]. In matrix optics, a simple 2×2 matrix connects the position and angle of paraxial rays at the input and output plane of an optical system through linear algebraic equations. Note that the application of the $ABCD$ law to a Gaussian beam connects the q-parameters of the beam [59].

The rear surface of the aspheric lens is considered to be spherical. This assumption provides a worst-case scenario for the lens model in terms of light collimation. The elements of an $ABCD$ matrix for a thick lens, $\mathbf{M}_{\text{lens}}$, with two spherical surfaces of different radii of curvature are [69]:

$$A = 1 - \frac{t_{\text{c}}(n-1)}{nR_1}, \tag{2.14}$$

$$B = \frac{t_{\text{c}}}{n}, \tag{2.15}$$

$$C = -(n-1)\left(\frac{1}{R_1} - \frac{1}{R_2}\right) - \frac{t_{\text{c}}(n-1)^2}{nR_1R_2}, \tag{2.16}$$

$$D = 1 + \frac{t_{\text{c}}(n-1)}{nR_2}. \tag{2.17}$$

The parameters t_{c} and n represent the thickness and the refractive index of the lens, respectively. Also, R_1 and R_2 are the radii of the input and output surface of the lens, respectively. If a collimation lens is placed at its focal point as specified in the respective data sheet, the distance between the emission point of source and the input lens surface is termed back focal length, and is given by [69]:

$$\beta = f\left[1 - \frac{t_{\text{c}}(n-1)}{nR_1}\right], \tag{2.18}$$

where quantity f denotes the effective focal length. The q- parameters of the beam for the x- and y- axes at $z = d_0$ and $z = d_0 + t_{\text{c}}$ are connected through the relationships [59]:

$$q_{2\text{x}} = \frac{Aq_{1\text{x}} + B}{Cq_{1\text{x}} + D} \tag{2.19}$$

and

$$q_{2\text{y}} = \frac{Aq_{1\text{y}} + B}{Cq_{1\text{y}} + D}. \tag{2.20}$$

Also, the q- parameters of the beam at $z = d_0 + t_{\text{c}}$ are given by:

$$\frac{1}{q_{2\text{x}}} = \frac{1}{R_{2\text{x}}} - j\frac{\lambda_0}{\pi W_{2\text{x}}^2} \tag{2.21}$$

and

$$\frac{1}{q_{2\mathrm{y}}} = \frac{1}{R_{2\mathrm{y}}} - j\frac{\lambda_0}{\pi W_{2\mathrm{y}}^2}. \tag{2.22}$$

Parameters $W_{2\mathrm{x}}$ and $W_{2\mathrm{y}}$ represent the beam radii along the x- and y- axes at the tangent plane to the output surface of the lens ($z = d_0 + t_\mathrm{c}$). Also, $R_{2\mathrm{x}}$ and $R_{2\mathrm{y}}$ denote the radii of curvature of the reshaped Gaussian beam from the lens at $z = d_0 + t_\mathrm{c}$. Then, all of these quantities can be calculated from:

$$R_{2\mathrm{x}} = \frac{1}{\mathrm{Re}\{1/q_{2\mathrm{x}}\}}, \tag{2.23}$$

$$R_{2\mathrm{y}} = \frac{1}{\mathrm{Re}\{1/q_{2\mathrm{y}}\}}, \tag{2.24}$$

$$W_{2\mathrm{x}} = \sqrt{-\frac{\lambda_0}{\pi \mathrm{Im}\{1/q_{2\mathrm{x}}\}}} \tag{2.25}$$

and

$$W_{2\mathrm{y}} = \sqrt{-\frac{\lambda_0}{\pi \mathrm{Im}\{1/q_{2\mathrm{y}}\}}}. \tag{2.26}$$

Operators Re$\{.\}$ and Im$\{.\}$ represent the real and imaginary parts of $1/q_{2\mathrm{x}}$ and $1/q_{2\mathrm{y}}$, and are calculated by (2.19) and (2.20), respectively.

2.3.2.3 Reshaped beam from the lens

The distance between the reshaped beam waists and the tangent plane to the output surface of the lens in the x- and y- direction are $d_{1\mathrm{x}}$ and $d_{1\mathrm{y}}$, respectively. These values of distance can be computed by [59]:

$$d_{1\mathrm{x}} = -\frac{R_{2\mathrm{x}}}{1 + \left[\lambda_0 R_{2\mathrm{x}}/\left(\pi W_{2\mathrm{x}}^2\right)\right]^2} \tag{2.27}$$

and

$$d_{1\mathrm{y}} = -\frac{R_{2\mathrm{y}}}{1 + \left[\lambda_0 R_{2\mathrm{y}}/\left(\pi W_{2\mathrm{y}}^2\right)\right]^2}. \tag{2.28}$$

Also, the waists of the reshaped Gaussian beam, $W_{3\mathrm{x}}$ and $W_{3\mathrm{y}}$, are given by [59]:

$$W_{3\mathrm{x}} = \frac{W_{2\mathrm{x}}}{\sqrt{1 + \left[\pi W_{2\mathrm{x}}^2/\left(\lambda_0 R_{2\mathrm{x}}\right)\right]^2}} \tag{2.29}$$

and

$$W_{3\mathrm{y}} = \frac{W_{2\mathrm{y}}}{\sqrt{1 + \left[\pi W_{2\mathrm{y}}^2/\left(\lambda_0 R_{2\mathrm{y}}\right)\right]^2}}, \tag{2.30}$$

along the x- and y- axis, respectively.

Now, the reshaped beam radius along the x- axis can be expressed as a function of distance from the vertex of output surface of the lens by:

$$W'_{\mathrm{x}}(z') = W_{3\mathrm{x}}\sqrt{1 + \left(\frac{z'}{z_{3\mathrm{x}}}\right)^2}, \tag{2.31}$$

where $z' = z - d_0 - t_{\mathrm{c}} - d_{1\mathrm{x}} \geq -d_{1\mathrm{x}}$ is a substituted variable for distance, and $z_{3\mathrm{x}} = \pi W_{3\mathrm{x}}^2/\lambda_0$ is the Rayleigh range along the x- axis. Similarly, the reshaped beam radius along the y- direction is given as a function of distance from the vertex of output surface of the lens by:

$$W'_{\mathrm{y}}(z'') = W_{3\mathrm{y}}\sqrt{1 + \left(\frac{z''}{z_{3\mathrm{y}}}\right)^2}, \tag{2.32}$$

where $z'' = z - d_0 - t_{\mathrm{c}} - d_{1\mathrm{y}} \geq -d_{1\mathrm{y}}$ is another substituted variable for distance, and $z_{3\mathrm{y}} = \pi W_{3\mathrm{y}}^2/\lambda_0$ is the Rayleigh range along the y- axis.

The reshaped Gaussian beam intensity can be computed according to (2.13) by:

$$G'(x, y, z) = \frac{2(1-r)P_{\mathrm{Tx,o}}}{\pi W'_{\mathrm{x}}(z')W'_{\mathrm{y}}(z'')} \exp\left\{ -2\left[\frac{x^2}{W'^2_{\mathrm{x}}(z')} + \frac{y^2}{W'^2_{\mathrm{y}}(z'')}\right]\right\}, \tag{2.33}$$

where $z \geq d_0 + t_{\mathrm{c}}$ and r denotes the reflectance of the lens.

2.3.2.4 Total system's $ABCD$ matrix

An alternative method to relate the q- parameters of the Gaussian beam at $z = 0$ and $z = d + d_0 + t_{\mathrm{c}}$, where d denotes the distance of the vertex of output lens surface from the input plane of solar receiver, is the use of an $ABCD$ matrix for the total optical system. Three matrices can be used to model the free space between the LD and the input surface of the lens; the lens; and the free space between the output lens surface and input surface of the solar receiver.

In particular, the $ABCD$ matrix of free space between the LD and the lens placed at $z = d_0$

is [60]:

$$\mathbf{M}_1 = \begin{bmatrix} 1 & d_0 \\ 0 & 1 \end{bmatrix}. \tag{2.34}$$

Also, the $ABCD$ matrix of free space between the output of the lens and the incidence plane to the solar panel is calculated by:

$$\mathbf{M}_2 = \begin{bmatrix} 1 & d + d_0 + t_\mathrm{c} \\ 0 & 1 \end{bmatrix}. \tag{2.35}$$

Therefore, the $ABCD$ matrix for the entire optical link can be written as the product of ray transfer matrices of the individual components [60]:

$$\mathbf{M} = \mathbf{M}_2\mathbf{M}_{\text{lens}}\mathbf{M}_1 = \begin{bmatrix} A' & B' \\ C' & D' \end{bmatrix}. \tag{2.36}$$

The elements of $\mathbf{M}_{\text{lens}}$ are given in (2.14)–(2.17). Also, the elements of $\mathbf{M}$ are calculated to be:

$$A' = 1 - \frac{t_\mathrm{c}(n-1)}{nR_1} - (d + d_0 + t_\mathrm{c})\left[(n-1)\left(\frac{1}{R_1} - \frac{1}{R_2}\right) + \frac{t_\mathrm{c}(n-1)^2}{nR_1R_2}\right], \tag{2.37}$$

$$\begin{aligned} B' = {} & d_0 - d_0\frac{t_\mathrm{c}(n-1)}{nR_1} - d_0(d + d_0 + t_\mathrm{c})\left[(n-1)\left(\frac{1}{R_1} - \frac{1}{R_2}\right) + \frac{t_\mathrm{c}(n-1)^2}{nR_1R_2}\right] + \\ & + \frac{t_\mathrm{c}}{n} + (d + d_0 + t_\mathrm{c})\left[1 + \frac{t_\mathrm{c}(n-1)}{nR_2}\right], \end{aligned} \tag{2.38}$$

$$C' = -(n-1)\left(\frac{1}{R_1} - \frac{1}{R_2}\right) - \frac{t_\mathrm{c}(n-1)^2}{nR_1R_2}, \tag{2.39}$$

$$D' = -d_0(n-1)\left(\frac{1}{R_1} - \frac{1}{R_2}\right) - d_0\frac{t_\mathrm{c}(n-1)^2}{nR_1R_2} + 1 + \frac{t_\mathrm{c}(n-1)}{nR_2}. \tag{2.40}$$

Therefore, the general $ABCD$ matrix $\mathbf{M}$ is applied to the elliptical Gaussian beam using the transformations [59]:

$$q_{4\mathrm{x}} = \frac{A'q_{0\mathrm{x}} + B'}{C'q_{0\mathrm{x}} + D'} \tag{2.41}$$

and

$$q_{4\mathrm{y}} = \frac{A'q_{0\mathrm{y}} + B'}{C'q_{0\mathrm{y}} + D'}, \tag{2.42}$$

where $q_{0\mathrm{x}} = j\pi W_{0\mathrm{x}}^2/\lambda_0$ and $q_{0\mathrm{y}} = j\pi W_{0\mathrm{y}}^2/\lambda_0$ denote the q- parameters of the Gaussian beam at the LD emission point, i.e. $z = 0$, along the x- and y- axis, respectively; and $q_{4\mathrm{x}}$ and

q_{4y} are the q- parameters of the Gaussian beam at the input plane of the solar receiver, i.e. $z = d + d_0 + t_c$, along the x- and y- axis, respectively. Substituting the values of q_{0x} and q_{0y} to (2.41) and (2.42), the inverse of q_{4x} and q_{4y} are calculated to be:

$$\frac{1}{q_{4x}} = \frac{A'C'\left(\frac{\pi W_{0x}^2}{\lambda_0}\right)^2 + B'D'}{\left(A'\frac{\pi W_{0x}^2}{\lambda_0}\right)^2 + B'^2} - j\frac{\frac{\pi W_{0x}^2}{\lambda_0}}{\left(A'\frac{\pi W_{0x}^2}{\lambda_0}\right)^2 + B'^2} \tag{2.43}$$

and

$$\frac{1}{q_{4y}} = \frac{A'C'\left(\frac{\pi W_{0y}^2}{\lambda_0}\right)^2 + B'D'}{\left(A'\frac{\pi W_{0y}^2}{\lambda_0}\right)^2 + B'^2} - j\frac{\frac{\pi W_{0y}^2}{\lambda_0}}{\left(A'\frac{\pi W_{0y}^2}{\lambda_0}\right)^2 + B'^2}, \tag{2.44}$$

respectively. The proof of (2.43) and (2.44) is given in Appendix A. The inverse terms of q_{4x} and q_{4y} are also given by [59]:

$$\frac{1}{q_{4x}} = \frac{1}{R_{4x}} - j\frac{\lambda_0}{\pi W_{4x}^2} \tag{2.45}$$

and

$$\frac{1}{q_{4y}} = \frac{1}{R_{4y}} - j\frac{\lambda_0}{\pi W_{4y}^2}, \tag{2.46}$$

where R_{4x} and R_{4y} denote the beam radii of curvature at $z = d + d_0 + t_c$ along the x- and y- axis, respectively. Also, the quantities W_{4x} and W_{4y} represent the beam radii at $z = d + d_0 + t_c$ along the x- and y- axis, respectively. Since the imaginary parts of (2.43) and (2.45) are equal, the beam radius at the solar receiver along x- axis is given by:

$$W_{4x} = W_{4x}(d) = \frac{\lambda_0}{\pi W_{0x}}\sqrt{\left(A'\frac{\pi W_{0x}^2}{\lambda_0}\right)^2 + B'^2}. \tag{2.47}$$

Similarly, the imaginary parts of (2.44) and (2.46) are equal, and therefore the beam radius at the solar receiver along y- axis is given by:

$$W_{4y} = W_{4y}(d) = \frac{\lambda_0}{\pi W_{0y}}\sqrt{\left(A'\frac{\pi W_{0y}^2}{\lambda_0}\right)^2 + B'^2}. \tag{2.48}$$

2.3.3 Solar panel physical model and curve fitting

One of the widely used solar cell models is the single diode exponential one [34]. Since most of the receivers in the experimental studies are PV panels and not cells, a single diode based physical model of a solar panel proposed in [70] is considered. The solar panel consists of N_c

cells connected in series. The physical equivalent circuit of that model is shown in Figure 2.5. A variable resistor, R_{L}, is connected to the output branch, HH', of the solar receiver, while no load resistor is considered in [70]. Parasitic resistance effects of this PV panel are modelled by an effective series resistance, $R_{\mathrm{S,eff}}$, and an effective shunt resistance, $R_{\mathrm{P,eff}}$. The main factors that contribute to the series resistance generation are the current flow across the p-n junction of the cells; the contact resistance between the metallic grid and the semiconductor; and the resistance between the top and rear metallic contacts. The shunt resistance is caused mainly by manufacturing imperfections rather than a flawed design of solar cells.

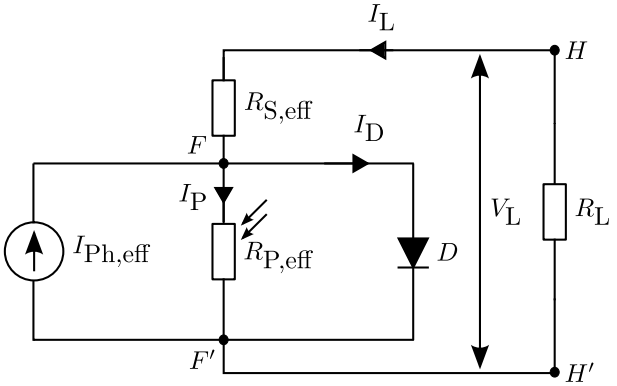

Figure 2.5: *Physical equivalent circuit of the solar panel to an effective single solar cell model.*

The application of Kirchhoff's current law to the circuit node F in Figure 2.5 gives:

$$I_{\mathrm{Ph,eff}} + I_{\mathrm{L}} - I_{\mathrm{P}} - I_{\mathrm{D}} = 0, \tag{2.49}$$

where $I_{\mathrm{Ph,eff}}$ is the effective generated photo-current; I_{L} denotes the load current; I_{P} is the parallel current to the source flowing through the branch FF'; and I_{D} is the forward current of the diode. The current I_{D} is given by the Shockley diode equation [70]:

$$I_{\mathrm{D}} = I_{0,\mathrm{eff}}\left[\exp\left(\frac{q_{\mathrm{e}}V_{\mathrm{D}}}{A_{\mathrm{eff}}k_{\mathrm{B}}T}\right) - 1\right], \tag{2.50}$$

where V_{D} is the voltage across the diode and is given by:

$$V_{\mathrm{D}} = -(V_{\mathrm{L}} + R_{\mathrm{S,eff}}I_{\mathrm{L}}). \tag{2.51}$$

Thus, the forward current of the diode can be written using (2.51) as:

$$I_{\mathrm{D}} = I_{0,\mathrm{eff}}\left\{\exp\left[\frac{-q_{\mathrm{e}}(V_{\mathrm{L}} + R_{\mathrm{S,eff}}I_{\mathrm{L}})}{A_{\mathrm{eff}}k_{\mathrm{B}}T}\right] - 1\right\}. \tag{2.52}$$

The value of $I_{0,\text{eff}}$ represents the effective dark saturation current of the diode. The physical constants $q_\text{e} = 1.602 \times 10^{-19}\,\text{C}$ and $k_\text{B} = 8.617 \times 10^{-5}\,\text{eV/K}$ denote the electron charge and Boltzmann constant, respectively. The temperature of the PV panel is assumed to be $T = 298\,\text{K}$. The quantities A_eff and V_L represent the effective ideality factor of the diode and the load voltage, respectively. Kirchhoff's voltage law is applied to the loop $F'H'HF$, and the current I_P is computed by:

$$I_\text{P} = -\frac{V_\text{L} + R_\text{S,eff} I_\text{L}}{R_\text{P,eff}}. \tag{2.53}$$

A transcendental relationship connects the load current and load voltage. This is observed by the substitution of I_D for the second part of (2.52) and I_P for the second part of (2.53) in (2.49). Transcendental equations have only approximate numerical solutions and do not have closed form solutions. The electrical power, P_L, harvested by the load resistor is given by $P_\text{L} = V_\text{L} I_\text{L}$.

This particular model has two measurable parameters, I_L and V_L, and five unknown parameters, $I_{0,\text{eff}}$, $R_\text{S,eff}$, A_eff, $R_\text{P,eff}$ and $I_\text{Ph,eff}$. These parameters are strongly dependent on the values of optical power incident on the panel. An estimation method of the five unknown parameters is followed by the application of a simple exhaustive search algorithm with discrete search space. The optimization problem that is solved can be expressed based on [71] as follows:

$$\min_{\substack{I_{0,\text{eff}}, R_\text{S,eff}, A_\text{eff} \\ R_\text{P,eff}, I_\text{Ph,eff}}} \sum_{i=1}^{21} \Bigg| I_\text{Ph,eff} + I_\text{L}(i) + \frac{V_\text{L}(i) + R_\text{S,eff} I_\text{L}(i)}{R_\text{P,eff}} - I_{0,\text{eff}} \left\{ \exp\left\{ \frac{-q_\text{e}\left[V_\text{L}(i) + R_\text{S,eff} I_\text{L}(i)\right]}{A_\text{eff} k_\text{B} T} \right\} - 1 \right\} \Bigg| \tag{2.54}$$

$$\text{subject to :} \quad I_{0,\text{eff,min}} \leq I_{0,\text{eff}} \leq I_{0,\text{eff,max}} \tag{2.55}$$

$$R_\text{S,eff,min} \leq R_\text{S,eff} \leq R_\text{S,eff,max} \tag{2.56}$$

$$A_\text{eff,min} \leq A_\text{eff} \leq A_\text{eff,max} \tag{2.57}$$

$$R_\text{P,eff,min} \leq R_\text{P,eff} \leq R_\text{P,eff,max} \tag{2.58}$$

$$I_\text{Ph,eff,min} \leq I_\text{Ph,eff} \leq I_\text{Ph,eff,max}. \tag{2.59}$$

Twenty one measurements are conducted for every V-P curve of the WPT systems implemented in the experiments. The subscripts 'min' and 'max' of each of the five unknown parameters of (2.55)–(2.59) denote the real positive minimum and maximum value of the finite search space, respectively. The five identified parameters are first refined by the application of

'fsolve' in Matlab and the resulting values are applied to (2.49)–(2.53) for curve fitting of the experimental data. Note that the experimental measurements of I_{L} and V_{L} are also used for the determination of a local solution to this non-linear curve fitting problem [72].

2.3.4 Total link and components power efficiency

An important aspect of the technology of wireless power transmission and harvesting is the total efficiency of a link that is a function of the efficiency of components. The external power efficiency of a LD can be defined as:

$$\eta_{\mathrm{LD}} = \frac{P_{\mathrm{Tx,o}}}{P_{\mathrm{in}}} \times 100\%\,, \tag{2.60}$$

where P_{in} is the DC input electrical power to the LD.

The OWPT links are created under line-of-sight (LoS) conditions. So long as the experiments are conducted in an indoor environment, no atmospheric attenuation of the laser beam due to absorption from molecules and scattering effects (Mie or Rayleigh) with aerosol particles is considered [48, 73]. Therefore, only geometrical losses of the transmitted optical power are assumed due to the laser beam divergence over distance.

In practice, the typical geometry of a solar receiver (cell or panel) is rectangular with an effective area of $S_{\mathrm{eff}} = 2x_0 \times 2y_0$, where x_0 is the half length and y_0 is the half width. The ratio of the optical power collected by the rectangular solar receiver at a distance of $z \geq d_0 + t_{\mathrm{c}}$, $P_{\mathrm{Rx,o}}(z)$, over the total transmitted optical power can be defined as the collection efficiency, $\eta_{\mathrm{c}}(z)$. This factor can be calculated in the case of a single optical link by:

$$\eta_{\mathrm{c}}(z) = \frac{P_{\mathrm{Rx,o}}(z)}{(1-r)P_{\mathrm{Tx,o}}} \times 100\% = \mathrm{erf}\left[\frac{\sqrt{2}x_0}{W'_{\mathrm{x}}(z')}\right]\mathrm{erf}\left[\frac{\sqrt{2}y_0}{W'_{\mathrm{y}}(z'')}\right] \times 100\%\cdot \tag{2.61}$$

Quantities $W'_{\mathrm{x}}(z')$ and $W'_{\mathrm{y}}(z'')$ are given by (2.31) and (2.32), respectively. An analytical derivation of (2.61) is provided in Appendix A. The value of $\eta_{\mathrm{c}}(z)$ provides information about the geometrical losses of the optical link. Note that the geometrical losses are determined by the degree of collimation of an optical source.

The most important metric of the energy efficiency of a solar panel or cell is the optical-to-electrical conversion efficiency. In the particular design, the conversion efficiency of the solar

receiver is expressed as a function of z and is computed by [34]:

$$\eta_{\text{sr}}(z) = \frac{P_{\text{m}}}{P_{\text{Rx,o}}(z)} \times 100\%\,, \tag{2.62}$$

where P_{m} denotes the maximum electrical power and is given by $P_{\text{m}} = V_{\text{m}} I_{\text{m}}$. Parameters V_{m} and I_{m} represent the voltage and current at the maximum power point of the panel, respectively. Also, the fill factor (FF) or curve factor (CF) of the PV panel is given by [34]:

$$f_{\text{sr}} = \frac{V_{\text{m}} I_{\text{m}}}{V_{\text{oc}} I_{\text{sc}}} \times 100\%\cdot \tag{2.63}$$

This factor shows how well the circuit approximates the ideal behaviour of a current source. where V_{oc} and I_{sc} denote the open-circuit voltage and short-circuit current, respectively. The product $V_{\text{oc}} I_{\text{sc}}$ represents the ideal harvested electrical power of the PV panel or cell. The responsivity of a solar receiver can be defined as:

$$\rho(z) = \frac{I_{\text{Ph,eff}}}{P_{\text{Rx,o}}(z)}\cdot \tag{2.64}$$

A common assumption of $I_{\text{Ph,eff}} \simeq I_{\text{sc}}$ is made practically [74]. This is explained by the low series resistance and high parallel resistance of the solar panel. In this case, the responsivity becomes a purely measurable quantity as both the short-circuit current and the received optical power can be measured.

The power efficiency of a solar panel is typically given as a function of the temperature of the cells T and the received solar irradiance, G_{solar}, by [75]:

$$\eta_{\text{sr}} = \eta_{\text{ref}}[1 - \beta_0(T - T_{\text{ref}}) + \gamma_0 \log_{10}(G_{\text{solar}})], \tag{2.65}$$

where η_{ref} denotes the reference efficiency of the solar panel at a reference temperature $T_{\text{ref}} = 25\,^{\circ}\text{C}$; and β_0 and γ_0 are the temperature and solar irradiance coefficient of the solar panel, respectively. Typical values of $\beta_0 = 4.8 \times 10^{-3}\,^{\circ}\text{C}^{-1}$ and $\gamma_0 = 0.12$ are considered for the Si material [75]. The solar panel efficiency is given as a function of the cells temperature in Figure 2.6. The reference PV efficiency and received solar irradiance are assumed to be 12.5% and $200\,\text{W/m}^2$, respectively [75]. The PV efficiency is shown to decrease linearly with the temperature of the cells that is dependent on environmental conditions [75].

The variations of V_{oc}, f_{sr} and η_{sr} with the solar irradiance of a typical c-Si PV cell are given

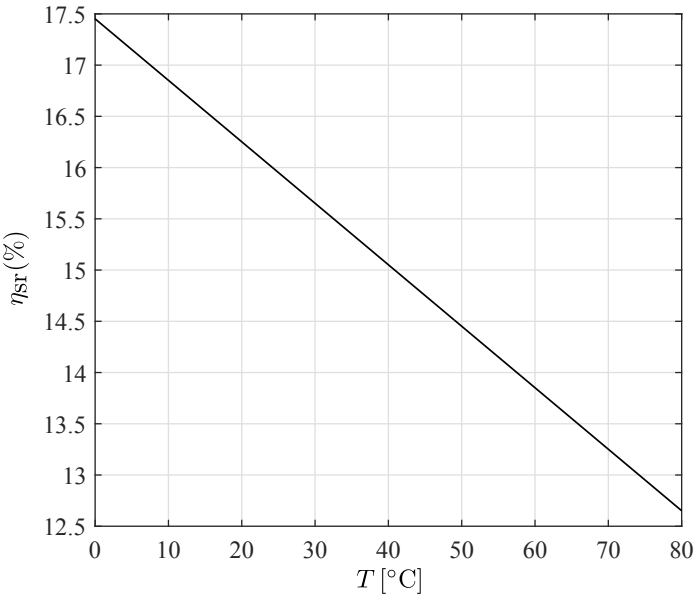

Figure 2.6: *Solar panel efficiency as a function of cells temperature.*

in Figure 2.7 [14]. The well-known single diode based model is used for the equivalent physical circuit of the solar cell [34]. The white and black markers represent the theoretical and experimental values, respectively, of the open circuit voltage (V_{oc}), the CF or FF and the solar cell efficiency (η). The FF and the efficiency of the PV cell are shown to have a similar behaviour with the increase in solar irradiance. The CF increases to a maximum value of 0.73 at $70\,\mathrm{mW/cm^2}$ according to the dashed line and then decreases monotonically with the increased input intensity. The efficiency curve increases to the highest value of 13.5% at $83\,\mathrm{mW/cm^2}$ based on the dashed line and decreases constantly at higher illumination intensities. Note that the FF and the efficiency increase with almost the same rate in the low region of optical intensity between $20\,\mathrm{mW/cm^2}$ and $40\,\mathrm{mW/cm^2}$, while the FF decreases with a larger rate (or faster) than that of the efficiency in the higher range of intensity, i.e. between $110\,\mathrm{mW/cm^2}$ and $160\,\mathrm{mW/cm^2}$.

Finally, the maximum link efficiency is computed by:

$$\eta_{\mathrm{max}} = \frac{P_{\mathrm{m}}}{P_{\mathrm{in}}} \times 100\%\cdot \tag{2.66}$$

The combination of (2.60)–(2.66) forms an expression of the maximum link efficiency as a

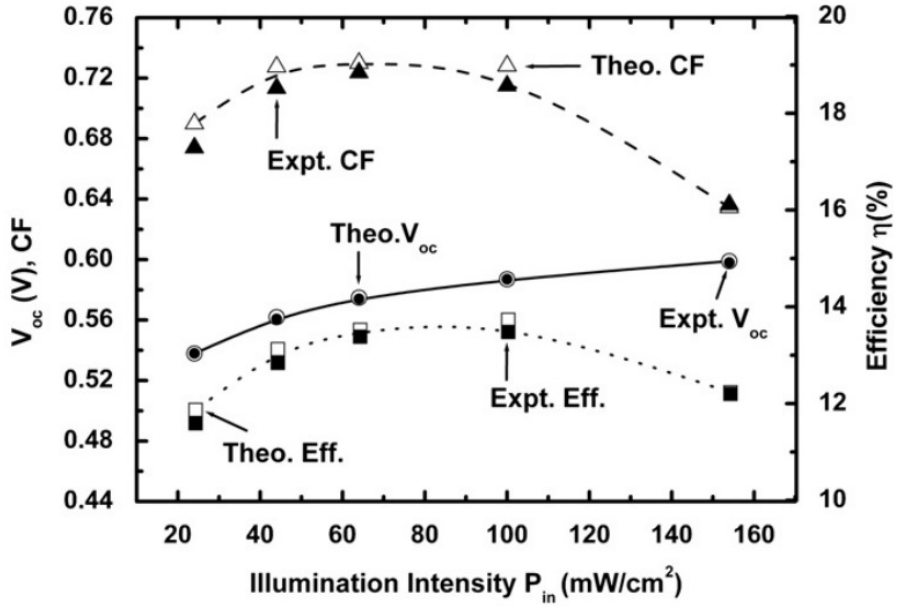

Figure 2.7: *Open circuit voltage, curve factor and power efficiency of a Si PV cell as a function of solar intensity [14].*

function of the LD, lens, collection and solar receiver efficiency given by:

$$\eta_{\text{max}} = \eta_{\text{LD}}(1-r)\eta_{\text{c}}(z)\eta_{\text{sr}}(z) \times 100\% = \eta_{\text{LD}}(1-r)\eta_{\text{c}}(z)f_{\text{sr}}\rho(z)V_{\text{oc}} \times 100\%, \qquad (2.67)$$

where the assumption $I_{\text{Ph,eff}} \simeq I_{\text{sc}}$ is made.

2.4 Summary

In this chapter, a review of previous work with respect to RF and optical systems designed for WPT and their applications was given. Efficiency values of different solar cell technologies were reported from literature. The fundamental differences in the operation of LEDs and LDs were discussed. More importantly, an overview of the optimum wavelengths for optical EH was given in accordance with the eye safety, atmospheric absorption and spectral response of Si solar cells. Also, a discussion of the limitations imposed by an atmospheric channel to a communication signal with respective potential solutions was provided. In addition, the physical models describing a laser based link for WPT were presented. In particular, an elliptical Gaussian propagation model was applied to a LD and an effective single diode based solar cell equivalent model was used to analyse the electrical behaviour of a solar panel. Collimation

lenses and free space were modelled using $ABCD$ matrices. These models are connected to predict for the first time the end-to-end power efficiency of a laser based WPT system. Thus, they offer the basis for the experimental and simulation work given in the next chapters.

Chapter 3
White light-emitting diode based wireless power transfer systems: Energy efficiency

3.1 Introduction

The technology of visible light communications (VLC) has been demonstrated to be able to provide high speed data transfer [53, 76]. While the communication capabilities have been investigated fairly well, a limited number of studies has been presented for the energy harvesting (EH) potential of a VLC link [12].

Typical values of power consumption of $6\,\mathrm{W}-10\,\mathrm{W}$ are currently reported for small cells (SCs) and are expected to decrease to $5\,\mathrm{W}$ by 2020 [9]. While $5.2\,\mathrm{W}$ of power consumption have already been reported for femtocells [7, 10], the use of exclusively passive components is considered in this work in order to reduce power consumption more than the reported values. Also, all the signal processing functions are assumed to be moved to a central unit. Under these main assumptions, $1\,\mathrm{W}$ of electrical power is considered to be required for the operation of a small radio frequency (RF) cell.

Thus, the objective of this study is to harvest $1\,\mathrm{W}$ of electrical power implementing an indoor visible light (VL) link. The link consists of a white light-emitting diode (WLED) and a solar panel. The harvested power and total efficiency are investigated for the optical wireless (OW) link created by (a) the single WLED and (b) the WLED with collimation optics – a spherical lens, a reflector and a parabolic mirror (PM). An analytical model is developed for the first time for an end-to-end link used for EH from LED based radiation to verify the measured data of the experiments. Ambient light is ensured to be negligible in the measurements and does not contribute to the collected optical power of the solar panel.

In this chapter, the PM based link is shown to achieve the largest amount of harvested power due to the largest dimensions of the mirror. An increase in the dimensions of optics results in an

increase of the directivity of light according to the brightness theorem [77, 78]. The maximum harvested power and link efficiency are measured to be 18.3 mW and 0.1%, respectively, when the PM is used for light collimation. Since these levels are relatively low for SC EH, the use of laser diodes (LDs) and solar cells of higher efficiency is considered in the next chapters. Most importantly, the developed analytical model is combined with simple electrical measurements extracting for the first time the ratio of optical-to-electrical power efficiency over the fill factor (FF) of the solar panel for different scenarios of light collimation. Thus, these extracted parameters could be scaled for respective future experiments conducted at longer link distances and with larger components.

The rest of this chapter is organised as follows. In Section 3.2 the analytical framework is provided. The selected components are given in Section 3.3. The objective, methodology, results and discussion of Studies I–III are provided in Sections 3.4–3.6, respectively. Finally, a summary of the chapter is given in Section 3.7.

3.2 Analytical framework

An optical source is characterised by a value of 'brightness', i.e. the optical power radiated per solid angle unit per emitted surface area unit. The 'optical intensity', known also as 'irradiance', another important quantity of a light source, is defined as the transmitted optical power per unit of emitted surface area. The structure of surface light-emitting diodes (LEDs) is the simplest one and is mostly met in high brightness WLEDs. Surface LEDs are characterised by a Lambertian intensity distribution. In other words, the optical source has the same luminosity when it is observed from any direction. The intensity varies proportionally to $\cos(\phi)$, where ϕ denotes the angle from the normal to the emission plane. A decrease in the intensity value by half occurs for an angle of $\phi_{1/2} = 60°$. The size $\phi_{1/2}$ is known as the 'semi-angle of half power' and is used as a metric of light collimation. Therefore, although the Lambertian radiation pattern of a LED with $\phi_{1/2} = 60°$ is very convenient for illumination coverage of large areas, this is a major obstacle for efficient wireless energy transfer (WET) of light. To overcome the wide emission pattern of a LED, the use of well designed optical elements at the transmitter is required.

In this context, three different optical elements for light collimation are considered: a plano-convex (PCX) lens, a reflector and a PM. The receiver consists of a solar panel with a number

of cells connected in series. Also, a variable resistor is connected to the solar panel output representing the load that consumes the harvested electrical power. A block diagram of the link designed for optical wireless power transfer (OWPT) is given in Figure 3.1.

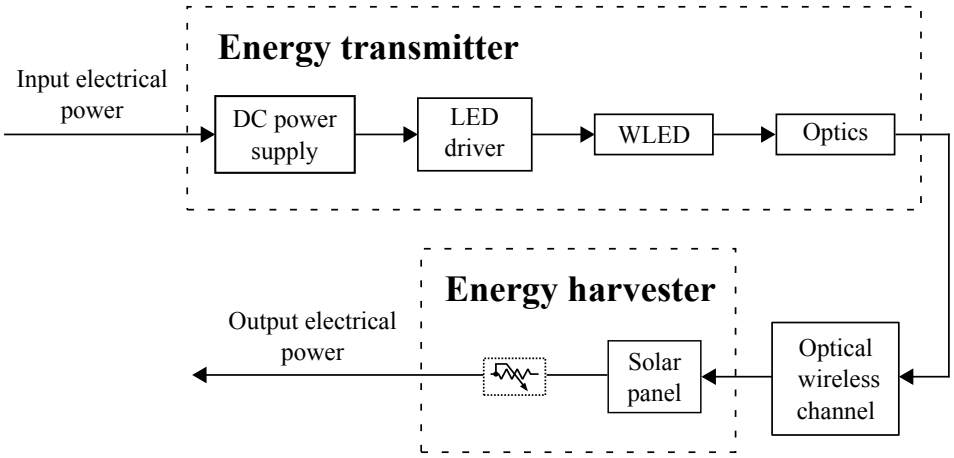

Figure 3.1: *Block diagram of the WLED based link with collimation optics.*

The uncollimated light transmission of a bare WLED is investigated in Section 3.2.1, while the transmission of power using optics is studied in Section 3.2.2. The planes of the optical source and the solar panel are considered to be parallel. It is also assumed that perfect alignment of the optical axes among the WLED, the respective collimation optics and the solar panel is attained. Therefore, line-of-sight (LoS) conditions are assumed for the OWPT channel [79].

3.2.1 Single WLED based link

The electrical power supply to an electronic driver for LEDs is given by $P_{\text{in,d}} = V_{\text{in}} I_{\text{in}}$, where V_{in} and I_{in} denote the input to the LED driver voltage and current, respectively. The power efficiency of the driver can be defined as:

$$\eta_{\text{d}} = \frac{P_{\text{in}}}{P_{\text{in,d}}} \times 100\%\,, \tag{3.1}$$

where P_{in} is the input electrical power to the WLED. The photometric unit of luminous flux of a WLED, Φ, can be expressed as [80]:

$$\Phi = 683 \frac{\text{lm}}{\text{W}} \int_{380\,\text{nm}}^{720\,\text{nm}} p(\lambda) V_{\text{es}}(\lambda) \text{d}\lambda\,, \tag{3.2}$$

where λ is the variable wavelength in the visible light spectrum, $p(\lambda)$ denotes the power spectral distribution (PSD) of the source and $V_{\text{es}}(\lambda)$ represents the eye sensitivity function. The luminous efficiency, also known as luminous efficacy [80], of the source is defined as the ratio of the luminous flux over the input electrical power to the LED and is given by:

$$\eta_{\text{LED}} = \frac{\Phi}{P_{\text{in}}}. \tag{3.3}$$

The manufacturers' data sheets for WLEDs give a graph of the relative PSD as a function of the wavelength. For this reason, (3.2) is written as:

$$\Phi = 683 \frac{\text{lm}}{\text{W}} P_{\text{LED,o,m}}(\lambda_{\text{m}}) \int_{380\,\text{nm}}^{720\,\text{nm}} b(\lambda) V_{\text{es}}(\lambda) \text{d}\lambda\,, \tag{3.4}$$

where $P_{\text{LED,o,m}}(\lambda_{\text{m}})$ denotes the maximum optical power at a specific wavelength λ_{m}. The term $b(\lambda)$ represents the relative PSD of the light source and is given by $b(\lambda) = p(\lambda)/P_{\text{LED,o,m}}(\lambda_{\text{m}})$. The total optical power of the WLED, $P_{\text{LED,o}}$, can be determined as follows [80]:

$$P_{\text{LED,o}} = P_{\text{LED,o,m}}(\lambda_{\text{m}}) \int_{380\,\text{nm}}^{720\,\text{nm}} b(\lambda) \text{d}\lambda. \tag{3.5}$$

The solution of (3.4) for $P_{\text{LED,o,m}}(\lambda_{\text{m}})$ is substituted to (3.5). Also, (3.1) and (3.3) are taken into account, and the resulting formula expresses the output optical power of the WLED as a function of the input electrical power to the driver:

$$P_{\text{LED,o}} = \frac{\eta_{\text{d}} \eta_{\text{LED}} \int_{380\,\text{nm}}^{720\,\text{nm}} b(\lambda) \text{d}\lambda}{683 \frac{\text{lm}}{\text{W}} \int_{380\,\text{nm}}^{720\,\text{nm}} b(\lambda) V_{\text{es}}(\lambda) \text{d}\lambda} P_{\text{in,d}}. \tag{3.6}$$

The practical importance of (3.6) is that all the parameters of the second part can be directly obtained from the data sheet of the WLED [81]. The values of $V_{\text{es}}(\lambda)$ can be acquired from [80].

The direct current (DC) gain of the LoS channel according to the generalised Lambertian law is calculated by [79, 82]:

$$H_{\text{LoS}} = \frac{(m+1) S_{\text{eff}}}{2\pi d^2}\,, \tag{3.7}$$

where m denotes the Lambertian order of the WLED, S_{eff} is the effective area of the solar panel and d is the link distance. The DC gain of a LoS channel provides information about the geometrical losses of the optical link. In fact, the geometrical losses are determined by the

efficiency of collimation of the optical source. The Lambertian order is computed by:

$$m = -\frac{\ln(2)}{\ln\left[\cos(\phi_{1/2})\right]}, \tag{3.8}$$

where $\phi_{1/2}$ is the semi-angle of half power in the radiation pattern of the WLED [79].

The optical power received by the photovoltaic (PV) panel at its input plane, $P_{\text{Rx,o}}$, can be calculated by:

$$P_{\text{Rx,o}} = H_{\text{LoS}} P_{\text{LED,o}}. \tag{3.9}$$

An ideal harvested electrical power of the solar panel can be defined as $P_{\text{id}} = V_{\text{oc}} I_{\text{sc}}$, where V_{oc} is the open-circuit voltage and I_{sc} denotes the short-circuit current.

The most important metric of the energy efficiency of a solar panel or cell is the optical-to-electrical conversion efficiency. This factor is computed by [34]:

$$\eta_{\text{sr}} = \frac{P_{\text{m}}}{P_{\text{Rx,o}}} \times 100\%, \tag{3.10}$$

where P_{m} denotes the maximum electrical power and is given by $P_{\text{m}} = V_{\text{m}} I_{\text{m}}$. Also, V_{m} and I_{m} represent the voltage and current at the maximum power point (MPP) of the panel, respectively. The FF of a PV panel, f_{sr}, is given by [34]:

$$f_{\text{sr}} = \frac{P_{\text{m}}}{P_{\text{id}}} \times 100\%. \tag{3.11}$$

This parameter shows how well the circuit approximates the ideal behaviour of a current source. The combination of (3.6)–(3.11) results in the following relationship:

$$P_{\text{id}} = \frac{\eta_{\text{d}} \eta_{\text{LED}} \int_{380\,\text{nm}}^{720\,\text{nm}} b(\lambda) \text{d}\lambda \left\{ -\frac{\ln(2)}{\ln\left[\cos(\phi_{1/2})\right]} + 1 \right\} S_{\text{eff}} k}{683 \frac{\text{lm}}{\text{W}} \int_{380\,\text{nm}}^{720\,\text{nm}} b(\lambda) V_{\text{es}}(\lambda) \text{d}\lambda \, 2\pi d^2} P_{\text{in,d}}, \tag{3.12}$$

where $k = \eta_{\text{sr}} / f_{\text{sr}}$ is defined as the ratio of power efficiency over the FF of the solar panel. The values of η_{sr} and f_{sr} are highly dependent on the received optical power, the temperature and the form of incident illumination on the PV panel [13, 14, 42]. The power efficiency and FF of the panel are dependent on $P_{\text{Rx,o}}$, i.e. $k = k(P_{\text{Rx,o}})$. The optical power collected by the solar panel varies with the link distance and the collimation degree of the optical source. To the best of the author's knowledge, there is no analytical model in the literature able to predict

the variation of η_{sr} and f_{sr}, and therefore k, as a function of the optical power received from an artificial electromagnetic source. Thus, these k parameters are extracted from simple electrical measurements of the ideal harvested power, as shown in Sections 3.4 and 3.5. Measurements of the optical power would require much more time because of the small area of 1 cm^2 of a typical spectral irradiance receiver compared with the large collection area of the solar panel. As a next step, these values could be used to model different link setups and their accuracy should be verified experimentally. More importantly, the extracted k parameters could be scaled for respective experiments considering longer link distances and larger components.

The maximum total electrical efficiency of the link is given by:

$$\eta_{\text{max}} = \frac{P_{\text{m}}}{P_{\text{in,d}}} \times 100\%. \tag{3.13}$$

The maximum total electrical link efficiency can be expressed by the combination of (3.11)–(3.13) as:

$$\begin{aligned}\eta_{\text{max}} &= \frac{\eta_{\text{d}}\eta_{\text{LED}} \int_{380\,\text{nm}}^{720\,\text{nm}} b(\lambda)\text{d}\lambda \left\{ - \frac{\ln(2)}{\ln\left[\cos(\phi_{1/2})\right]} + 1 \right\} S_{\text{eff}}\eta_{\text{sr}}}{683\frac{\text{lm}}{\text{W}} \int_{380\,\text{nm}}^{720\,\text{nm}} b(\lambda)V_{\text{es}}(\lambda)\text{d}\lambda \, 2\pi d^2} \times 100\% \\ &= \eta_{\text{Tx}} H_{\text{LoS}} \eta_{\text{sr}} \times 100\%, \end{aligned} \tag{3.14}$$

where the total efficiency of the transmitter is defined by:

$$\eta_{\text{Tx}} = \eta_{\text{d}} \frac{\eta_{\text{LED}} \int_{380\,\text{nm}}^{720\,\text{nm}} b(\lambda)\text{d}\lambda}{683\frac{\text{lm}}{\text{W}} \int_{380\,\text{nm}}^{720\,\text{nm}} b(\lambda)V_{\text{es}}(\lambda)\text{d}\lambda} \times 100\%. \tag{3.15}$$

3.2.2 Single WLED based links with collimation optics

The use of optical elements for light collimation at the transmitter modifies the radiation pattern of the optical source. Also, optical losses due to absorption and scattering are induced by the material and surface roughness of the optics, respectively.

The etendue law, also known as brightness theorem, states that the product of the source area and the solid angle subtended by the system's entrance pupil as seen by the source either remains constant or increases in an optical system with passive components [77, 78]. So long as the LED source and the collimation optics have a circular symmetry, the brightness theorem can be applied to a single dimension of the problem of geometrical optics, shown in Figure 3.2.

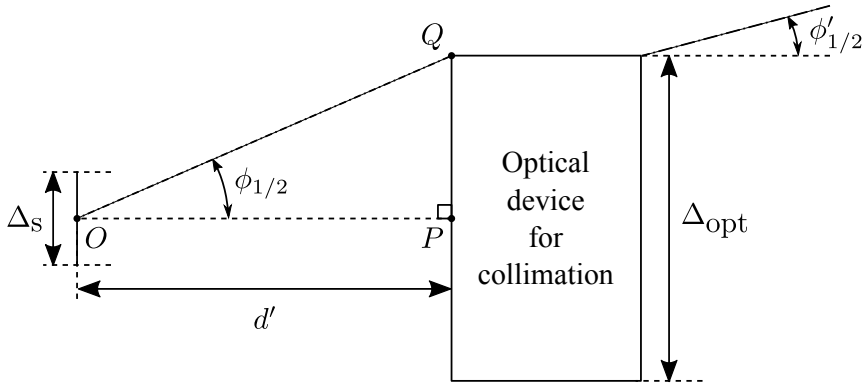

Figure 3.2: *Geometry of a surface LED and a collimation optical device.*

In this case, the etendue law can be expressed by:

$$\frac{\Delta_s}{2}\phi_{1/2} \leq \frac{\Delta_{opt}}{2}\phi'_{1/2} \Leftrightarrow \Delta_s\phi_{1/2} \leq \Delta_{opt}\phi'_{1/2}\,, \tag{3.16}$$

where Δ_s denotes the diameter of the WLED; and Δ_{opt} is the diameter of the collimation optics considered to be the same at the input and output plane. In the right triangle OPQ, the tangent of $\phi_{1/2}$ is given by:

$$\tan(\phi_{1/2}) = \frac{\Delta_{opt}/2}{d'} = \frac{\Delta_{opt}}{2d'}\,, \tag{3.17}$$

where d' is the distance between the optical source and the input plane of the optics. The approximation of small angles, i.e. $\phi_{1/2} \ll 1\,\text{rad}$, gives $\tan(\phi_{1/2}) \approx \phi_{1/2}$. Thus, the application of $\phi_{1/2} = \Delta_{opt}/(2d')$ to (3.16) provides a lower bound for the semi-angle of half power of the extended optical source and is expressed by [83]:

$$\phi'_{1/2} \geq \frac{\Delta_s}{2d'}. \tag{3.18}$$

When a PCX spherical lens is placed at its focal point, geometrical optical losses are induced by the diffuse light of the WLED. The optical power collected by the planar surface of the lens can be calculated applying $S_{eff} = \pi(\Delta_l/2)^2$ to (3.7) and using (3.9) by:

$$P_{Rx,o,l} = \frac{(m+1)\Delta_l^2}{8d'^2}P_{LED,o} \overset{(3.8)}{=} \frac{\left\{-\frac{\ln(2)}{\ln\left[\cos(\phi_{1/2})\right]}+1\right\}\Delta_l^2}{8d'^2}P_{LED,o}\,, \tag{3.19}$$

where Δ_{l} is the lens diameter. The optical power transmitted by the lens at its output spherical surface is given by $P_{\text{Tx,o,l}} = (1-r)P_{\text{Rx,o,l}}$, where r denotes the reflectance of the lens. Therefore, the optical efficiency of the extended source – WLED and lens – is defined as the ratio of transmitted optical power of the lens over the output optical power of the LED and is computed by:

$$\eta_{\text{opt}} = \frac{P_{\text{Tx,o,l}}}{P_{\text{LED,o}}} \times 100\% \overset{(3.19)}{=} \frac{(1-r)\left\{ -\frac{\ln(2)}{\ln\left[\cos(\phi_{1/2})\right]} + 1 \right\}\Delta_{\text{l}}^2}{8d'^2} \times 100\%. \tag{3.20}$$

The ideal electrical power harvested by the solar panel is given by:

$$P'_{\text{id}} = \frac{\eta_{\text{d}}\eta_{\text{LED}} \int_{380\,\text{nm}}^{720\,\text{nm}} b(\lambda)\text{d}\lambda\, \eta_{\text{opt}} \left\{ -\frac{\ln(2)}{\ln\left[\cos(\phi'_{1/2})\right]} + 1 \right\} S_{\text{eff}} k'}{683\frac{\text{lm}}{\text{W}} \int_{380\,\text{nm}}^{720\,\text{nm}} b(\lambda) V_{\text{es}}(\lambda)\text{d}\lambda\, 2\pi d^2} P_{\text{in,d}}\,, \tag{3.21}$$

where η_{opt} denotes the optical efficiency of the collimation optics, i.e. the transmitted optical power of the optics over the output optical power of the LED; $\phi'_{1/2}$ is the semi-angle of half power in the radiation pattern of the extended source, i.e. optical source with collimation optics; and $k' = \eta'_{\text{sr}}/f'_{\text{sr}}$ represents the ratio of efficiency over the FF of the solar panel. Parameter k' is used instead of k due to the higher expected levels of optical power received by the solar panel.

The maximum total electrical efficiency of the link can be written:

$$\begin{aligned}\eta'_{\text{max}} &= \frac{\eta_{\text{d}}\eta_{\text{LED}} \int_{380\,\text{nm}}^{720\,\text{nm}} b(\lambda)\text{d}\lambda\, \eta_{\text{opt}} \left\{ -\frac{\ln(2)}{\ln\left[\cos(\phi'_{1/2})\right]} + 1 \right\} S_{\text{eff}} \eta'_{\text{sr}}}{683\frac{\text{lm}}{\text{W}} \int_{380\,\text{nm}}^{720\,\text{nm}} b(\lambda) V_{\text{es}}(\lambda)\text{d}\lambda\, 2\pi d^2} \times 100\% \\ &= \eta'_{\text{Tx}} H'_{\text{LoS}} \eta'_{\text{sr}} \times 100\%,\end{aligned} \tag{3.22}$$

where H'_{LoS} is the – modified by the collimation optics – DC gain of the LoS channel. The total efficiency of the transmitter is given by:

$$\eta'_{\text{Tx}} = \eta_{\text{d}} \frac{\eta_{\text{LED}} \int_{380\,\text{nm}}^{720\,\text{nm}} b(\lambda)\text{d}\lambda}{683\frac{\text{lm}}{\text{W}} \int_{380\,\text{nm}}^{720\,\text{nm}} b(\lambda) V_{\text{es}}(\lambda)\text{d}\lambda} \eta_{\text{opt}} \times 100\%. \tag{3.23}$$

3.3 System components

The selected PV panel is based on an amorphous silicon (a-Si) material. The main reason is that a-Si solar cells present the best responsivity in the VL spectrum of $380\,\text{nm}-720\,\text{nm}$ compared to other technologies such as these of crystalline silicon (c-Si), cadmium telluride and copper indium gallium selenide [84, 85].

The physical, optical and electrical characteristics of the LED and a-Si solar panel are given in Table 3.1. The measured power efficiency of the driver is 88%. The WLED used is a high

Table 3.1: *Data sheet parameters of LED and solar panel*

White light-emitting diode (WLED)			Amorphous silicon (a-Si) solar panel		
Parameter	Unit	Value	Parameter	Unit	Value
Δ_{s}	[mm]	16	S_{eff}	[cm^2]	723.52
Φ	[lm]	2200*	P_{m}	[W]	5.15†
η_{LED}	[lm/W]	102*	η_{sr}	(%)	7.12†
$\phi_{1/2}$	[deg]	60*	f_{sr}	(%)	82.16†

*Typical values.
†Standard test conditions values.

brightness BXRA-40E2200-B-00 Bridgelux array of 24 chips [81]. The main component of the receiver is an A+ Life PA6-005 solar panel with a number of 20 thin films or cells connected in series. The dimensions of the rectangular PV panel are $30.4 \times 23.8\,\text{cm}^2$.

The geometrical and optical features of the three collimation optics are given in Table 3.2. First,

Table 3.2: *Data sheet parameters of collimation optics*

Spherical plano-convex (PCX) lens			Reflector			Parabolic mirror (PM)		
Parameter	Unit	Value	Parameter	Unit	Value	Parameter	Unit	Value
Δ_{l}	[cm]	7.5	Δ_{r}	[cm]	11.10	$\Delta_{\text{PM,max}}$	[cm]	60.96
f	[cm]	7.5	h_{r}	[cm]	8.62	f''	[cm]	15.24
r	(%)	1.5	r'	(%)	22.00	$\Delta_{\text{PM,min}}$	[cm]	3.81

an Edmund optics PCX spherical lens made of borosilicate glass Schott BK7 with magnesium fluoride anti-reflection coating [86] is placed in front of the optical source. Secondly, a spot-light CN12159 LENA-S-DL LEDiL reflector made of polycarbonate is used. The external diameter and height of the reflector are denoted by Δ_{r} and h_{r}, respectively. The reflectance of the reflector is defined as the ratio of the transmitted optical power over the collected optical

power and is represented by r'. The respective data sheet values of the LED and the reflector are applied to (3.16) with $\Delta_{\text{opt}} = \Delta_{\text{r}}$; thus, the semi-angle of half power of the reflector can be assumed to be $\phi'_{1/2} = 9.5°$. Also, an uncoated aluminium Edmund optics on-axis PM is used for light collimation. The maximum and minimum aperture diameters are represented by $\Delta_{\text{PM,max}}$ and $\Delta_{\text{PM,min}}$, respectively, and f'' is the effective focal length of the mirror. The semi-angle of half power of the mirror is calculated to be $\phi'_{1/2} = 3°$ substituting $\Delta_{\text{s}} = 1.6\,\text{cm}$ and $d' = 16.8\,\text{cm}$ to (3.18). Since the centre of the mirror has a circular hole, the optical losses are taken into account in the analytical model.

3.4 Study I: Ideal harvested power versus distance

The objective of Study I is to compare the variation of the ideal harvested electrical power as a function of distance for five scenarios using the same electrical power dissipation at the transmitter. Thus, the scenario that achieves the largest total power efficiency can be determined. More importantly, the measured values of ideal harvested power are used in the analytical model in order to determine the unknown k and k' parameters.

The parameters V_{oc} and I_{sc} are measured for a distance range of $[0.5, 5]\,\text{m}$ using increments of $0.5\,\text{m}$ in order to compute P_{id}. The electrical power consumption of the transmitter, i.e. $P_{\text{in,d}}$, is kept constant and equal to $18.3\,\text{W}$.

In Scenario I, the WLED is used in the absence of any optical device for collimation at the transmitter. In Scenario II, the optical setup of the transmitter includes the WLED and the spherical PCX lens. The lens is placed at the focal point and has a distance of $f = 7.5\,\text{cm}$ from the vertex of the circular surface of the WLED. In Scenario III, the optical transmitter comprises the WLED with the reflector. In Scenario IV, the optical part of the transmitter consists of the WLED and the spherical PCX lens. However, the lens is located at $d' = 2.5\,\text{cm}$ from the optical source because the ideal harvested electrical power is maximised at the particular distance. This is observed in the experiments by the measured values of V_{oc} and I_{sc}. In Scenario V, the transmitter includes the WLED and the large PM. The position of the PM is at $d' = 16.8\,\text{cm}$ from the WLED because the value of P'_{id} is maximised. The last four experimental scenarios are shown in Figure 3.3. Also, the OW link created at a distance of $4\,\text{m}$ in Scenario V is shown in Figure 3.4.

The analytical results of Study I are presented in Figure 3.5. These graphs are derived using

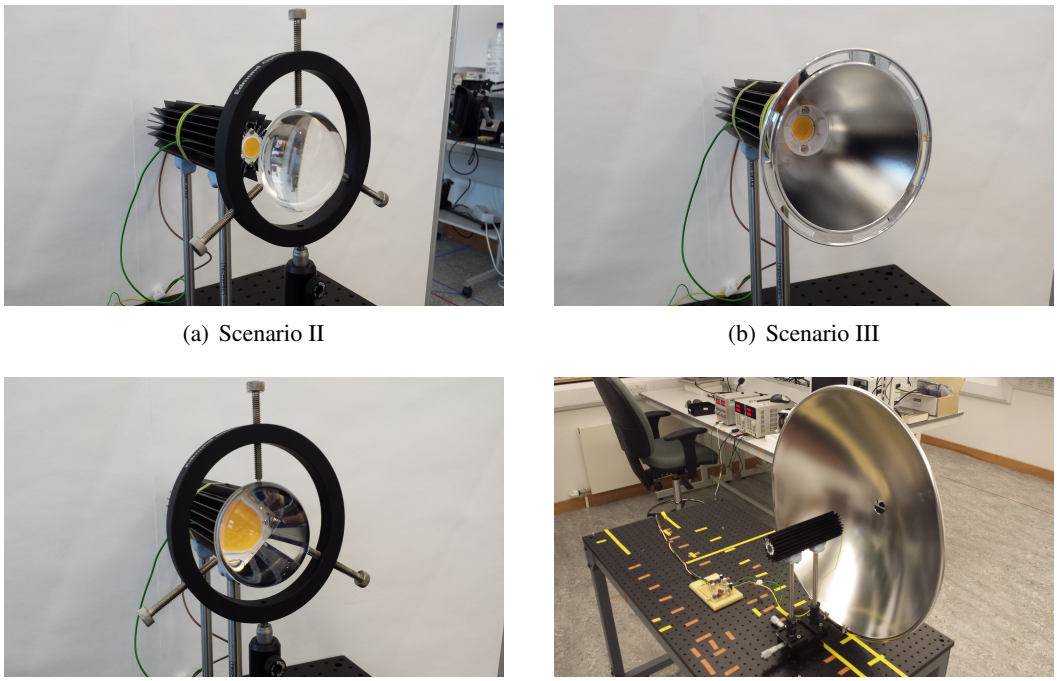

(a) Scenario II (b) Scenario III

(c) Scenario IV (d) Scenario V

Figure 3.3: *Study I: Transmitter configuration of four experimental scenarios.*

(3.12), (3.16)–(3.20) and (3.21). The system that uses the PCX lens located at its focal point exhibits an almost constant gain of 10 dB over the single LED link for distances greater than 1.5 m. The spot-light reflector collects and transmits more rays from the WLED compared with the PCX lens due to its closed cone surface. The PCX lens placed at its focal point does not capture much light because of its small size and the wide semi-angle of half power of the LED. To overcome the lens optical losses, the fourth experimental scenario of Study I was conducted. As a result, the light output of the lens increases, but the collimation or directivity of the beam decreases. A small gain of approximately 1.2 dB is achieved when the lens is located at its optimised position compared to the system with the reflector. The last scenario with the large PM attains the best performance in terms of energy efficiency. As the distance increases, the ideal harvested electrical power decreases with a lower rate of change compared to the other configurations. This is due to the increase in the effective surface area of the PM, i.e. the paraboloid surface area that reflects the collected LED rays by the solar panel, that compensates the channel losses with increased distance. At a distance of 5 m, the mirror exhibits a gain of 10.5 dB compared to the system with optimised lens positioning. Overall, the gain of the system with the PM is 28.4 dB at a distance of 5 m compared to the single LED link.

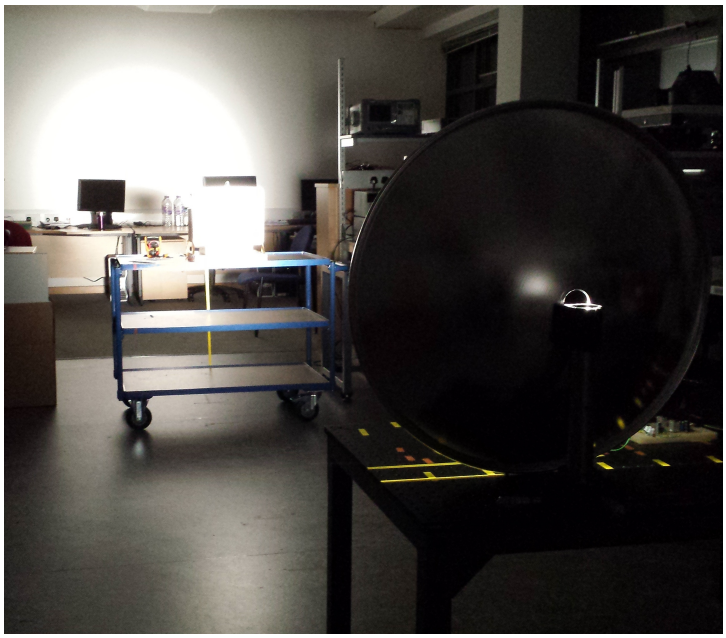

Figure 3.4: *Study I: Optical wireless power transfer link implemented in Scenario V.*

The theoretical parameters k and k' are extracted in the distance range of $[0.5, 5]$ m measuring the values of P_{id} and P'_{id} and applying them to the theoretical model. Parameters k of Scenario I and k' of Scenarios II–V are given in Table 3.3. These parameters denote the ratio of ideal electrical harvested power over the received optical power, as observed by the division of the two parts of (3.10) and (3.11). In Scenario I, the received optical power and k decrease as the distance increases. Therefore, P_{id} decreases with a larger rate than $P_{\text{Rx,o}}$. Also, the power efficiency decreases faster than the FF of the solar panel according to the definition of k and Figure 2.7; thus, it can be inferred that the received optical power is at lower levels than the maximum efficiency point. In Scenarios III and IV, parameter k' increases, while P'_{id} decreases with distance up to 1.5 m. This means that the received optical power decreases with a faster rate than P'_{id} up to 1.5 m and with a slower rate than P'_{id} for $1.5\,\text{m} \leq d \leq 5\,\text{m}$. The behaviour of k'-parameter which increases and then decreases can be attributed to the fact that the solar panel efficiency increases reaching its highest value and then decreases as the optical power decreases based on Figure 2.7. Note that in the PM based link, parameter k' increases up to a longer distance of 3.5 m compared with the other scenarios. This is because $P_{\text{Rx,o}}$ takes higher values than these of the other collimation scenarios in Figure 2.7; therefore, the solar panel efficiency reaches the maximum value at the distance of 3.5 m and is reduced after that point.

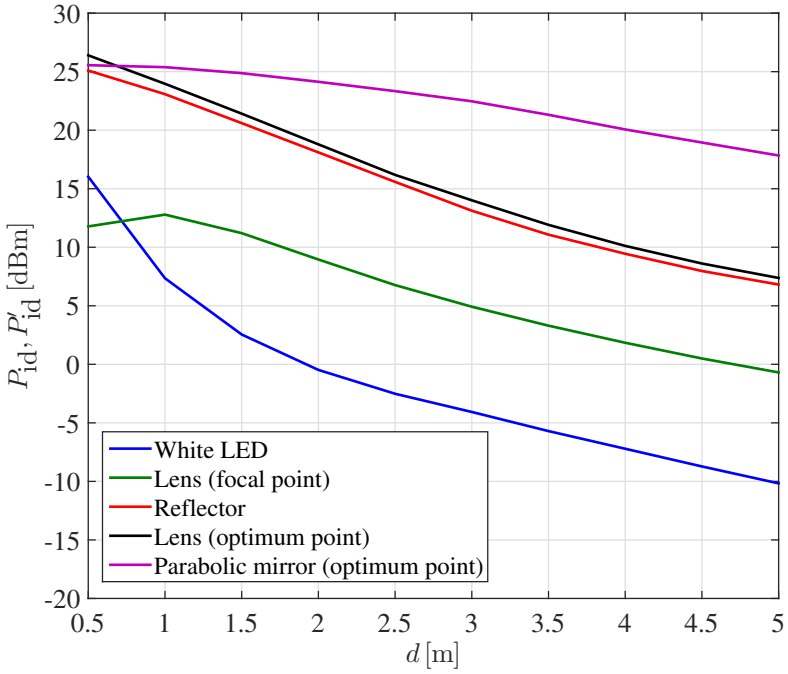

Figure 3.5: *Study I: Ideal harvested electrical power as a function of distance.*

Table 3.3: *Parameters k and k' in Study I*

d [m]		0.5	1.0	1.5	2.0	2.5	3.0	3.5	4.0	4.5	5.0
I	k (%)	8.7	4.7	3.5	3.1	3.0	3.1	2.9	2.6	2.4	2.1
II	k' (%)	0.6	1.2	1.7	1.8	1.7	1.6	1.5	1.4	1.3	1.2
III		3.5	8.8	11.2	11.2	9.8	8.0	6.8	6.1	5.5	5.2
IV		6.3	14.4	18.0	17.5	15.0	13.1	11.0	9.5	8.5	7.9
V		0.3	1.0	2.0	3.0	3.9	4.6	4.8	4.7	4.6	4.4

3.5 Study II: Ideal harvested power versus input power

The objective of Study II is to observe how the ideal harvested electrical power scales with the power consumption at the transmitter for the three scenarios that achieved the highest efficiency in Study I. Again, parameters k' are derived through the application of the measured values of P'_{id} to (3.21).

In Study II, the link distance is fixed to $5\,\mathrm{m}$. The experimental values of V_{oc} and I_{sc} are obtained as $P_{\mathrm{in,d}}$ is modified from $3.25\,\mathrm{W}$ to $30.3\,\mathrm{W}$. Thus, the ideal harvested electrical power is calculated for the three experimental systems.

The analytical results are illustrated in Figure 3.6. These graphs are derived using (3.12) and

(3.21). The logarithmic scale is used for P'_{id} in y- axis, because the difference of the black and red curve can be better observed in dBm compared with the linear scale in mW. The curve of the

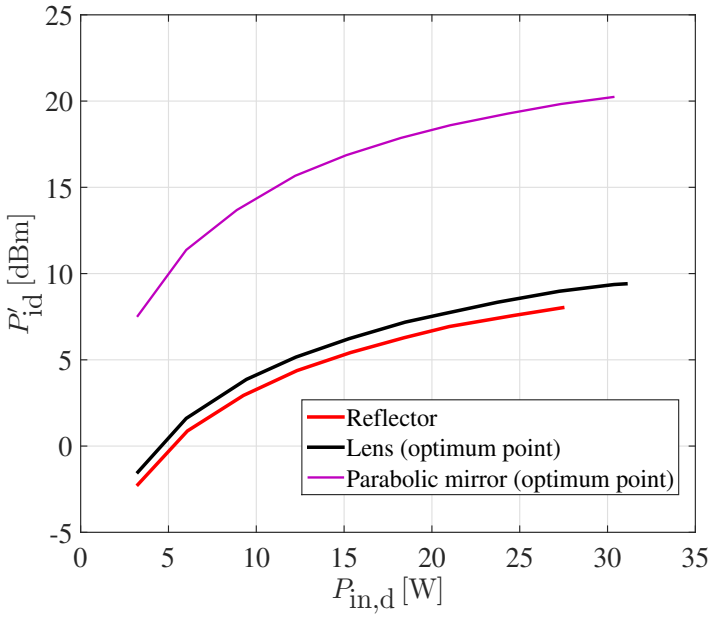

Figure 3.6: *Study II: Ideal harvested electrical power versus the transmitter's consumed electrical power at $d = 5$ m.*

system using the mirror presents a greater rate of increase compared to the graphs of the other two systems. This means that the PM offers the greatest total maximum efficiency of all of the EH systems. The scenario comprising the lens attains a gain of approximately 1.5 dB compared to the system with the reflector. The use of the large PM offers a performance superiority in terms of harvested power of about 10 dB and 11.5 dB in comparison with the other two systems.

The determined values of k' of the three scenarios are given in Table 3.4. As the input electrical power to the optical source increases, the collected optical power from the solar panel increases. Since the ratio k' increases, the ideal harvested electrical power increases with a larger rate than the received optical power.

3.6 Study III: Harvested power versus load voltage

The objective of Study III is to determine the peak harvested power and resistor value at the MPP of the solar panel for Scenario V.

Table 3.4: *Parameters k' in Study II*

III	$P_{\text{in,d}}$ [W]	3.3	6.1	9.3	12.3	15.4	18.4	21.0	24.6	27.5		
	k' (%)	3.3	3.7	4.0	4.3	4.5	4.7	4.9	5.0	5.1		
IV	$P_{\text{in,d}}$ [W]	3.3	6.0	9.4	12.3	15.3	18.5	20.7	23.7	27.3	30.4	31.1
	k' (%)	5.2	5.9	6.5	6.9	7.3	7.7	7.9	8.2	8.6	8.7	8.6
V	$P_{\text{in,d}}$ [W]	3.3	6.0	8.9	12.2	15.1	18.2	21.0	24.3	27.3	30.3	
	k' (%)	2.1	2.8	3.3	3.9	4.3	4.6	4.8	5.0	5.2	5.3	

In this last experiment, the setup of the PM based transmitter is selected, as it achieved the best performance in terms of energy efficiency in Studies I and II. Different variable resistors are connected to the output of the solar panel. The resistance value of each variable resistor is modified for the measurement of the load current and voltage. Thus, the actual harvested electrical power of the PV panel is calculated.

The measured data of Study III fitted by two quadratic curves are shown in Figure 3.7. The

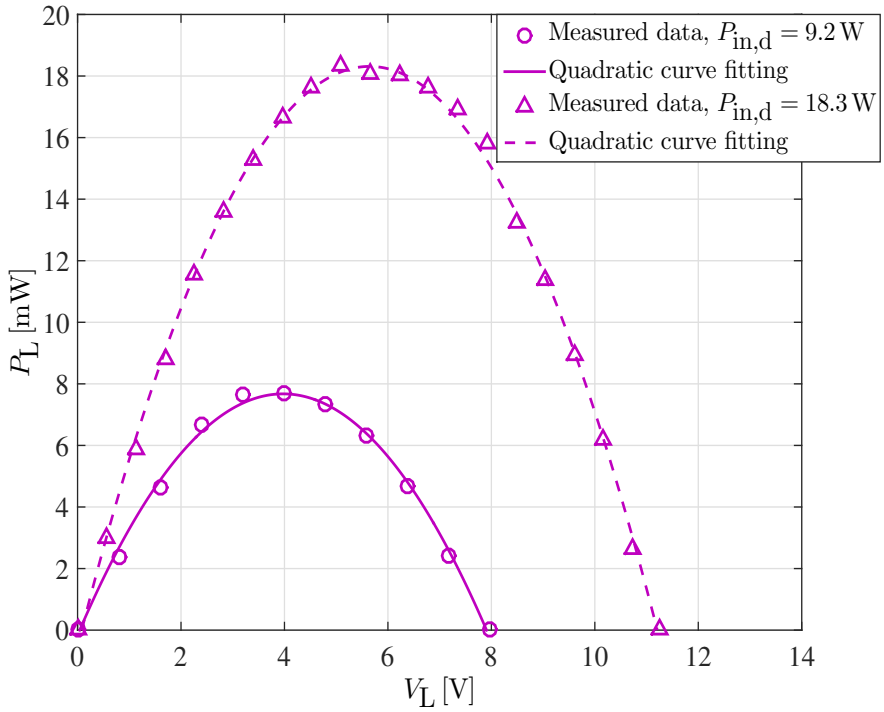

Figure 3.7: *Study III: Harvested electrical power versus the load voltage of the mirror based system at $d = 5\,m$.*

measured values of the electrical parameters of Study III are summarised in Table 3.5. Based on the measured data of Table 3.5, the values of $P_{\text{in,d}}$, P'_{id} and P_{m} can be calculated by the

products of the respective voltage and current. Therefore, the values of $P'_{\text{id}} = 24.71\,\text{mW}$ and $P_{\text{m}} = 7.69\,\text{mW}$ are obtained for $P_{\text{in,d}} = 9.19\,\text{W}$ that is in the low power region of the LED's dynamic range. The FF of the panel and the total maximum efficiency of the link are calculated to be 31.12% and 0.084% using (3.11) and (3.13), respectively. The resistor value at the MPP of the panel is $1.43\,\text{k}\Omega$. In addition, it is found that $P'_{\text{id}} = 60.67\,\text{mW}$ and $P_{\text{m}} = 18.32\,\text{mW}$ for $P_{\text{in,d}} = 18.3\,\text{W}$, i.e. in the middle power region of the WLED's dynamic range. It is also calculated that $f_{\text{sr}} = 30.2\%$ and $\eta_{\text{max}} = 0.1\%$. In this case, the measured load is $R_{\text{L}} = 2.07\,\text{k}\Omega$. A comparison of Tables 3.1 and 3.5 indicates that the measured values of the OWPT system with the PM are significantly lower than the respective data sheet electrical characteristics of the solar panel. This is explained by the fact that the spectral content of sun radiation is significantly wider than the VL spectrum of the WLED. More importantly, the received levels of optical irradiance from sunlight are in the order of $100\,\text{mW/cm}^2$, while the irradiance of the PM based system is expected to be in the order of some units of mW/cm^2 in practice.

Table 3.5: *Measured data of Study III*

V_{in} [V]	I_{in} [mA]	V_{oc} [V]	I_{sc} [mA]	V_{m} [V]	I_{m} [mA]
34.3	268	7.97	3.1	3.99	1.93
36.1	507	11.24	5.4	5.09	3.6

3.7 Summary

In this chapter, the limits of WET using off-the-shelf PV devices and WLEDs with bespoke optical subsystems were investigated with the goal to harvest 1 W of electrical power. This was considered to be the typical power needed to operate the access point of a small RF wireless cell. A VL wireless link was implemented at $5\,\text{m}$ using a high brightness WLED and an a-Si solar panel. Condition of darkness were considered because the SC needs to harvest power even in the absence of ambient light – especially sunlight. Since the radiation pattern of the WLED was wide, three different optical devices – a lens, a reflector and a PM – were used for light collimation. The maximum power efficiency of the link was achieved using the large PM as the directionality of light was maximised. This was attributed to the brightness theorem which shows that the angle divergence and the diameter of an optical beam are inversely proportional. Despite the most efficient light collimation offered by the PM, the measured link efficiency and harvested power were 0.1% and $18.3\,\text{mW}$, respectively. The low efficiency and harvested power of the PM based link were attributed to the significant geometrical losses and the low

power efficiency of the a-Si PV panel. Therefore, the next step was determined to be the use of LD arrays and c-Si solar cells to increase the power link efficiency and harvest 1 W.

Most importantly, an analytical model was developed for the entire link considering OWPT exclusively from artificial radiation sources to PV panels. This theoretical model was combined with uncomplicated electrical measurements in order to extract the – k parameters – ratio of optical-to-electrical power efficiency over the FF of the solar panel for different scenarios of light collimation. As a next step, the determined parameters will be used to model different link setups in order to verify their accuracy experimentally. Thus, k parameters could be used for future large scale experiments carried out at longer link distances and with larger components.

Chapter 4
Red laser based wireless power transfer systems: Energy efficiency and collimation

4.1 Introduction

The harvested power and link efficiency levels in Chapter 3 are in the order of mW and only 0.1%, respectively. In this chapter, the optical wireless (OW) links are created by diodes of light amplification by stimulated emission of radiation (laser) and crystalline silicon (c-Si) solar panels or cells in order to increase the power efficiency of the link. Laser diodes have higher directivity than light-emitting diodes (LEDs) and c-Si cells have higher efficiency than amorphous silicon (a-Si) cells.

Two studies are reported in this chapter. In Study I, a small number of laser diodes (LDs) is used for optical power transmission in the order of mW for maintaining the classification of the laser system as low as possible. The objective is to investigate how the electrical harvested power varies with the increase in the number of LDs used at the transmitter. Then, the required number of LDs for harvesting $1\,\mathrm{W}$ at the receiver will be estimated using the analytical framework of Chapter 2. However, since the experimental distance in Study I is only $5.2\,\mathrm{m}$ and the concept of power supply to small cells (SCs) refers to practical link distances of $100\,\mathrm{m}-300\,\mathrm{m}$, the operation of the OW link at longer distances needs to be affirmed. For this reason, Study II is undertaken for the determination of the laser beam divergence. A targeted value of $1\,\mathrm{mrad}$ is considered because the beam diameter is only $10\,\mathrm{cm}$ at $100\,\mathrm{m}$, assuming the LD to be a point source. Therefore, the geometrical losses of such a laser link could be compensated by the use of a receiver with a large aperture.

In Study I, the implemented optical wireless power transfer (OWPT) links operate at a distance of $5.2\,\mathrm{m}$ in order to compare metrics of electrical performance (such as total power efficiency and harvested power) with the respective parameters measured in Chapter 3. A significant improvement of the total power efficiency of the link by 31.7 times is shown. Also, the physical

model from Chapter 2 developed for the propagation of an elliptical Gaussian beam through a lens to free space is used to obtain the laser classification and to determine the irradiance limits for eye safety [46]. The effective single diode physical model of the solar panel [70], presented in Chapter 2, is applied to the experimental data for curve fitting. Most importantly, the analytical models are used to estimate the number of optical transmitters, i.e. LDs and collimation lenses, required to achieve 1 W of harvested power. Since the total link efficiency is a function of the efficiency of the components, the efficiency of the LDs and solar cell is measured to determine the geometrical losses. The performance of this link in terms of total efficiency is fairly compared with a state-of-the-art (SotA) inductive power transfer system (IPTS) with optimally shaped dipole coils [21]; this shows an improvement by 2.7 times. The maximum harvested power is measured to be only 25.7 mW; and an estimated number of 61 LDs and lenses is shown to be required for harvesting 1 W.

In Study II, a single LD is used with a large lens for light collimation. Also, the physical model of the Gaussian beam propagation is applied to the experimental measured points of irradiance. Thus, divergence values of full width at 36.8% of the peak intensity of 3 mrad and 5.75 mrad are reported along the small and large axes of the beam, respectively. These values correspond to an average beam divergence of 4.4 mrad that is 4.4 times the targeted value of 1 mrad. Therefore, it can be concluded that the developed OW link is capable of transmitting power efficiently at long distances, such as 100 m−300 m.

The rest of the chapter is organised as follows. The study of total link and components power efficiency is given in Section 4.2. In Section 4.3, the study of laser beam collimation is provided. Finally, a summary of the chapter is given in Section 4.4.

4.2 Study I: Total link and components power efficiency

The eye safety regulations and experimental system with respective results and discussion of Study I are given below.

4.2.1 Eye safety regulations

Important parameters for eye safety are given below for the LD used in all of the experiments and the LD and collimation lens used in Scenario III of Experiment II according to the British

Standard BS EN 60825-1:2014 [46]. The classification process is shown analytically in Appendices B.1 and B.2.

4.2.1.1 Single LD

The LD used in the experiments (i.e. HL6544FM) has not been classified by the manufacturer [63]. For this reason, a methodology for its classification is presented in Appendix B.1, based on [46]. This methodology leads to the conclusion that the LD is classified as Class 3B. Laser products of Class 3B are normally hazardous when there is intrabeam ocular exposure, i.e. within the nominal ocular hazard distance (NOHD), d_{NOHD}, according to [46]. Also, the viewing of diffuse reflections is normally safe. The accessible emission limit (AEL), κ, of Class 3B is $\kappa = 500\,\text{mW}$ according to Table 8 of [46]. The maximum permissible exposure (MPE), ν, is determined from Table A.1 [46] to be $\nu = 10\,\text{W/m}^2 = 1\,\text{mW/cm}^2$. The LD irradiance measured from a square aperture stop with side length $2x_0$ at a distance z is computed by:

$$G_{\text{Rx}}(z) = \frac{\text{erf}\left[\frac{\sqrt{2}x_0}{W_{\text{x}}(z)}\right]\text{erf}\left[\frac{\sqrt{2}x_0}{W_{\text{y}}(z)}\right]P_{\text{Tx,o,m}}}{(2x_0)^2}\,, \tag{4.1}$$

where $P_{\text{Tx,o,m}}$ denotes the maximum output optical power of the LD; and $W_{\text{x}}(z)$ and $W_{\text{y}}(z)$ are the Gaussian beam radii along x- and y- axes given by (2.3) and (2.4), respectively. In order to determine the NOHD, the inequality $G_{\text{Rx}}(d_{\text{NOHD}}) \leq \nu = 1\,\text{mW/cm}^2$ needs to be solved. The graphical solution of this inequality, i.e. the intersection point of the two curves representing $G_{\text{Rx}}(z)$ and ν, for the applied values of λ_0 to x_0 given in Table 4.1, to (2.3), (2.4) and (4.1) results in $d_{\text{NOHD}} = 63\,\text{cm}$. Therefore, a safe setup requires proper enclosure of the beam inside a tube with a length of $63\,\text{cm}$ from the LD. This is because visual access to the laser beam and its specular reflections inside the NOHD must be prevented.

4.2.1.2 Laser diode and collimation lens

When the optical beam of a LD is collimated by the use of a lens, its optical and geometrical characteristics are modified compared with the use case of a single LD. Therefore, reclassification of the laser is required. This process is analysed in Appendix B.2. Even in this case, the laser system is classified as Class 3B. Again, the AEL is $500\,\text{mW}$. However, the MPE is given in Table A.2 of [46] by $\nu = 18C_6T_2^{-0.25}\,[\text{W/m}^2]$ for $t > T_2$, where C_6 is a correction factor computed in Appendix B.2 to be 10.867. Parameter T_2 is determined from Table 9 of [46] to be

Table 4.1: *Analytical parameters for the determination of d_{NOHD}*

Parameter	Unit	Value
Operating wavelength of LD, λ_0	[nm]	660.00
$P_{\text{Tx,o,m}}$	[mW]	130.00
Gaussian beam waist along x- axis at the rectangular emission cross section of the LD, $W_{0\text{x}}$	[µm]	1.92
Gaussian beam waist along y- axis at the rectangular emission cross section of the LD, $W_{0\text{y}}$	[µm]	1.12
x_0	[mm]	3.50
Distance between the emission point of the LD and the vertex of the input lens surface, d_0	[mm]	3.25
Gaussian beam radius along x- axis at the input lens plane, $W_{1\text{x}}$	[µm]	355.62
Gaussian beam radius along y- axis at the input lens plane, $W_{1\text{y}}$	[µm]	609.62
Radius of curvature of the Gaussian beam along x- axis at the tangent plane to the input lens surface, $R_{1\text{x}}$	[mm]	3.25
Radius of curvature of the Gaussian beam along y- axis at the tangent plane to the input lens surface, $R_{1\text{y}}$	[mm]	3.25
First element of the $ABCD$ matrix of the thick lens, A	-	0.836
Second element of the $ABCD$ matrix of the thick lens, B	[mm]	4.93
Third element of the $ABCD$ matrix of the thick lens, C	[cm^{-1}]	-1.247
Fourth element of the $ABCD$ matrix of the thick lens, D	-	0.46
Radius of curvature of the Gaussian beam along x- axis at the tangent plane to the output lens surface, $R_{2\text{x}}$	[cm]	13.93
Radius of curvature of the Gaussian beam along y- axis at the tangent plane to the output lens surface, $R_{2\text{y}}$	[cm]	13.93
Gaussian beam radius along x- axis at the output lens plane, $W_{2\text{x}}$	[µm]	837.21
Gaussian beam radius along y- axis at the output lens plane, $W_{2\text{y}}$	[mm]	1.44
Distance of the Gaussian beam waist along x- axis reshaped by the lens and the vertex of the output lens surface, $d_{1\text{x}}$	[cm]	-13.91
Distance of the Gaussian beam waist along y- axis reshaped by the lens and the vertex of the output lens surface, $d_{1\text{y}}$	[cm]	-13.93

$T_2 = 10 \times 10^{[(\alpha-\alpha_{\text{min}})/98.5]} = 10 \times 10^{[(16.3-1.5)/98.5]} = 14.13\,\text{s}$, where α and α_{min} are defined and determined in Appendices B.1 and B.2. Therefore, the value of MPE is calculated to be $\nu = 18 \times 10.867 \times 14.13^{-0.25} = 100.89\,\text{W/m}^2 = 10.09\,\text{mW/cm}^2$. Here, the irradiance of the optical transmitter measured from a square aperture stop with side length $2x_0$ at a distance z is given by:

$$G'_{\text{Rx}}(z) = \frac{\text{erf}\left[\frac{\sqrt{2}x_0}{W'_{\text{x}}(z')}\right]\text{erf}\left[\frac{\sqrt{2}x_0}{W'_{\text{y}}(z'')}\right]P_{\text{Tx,o,m}}}{(2x_0)^2}\,, \tag{4.2}$$

where the assumption $(1-r) \simeq 1$ is made (r is the lens reflectance); and $W'_{\text{x}}(z')$ and $W'_{\text{y}}(z'')$ are the reshaped Gaussian beam radii along x- and y- axes given by (2.31) and (2.32), respectively. Again, the inequality $G'_{\text{Rx}}(d_{\text{NOHD}}) \leq \nu = 10.09\,\text{mW/cm}^2$ needs to be solved for the

determination of d_{NOHD}. This inequality is solved graphically by the application of the values of Table 4.1 to (2.1)–(2.10), (2.14)–(2.32) and, finally, (4.2). The resulting value of NOHD is $d_{\text{NOHD}} = 3.6\,\text{m}$, and this means that the laser beam must be enclosed into a shielding tube of length of $3.6\,\text{m}$ from the output surface of the lens for eye safety. For a safer practical setup with a smaller NOHD, either the distance between the LD and the lens should be modified so that the beam becomes more divergent inducing more geometrical losses to the link, or the transmission power should decrease according to the MPE level.

4.2.2 Experimental system and results

The selected components, Experiment I, Experiment II, Experiment III and Experiment IV are given below. Apart from Experiment I, the rest of the experiments are conducted in the absence of ambient light corresponding to OWPT to SCs during nighttime.

The system block diagram created for wireless power transfer (WPT) in Experiments I and II is shown in Figure 4.1. First, an amount of electrical power, P_{in}, is supplied to a number, N_{Tx}, of optical transmitters. The LDs are connected in parallel. The optical power generated from either a single LD or multiple LDs, $P_{\text{Tx,o}}$, is passed through a single lens or multiple lenses for beam collimation. Distance d_0 is adjusted so that the product of V_{oc} and I_{sc} is maximised at the solar receiver. Parameters V_{oc} and I_{sc} represent the open-circuit voltage and short-circuit current of the solar panel or cell, respectively. The output optical power of a single lens or multiple lenses, $(1-r)P_{\text{Tx,o}}$, is transmitted through an indoor line-of-sight wireless channel that induces mostly geometrical and misalignment losses. The optical power collected from the solar receiver is $P_{\text{Rx,o}}$. A final amount of electrical power, P_{L}, is harvested from a variable resistor that represents the load of the photovoltaic (PV) panel or cell.

In Experiments I and II, the fill factor (FF) of the solar receiver f_{sr}, the maximum total electrical efficiency of the link η_{max}, and the maximum electrical power harvested by the load P_{m} are determined. Parameters f_{sr} and η_{max} can be calculated using (2.63) and (2.66), respectively. For this reason, the variable resistor is modified for the measurement of 21 pairs of $(V_{\text{L}}, I_{\text{L}})$ by the use of two multimeters. Variables V_{L} and I_{L} denote the load voltage and load current, respectively. The number of measurements is selected to be 21, as this is considered to be an acceptable compromise between time and resolution. More importantly, the objective function of (2.54) takes the value of 5.37×10^{-4} for 21 points of one of the curves. The decrease in the number of measured data to 20 and 19 results in the values of 5.36×10^{-4} and 5.39×10^{-4},

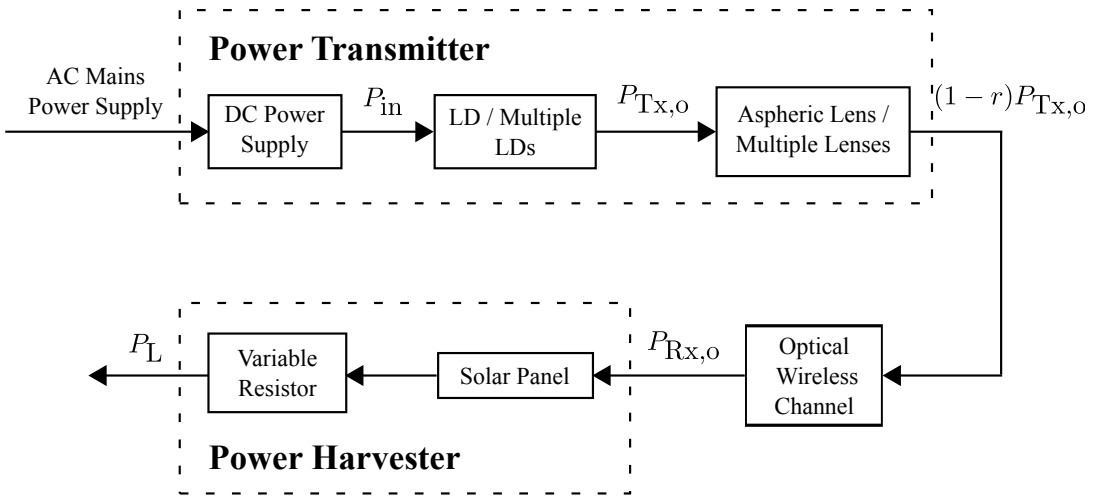

Figure 4.1: *Block diagram of the systems implemented for OWPT in Experiments I and II.*

respectively, for the objective function. Thus, there is a convergence to 5.4×10^{-4}. Also, the respective values of the load resistance, R_{L}, are measured. The values of V_{L} and I_{L} are in the range $[0, V_{\text{oc}}]$ and $[0, I_{\text{sc}}]$, respectively. The link distance measured from the output surface of the lens to the input plane of the receiver is $5.2\,\text{m}$.

4.2.2.1 System components

A single mode Opnext HL6544FM high power LD with a multi-quantum well (MQW) structure is used as the optical source for power transmission [63]. This laser is a continuous wave source. The semiconductor material of this LD is aluminium gallium indium phosphide. The selected wavelength of $660\,\text{nm}$ allows for a visible and, therefore, practically uncomplicated alignment of the link components. Also, the spectral responsivity of c-Si receivers has a large value in the red region of the visible light (VL) spectrum [87, 88]. Moreover, in terms of eye safety, the natural aversion response constitutes an inherent protection factor when there is exposure to bright VL [46]. The data sheet parameters of the selected LD are given in Table 4.2. Angles ϑ_{x} and ϑ_{y} are the beam divergences which refer to the full width at half maximum (FWHM) intensity along the parallel and perpendicular plane to the junction, respectively. The size η_{LD} denotes the power efficiency of the LD and is defined as the ratio of the output optical power over the input electrical power. The linewidth of the red LD is not provided by the manufacturer. Thus, a spectral irradiance receiver Labsphere E-1000 is used for the measurement of the spectral FWHM. To avoid the saturation of the receiver, the forward voltage and current of the diode are $2.07\,\text{V}$ and $50\,\text{mA}$, respectively. The FWHM is determined to be $6.24\,\text{nm}$. However,

note that the linewidth could be affected by the temperature of the LD; therefore, this value is expected to change at higher output power levels.

The relatively large angular divergence of the optical source requires the use of a precise lens for light collimation. Although lenses with spherical surfaces are low cost and are relatively uncomplicated to manufacture, they have spherical aberrations [69]. This inherent defect of spherical lenses prevents efficient light collimation. In contrast, the complex geometry of aspheres allows for correction of spherical aberration and creates collimated beams of better quality [69]. Therefore, two aspheric condenser lenses are used in the experiments. The first condenser lens is an ACL12708U-A with anti-reflection coating (ARC) and the second lens is an uncoated ACL4532 [89, 90]. The data sheet parameters of the two aspheric lenses are given in Table 4.2. Parameter Δ_{l} represents the lens diameter. Quantities R_1 and R_2 denote the radii of the input and output surface of the lens, respectively. The sizes t_{c}, f and n are the thickness, effective focal length and refractive index of the lens, respectively.

Table 4.2: *Data sheet parameters of red LD and lenses*

Laser diode (LD)			Coated aspheric lens			Uncoated aspheric lens		
Param.	Unit	Value	Param.	Unit	Value	Param.	Unit	Value
λ_0	[nm]	660.0	Δ_{l}	[cm]	1.27	Δ_{l}	[cm]	4.50
ϑ_{x}	[mrad]	174.5*	R_1	[mm]	15.65	R_1	[mm]	130.00
	[deg]	10.0*	R_2	[mm]	−4.75	R_2	[mm]	−18.28
ϑ_{y}	[mrad]	296.7*	t_{c}	[mm]	7.50	t_{c}	[mm]	18.50
	[deg]	17.0*	f	[mm]	8.02	f	[mm]	32.00
$P_{\text{Tx,o}}$	[mW]	50.0**	n	-	1.52	n	-	1.52
η_{LD}	(%)	22.2**	r	(%)	0.25	r	(%)	10.00

*Full width at half maximum (FWHM) values.
**Typical values.

The selected off-the-shelf optical receivers are two multi-c-Si solar panels and a mono-c-Si solar cell. In general, mono-c-Si cells have larger efficiency and are more expensive than multi-c-Si cells. The data sheet parameters of the three solar receivers used for OWPT are summarised in Table 4.3. Parameter N_{c} denotes the number of solar cells that are connected in series. Size S_{eff} is the effective area of the PV receiver. Quantity η_{sr} represents the power conversion efficiency of the solar panel or cell. Initially, the use of a SX 305 PV panel in Experiment I and Scenario I of Experiment II is investigated in terms of energy harvesting (EH) [91]. This solar panel comprises 36 multi-c-Si cells with silicon nitride ARC. The cells are placed in the form of a 4×9 matrix and are connected in series. The total effective area of the panel is

Table 4.3: *Data sheet parameters of solar receivers*

Multi-crystalline silicon (multi-c-Si) solar panel #1			Multi-crystalline silicon (multi-c-Si) solar panel #2			Mono-crystalline silicon (mono-c-Si) solar cell		
Param.	Unit	Value	Param.	Unit	Value	Param.	Unit	Value
N_c	-	36	N_c	-	8	N_c	-	1
S_{eff}	[cm^2]	389.88	S_{eff}	[cm^2]	68.64	S_{eff}	[cm^2]	156.25
P_m	[W]	4.50†	P_m	[W]	0.80†	P_m	[W]	2.91†
η_{sr}	(%)	11.54†	η_{sr}	(%)	11.66†	η_{sr}	(%)	18.62†
f_{sr}	(%)	73.17†	f_{sr}	(%)	72.46†	f_{sr}	(%)	78.53†

†Standard test conditions (STC) values.

$17.1 \times 22.8\,\text{cm}^2$. Also, a MC-SP0.8-NF-GCS multi-c-Si panel with eight cells connected in series is used in Scenario II of Experiment II [92]. The dimensions of this panel are $8.8 \times 7.8\,\text{cm}^2$. The two multi-c-Si solar receivers are shown in Figure 4.2 for a comparison of their size. Finally, the mono-c-Si cell has the dimensions of $12.5 \times 12.5\,\text{cm}^2$ and is used in Scenario III of Experiment II [93].

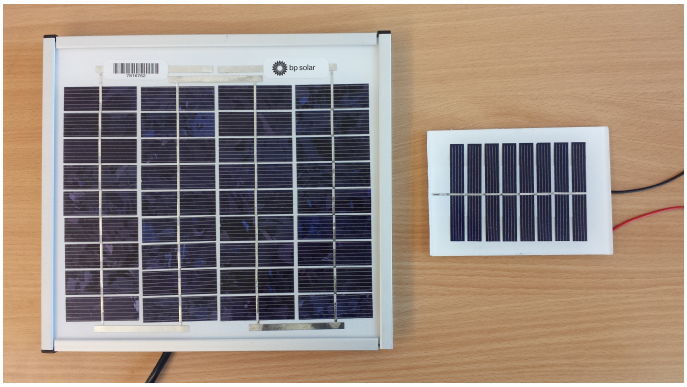

Figure 4.2: *Size comparison of the two multi-c-Si solar panels.*

4.2.2.2 Experiment I: Method and setup

Two experimental scenarios are implemented in Experiment I. A single pair of LD-lens is used in these scenarios. The transmitter comprises the uncoated 4.5 cm lens placed at 2.6 cm from the LD in the first scenario. The second scenario is realised by the use of the coated 1.3 cm lens at 3.75 mm from the LD. An illustration of this scenario is given in Figure 4.3(a) for the link distance of 5.2 m. Also, the PV panel area is 'overfilled' with the red laser beam, i.e. the elliptical beam illuminates the total area of the rectangular panel and a small region around it, as shown in Figure 4.4(a).

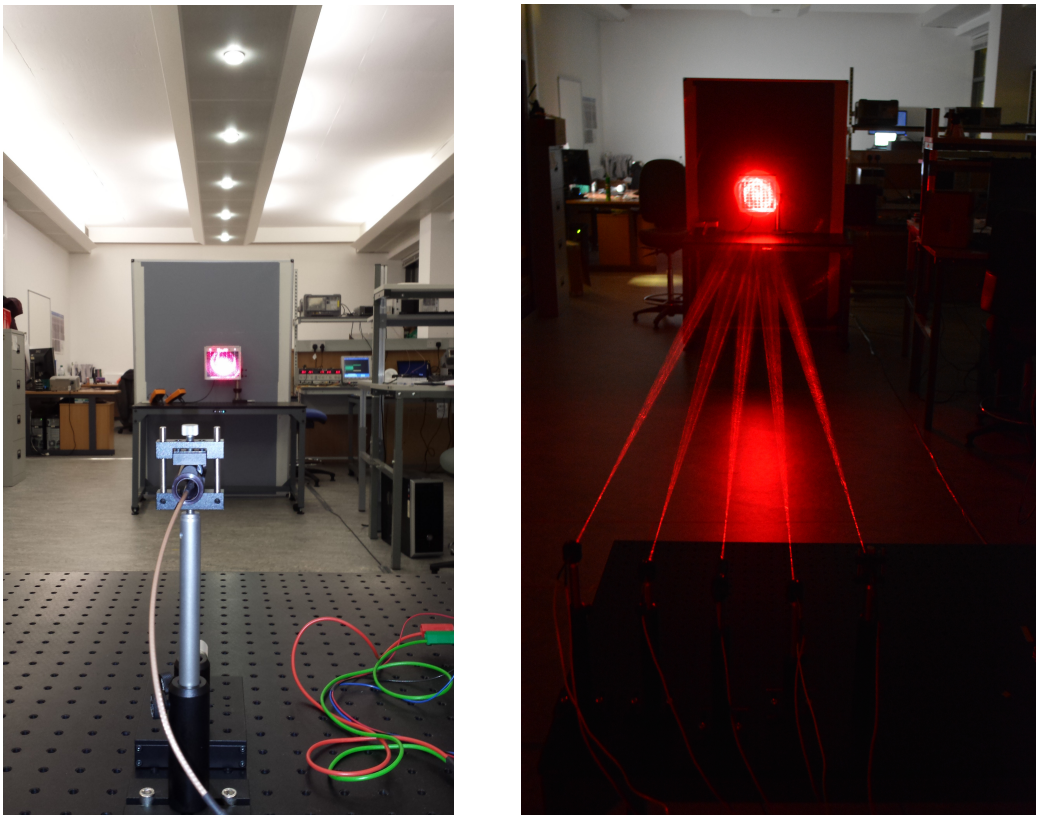

(a) Scenario II of Experiment I.

(b) Scenario I of Experiment II with $N_{\text{Tx}} = 5$.

Figure 4.3: *Experimental red laser links for OWPT to a multi-c-Si panel (a) with ambient light, and (b) without ambient light.*

4.2.2.3 Experiment I: Calculation of the LD parameters

In the far field pattern diagram from [63], the parallel and perpendicular to the junction beam divergences corresponding to the full width at 0^{th} intensity point are $2\vartheta_{\text{x}} = 40°= 698.13\,\text{mrad}$ and $2\vartheta_{\text{y}} = 80°= 1.4\,\text{rad}$, respectively. The elliptical cone defined from these values of angular divergence contains 100% of the optical power. Solving (2.1) and (2.2) for $W_{0\text{x}}$ and $W_{0\text{y}}$ results in $W_{0\text{x}} = \lambda_0/[\pi\tan(\vartheta_{\text{x}})] = 660/[\pi\tan(20°)] = 577.2\,\text{nm}$, and $W_{0\text{y}} = \lambda_0/[\pi\tan(\vartheta_{\text{y}})] = 660/[\pi\tan(40°)] = 250.37\,\text{nm}$, respectively. Therefore, the rectangular cross section of the MQW laser source has length $l = 2W_{0\text{x}} = 1.15\,\mu\text{m}$, and width $w = 2W_{0\text{y}} = 500.74\,\text{nm} \simeq 0.5\,\mu\text{m}$. The Rayleigh range – given in Chapter 2 – along the x- and y- axis is calculated to be $z_{0\text{x}} = \pi(577.2^2 \times 10^{-9})/660 = 1.586\,\mu\text{m}$, and $z_{0\text{y}} = \pi(250.37^2 \times 10^{-9})/660 = 0.298\,\mu\text{m}$, respectively. An output optical power $P_{\text{Tx,o}} = 62.6\,\text{mW}$ of the LD can be computed for a forward current of $120\,\text{mA}$ from [63]. Therefore, for a direct current (DC) input power

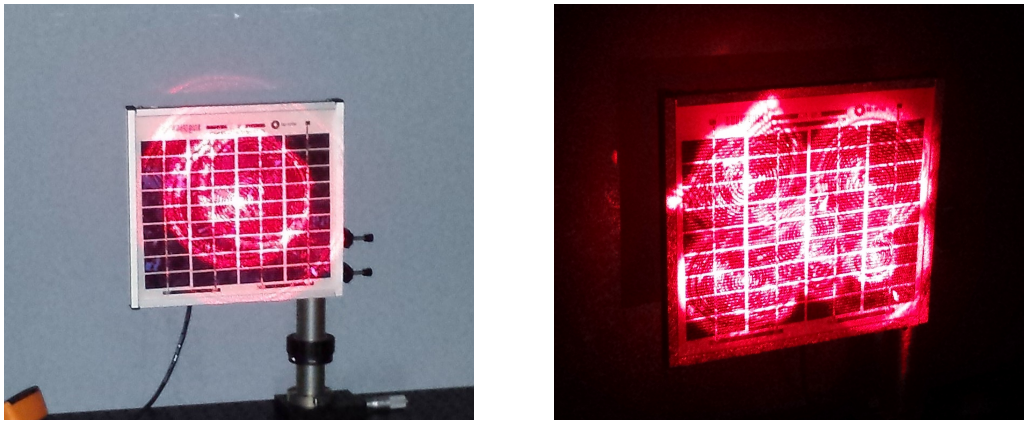

(a) Scenario II of Experiment I.

(b) Scenario I of Experiment II with $N_{\text{Tx}} = 5$.

Figure 4.4: *Illumination of (a) the whole area of solar panel by a single laser beam and (b) different cells of the panel by five laser beams.*

$P_{\text{in}} = 282\,\text{mW}$, the external power efficiency of the LD is $\eta_{\text{LD}} = 22.2\%$.

4.2.2.4 Experiment I: Analytical results

An illustration of the Gaussian beam radii along the axes of x and y as a function of distance for five theoretical scenarios is shown in Figure 4.5. These curves are derived using (2.34)–(2.48). The system performance criterion is the collection of 100% of optical power from the solar panel.

Light collimation is improved in both axes by the addition of any of the two ($1.3\,\text{cm}$ or $4.5\,\text{cm}$) lenses compared to the non-collimated scenario (single LD). In the cases of setting the lenses at their focal points (pairs of orange and magenta lines), the scenario of the $4.5\,\text{cm}$ lens achieves better light transmission than that of the $1.3\,\text{cm}$ one.

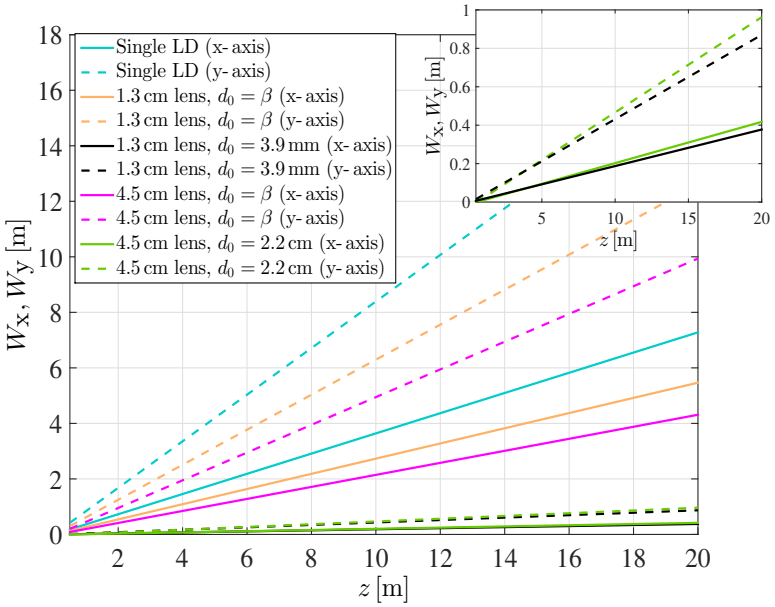

Figure 4.5: *Theoretical illustration of beam radius as a function of distance.*

This effect can be attributed to the longer radii of curvature of ACL4532 (see Table 4.2) resulting in larger beam waists and Rayleigh ranges. Similar performance is attained for the lens based scenarios (pairs of black and green lines), when the lenses are placed at the distances of 3.9 mm and 2.2 cm from the LD, respectively. Most importantly, it is observed that light collimation is further improved when either of the two aspheric lenses is placed out of its focus and much closer to the LD. This is because the laser beam uses a smaller lens surface and the marginal rays are better collimated when focusing at larger distances. This theoretical effect indicates that in the experimental links the LD-lens distances should be set close to the theoretical values of 3.9 mm and 2.2 cm.

4.2.2.5 Experiment I: Measured data and curve fitting

The experimental data of (V_L, P_L) of Experiment I are shown in Figure 4.6. Basic polynomial curve fitting is applied to each set of measurements. In terms of maximum harvested power, a gain factor of 1.2 is attained by the last scenario (black solid line) compared to the first one (magenta solid line) when the dissipated power at the transmitter is 315 mW. This finding is explained by the fact that the uncoated 4.5 cm lens attenuates the transmitted optical power to the solar panel more than the 1.3 cm lens with ARC. This difference is also noticeable in the

reflectance values of lenses, as presented in Table 4.2.

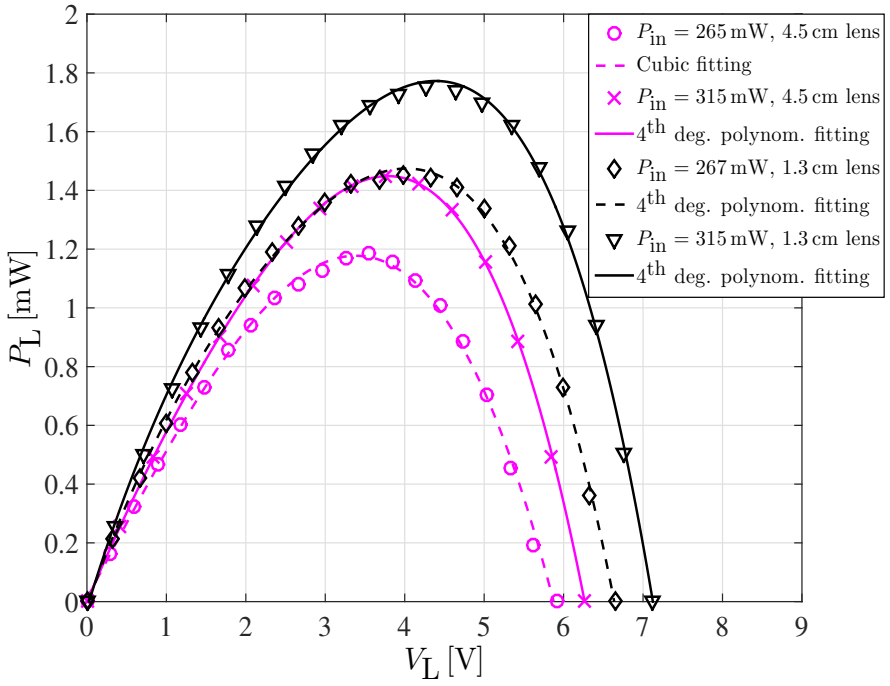

Figure 4.6: *Experiment I: Load voltage versus harvested power curves.*

4.2.2.6 Experiment II: Method and setup

Experiment II consists of three different scenarios. The coated aspheric lens with a diameter of 1.3 cm is used in all of these scenarios. In Scenario I, the number of LD-lens combinations, i.e. N_{Tx}, scales from one to five, respectively. Different laser beams 'overfill' the same total area of the panel. The 5.2 m red light link created by five diodes illuminating the whole area of the panel is shown in Figure 4.3(b). Also, five optical transmitters are used pointing the laser beams at different regions of the solar panel. Therefore, different cells are illuminated by the five optical sources in this case as shown in Figure 4.4(b).

In Scenario II, the value of N_{Tx} scales from one to four. In Figure 4.7(a), the pattern of two optical transmitters on the PV panel is illustrated. In Scenario III, the number of N_{Tx} increases from one to three. In Figure 4.7(b), the laser beam pattern on the solar cell for $N_{\text{Tx}} = 3$ and the measured voltage and current of the load are shown.

The experimental measurements of P_{L} over V_{L} for Scenarios I, II and III are shown in Figures

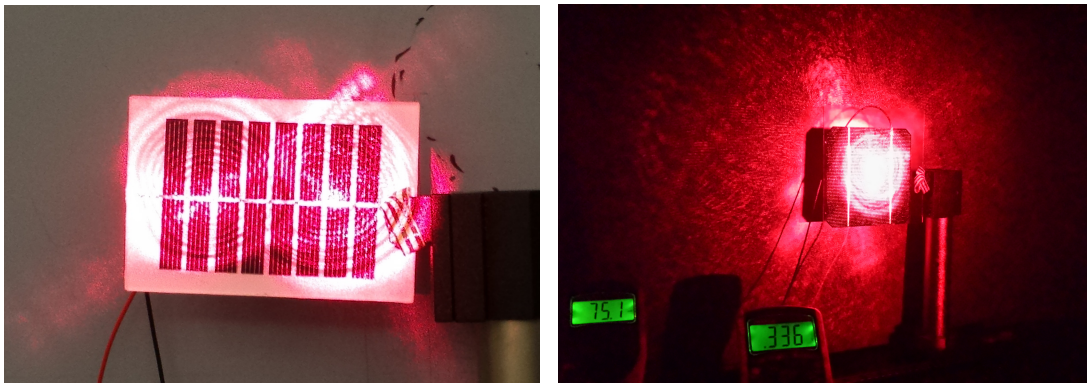

(a) Scenario II of Experiment II. (b) Scenario III of Experiment II.

Figure 4.7: *Beam pattern formed by (a) two optical transmitters on the multi-c-Si panel and (b) three optical transmitters on the mono-c-Si cell with P_m measurement.*

4.8, 4.9 and 4.10, respectively. The curves labelled as 'Physical Model' are generated by a local solution of (2.54). The measured parameters of all the three scenarios are summarised in Table 4.4 and the respective parameters of the parabolic mirror (PM) based OW link shown in Chapter 3 are given for comparison. Also, the five estimated parameters of the model of solar receiver are given in Table 4.5. The values of $I_{0,\text{eff}}$ and $I_{\text{Ph,eff}}$ give the effective dark saturation current of the diode and the effective generated photo-current, respectively. Parameters $R_{\text{S,eff}}$ and $R_{\text{P,eff}}$ represent the effective series resistance and the effective shunt resistance of the panel/cell, respectively. The quantity A_{eff} is the effective ideality factor of the diode.

Note that a peak harvested power is observed for each V-P curve in Scenarios I, II and III. The peak electrical power harvested from a solar receiver is feasible under the conditions of perfect load matching. In this case, the characteristic resistance of the solar receiver, i.e. the output resistance at the maximum power point (MPP), is equal to the resistance of the load [39]. Thus, the maximum possible amount of electrical power is transferred to the load connected to the output of the solar cell or panel.

4.2.2.7 Experiment II: Results and discussion of Scenario I

Generally, the FF values denote a low energy efficiency of the panel, as observed in Table 4.4. This is attributed to both the low irradiance levels received as well as mismatch losses of the cells. As long as the irradiance distribution of the laser beam is elliptical and Gaussian, the cells placed at the edges of the PV panel are illuminated with lower optical power compared

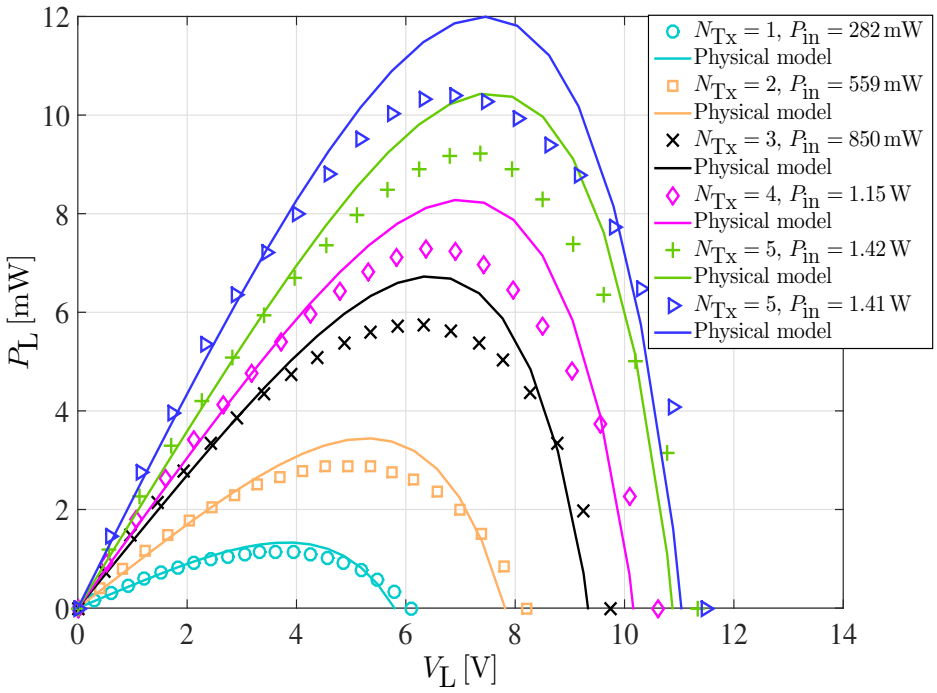

Figure 4.8: *Experiment II: Load voltage versus harvested power curves for Scenario I.*

with the centrally placed cells. Power generated by cells with higher illumination levels can be dissipated by cells with lower irradiance levels instead of the load. Therefore, the electrical output of the entire panel is determined by the cells with the lowest performance. The increase in η_{max} with the number of LDs used is due to a respective increase in the solar panel efficiency. However, this trend is not confirmed in the cases of $N_{\mathrm{Tx}} = 4$ and $N_{\mathrm{Tx}} = 5$. This can be explained by imperfections induced from the implementation of the optical transmitters. In particular, the fourth LD added to the system is mounted on a slotted lens tube, while the others on closed-surface cylindrical tubes. Thus, more optical losses could be induced by the fourth optical transmitter; therefore, the maximum link efficiency for $N_{\mathrm{Tx}} = 4$ and $N_{\mathrm{Tx}} = 5$ (overlapping beams on the whole area of the panel) is less than that of $N_{\mathrm{Tx}} = 3$. Although the best measured value of $\eta_{\mathrm{max}} = 0.74\%$ is very low, note that the maximum possible is 2.56% for the components used ($22.2\% \times 11.54\% = 2.56\%$). This theoretical upper bound can be approximated by increasing N_{Tx}. The five unknown parameters of solar panel scale with an increase in $P_{\mathrm{Rx,o}}$ due to a respective increase in N_{Tx}, and this is in agreement with [94].

4.2.2.8 Experiment II: Results and discussion of Scenario II

In Scenario II, the values of f_{sr}, η_{max} and P_m are quite low when one optical transmitter is used. In this case, the laser beam illuminates the whole rectangular area of the solar panel. Again, cells placed at the edges of the panel receive less optical power compared with the centrally placed ones due to the elliptical and Gaussian beam profile. As a result, the total electrical output of the PV panel is determined by cells with the lowest electrical performance.

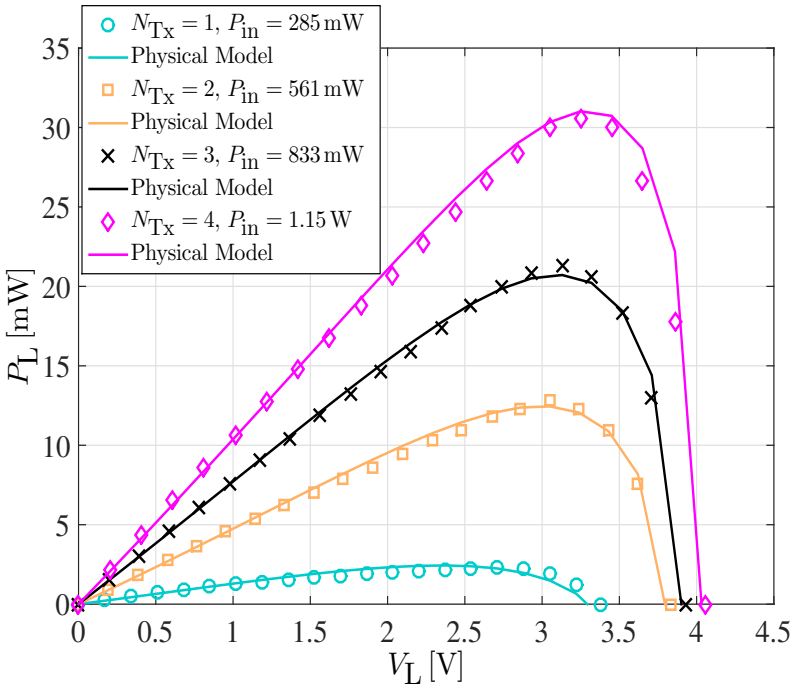

Figure 4.9: *Experiment II: Load voltage versus harvested power curves for Scenario II.*

A significant increase in the values of f_{sr}, η_{max} and P_m by at least 1.5, 2.9 and 5.6 times, respectively, is observed when $N_{Tx} > 1$ compared with the case of $N_{Tx} = 1$. When the number of optical transmitters is larger than one, the laser beams cover smaller circular and elliptical areas mainly inside the panel area illuminating different cells as shown in Figure 4.7(a) for $N_{Tx} = 2$. Thus, a more uniformly illuminated pattern is formed and the effect of mismatch losses becomes less significant. As N_{Tx} increases from two to four, the values of f_{sr}, η_{max} and P_m increase gently, as expected due to the respective increase in $P_{Rx,o}$ and, therefore, η_{sr}. The eight-cell multi-c-Si solar panel presents a significantly large f_{sr} value of 69% in the case of $N_{Tx} = 4$. Therefore, this receiver has a very high energy efficiency that is very close to its standard test conditions (STC) value of 72.46%.

The values of f_{sr}, η_{max} and P_m for $N_{Tx} = 4$ are increased by the multiplication factors of 2, 26.6 and 1.7, respectively, compared with the values of the same parameters of the PM based OW link shown in Chapter 3. This significantly improved performance, especially for η_{max}, is attributed to the large restriction of geometrical losses by the use of the more directive optical sources of LDs compared with LEDs, and to the higher energy efficiency of multi-c-Si than that of a-Si technology of solar panels. Also, f_{sr}, η_{max} and P_m for $N_{Tx} = 4$ are increased by the factors of 1.8, 4.2 and 4.2, respectively, compared with the same parameters obtained in Scenario I. These improved values are obtained due to the decrease in dimensions and number of cells of the solar panel that allows for the concentration of more optical power uniformly distributed on the cells. Thus, the effect of mismatch losses is less significant than that in Scenario I. Uniform illumination over the different in-series connected cells of a solar panel is desired to maximise its electrical output [38]. Otherwise, the solar cell of the poorest illumination mostly contributes to the total generated photo-current of the panel.

The resistance load values measured at the MPP decrease from 3.2 kΩ to 344 Ω, while the received optical power increases. For a practical R_L value of 50 Ω, better load matching can be achieved either by an increase in N_{Tx} and therefore $P_{Rx,o}$, or by the use of a DC-to-DC converter for maximum power point tracking [95].

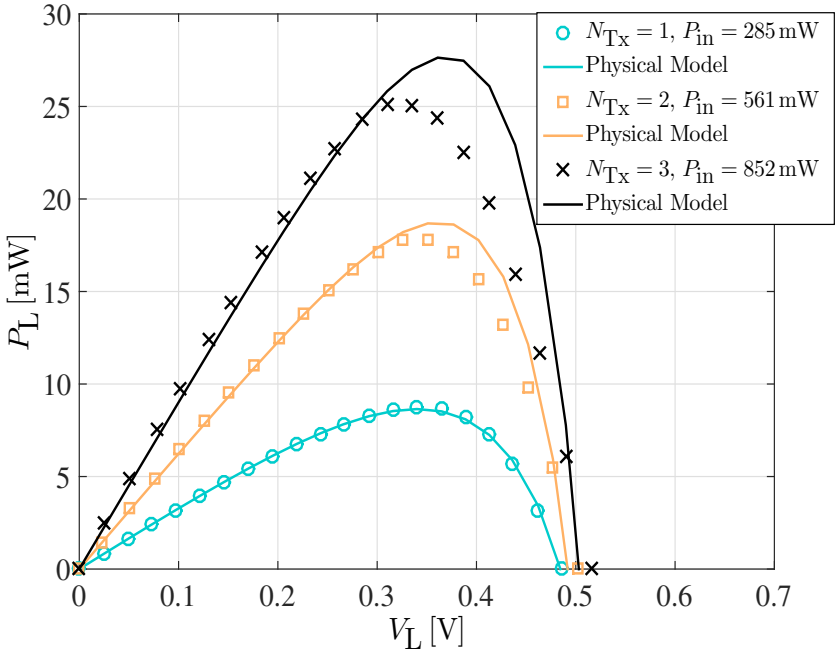

Figure 4.10: *Experiment II: Load voltage versus harvested power curves for Scenario III.*

Table 4.4: *Measured parameters in Experiment II and Chapter 3*

Scenario	N_{Tx}	d_0 [mm]	f_{sr} (%)	η_{max} (%)	P_{m} [mW]	$R_{\text{L}}^{\dagger}$ [kΩ]
I	1	3.8^{***}	34.41	0.40	1.1	11.51
	2		34.69	0.52	2.9	8.45
	3		36.98	0.67	5.7	6.98
	4		39.27	0.63	7.3	5.57
	5		38.75	0.65	9.2	5.87
			36.20	0.74	10.4	4.56
II	1	7.0^{*}	45.08	0.80	2.3	3.20
	2	6.0^{*}	66.89	2.28	12.8	0.73
	3	5.5^{*}	68.55	2.56	21.3	0.46
	4	5.0^{*}	69.03	2.66	30.6	0.34
III	1	3.25^{**}	53.35	3.06	8.7	$13.5 \cdot 10^{-3}$
	2	3.25^{***}	54.20	3.17	17.8	$7.3 \cdot 10^{-3}$
	3		49.39	3.06	25.7	$4.0 \cdot 10^{-3}$
V in Chapter 3	1	168.0	31.12	0.08	7.7	1.43
			30.20	0.10	18.3	2.07

Tolerance of $^{*} \pm 0.5$ mm, $^{**} \pm 0.75$ mm and $^{***} \pm 0.25$ mm.
†Measured at the maximum power point (MPP).

4.2.2.9 Experiment II: Results and discussion of Scenario III

In Scenario III, the values of f_{sr} and η_{max} are expected to increase as the number of optical transmitters increases. However, this expectation is not confirmed in the case of $N_{\text{Tx}} = 3$. This is explained by the significantly low decrease in effective series resistance value from $80\,\text{m}\Omega$ ($N_{\text{Tx}} = 2$) to $30\,\text{m}\Omega$ ($N_{\text{Tx}} = 3$) compared with the transition from $1.04\,\Omega$ ($N_{\text{Tx}} = 1$) to $80\,\text{m}\Omega$ ($N_{\text{Tx}} = 2$), as shown in Table 4.5. Therefore, more power is dissipated in the series resistance and, finally, the FF and efficiency of the solar cell decrease. Comparing Figures 4.11 and 2.7, it can be inferred that the solar cell efficiency reaches its maximum value when two laser transmitters are used ($N_{\text{Tx}} = 2$). The series resistance of the cell decreases, when the incident optical power increases. This is attributed to the increase in the conductivity of the active layer [13]. Also, note that the curve of maximum link efficiency as a function of harvested power in Scenario III shown in Figure 4.11 is in close agreement with the curve of solar cell efficiency versus incident optical power in [14].

Comparing all of the three scenarios, the best value of $\eta_{\text{max}} = 3.17\%$ is achieved in the case of $N_{\text{Tx}} = 2$ for Scenario III. Note that this value of maximum link efficiency is low because of the low values of η_{LD} and $\eta_{\text{sr}}(5.2\,\text{m})$ as shown in Experiments III and IV.

A comparison of the values of f_{sr} and η_{max} for $N_{\text{Tx}} = 2$ with the values of the same parameters

of the PM based OW link in Chapter 3 shows an increase of 1.6 and 32 times, respectively. The same comparison with the results of Scenario II presents an increase by 1.6 and 6.2 times, respectively. Also, quantity P_{m} for $N_{\mathrm{Tx}} = 3$ is increased by the factors of 1.4 and 4.4 compared with Scenario V of Chapter 3 and Scenario II, respectively. A slightly better performance in terms of $\eta_{\max}$ of Scenario III compared with Scenario II is observed. This is attributed to the larger optical-to-electrical conversion efficiency of mono-c-Si cell than that of multi-c-Si panel as expected by observing Table 4.3. Also, the larger area of 2.3 times of the PV cell compared with the solar panel allows for the reception of a larger amount of $P_{\mathrm{Rx,o}}$ reducing the geometrical losses.

Finally, the measured values of R_{L} at the MPP are quite low due to the low values of V_{L}. Therefore, matching of the output of the cell with a practical load of $50\,\Omega$ can be achieved either by a DC-to-DC converter or by the connection of a large number of cells in series.

Table 4.5: *Estimated parameters of solar receiver model for Experiment II*

Scenario	N_{Tx}	$I_{0,\mathrm{eff}}$ [μA]	$R_{\mathrm{S,eff}}$ [kΩ]	A_{eff}	$R_{\mathrm{P,eff}}$ [kΩ]	$I_{\mathrm{Ph,eff}}$ [mA]
I	1	117.3	1.50	120.0	32.0	0.47
	2	103.9	0.95	125.0	35.5	0.86
	3	115.8	0.85	135.0	38.0	1.4
	4	111.8	0.75	140.0	40.5	1.5
	5	116.9	0.65	145.0	41.5	1.8
		229.2	0.60	175.0	42.0	2.2
II	1	312.83	0.50	65.0	5.0	1.3
	2	54.69	0.11	32.0	4.0	4.7
	3	52.96	0.07	30.0	4.5	7.7
	4	21.85	0.05	25.0	3.0	10.2
III	1	675.57	$1.04 \cdot 10^{-3}$	4.82	26.3	33.3
	2	107.89	$0.08 \cdot 10^{-3}$	3.02	27.0	62.6
	3	144.29	$0.03 \cdot 10^{-3}$	3.05	90.0	90.5

4.2.2.10 Experiment II: Comparison with an IPTS

In [21], a SotA experimental study is presented by the implementation of an IPTS with dipole coils able to deliver amounts of power in the order of hundreds of W. In Figure 16 of [21],

the power efficiency measured from the input of the inverter to the load resistor is plotted as a function of the power harvested from the load for different values of distance of 2 m, 3 m, 4 m and 5 m. The operating frequency of the system is 105 kHz [21]. A comparison of the OW systems implemented in the three scenarios of Experiment II and the IPTS is shown in Figure 4.11 in terms of total power efficiency at a distance of 5 m. When Scenario III is applied,

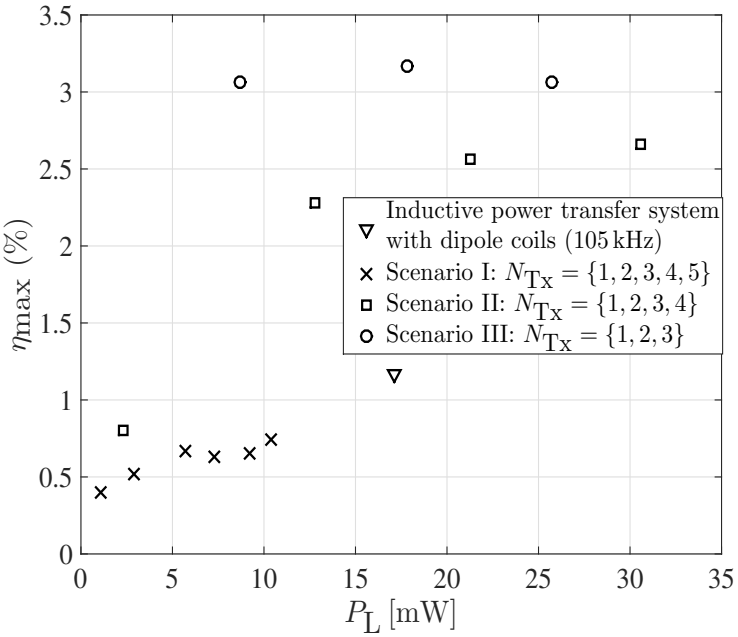

Figure 4.11: *Experimental maximum link efficiency versus the maximum harvested electrical power.*

the maximum link efficiency is improved from a value of 1.17% to 3.17% that represents a significant increase of 2.7 times. Therefore, taking into account the fact that IPTSs are designed to operate at short distances of a few cm [17] or m [21], the developed OW link with two LDs has an acceptable value of $\eta_{\max}$ and the link distance can be further extended.

4.2.2.11 Experiment III

The objective of Experiment III is to determine the efficiency values of each of the four LDs, used in Scenario II of Experiment II, as a function of their input power. Therefore, the output optical power of each LD is measured for 22 different values of input electrical power. Again, this number of measurements is considered to be sufficient for the resolution of the respective graph and the required time for the experiment. A Thorlabs S121B silicon sensor with a square

area of $1 \times 1\,\text{cm}^2$ is placed at $1.5\,\text{mm}$ from each LD in order to collect and measure the total amount of optical power of each laser beam. The mean values of experimental data are fit by two simple quadratic curves applied to the two operation regions of the device. These two regions are characterised by spontaneous and stimulated emission, respectively.

The external power efficiency of the four LDs is shown in Figure 4.12 as a function of P_{in}. The

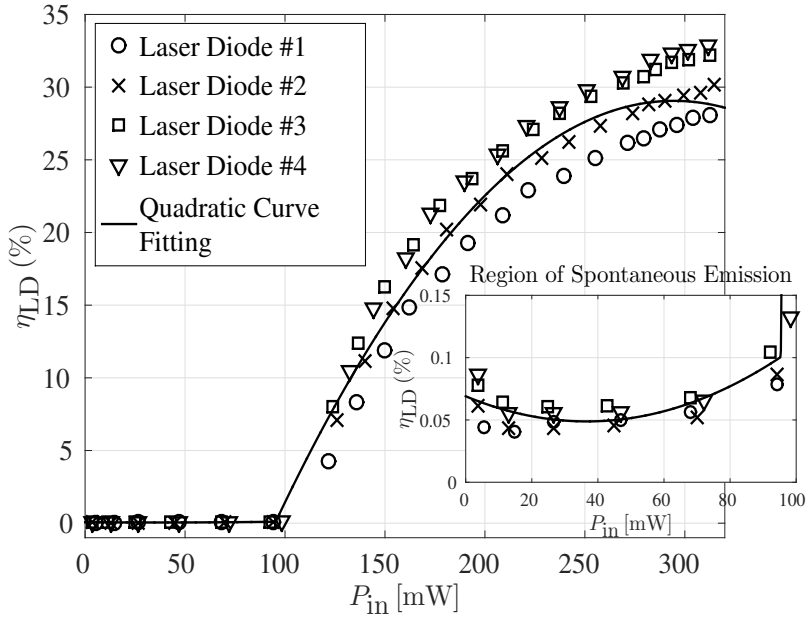

Figure 4.12: *Experiment III: Laser diodes efficiency versus input electrical power.*

maximum efficiency values of the four LDs shown as #1, #2, #3 and #4 are measured to be 28.1%, 30.2%, 32.2% and 32.9%, respectively. In the first region of the theoretical curve, the output optical power remains at very low levels of up to $94.6\,\mu\text{W}$, as P_{in} increases from 0 to $95.4\,\text{mW}$. Also, for the same values of P_{in}, the mean value of power efficiency of the four LDs ranges from 0.05% to 0.1%. This region of applied P_{in} causes spontaneous emission to the LD, one of the basic forms of interaction between atoms and photons in quantum physics [96]. In the second region of the theoretical curve, $P_{\text{Tx,o}}$ increases significantly up to $86.1\,\text{mW}$ with a respective efficiency of 29.1%, while P_{in} scales from $95.4\,\text{mW}$ to $320\,\text{mW}$. This region of P_{in} induces stimulated emission to the optical source [96].

In order to compare the variation between the four LDs, the error in efficiency, ϵ_{eff} (%), is used and is defined as the difference in theoretical efficiency by the experimental efficiency data for each LD. Figure 4.13 shows how the error in efficiency of the four LDs scales with the input

electrical power of each LD. The mean squared error (MSE) in power efficiency of each of the LDs is calculated to be $3.52 \cdot 10^{-4}$, $3.46 \cdot 10^{-4}$, $3.13 \cdot 10^{-5}$ and $4.89 \cdot 10^{-4}$. This means that the LD shown as #3 in Figure 4.12 and Figure 4.13 best approximates the efficiency values of the theoretical curve. In the case of a large number of LDs, such as the 42 laser based transmitter designed in Chapter 5, the variation of LDs is expected to affect the harvested power. Therefore, to affirm 1 W with high confidence, the required number of optical sources should be estimated based on the LD with the lowest efficiency.

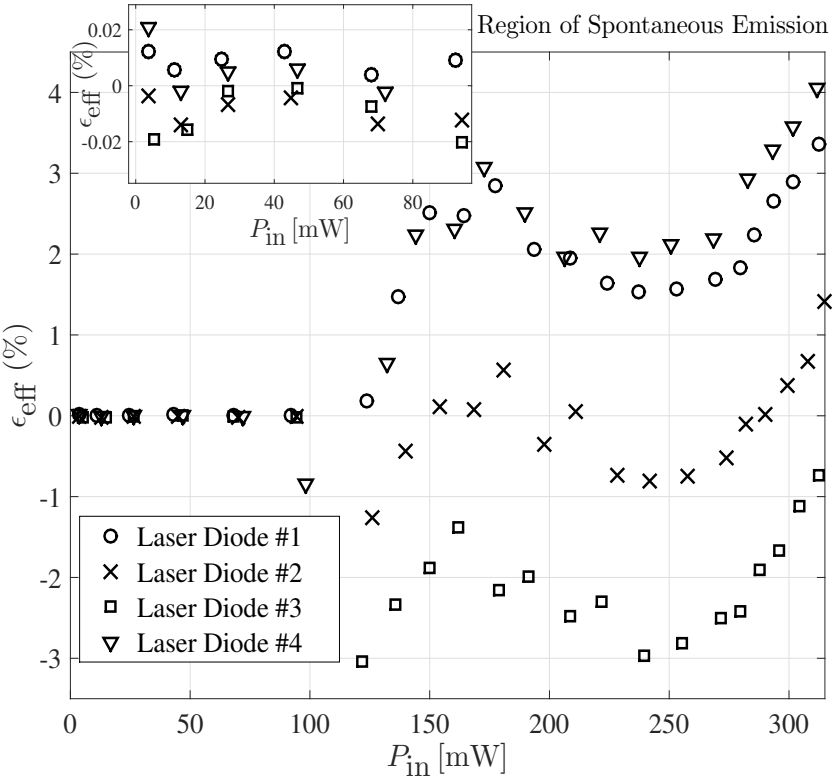

Figure 4.13: *Experiment III: Efficiency error as a function of input electrical power for four LDs.*

4.2.2.12 Experiment IV

Experiment IV is undertaken for the determination of the solar cell efficiency. Two LDs with aspheric lenses are transmitting power to the mono-c-Si cell placed at a distance of 5.2 m. The electrical input power is 561.3 mW. The S121B sensor is used for the measurement of 25 values of power, P_{s}, at a distance of 3.4 cm from the solar cell. The 25 measurements are considered to provide a good resolution of the optical power of the laser beams. The measurement points are

located on a square grid as shown in Figure 4.14. The distance between two consecutive points is $2.08\,\text{cm}$. The average irradiance of the 25 measured points is computed and is multiplied by S_{eff}. Therefore, the value of $P_{\text{Rx,o}}(5.2\,\text{m})$ is calculated, and the parameters $\eta_{\text{sr}}(5.2\,\text{m})$, $\rho(5.2\,\text{m})$ and $\eta_{\text{c}}(5.2\,\text{m})$ are determined from (2.62), (2.64) and (2.67), respectively. Quantities $\rho(z)$ and $\eta_{\text{c}}(z)$ denote the responsivity and collection efficiency of the PV receiver, respectively, as a function of distance z.

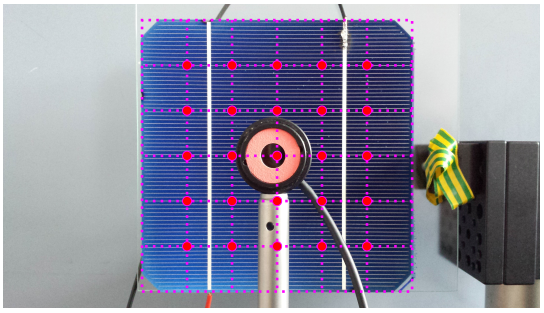

Figure 4.14: *Experiment IV: Measurement points of power for the calculation of $P_{Rx,o}$ in front of the solar cell.*

The 25 measured data of P_{s} are shown in Figure 4.15 versus the x- and y- dimensions of the solar cell. The power of each of the two optical transmitters measured at the (x, y, z) points – Cartesian coordinates – of $(0, 0, 3.7\,\text{cm})$ and $(0, 0, 3.2\,\text{cm})$ is $74.58\,\text{mW}$ and $72.8\,\text{mW}$, respectively. These values are significantly attenuated at a distance of $5.2\,\text{m}$ from the transmitters. In particular, the maximum optical power measured at the (x, y, z) point of $(0, 2.08\,\text{cm}, 5.2\,\text{m})$ is $3.12\,\text{mW}$. The average irradiance value of these 25 measurements is $0.86\,\text{mW}/(1\,\text{cm}^2) = 0.86\,\text{mW/cm}^2$. Therefore, the received optical power of the cell is calculated to be $P_{\text{Rx,o}}(5.2\,\text{m}) = 0.86 \times 12.5^2 = 134.38\,\text{mW}$.

The application of $P_{\text{m}} = 17.8\,\text{mW}$ and $P_{\text{Rx,o}} = 134.38\,\text{mW}$ to (2.62) results in $\eta_{\text{sr}}(5.2\,\text{m}) = 13.25\%$ in the case of $N_{\text{Tx}} = 2$. This value of solar receiver efficiency is 5.37% lower than the respective one at STC (see Table 4.3). For this reason, the specific mono-c-Si cell is selected to be the receiver in the simulation model developed for the objective of harvesting $1\,\text{W}$ in Chapter 5. Moreover, the maximum power that this cell can generate under STC is $2.91\,\text{W}$ according to Table 4.3 that is larger than the required amount of $1\,\text{W}$.

So long as the experimental value of $\eta_{\text{sr}}(5.2\,\text{m})$ is now known, an estimation of the collection efficiency can be carried out using (2.67). The term $(1-r)$ of (2.67) is assumed to be negligible because $r = 0.0025 \ll 1$. The input electrical power of $561\,\text{mW}$ is equally supplied to the two

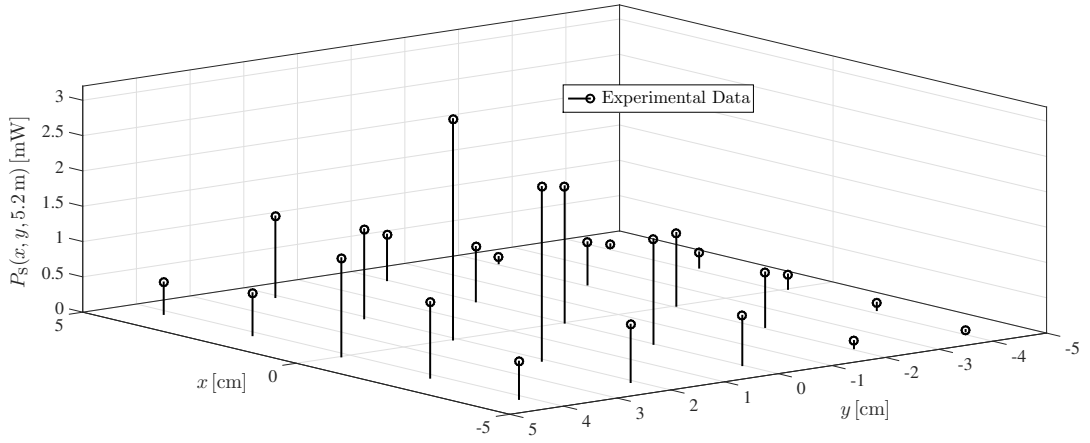

Figure 4.15: *Experiment IV: Optical power measured by S121B sensor on the x-y transverse plane of the solar cell.*

optical transmitters. Thus, the electrical-to-optical efficiency of two optical transmitters for $P_{\text{in}} = 561\,\text{mW}$ is the same as η_{LD} of $N_{\text{Tx}} = 1$ for $P_{\text{in}} = 280.5\,\text{mW}$. Also, a mean value of $\eta_{\text{LD}} = 26.76\%$ is calculated for $P_{\text{in}} = 280.5\,\text{mW}$ based on the quadratic curve fitting of Figure 4.12. Therefore, the application of $\eta_{\text{max}} = 0.0317$, $\eta_{\text{LD}} = 0.2676$ and $\eta_{\text{sr}}(5.2\,\text{m}) = 0.1325$ to (2.67) results in the collection efficiency value of $\eta_{\text{c}}(5.2\,\text{m}) = 89.4\%$. This very high value allows for the characterisation of the link with two LDs as highly directive so that it effectively delivers $134.38\,\text{mW}$ to a solar cell area of $12.5 \times 12.5\,\text{cm}^2$ placed at $5.2\,\text{m}$ with only 10.6% of optical losses.

Finally, the application of $I_{\text{Ph,eff}} = 62.6\,\text{mA}$ and $P_{\text{Rx,o}}(5.2\,\text{m}) = 134.38\,\text{mW}$ to (2.64) gives an estimated responsivity of $\rho(5.2\,\text{m}) = 0.47\,\text{mA/mW}$. An experimental value of responsivity of $\rho(5.2\,\text{m}) = 0.49\,\text{mA/mW}$ is obtained under the assumption of $I_{\text{Ph,eff}} \simeq I_{\text{sc}} = 65.4\,\text{mA}$.

4.2.2.13 Estimation of the number of optical transmitters

Let $N_{\text{Tx,req}}$ be the required number of pairs of LDs and lenses for $P_{\text{m}} = 1\,\text{W}$ at the link distance $d = 5.2\,\text{m}$. In Scenario I of Experiment II, a value of $V_{\text{m}} = 6.89\,\text{V}$ is achieved for five optical transmitters with $P_{\text{m}} = 10.39\,\text{mW}$. Therefore, a maximum possible value of $V'_{\text{m}} = 16.5\,\text{V}$ can be assumed for the solar panel at high illumination levels for harvesting $P'_{\text{m}} = 1\,\text{W}$ according to [91]. The load current at MPP is calculated to be $I'_{\text{m}} = 1/16.5 = 60.6\,\text{mA}$. The values of $16.5\,\text{V}$ and $60.6\,\text{mA}$ are substituted for V_{L} and I_{L}, respectively, in the 'exhaustive' search algorithm (2.54). This results in the following set of parameters $(1.1\,\text{mA}, 0.1\,\Omega, 290, 90\,\text{k}\Omega, 69.1\,\text{mA})$.

The responsivity of the solar panel is assumed to be $\rho = \rho(5.2\text{ m}) = 0.01\,\text{mA/mW}$. Solving (2.64) for $P_{\text{Rx,o}}$ results in $P_{\text{Rx,o}} = I_{\text{Ph,eff}}/\rho = 69.1/0.01 = 6.91\,\text{W}$. The total amount of optical power is considered to be received from the panel, i.e. $P_{\text{Rx,o}} = N_{\text{Tx,req}} P_{\text{Tx,o}}$. Therefore, the required number of optical transmitters is calculated to be $N_{\text{Tx,req}} = P_{\text{Rx,o}}/P_{\text{Tx,o}} = 6.91/(62.6 \times 10^{-3}) \approx 110$.

In Scenario III of Experiment II, a value of $V_{\text{m}} = 351\,\text{mV}$ is achieved with $P_{\text{m}} = 17.8\,\text{mW}$ for $N_{\text{Tx}} = 2$. Therefore, a required voltage $V'_{\text{m}} = 537\,\text{mV}$ is assumed for the solar cell at high illumination levels for attaining $P'_{\text{m}} = 1\,\text{W}$ according to [93]. The load current at MPP is calculated to be $I'_{\text{m}} = 1/0.537 = 1.86\,\text{A}$. The values of $537\,\text{mV}$ and $1.86\,\text{A}$ are substituted for V_{L} and I_{L}, respectively, in the 'exhaustive' search algorithm (2.54). This results in the following set of parameters $(I_{0,\text{eff}}, R_{\text{S,eff}}, A_{\text{eff}}, R_{\text{P,eff}}, I_{\text{Ph,eff}}) = (83.9\,\text{pA},\ 0.5\,\text{m}\Omega,\ 1,\ 500\,\text{k}\Omega,\ 1.96\,\text{A})$. The responsivity of the solar panel is considered to be $\rho = 0.49\,\text{A/W}$, as measured in Experiment IV. Solving (2.64) for $P_{\text{Rx,o}}$ results in $P_{\text{Rx,o}} = I_{\text{Ph,eff}}/\rho = 1.96/0.49 = 4\,\text{W}$. An assumption of 10.6% of geometrical optical losses is made, as measured in Experiment IV. Thus, the transmitted optical power is calculated to be $P_{\text{Tx,o}} = P_{\text{Rx,o}}/\eta_{\text{c}} = 4/0.894 = 4.47\,\text{W}$. Therefore, the required number of optical transmitters is calculated to be $N_{\text{Tx,req}} = 4.47/(73.69 \times 10^{-3}) \approx 61$, where $73.69\,\text{mW}$ is the average output optical power of the two LDs measured in Experiment III.

4.3 Study II: Beam collimation

The experimental system, results and discussion of Study II are given below.

4.3.1 Experimental system

In this experimental study, the use of a large diameter lens is investigated for beam collimation. The motivation of using a relatively large optical element in front of the LD is two-fold. Firstly, a decreased beam divergence and, therefore, efficient beam collimation can be achieved by a respective increase in dimensions of the lens according to the etendue law [77, 78]. Also, a lens with large diameter is able to spread the optical power received from the LD decreasing the irradiance values along any of its transverse planes. Therefore, eye safety is improved, and the product of LD-lens can be classified as a lower Class [46].

The Edmund optics plano-convex (PCX) spherical lens – used for collimation in the experiments of Chapter 3 – is used [86]. The diameter, effective focal length and reflectance values of the spherical PCX lens are given in Table 3.2. The remaining data sheet parameters of the spherical lens are $R_1 \to \infty$, $R_2 = -38.76\,\text{mm}$, $t_\text{c} = 32.68\,\text{mm}$ and $n = 1.52$ [86].

The beam generated from the LD is collimated by the lens placed at $d_0 = 5.15\,\text{cm}$ from the LD with a tolerance of $\pm 0.5\,\text{mm}$. The optical power emitted from the LD is measured to be $4.76\,\text{mW}$. The pattern of circular and elliptical image of the lens and LD, respectively, at $4\,\text{m}$ from the output surface of the lens are shown in Figure 4.16. The beam divergence is defined and determined in two different ways.

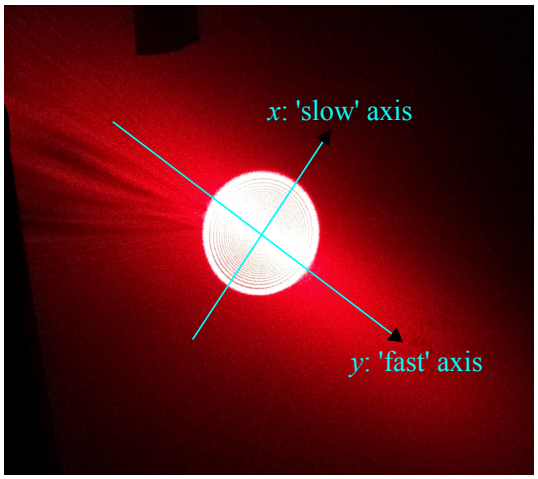

Figure 4.16: *Laser beam pattern and vertical axes for the determination of beam divergence.*

First, the beam divergence is defined as the plane angle of the truncated cone created by the circular image that is measured at two different link distances, d_1 and d_2. In particular, the diameter of the circular image, D_im, is measured at $d_1 = 4\,\text{m}$ and $d_2 = 8\,\text{m}$, respectively. In this case, the beam divergence is calculated by:

$$\psi = 2\tan^{-1}\left[\frac{D_\text{im}(d_2) - D_\text{im}(d_1)}{2(d_2 - d_1)}\right]. \tag{4.3}$$

Also, note that the new beam waist is located before the distance of $4\,\text{m}$ so that the images at $4\,\text{m}$ and $8\,\text{m}$ belong entirely to a diverging cone.

Since the first definition does not include any information of the beam intensity, a second definition is used. In particular, the half width of the beam is estimated at the two points where the irradiance is decreased by $1/e \simeq 0.368$ times or 36.8% of the peak irradiance. This is in

accordance with the definition of the $1/e$ beam width in BS EN 60825-1:2014 [46]. For this reason, appropriate curve fitting based on the analytical framework from Chapter 2 is applied to the data measured along the slow x- and fast y- axes, respectively. A number of 23 irradiance measurements which gives a good resolution of the total optical power of the beam is conducted at the distances of $4\,\text{m}$ and $8\,\text{m}$ inside the semi-circle of the image. Also, the illumination symmetry around both axes enables the calculation of the received optical power inside the circular image. Here, the beam divergence along the x- and y- axis is calculated by:

$$\psi_{\text{x}} = 2\tan^{-1}\left[\frac{W'_{\text{x}}(d_2) - W'_{\text{x}}(d_1)}{d_2 - d_1}\right] \tag{4.4}$$

and

$$\psi_{\text{y}} = 2\tan^{-1}\left[\frac{W'_{\text{y}}(d_2) - W'_{\text{y}}(d_1)}{d_2 - d_1}\right], \tag{4.5}$$

respectively. The values of $W'_{\text{x}}(z)$ and $W'_{\text{y}}(z)$ denote the beam radii up to the $1/e$ points of peak irradiance along the x- and y- direction and have been defined in (2.31) and (2.32), respectively.

4.3.2 Results and discussion

The diameters of the circular images at $4\,\text{m}$ and $8\,\text{m}$ are measured to be $2.9\,\text{cm}$ and $3.75\,\text{cm}$, respectively. Thus, the application of $d_1 = 4\,\text{m}$, $d_2 = 8\,\text{m}$, $D_{\text{im}}(4\,\text{m}) = 2.9\,\text{cm}$ and $D_{\text{im}}(8\,\text{m}) = 3.75\,\text{cm}$ to (4.3) results in a measured beam divergence of $\psi = 2.12\,\text{mrad}$. This value is more than twice the targeted divergence of $1\,\text{mrad}$ that is achievable by the use of a lens with even larger diameter than that of the spherical one. Also, the optical power contained in the circular image is measured to be $1.94\,\text{mW}$ and $1.87\,\text{mW}$ at $d_1 = 4\,\text{m}$ and $d_2 = 8\,\text{m}$, respectively. Therefore, 40.8% and 39.3% of the transmitted optical power of $P_{\text{Tx,o}} = 4.76\,\text{mW}$ is included in the circular image at $4\,\text{m}$ and $8\,\text{m}$, respectively. This means that the lens placed at $5.15\,\text{cm}$ from the LD fails to collect and collimate the whole optical power of the source inducing geometrical losses. Finally, the elliptical image (see Fig. 4.16) includes the remaining amount of optical power.

The experimental data of intensity at $4\,\text{m}$ and $8\,\text{m}$ fitted by the respective curves of analytical model are shown in Figure 4.17. The curves labelled as 'Analytical Model' are derived by the use of (2.1)–(2.10) and (2.14)–(2.33). The analytical parameters used for curve fitting of the experimental data are shown in Table 4.6. Parameter G_0 denotes the peak intensity of the Gaussian beam at the emission point of the LD. Quantities $W_{3\text{x}}$ and $W_{3\text{y}}$ represent the

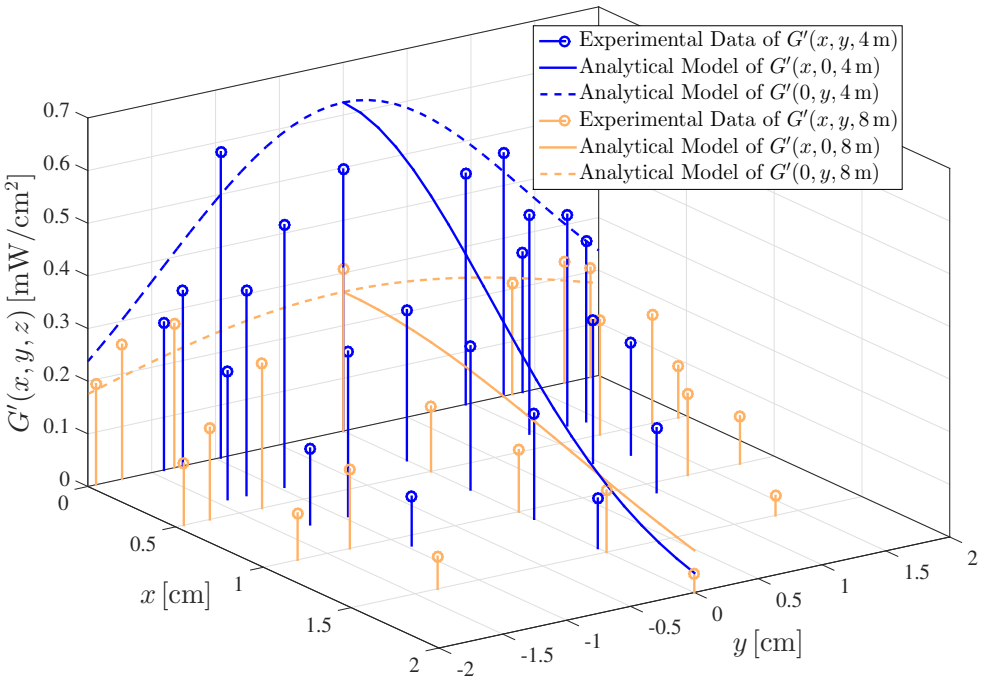

Figure 4.17: *Study II: Data of irradiance on the x-y transverse plane of the laser beam at $4\,m$ and $8\,m$ accompanied by the respective analytical model curves.*

Gaussian beam waists along x- and y- axes, respectively, which are reshaped by the lens. The MSE in irradiance is calculated to be $1.6 \cdot 10^{-2}$ at $4\,\mathrm{m}$ and $3.2 \cdot 10^{-3}$ at $8\,\mathrm{m}$. The slight deviation of some measured data points from the elliptical Gaussian fitting is explained by the existence of the diffraction effect [97]. This effect occurs when an optical wave passes through an aperture and is strongly dependent on the distance between the aperture and the observation plane, the wavelength and the aperture dimensions. In particular, here the diffraction effect stems from the transmission of the laser beam through the circular aperture of the lens mount to free space. The dark and bright fringes observed in the circular image of Figure 4.16 and in Figure 4.7(a) can also be attributed to the sharp intensity distribution of the generated laser beam at its waist [98]. Also, even slight misalignment between the optical source and the lens can significantly affect the beam irradiance pattern observed at the far field. The application of the physical model of the elliptical Gaussian beam for curve fitting results in the values of $W'_{\mathrm{x}}(4\,\mathrm{m}) = 1.2\,\mathrm{cm}$ and $W'_{\mathrm{x}}(8\,\mathrm{m}) = 1.8\,\mathrm{cm}$. Therefore, the application of these values to (4.4) yields $\psi_{\mathrm{x}} = 3\,\mathrm{mrad}$. Similarly, the beam radius along the y- axis is calculated to be $W'_{\mathrm{y}}(4\,\mathrm{m}) = 2\,\mathrm{cm}$ and $W'_{\mathrm{y}}(8\,\mathrm{m}) = 3.15\,\mathrm{cm}$. Therefore, the beam divergence of the 'fast' axis is

computed to be $\psi_{\mathrm{y}} = 5.75$ mrad by (4.5).

Table 4.6: *Analytical parameters for curve fitting of data in Study II*

Parameter	Unit	Value	Parameter	Unit	Value
$P_{\mathrm{Tx,o}}$	[mW]	4.76	A	-	1.00
λ_0	[nm]	660.00	B	[mm]	21.50
ϑ_{x}	[deg]	6.25	C	[m^{-1}]	-13.42
ϑ_{y}	[deg]	10.60	D	-	0.712
$W_{0\mathrm{x}}$	[μm]	1.92	$W_{2\mathrm{x}}$	[mm]	7.99
$W_{0\mathrm{y}}$	[μm]	1.12	$W_{2\mathrm{y}}$	[mm]	13.66
G_0	[kW/cm^2]	140.70	$R_{2\mathrm{x}}$	[m]	3.54
d_0	[cm]	5.15	$R_{2\mathrm{y}}$	[m]	3.54
$W_{1\mathrm{x}}$	[mm]	5.64	$d_{1\mathrm{x}}$	[m]	-3.54
$W_{1\mathrm{y}}$	[mm]	9.64	$d_{1\mathrm{y}}$	[m]	-3.54
$R_{1\mathrm{x}}$	[mm]	51.50	$W_{3\mathrm{x}}$	[μm]	92.93
$R_{1\mathrm{y}}$	[mm]	51.50	$W_{3\mathrm{y}}$	[μm]	54.39

The MPE of the 660 nm wavelength at link distances of the order of 100 m to 300 m is expected to be determined assuming that the laser transmitter is a point source. This is because the correction factor C_6 and the angular subtense, α, of an extended source decrease with an increase in distance [46]. Thus, it is expected to have $\nu = 1$ mW/cm^2 according to Figure 2.1. Therefore, the maximum optical power that is allowed to be transmitted through the 7.5 cm diameter lens is calculated to be $(1\,\mathrm{mW/cm^2}) \times \pi(3.75\,\mathrm{cm})^2 = 44.2$ mW. In Section 4.2.2.13, it is predicted that the required number of LDs and small lenses is 61 for harvesting 1 W by the mono-c-Si cell. The average output optical power per diode is measured to be 73.7 mW; thus, the total transmitted power by the 61 diodes is required to be $4496\,\mathrm{mW} \simeq 4.5$ W. Therefore, the required number of red LDs and 7.5 cm spherical lenses is calculated to be $(4496\,\mathrm{mW})/(44.2\,\mathrm{mW}) = 102$. However, such a square array of 10×10 red LDs with lenses results in the transmitter dimensions of $75 \times 75\,\mathrm{cm}^2$, which are considered to be unsuitable for the practical application of SC EH. Also, a large module of mono-c-Si PV cells would be an appropriate selection for the receiver; one of the challenges would be to illuminate each cell uniformly at the power levels of their maximum efficiency.

4.4 Summary

In this chapter, the limits of indoor OWPT were investigated in the absence of ambient light considering the use of LDs and c-Si solar cells. In particular, an experimental study was under-

taken to determine the harvested power and power efficiency of the link and its components. Up to five red LDs with collimation lenses were used for power transmission. This small number of diodes was selected for reasons of eye safety. A 36-cell multi-c-Si solar panel, an eight-cell multi-c-Si solar panel and a mono-c-Si PV cell were placed at $5.2\,\text{m}$ from the optical transmitters to compare their energy efficiency. The highest energy efficiency with a FF of 69% and the maximum harvested power of $30.6\,\text{mW}$ were achieved by the eight-cell solar panel when four LDs were used. The highest total power efficiency of 3.2% for a harvested power level of $17.8\,\text{mW}$ was attained by the link created using two optical transmitters and the mono-c-Si solar cell. The value of power efficiency was shown to be improved by 31.7 and 4.3 times compared with the links comprising the white LED and PM given in Chapter 3 and the five LDs and 36-cell PV panel, respectively. The link efficiency of 3.2% is relatively low because the average efficiency of two LDs and the solar cell efficiency were measured to be 26.8% and 13.3%, respectively. Yet the geometrical losses were determined to be only 10.6%. This low link efficiency value is not the absolute maximum using today's components, but can be increased by a respective increase in the components efficiency. This could be achieved using infrared LDs of high conversion efficiency, e.g. 54% at $975\,\text{nm}$, along with monochromatic laser power converters, as shown in the next chapter. Also, the optical link of two red LDs and the solar cell was compared in terms of total power efficiency with a SotA IPTS; an improvement by 2.7 times was shown. Therefore, the concept of indoor OWPT can be concluded to have an acceptable efficiency of comparable levels with RF based EH systems. The additional harvested power from sunlight is expected to offer performance superiority to OWPT systems compared with RF based WPT systems. This is because solar devices are able to harvest power simultaneously from man-made optical sources, such as lasers, and a natural resource, i.e. sunlight, while typical rectennas or induction coils lack this advantage in the RF domain. Most importantly, the analytical framework for an elliptical Gaussian beam and the single diode based solar panel physical model given in Chapter 2 were used to estimate the number of optical transmitters required to harvest $1\,\text{W}$. As a result, 110 red LDs and lenses were shown to be needed, when the 36-cell solar panel was considered, and 61 optical transmitters were shown to be required assuming the use of the solar cell.

The experimental distance of $5.2\,\text{m}$ was short given that practical wireless links of $100\,\text{m}$ to $300\,\text{m}$ were considered to be required for SC EH. Hence, the laser beam divergence was defined and measured in two different ways with a targeted value of $1\,\text{mrad}$. The red LD was used with a large spherical lens for light collimation. The physical model of the elliptical Gaussian beam

was used for curve fitting of the experimental data. Thus, an average full width divergence of 4.4 mrad at 36.8% of peak irradiance was determined. In order to achieve the targeted value of 1 mrad, the use of a lens of larger diameter should be considered. Also, a divergence of 2.1 mrad was calculated measuring the diameters of two circular beam images. Despite the fact that the achieved beam divergences were larger than 1 mrad, the additional optical losses can be counterbalanced by the use of a large solar panel. To affirm eye safety, the maximum permissible optical power of a single transmitter comprising a red LD and the 7.5 cm lens was calculated to be 44.2 mW. However, the required number of diodes and lenses for harvesting 1 W was predicted to be 102; thus, the total area of the transmitter was $75 \times 75\,\text{cm}^2$ that is not suitable for the application of OWPT to SCs. The developed power transmitter can be concluded to be capable of operating as the basic part of an array of 102 diodes and lenses at 100 m to 300 m according to the analysis. One more engineering challenge was mentioned to be the uniform radiation of the mono-c-Si cells of a large PV module at the levels of their maximum power efficiency.

Chapter 5
Infrared laser based wireless power transfer systems: Harvesting 1 W

5.1 Introduction

In this chapter, three simulation designs of a 100 m infrared (IR) wireless link are investigated in Zemax for a harvested power of 1 W during darkness hours. Clear weather conditions are assumed and, thus, the atmospheric losses are not considered here [57]. In Zemax, the light propagation through an optical system is modelled using ray tracing. Complex physical effects such as diffraction, aberrations and scattering; and different optical components like mirrors, lenses and diffusers can be modelled in Zemax. Despite the fact that diffraction was observed in the laser beams of Chapter 4, this effect is considered to be insignificant in this chapter because the total measured optical power is of major importance and the dimensions of optics are quite increased in the last two studies.

In Chapter 4, the experimental levels of the transmitted power by five red diodes of light amplification by stimulated emission of radiation (laser) were in the order of mW. Also, a mono-crystalline silicon (mono-c-Si) cell was concluded to achieve higher efficiency compared with that of a multi-c-Si solar panel. As a next step, an array of 42 laser diodes (LDs) is designed in Study I for the transmission of an amount of optical power able to be converted to 1 W by the mono-c-Si cell. The LDs are selected to operate at 785 nm because of the higher efficiency than that of the 660 nm LDs used in Chapter 4. The targeted value of 1 W is shown to be feasible up to the distance of 30 m, but beam enclosure of Class 3B laser systems is required for eye safety [46].

The multi-laser transmitter of Study I is classified as Class 3B because a large amount of optical power passes through small diameter lenses for collimation. Eye safety can be affirmed by a significant increase in the dimensions of the collimation optics for a laser system classification as Class 1 that is the most stringent category [46]. In addition, 975 nm LDs can achieve high efficiency of more than 65% [33] and the responsivity of mono-c-Si cells is maximised from

0.9 μm to 1 μm [88]. Hence, a highly efficient single link is designed in Study II combining the use of a 10 W 975 nm LD and the mono-c-Si cell.

In Study II, two Powell lenses are used to modify the elliptical Gaussian beam of the LD into a uniform beam. A uniform illumination pattern is required for the maximum electrical performance of a solar cell. Also, two large mirrors are used at the transmitter and the receiver for beam collimation and collection, respectively. However, the intensity pattern on the solar cell is not uniform due to the large beam astigmatism induced by the Powell lenses. Therefore, the Powell lenses are not used in a second scenario of Study II. The targeted value of 1 W is shown to be feasible up to the distance of 100 m in both scenarios under the required eye safety conditions for a Class 1 system. Nevertheless, the transmitter and receiver are not suitable for a practical small cell (SC) power supply, because the mirror dimensions are in the order of m^3.

In order to decrease the mirror dimensions, a 1550 nm LD is used in Study III due to the high maximum permissible exposure (MPE) level of 100 mW/cm^2 [46]. Since silicon (Si) solar cells have low responsivity at 1.55 μm, the use of an indium gallium arsenide phosphide (InGaAsP) laser power converter (LPC) is considered at the receiver [15,34]. The main contribution of this chapter is given by this highly directive 1550 nm link that is shown to be capable of harvesting 1.2 W and meeting eye safety regulations for Class 1. Also, the dimensions of the transmitter and receiver are considered to be acceptable for a practical application of wireless power supply to SCs.

The rest of this chapter is organised as follows. In Section 5.2, the study of the multiple 785 nm laser link with the mono-c-Si solar cell is given. In Section 5.3, the single 975 nm laser link with the mono-c-Si solar cell is studied. Finally, the design of the single 1550 nm link with a LPC is provided in Section 5.4.

5.2 Study I: Multiple 785 nm LDs and mono-c-Si solar cell

The simulation model is given in Section 5.2.1. Eye safety regulations are provided in Section 5.2.2. An elliptical Gaussian propagation model was presented in Chapter 2 for a laser beam transmitted through a lens towards free space. This model is used to support the simulation results given in Section 5.2.3.

5.2.1 Simulation model

The optical design consists of the following objects: 'source diode', 'even asphere lens', 'array' and 'detector rectangle' created in the non-sequential components (NSC) mode. Optical rays hit a predefined sequence of the same surfaces in sequential ray tracing [99]. This limitation is overcome in non-sequential ray tracing; the physical positions and properties of the objects and the direction of the rays determine the objects which the rays hit. Also, rays may hit any part of any non-sequential object, and may hit the same object multiple times, or not at all. Since rays can propagate through the optical components in any order, ray paths of total internal reflection can be considered. While sequential mode is limited to the analysis of imaging and afocal systems, non-sequential mode can be used to analyse stray light, scattering and illumination in both imaging and non-imaging optics. So long as this work focuses on non-imaging systems which refer to the optimal transfer of light power from a source to a target, non-sequential ray tracing is used. Source diode is the most appropriate non-sequential object to model a LD because of the many detailed input parameters it offers. The even asphere lens is a suitable object used to model the complex shape of aspheric lenses.

Laser diodes and respective aspheric lenses are placed in a rectangular array with perfectly aligned optical axes as shown in Figure 5.1(a). Also, the $12.5 \times 12.5\,\mathrm{cm}^2$ detector rectangle modelling the mono-c-Si solar cell is shown at a 5 m link distance in Figure 5.1(b).

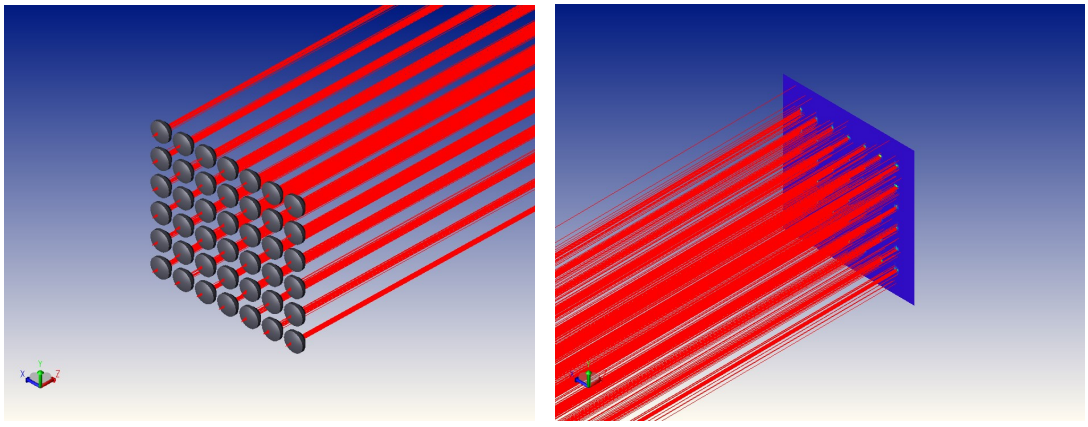

(a) (b)

Figure 5.1: *Non-sequential components shaded model of (a) the array of* 7×6 *LDs and aspheric lenses and (b) the square solar cell.*

The object source diode is used in Zemax for the simulation of a Panasonic LNCT22PK01WW

LD [64]. This is an off-the-shelf continuous wave (CW) optical source able to transmit a typical power, $P_{\text{Tx,o}}$, of 171.1 mW in the near infrared (NIR) region. Also, it has a typical efficiency of 27.4%, beam divergence parallel to the junction $\vartheta_{\parallel} = 7.5^{\circ}$ and beam divergence perpendicular to the junction $\vartheta_{\perp} = 15^{\circ}$ at FWHM intensity [64]. According to the model of source diode, the intensity of the beam generated from a rectangular source is given by:

$$G_{\text{sim}}(\theta_{\text{x}}, \theta_{\text{y}}) = G_{\text{sim,0}} \exp\left\{-2\left[\left(\frac{\theta_{\text{x}}}{a_{\text{x}}}\right)^{2S_{\text{x}}} + \left(\frac{\theta_{\text{y}}}{a_{\text{y}}}\right)^{2S_{\text{y}}}\right]\right\}, \tag{5.1}$$

where $G_{\text{sim,0}}$ denotes the overall peak intensity, note that the manufacturers of LDs give the relative instead of the absolute value of intensity; θ_{x} and θ_{y} are the angles in degrees along the x- and y- directions, respectively; and a_{x} and a_{y} are the angular divergences in degrees on the x-z and y-z planes, respectively. The angular divergences of FWHM are given by:

$$a_{\text{x}} = \frac{\vartheta_{\parallel}}{\sqrt{2\ln(2)}} \tag{5.2}$$

and

$$a_{\text{y}} = \frac{\vartheta_{\perp}}{\sqrt{2\ln(2)}}. \tag{5.3}$$

Also, the values of S_{x} and S_{y} are the 'super-Gaussian' factors along the x- and y- axes, respectively and range from 0.01 to 50. The special case of $S_{\text{x}} = S_{\text{y}} = 1$ corresponds to a typical elliptical Gaussian beam. The simulation parameters of the object source diode are given in Table 5.1. Quantity λ_0 is the operating wavelength of the LDs. Parameters N_{lr} and N_{anr} denote the number of layout rays and analysis rays, respectively. Also, N_{x} and N_{y} represent the number of LDs placed along the x- and y- axis, respectively. The values of Δx and Δy are the distances between the centres of two LDs and lenses placed consecutively along the x- and y- direction, respectively. Finally, $W_{0\text{x}}$ and $W_{0\text{y}}$ are the Gaussian beam waists along x- and y- axes, respectively, at the rectangular emission cross section of the diode.

Table 5.1: *Simulation parameters of* 785 *nm LDs*

Source diode	Parameter	N_{lr}	N_{anr}	$P_{\text{Tx,o}}$	λ_0	a_{x}	S_{x}	a_{y}
	Unit	-	-	[mW]	[nm]	[deg]	-	[deg]
	Value	10^3	10^7	171.1	785	6.37	1	12.74
	Parameter	S_{y}	N_{x}	N_{y}	Δx	Δy	$W_{0\text{x}}$	$W_{0\text{y}}$
	Unit	-	-	-	[mm]	[mm]	[nm]	[μm]
	Value	1	7	6	15.2	16.77	432.8	1.116

The object even asphere lens is used for the simulation of an ACL12708U-B lens [100]. This

optical element is identical to the ACL12708U-A one used in Experiments I, II and IV of Chapter 4. The anti-reflection coating (ARC) of ACL12708U-B is suitable for the wavelength range of $650\,\text{nm}-1050\,\text{nm}$, while the ARC of ACL12708U-A is tailored to $350\,\text{nm}-700\,\text{nm}$. Although aspheric coefficients of the rear surface of lens are not considered in the analytical model of Chapter 2, they are used in the simulation and their values are given in [100]. The array object is used for the creation of a rectangular array consisting of 7×6 identical aspheric lenses. The parent object of array is the even asphere lens. The detector rectangle is used for the simulation of the mono-c-Si cell [93] already used in Scenario III of Experiment II (see Chapter 4). The material of detector rectangle is selected to be 'absorb' and the number of pixels along the x- and y- dimension is 150×150. The square receiver, placed at $5\,\text{m}$ from the LDs array, and the collected optical rays are shown in Figure 5.1(b). The distance d_0 between each LD and its corresponding lens is set to be a variable. A value of $d_0 = 3.737\,\text{mm}$ is obtained from an optimisation approach for non-sequential optical systems. In particular, an orthogonal descent optimizer is initially used for the minimisation of a merit function. The merit function constitutes a measure of how well the optical design satisfies specific performance criteria by the modification of a set of parameters. In this case, the performance criteria are the total flux and spatial uniformity. This is because the optical power collected from the cell needs to be the maximum possible and the coherent irradiance must be as uniform as possible. Finally, the result of d_0 is refined by the use of a Hammer optimizer [101].

5.2.2 Eye safety regulations

Important parameters for eye safety are given below for the simulated optical transmitter according to the British Standard BS EN 60825-1:2014 [46]. The selected LD is classified as Class 3B according to the manufacturer [64]. The MPE in terms of irradiance is calculated to be $\nu = 1.5\,\text{mW/cm}^2$ similar to the methodology presented in Appendix B.1. Also, the nominal ocular hazard distance (NOHD) is determined to be $d_{\text{NOHD}} = 75\,\text{cm}$ and, therefore, the NIR beam radiation requires enclosure with a length of $75\,\text{cm}$.

The optical transmitter consisting of the LD and the lens is classified as Class 3B, similar to the methodology presented in Appendix B.2. The MPE is calculated to be $\nu = 6.66\,\text{mW/cm}^2$ and the NOHD is $d_{\text{NOHD}} = 54.3\,\text{m}$. Therefore, a shielding tube with a length of $54.3\,\text{m}$ is required which is unsuitable for practical applications.

5.2.3 Results and discussion

The received optical power, $P_{\mathrm{Rx,o}}$, of the 42 laser link is shown as a function of distance, z, in Figure 5.2 based on the analytical model – presented in Chapter 2 – and the simulation model. The theoretical curve is derived by the use of (2.1)–(2.10) and (2.14)–(2.32). Note that the reference point $z = 0$ denotes the tangent plane to the output surface of the lens and the beam widths refer to the FWHM intensity points. The parameters of the analytical model presented in Chapter 2 are used to verify the simulation model and are summarised in Table 5.2.

Parameter G_0 denotes the peak intensity of the Gaussian beam at the emission point of the LD. The sizes $W_{1\mathrm{x}}$ and $W_{1\mathrm{y}}$ represent the Gaussian beam radii along x- and y- axes, respectively, at the input lens plane. The radii of curvature of the Gaussian beam along x- and y- axes at the tangent plane to the input lens surface are given by $R_{1\mathrm{x}}$ and $R_{1\mathrm{y}}$, respectively. Parameters A, B, C and D are the four elements of the $ABCD$ matrix of the thick lens. Quantities $W_{2\mathrm{x}}$ and $W_{2\mathrm{y}}$ denote the Gaussian beam radii along x- and y- axes, respectively, at the output lens plane. The radii of curvature of the Gaussian beam along x- and y- axes at the tangent plane to the output lens surface are represented by $R_{2\mathrm{x}}$ and $R_{2\mathrm{y}}$, respectively. The sizes $d_{1\mathrm{x}}$ and $d_{1\mathrm{y}}$ are the distances of the Gaussian beam waists along x- and y- axes, respectively, reshaped by the lens and the vertex of the output lens surface. Quantities $W_{3\mathrm{x}}$ and $W_{3\mathrm{y}}$ represent the Gaussian beam waists along x- and y- axes, respectively, which are reshaped by the lens.

Table 5.2: *Analytical parameters*

Parameter	Unit	Value	Parameter	Unit	Value
$P_{\mathrm{Tx,o}}$	[mW]	171.10	$R_{1\mathrm{x}}$	[mm]	3.74
λ_0	[nm]	785.00	$R_{1\mathrm{y}}$	[mm]	3.74
ϑ_{x}	[deg]	3.75	A	-	0.836
ϑ_{y}	[deg]	7.50	B	[mm]	4.93
N_{x}	-	7	C	[cm^{-1}]	1.247
N_{y}	-	6	D	-	0.46
$\Delta\mathrm{x}$	[mm]	15.20	$W_{2\mathrm{x}}$	[µm]	528.19
$\Delta\mathrm{y}$	[mm]	16.77	$W_{2\mathrm{y}}$	[mm]	1.06
$W_{0\mathrm{x}}$	[µm]	3.81	$R_{2\mathrm{x}}$	[m]	−1.38
$W_{0\mathrm{y}}$	[µm]	1.90	$R_{2\mathrm{y}}$	[m]	−1.39
G_0	[MW/cm^2]	1.51	$d_{1\mathrm{x}}$	[cm]	54.63
d_0	[mm]	3.737	$d_{1\mathrm{y}}$	[m]	1.27
$W_{1\mathrm{x}}$	[µm]	244.97	$W_{3\mathrm{x}}$	[µm]	410.15
$W_{1\mathrm{y}}$	[µm]	491.99	$W_{3\mathrm{y}}$	[µm]	311.92

The two curves have a maximum gap of 1 dB at the distance of 100 m. According to the

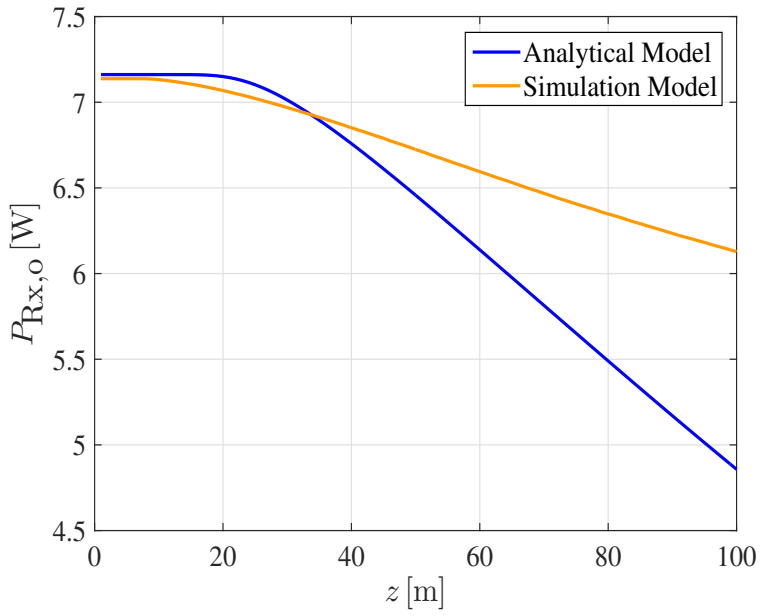

Figure 5.2: *Received optical power versus distance for two different models.*

analytical model, a value of optical power of 7.15 W is delivered effectively to 20 m. Also, a simulation based value of 7.13 W is able to be transferred to 10 m. After the distance of 20 m, the analytical curve falls with a larger rate compared with the simulation curve. This effect is attributed to the term $W'_{\mathrm{x}}(z')W'_{\mathrm{y}}(z'')$ that exists in the denominator of (2.33) in the theoretical model. Parameter $W'_{\mathrm{x}}(z')$ denotes the reshaped Gaussian beam radius along x- axis as a function of distance $z' = z - d_0 - t_{\mathrm{c}} - d_{1\mathrm{x}}$, where t_{c} is the lens thickness. Quantity $W'_{\mathrm{y}}(z'')$ represents the reshaped Gaussian beam radius along y- axis as a function of distance $z'' = z - d_0 - t_{\mathrm{c}} - d_{1\mathrm{y}}$. The product $W'_{\mathrm{x}}(z')W'_{\mathrm{y}}(z'')$ attenuates the irradiance and therefore the optical power faster than the respective irradiance of (5.1) of the simulation model. Also, the rear surface of the aspheric lens is modelled as spherical in the analytical model of Chapter 2 and this geometrical assumption makes light collimation less efficient. The geometrical losses of optical power are 0.09 dB and 0.1 dB at the link distance of 30 m for the analytical and simulation model, respectively. This means that the particular multiple laser based link presents a very large collection efficiency of 97.9% and 97.7% at 30 m according to theory and simulation, respectively. The optical-to-electrical efficiency of the particular cell is measured to be 13.25% for an input optical power of 134.38 mW in Experiment IV of Chapter 4. This optical power is assumed to be at the lower levels which result in lower power efficiency than the maximum

value according to Figure 2.7. Thus, the received optical power of about 7 W (see Figure 5.2) is expected to increase the power conversion efficiency of the cell. At the same time, the increase in the temperature of the cell is expected to reduce the value of η_{sr} based on Figure 2.6. Overall, the targeted value of 1 W is expected to be achieved in practice by this large amount of received optical power for link distance values of up to 30 m.

5.3 Study II: Single 975 nm LD and mono-c-Si solar cell

In this study a 10 W 975 nm LD is used for the creation of a highly efficient link. Scenario I and Scenario II are given in Section 5.3.1 and Section 5.3.2, respectively.

5.3.1 Scenario I: Powell lenses and mirrors

The objective, concept, simulation model, eye safety regulations, results and discussion of Scenario I are given below.

5.3.1.1 Objective and concept

The objective of Scenario I is to modify the elliptical Gaussian beam generated by the LD to a beam of uniform intensity in order to be transmitted safely towards free space. Note that a uniform irradiance profile along the entire free space optical link is desired to affirm that the beam has a constant irradiance lower than the maximum permissible irradiance for eye safety. Also, a uniform intensity beam profile is needed for the best electrical performance of the solar cell.

One of the potential methods to transform the Gaussian beam of a LD to a beam of uniform intensity is the use of Powell lenses [102]. Since the Gaussian beam is assumed to be elliptical and one Powell lens transforms the beam intensity only along a single dimension, two Powell lenses are required. Also, intensity modification of the beam is attained best, when the input beam is collimated. Therefore, two aspheric lenses are used to collimate the highly divergent beam of the LD. The laser beam expanded by the two Powell lenses is directed to an off-axis parabolic (OAP) mirror for collimation. The main advantage of an OAP mirror compared with an on-axis parabolic mirror is the avoidance of optical losses due to obscuration, since the optical axes of the source and the mirror are spatially separated. The receiver comprises

a second mirror of the same dimensions with the mirror used at the transmitter to collect and focus the beam on the solar cell.

5.3.1.2 Simulation model

The optical design consists of the following objects: source diode, even asphere lens, detector rectangle, 'CAD part: STEP/IGES/SAT' and 'standard surface' created in the NSC mode.

The source diode object is used to simulate a Sheaumann 10 W multi-mode CW LD with an efficiency of 53% [103]. The beam divergence of full width is $\vartheta_{\parallel} = 18^{\circ}$ and $\vartheta_{\perp} = 60^{\circ}$ at $1/e^2 \simeq 0.135$ or 13.5% of the peak intensity that is parallel and perpendicular to the junction, respectively. According to the model of the source diode, the angular divergences of full width at 13.5% of the peak intensity are calculated to be $a_{\mathrm{x}} = \vartheta_{\parallel}/2$ and $a_{\mathrm{y}} = \vartheta_{\perp}/2$. The simulation parameters of the LD are given in Table 5.3. The term τ represents the astigmatism of the beam generated from the LD. A value of $\tau = 30$ µm is considered, because the reported astigmatism of multi-mode LDs ranges from 10 µm to 50 µm [67, 104]. Since the rectangular emitter of the selected LD has an area of 400×1 µm^2, the beam waists, $W_{0\mathrm{x}}$ and $W_{0\mathrm{y}}$, along the slow and fast axes of the LD are assumed to be 200 µm and 0.5 µm, respectively. The even asphere lens

Table 5.3: *Simulation parameters of* 975 *nm LD*

Source diode	Parameter	N_{lr}	N_{anr}	$P_{\mathrm{Tx,o}}$	λ_0	τ
	Unit	-	-	[W]	[nm]	[µm]
	Value	10^3	10^7	10	975	30
	Parameter	a_{x}	a_{y}	$S_{\mathrm{x}}, S_{\mathrm{y}}$	$W_{0\mathrm{x}}$	$W_{0\mathrm{y}}$
	Unit	[deg]	[deg]	-	[µm]	[µm]
	Value	9	30	1	200	0.5

object is used to simulate a Thorlabs ACL12708U-B aspheric lens and a second aspheric lens based on Thorlabs ACL4532-B. The input surface of the second aspheric lens is considered to be planar. Two Powell lenses with ARC are used to achieve beam uniformity and they are modelled importing two CAD Part: STEP/IGES/SAT objects given by the manufacturer in Zemax. In particular, a Laserline Optics Powell lens is considered to shape the collimated input beam to a 45° narrow output beam [105]. A detector rectangle is placed at 60 cm from the source diode. The 'scale' parameters of the two CAD objects are determined to be 5.26 and 8.969 using an orthogonal descent optimizer subject to the maximisation of total flux and spatial uniformity of the detector rectangle. The first four optical components used for collimation,

uniformity and expansion of the LD's beam at the transmitter are shown in Figure 5.3.

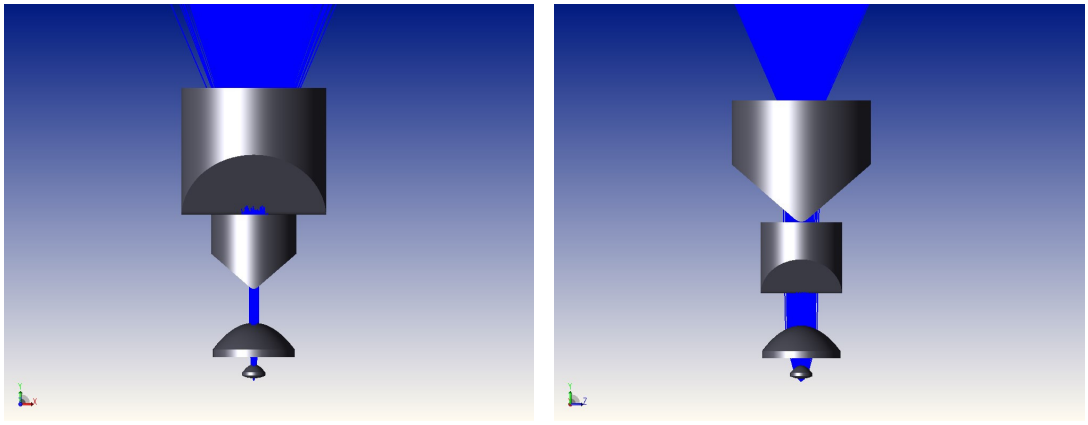

(a) (b)

Figure 5.3: *Non-sequential components shaded model of source diode and four lenses in series (a) on the x-y plane and (b) on the y-z plane at the transmitter.*

The standard surface object is used with a user defined aperture to create an off-axis rectangular section of a parabolic surface. Thus, two OAP mirrors with the dimensions of $1 \times 1.7 \times 1.7\,\mathrm{m}^3$ are designed and each placed at the transmitter and at the receiver. The optical axis of the LD forms an angle of $90°$ with the collimation mirror at the transmitter. An isometric view of the optical transmitter is shown in Figure 5.4(a). The receiver is shown on the y-z plane in Figure 5.4(b). The simulated 100 m link of Scenario I is shown on the x-z plane in Figure 5.5(a)

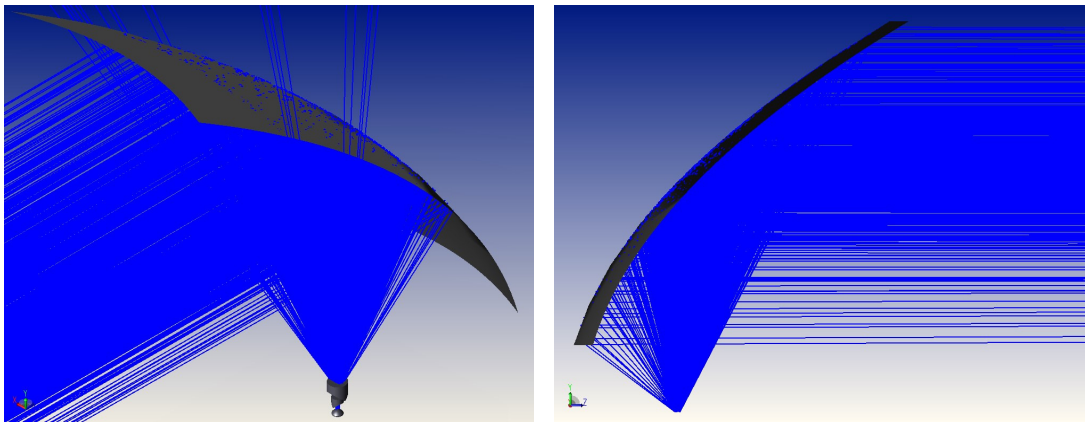

(a) (b)

Figure 5.4: *Non-sequential components shaded model of (a) the transmitter from an isometric view and (b) the receiver on the y-z plane.*

and on the y-z plane in Figure 5.5(b). It is observed that the laser beam reflected by the OAP

mirror of the transmitter converges up to 48.32 m and diverges after 57.02 m along the x- axis of the wireless link. The beam is highly collimated in the distance range of $[48.32, 57.02]$ m and a high density of rays is observed at 50 m. Thus, the beam irradiance needs to be measured by a circular aperture with a 5 cm diameter according to Condition 1 of Table 10 in [46] and to be compared with the MPE for eye safety at $z = 50$ m. Note that no circular detector can be used to plot data from a coherent source in Zemax. For this reason, a 5×5 cm^2 detector rectangle is used for the measurement of optical power. Thus, the beam irradiance, G_{Rx}, is computed by the ratio of the received optical power over the area of 25 cm^2. Also, a second detector rectangle

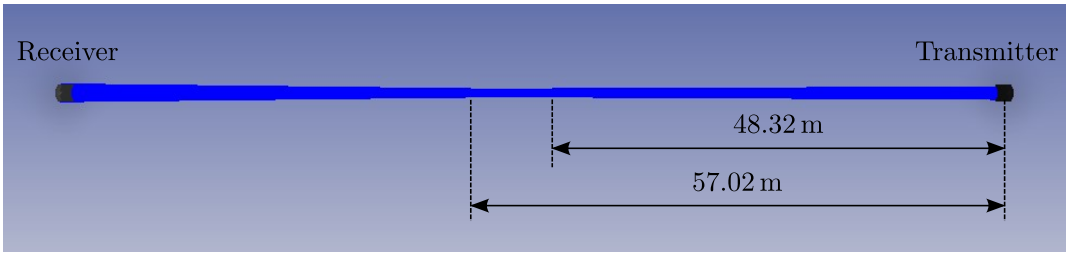

(a)

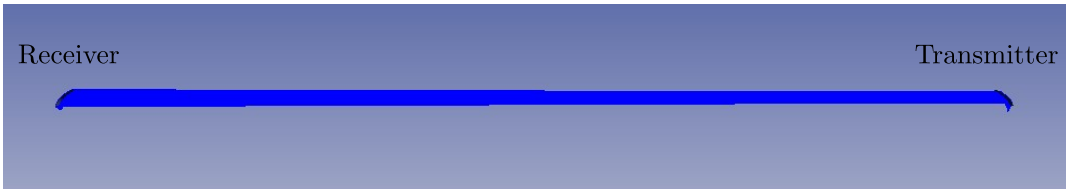

(b)

Figure 5.5: *Scenario I: Non-sequential components shaded model of the* 100 *m link (a) on the* x*-*z *plane and (b) on the* y*-*z *plane.*

with an area of 1.8×1.7 m^2 is placed at $z = 0$ and $z = 50$ m from the collimation mirror for the determination of the beam diameters at $1/e \simeq 0.368$ of peak intensity. Thus, the angular convergence of the beam along the x- axis is computed by $\phi_{\mathrm{x}} = 2\tan^{-1}[(D_{0\mathrm{x}} - D_{1\mathrm{x}})/100]$ and the beam convergence along y- axis is given by $\phi_{\mathrm{y}} = 2\tan^{-1}[(D_{0\mathrm{y}} - D_{1\mathrm{y}})/100]$. Parameters $D_{0\mathrm{x}}$ and $D_{0\mathrm{y}}$ denote the beam diameters at 36.8% of peak intensity at $z = 0$, i.e. the output plane of the transmitter mirror, along x- and y- axis, respectively. Also, $D_{1\mathrm{x}}$ and $D_{1\mathrm{y}}$ are the beam diameters at 36.8% of peak intensity at $z = 50$ m along x- and y- axis, respectively.

Finally, a detector rectangle is used to simulate a 5×5 cm^2 mono-c-Si cell at the receiver. The dimensions of the receiver are reduced by 6.25 times compared with these in Study I, because the total amount of optical power can be focused efficiently even on such a cell of smaller dimensions. The position of the cell is optimised by an orthogonal descent optimizer under the

condition of maximisation of the collected power.

5.3.1.3 Eye safety regulations

When the selected 10 W LD is classified as Class 4 by the manufacturer, proper shielding of the volume between the LD and the collimation mirror is required. Therefore, the use of a box is considered in order to enclose the beam and, thus, an extended optical source is created. Also, beam enclosure inside the volume of the collection mirror and the solar cell is required, because the focused beam is expected to have high irradiance levels.

According to Table A.2 of [46], the MPE for an extended source is given by:

$$\nu = \begin{cases} 18C_4C_6t^{-0.25} \ [\text{W/m}^2], & t \leq T_2 \\ 18C_4C_6T_2^{-0.25} \ [\text{W/m}^2], & t > T_2 \end{cases}, \tag{5.4}$$

where t denotes the exposure time in s. The correction factors T_2, C_4 and C_6 are given in Table 9 of [46]. A time base of $t = 100$ s is used according to the classification principle 4.3 e) of [46]. Parameter C_4 is calculated to be 3.548 for the wavelength of 975 nm. In case of 1.5 mrad $< \alpha \leq 100$ mrad, $T_2 = 10^{1+[(\alpha-1.5)/98.5]}$ and $C_6 = \alpha/1.5$, where α denotes the angular subtense. Since the laser beam reflected by the mirror of the transmitter is assumed to be rectangular, the angular subtense is computed by the arithmetic mean of the two angular dimensions of the source which are given by $\alpha_{\text{x}} = 2\tan^{-1}(D_{0\text{x}}/2z)$ and $\alpha_{\text{y}} = 2\tan^{-1}(D_{0\text{y}}/2z)$.

5.3.1.4 Results and discussion

The irradiance pattern of the detector placed at 60 cm from the diode is given in Figure 5.6. A relatively uniform rectangular pattern of beam intensity is created by the two Powell lenses. Three side lobes are observed at the top of the rectangle and a main lobe at the bottom of the detector.

The intensity pattern of the beam at $z = 50$ m from the output surface of the collimation mirror is shown in Figure 5.7. Note that the coherent irradiance is measured in mW/cm^2 on the 5×5 cm^2 receiver shown in the zoom inlay of Figure 5.7. The laser beam is shown to be 'squeezed' along the x- axis and takes a form similar to an hourglass. The beam diameters at $z = 50$ m are measured to be $D_{1\text{x}} = 8.62$ cm and $D_{1\text{y}} = 15.45$ cm. Also, the beam diameters at

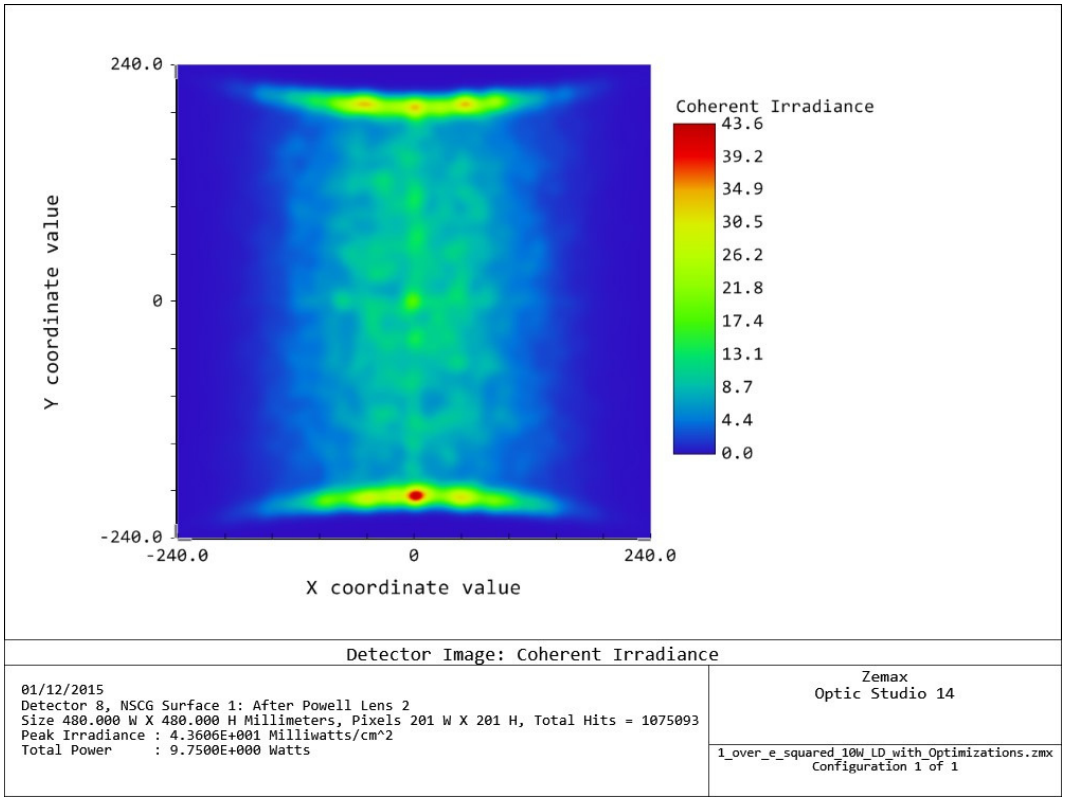

Figure 5.6: *Beam intensity as a function of x- and y- axes of a detector at 60 cm from the source.*

the output plane of the collimation mirror are $D_{0\mathrm{x}} = 33.03$ cm and $D_{0\mathrm{y}} = 67.03$ cm. Therefore, the beam convergence is calculated to be $\phi_{\mathrm{x}} = 5$ mrad and $\phi_{\mathrm{y}} = 10.6$ mrad along the x- and y- axis, respectively. The optical power collected by the $5 \times 5\,\mathrm{cm}^2$ receiver is measured to be 512.9 mW and, therefore, the beam irradiance is calculated to be $20.5\,\mathrm{mW/cm}^2$. The angular subtenses are calculated to be $\alpha_{\mathrm{x}} = 6.61$ mrad and $\alpha_{\mathrm{y}} = 13.41$ mrad along the x- and y- axes, respectively. Therefore, a mean angular subtense of $\alpha = 10.01$ mrad is computed. Thus, the required parameters for check of eye safety are calculated to be $T_2 = 12.2$ s, $C_6 = 6.67$ and, finally, the MPE is determined to be $\nu = 22.79\,\mathrm{mW/cm}^2 > G_{\mathrm{Rx}} = 20.5\,\mathrm{mW/cm}^2$. This means that the 50 m IR wireless link is eye safe.

The optical power collected by the solar cell is measured to be 8.6 W. The efficiency of the mono-c-Si cell was measured to be 13.3% for an input optical power of 189.53 mW at 660 nm in Chapter 4. The mono-c-Si cell has a larger spectral response and, therefore, quantum efficiency at 975 nm [88]. Thus, the targeted electrical power of 1 W is expected to be attained for the large optical power of 8.6 W received by the solar cell.

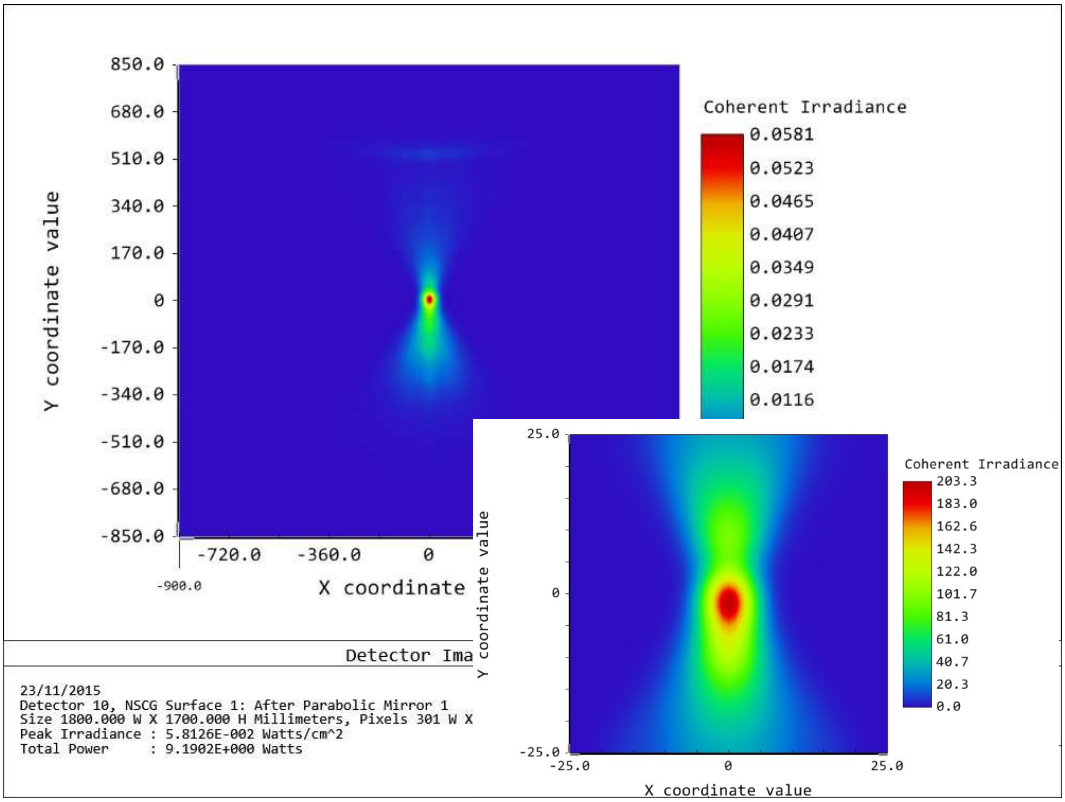

Figure 5.7: *Coherent beam intensity distribution measured by a* $1.8 \times 1.7\,m^2$ *detector and by a* $5 \times 5\,cm^2$ *detector at* $z = 50\,m$.

5.3.2 Scenario II: Mirrors

The motivation, concept, simulation model, results and discussion of Scenario II are given below.

5.3.2.1 Motivation and concept

Since the illumination pattern of the laser beam, transferred to the solar cell, is not uniform in Scenario I, the use of Powell lenses at the transmitter can be avoided. Therefore, here the elliptical Gaussian beam generated from the divergent LD at the transmitter is expanded towards a large OAP mirror for collimation. The receiver comprises a second mirror, with the same dimensions as the mirror used at the transmitter, to collect and focus the beam on the solar cell.

5.3.2.2 Simulation model

The optical design consists of the following objects: source diode, detector rectangle and standard surface created in the NSC mode. The parameters of source diode and standard surface have the same values with the respective objects in Scenario I. The number of analysis rays of the source diode is selected to be 10^9 in Scenario II, as the simulation time is reduced compared with Scenario I due to the use of less objects.

The simulated $100\,\text{m}$ link of Scenario II is shown on the x-z plane in Figure 5.8(a) and on the y-z plane in Figure 5.8(b).

(a)

(b)

Figure 5.8: *Scenario II: Non-sequential components shaded model of the* $100\,m$ *link (a) on the* x-z *plane and (b) on the* y-z *plane.*

It is observed that the laser beam is highly collimated in the free space between the two mirrors of the transmitter and the receiver. In this case, a $1 \times 1.7\,\text{m}^2$ detector is placed at the distances of $z = 0$, $z = 2\,\text{m}$, $z = 50\,\text{m}$, $z = 75\,\text{m}$ and $z = 96.89\,\text{m}$ from the output plane of the collimation mirror at the transmitter. Finally, the $5 \times 5\,\text{cm}^2$ detector rectangle that is modelling the mono-c-Si solar cell is placed at an optimised position of $z = 98.16\,\text{m}$ at the receiver to measure the maximum possible received optical power.

5.3.2.3 Results and discussion

The analytical parameters for eye safety and the simulated beam irradiance values are summarised in Table 5.4. The beam diameters are measured to be $D_{0\text{x}} = 17.07\,\text{cm}$ and $D_{0\text{y}} = 55.93\,\text{cm}$ at the output plane of the collimation mirror. It is observed that the MPE decreases

Table 5.4: *Eye safety parameters and beam irradiance*

Parameters	Units	Values			
z	[m]	2.00	50.00	75.00	96.89
α	[mrad]	92.65	7.30	4.87	3.77
T_2	[s]	84.21	11.45	10.82	10.54
C_6	-	61.77	4.87	3.25	2.51
ν	[mW/cm^2]	130.22	16.91	11.44	8.90
G_{Rx}	[mW/cm^2]	5.50	5.52	5.53	5.51

when the link distance increases. The beam irradiance remains at lower levels than the MPE up to the distance of 96.89 m. Therefore, eye safety is affirmed for the 975 nm wireless link up to 96.89 m, i.e. at the input plane of the collection mirror at the receiver. The lowest value of MPE is achieved for link distances greater than 100 m, when α has its minimum possible value, i.e. 1.5 mrad, $T_2 = 10$ s and $C_6 = 1$. In this case, the use of the second case of (5.4) results in $\nu = 3.59$ mW/cm^2. Thus, the MPE is expected to exceed the beam irradiance at distances greater than 100 m.

Since the beam diameters at $z = 50$ m are measured to be $D_{1\text{x}} = 17.01$ cm and $D_{1\text{y}} = 56.16$ cm, a beam convergence of $\phi_{\text{x}} = 12$ µrad and a beam divergence of $\phi_{\text{y}} = 46$ µrad are calculated. The received optical power of the cell is determined to be 8.66 W. Similarly to Scenario I, the targeted electrical power of 1 W is expected to be achieved for the large optical power of 8.66 W received by the solar cell.

Mirrors with dimensions in the order of m^3 are not considered practical for optical wireless power transfer to SCs. Thus, the simulation parameters of the dimensions of the mirrors and of $P_{\text{Tx,o}}$ are set to $15 \times 30 \times 30$ cm^3 and 5 W, respectively. However, eye safety regulations would not be met up to distances of 10 m, because from the simulation the beam irradiance is determined to be 44.75 mW/cm^2 which is 2.13 times larger than the calculated MPE. Therefore, this trade off between the dimensions of the transmitter and receiver and the MPE up to 100 m does not offer an acceptable solution for 975 nm.

5.4 Study III: Single 1550 nm LD and LPC

The motivation, simulation model, results and discussion of Study III are given below.

5.4.1 Motivation

The use of mirrors with practical dimensions, such as $15 \times 30 \times 30\,\text{cm}^3$, is not feasible using a $5\,\text{W}$ $975\,\text{nm}$ LD. This is because of the low MPE values, which decrease along the $100\,\text{m}$ link. Thus, the operational wavelength is modified to $1550\,\text{nm}$ because of its constant MPE of $100\,\text{mW/cm}^2$ along the entire link according to Table A.1 of [46]. However, Si solar cells have very low efficiency at $1550\,\text{nm}$ [34]; therefore, the use of an InGaAsP LPC is considered at the receiver [15]. The concept is the same as described in Section 5.3.2.1, but the parameters of the LD, mirrors and solar cell are different.

5.4.2 Simulation model

The source diode object is used to simulate an AKELA ALC-1550-04000-CB100 $4\,\text{W}$ multi-mode CW LD with a typical efficiency of 25%. The FWHM beam divergences of this LD are $\vartheta_{\parallel} = 9°$ and $\vartheta_{\perp} = 34°$. The simulation parameters of this laser source are given in Table 5.5. The rectangular emitter of the optical source has an area of $100 \times 1\,\mu\text{m}^2$.

Table 5.5: *Simulation parameters of* $1550\,nm$ *LD*

Source diode	Parameter	N_{lr}	N_{anr}	$P_{\text{Tx,o}}$	a_{x}	a_{y}
	Unit	-	-	[W]	[deg]	[deg]
	Value	10^3	10^9	4	7.64	28.88
	Parameter	S_{x}	S_{y}	τ	$W_{0\text{x}}$	$W_{0\text{y}}$
	Unit	-	-	[μm]	[μm]	[μm]
	Value	1.2	1	30	50	0.5

The standard surface object is used with a user defined aperture to create an off-axis elliptical section of a parabolic surface. As a first step, the dimensions of the OAP mirrors used at the transmitter and receiver are $h_{\text{m}} \times l_{\text{m}} \times w_{\text{m}} = 17.78 \times 17.78 \times 7.62\,\text{cm}^3$. Parameters h_{m}, l_{m} and w_{m} denote the height, length and width of the OAP mirror, respectively. Also, the effective reflected focal length, γ, defined as the distance between the focal point and the vertex of the OAP surface, at the transmitter is $20.32\,\text{cm}$. The simulation setup of the transmitter and the receiver is given on y-z plane in Figure 5.9. Quantity d_{lpc} represents the optimised distance along the y- axis of the LPC from the mirror at the receiver and is measured to be $19.69\,\text{cm}$.

A rectangular detector of $7.62 \times 17.78\,\text{cm}^2$ is used to observe the form of the collimated beam. It is placed at the link distances $z = 10\,\text{cm}$, $z = 20\,\text{m}$, $z = 40\,\text{m}$, $z = 60\,\text{m}$, $z = 80\,\text{m}$ and

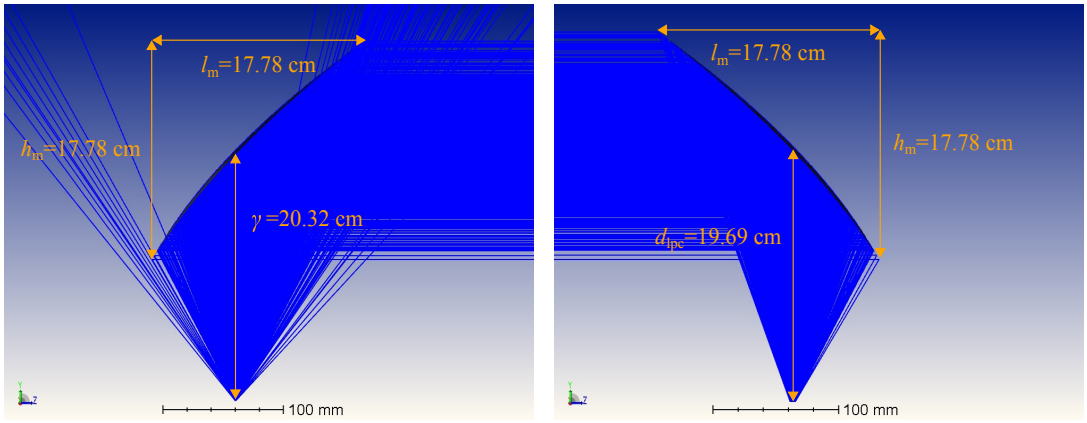

Figure 5.9: *Non-sequential components shaded model of (a) the transmitter and (b) the receiver on y-z plane.*

$z = 99.89$ m from the output plane of the collimation mirror.

The MPE level of 100 mW/cm^2 for a point source at 1.55 µm corresponds to a maximum permissible power of 9.62 mW measured by a circular aperture stop with a 3.5 mm diameter according to Table A.1 of [46]. Thus, a 3.102^2 mm^2 square detector is used for power measurements in Zemax, because it has the same area as the circular aperture stop. Since the $1/e$ beam diameters are in the order of a few cm, the square detector is placed at nine points of a square grid. Two consecutive points of the grid have a distance of 3.102 mm as shown in Figure 5.10. Each point corresponds to the centre of the square detector and the central point of the grid is placed at the position of peak irradiance of the super-Gaussian beam. Thus, the maximum beam irradiance from all of the nine points is determined for the link distances $z = 10$ cm, $z = 20$ m, $z = 40$ m, $z = 60$ m, $z = 80$ m and $z = 99.89$ m from the output plane of the collimation mirror. Finally, a detector rectangle of 5×5 mm^2 is used to model the 1550 nm LPC of [15].

5.4.3 Results and discussion

The maximum irradiance of the laser beam increases with the increase in link distance. This means that the laser beam focuses at the input plane of the receiver's mirror along z-axis; therefore, eye safety needs to be affirmed at $z = 99.89$ m. The intensity distribution of the elliptical super-Gaussian beam at $z = 99.89$ m is given in Figure 5.10. Also, the square grid and the central points, where the 3.102^2 mm^2 square detector is placed for the measurement

of optical power, are given in Figure 5.10. The elliptical beam is observed to be asymmetric

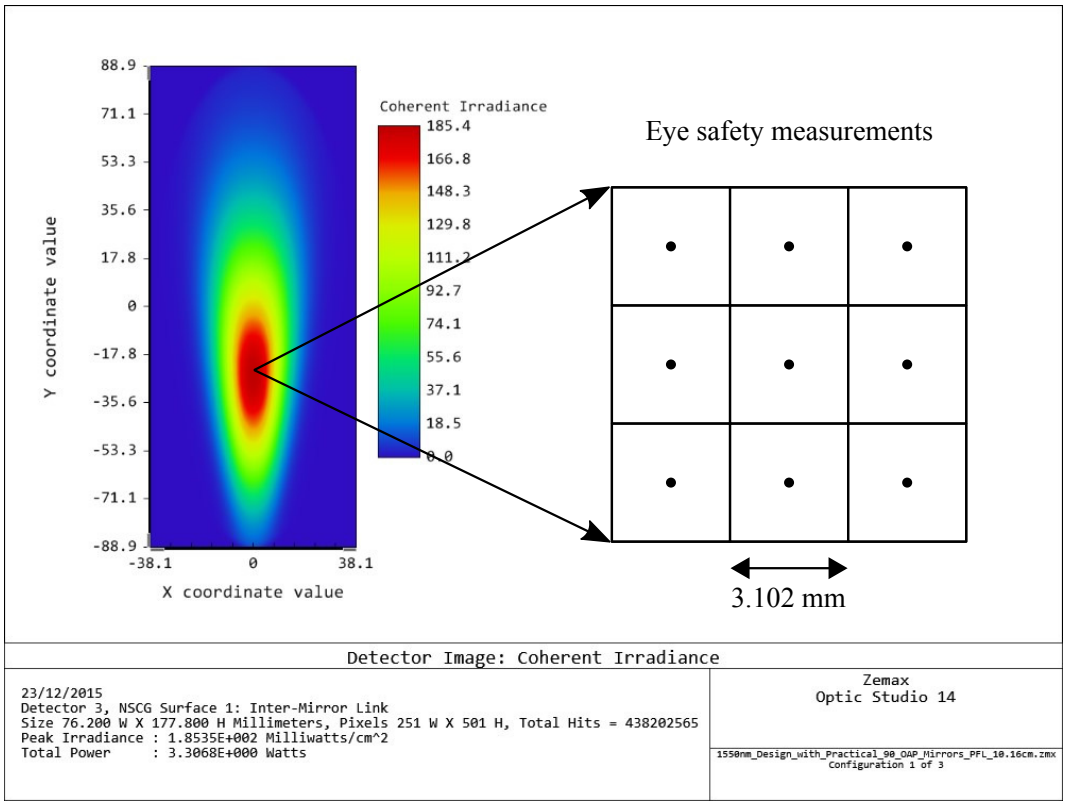

Figure 5.10: *Coherent beam intensity distribution measured by a* $7.62 \times 17.78\,cm^2$ *detector at* $z = 99.89\,m$ *and the square grid for eye safety measurements.*

around $y = -25$ mm that represents the central y- axis of the beam. In particular, the upper part of the beam is enlarged, while the lower part of the beam is shrunken compared to a normal elliptical Gaussian beam. This is because the reflected and collimated rays from the mirror at $y > -25$ mm travel longer distances along x- axis compared to the ones at $y < -25$ mm due to the off-axis placement of the LD and the mirror. This effect is known as coma or comatic aberration in optics.

The irradiance pattern of the laser beam measured by the 3.102^2 mm^2 square detector is given in Figure 5.11. The detector is placed at $(x, y, z) = (-0.29\,\text{mm}, -25\,\text{mm}, 99.89\,\text{m})$ that corresponds to the central square of the grid with the largest intensity value. Since the optical power is measured to be 9.818 mW, the beam irradiance is determined to be 102.03 mW/cm^2 that is 102% of $\nu = 100$ mW/cm^2. Therefore, in order to ensure eye safety for the designed 100 m wireless system and classify it as Class 1, the mirror dimensions need to increase slightly. In particular, the increase of the length and width of the OAP mirrors by only 3.8 cm results in

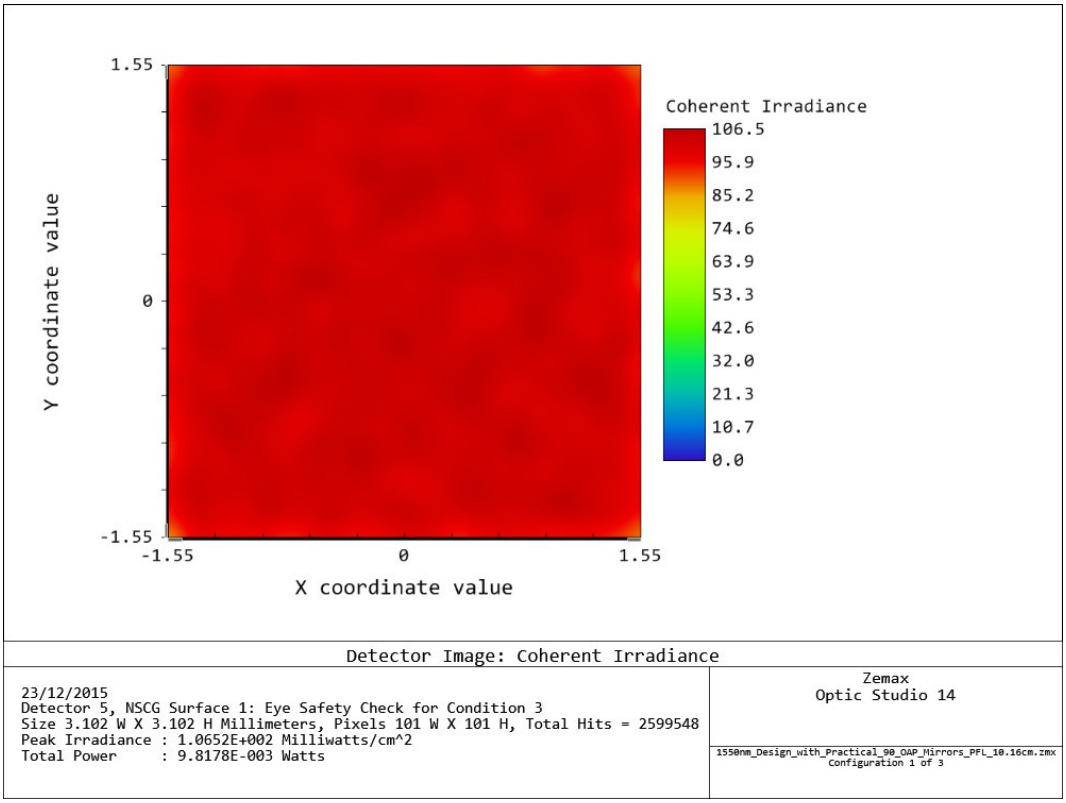

Figure 5.11: *Beam intensity pattern measured by a* 3.102^2 *mm*^{2} *square detector at* $z = 99.89$ *m for eye safety check.*

$G_{\mathrm{Rx}} = 70.2\,\mathrm{mW/cm^2}$ at $z = 100\,\mathrm{m}$ (see Table 5.6).

The beam diameters at 36.8% of peak intensity are measured to be $D_{0\mathrm{x}} = 27.02\,\mathrm{mm}$ and $D_{0\mathrm{y}} = 90.76\,\mathrm{mm}$ at $z = z_1 = 10\,\mathrm{cm}$ along the x- and y- axis, respectively. Also, the beam diameters at 36.8% of maximum irradiance are measured to be $D_{1\mathrm{x}} = 24.51\,\mathrm{mm}$ and $D_{1\mathrm{y}} = 90.92\,\mathrm{mm}$ at $z = z_2 = 99.89\,\mathrm{m}$ along the x- and y- axis, respectively. Therefore, the beam convergence along x- axis is given by $\phi_{\mathrm{x}} = \tan^{-1}[(D_{0\mathrm{x}} - D_{1\mathrm{x}})/(z_2 - z_1)]$ and is determined to be $25.2\,\mu\mathrm{rad}$. Similarly, the beam divergence along y- axis is calculated by $\phi_{\mathrm{y}} = \tan^{-1}[(D_{1\mathrm{y}} - D_{0\mathrm{y}})/(z_2 - z_1)]$ and has a value of $1.6\,\mu\mathrm{rad}$.

The irradiance pattern of the laser beam focused on the $5 \times 5\,\mathrm{mm^2}$ solar cell is given in Figure 5.12. The optical power received by the solar cell is measured to be $3.12\,\mathrm{W}$. This means that the total geometrical losses of the $100\,\mathrm{m}$ IR link are 22%. The selected material of the mirrors will affect the received optical power due to absorption and scattering losses. The minimum reflectance at $1550\,\mathrm{nm}$ is 94% for the metallic mirror coating of protected aluminium (Al), as shown in Figure 4 of [106]. Also, the metallic mirror coating of protected gold has a maximum

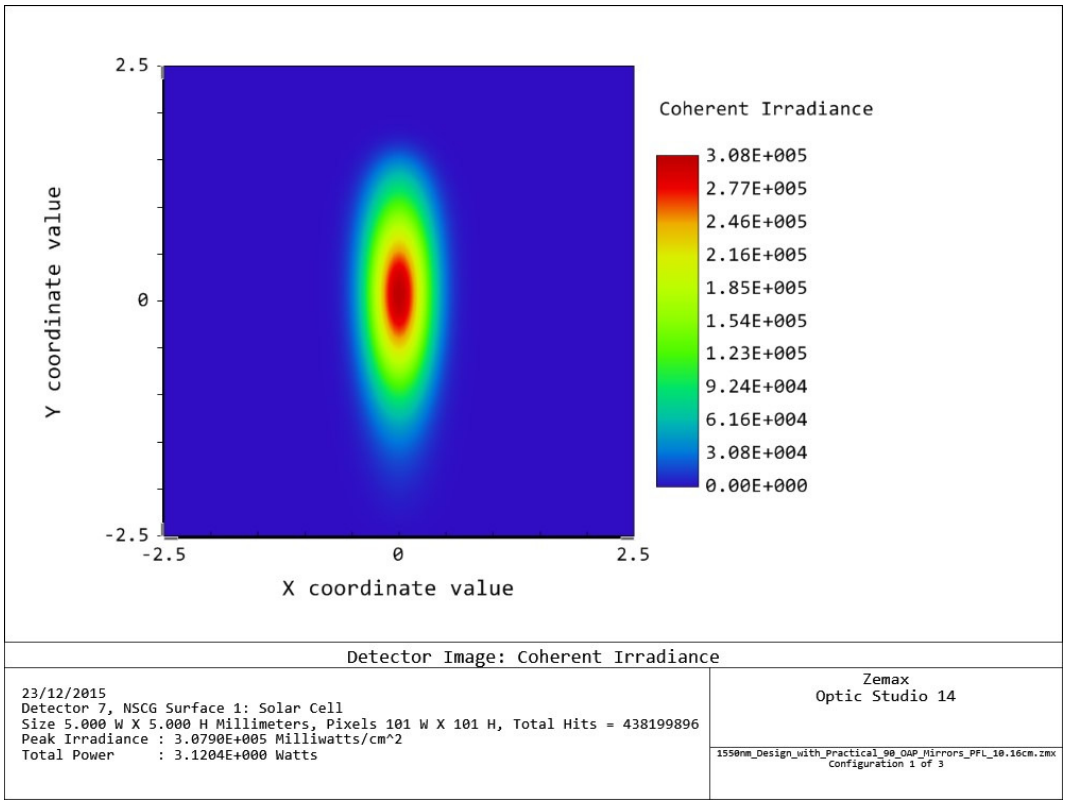

Figure 5.12: *Coherent irradiance of laser beam collected by the LPC.*

reflectance of 97.5% at 1550 nm according to Figure 4 of [106]. Therefore, the use of two mirrors with protected Al coating – worst-case scenario – results in a received optical power of $0.94^2 \times 3.12 = 2.77$ W. A power efficiency of 42% is achieved by the LPC in [15] for 237.5 mW/cm^2 of received irradiance; this corresponds to collected optical power of 59.4 mW. Therefore, in order to affirm the same efficiency, the required number of cells is calculated to be $2.77/(59.4 \times 10^{-3}) \approx 47$. In this case, the harvested electrical power is expected to be 0.42×2.77 W$= 1.16$ W. The use of a Powell lens before the solar cell would contribute to the creation of uniform illumination on the 47 cells.

Finally, the required mirror dimensions for an operation of the 100 m link at a maximum beam irradiance of ν, $2\nu/3$ and $\nu/2$ are summarised in Table 5.6. When the beam irradiance decreases from ν to $\nu/2$ at the receiver, the volume of the mirrors is shown to increase by 1.94 times.

Table 5.6: *Mirror dimensions for a beam irradiance equal to (a) MPE, (b) two thirds of MPE and (c) half of MPE*

Parameters	$h_{\mathrm{m}} \times l_{\mathrm{m}} \times w_{\mathrm{m}}$	γ	z	G_{Rx}
Units	[cm^3]	[cm]	[m]	$\left[\mathrm{mW/cm^2}\right]$
Values	$17.8 \times 17.8 \times 7.6$	20.3	0.1	92.7
			20.0	94.3
			40.0	96.2
			60.0	97.8
			80.0	99.9
			99.89	$102.0 \simeq \nu$
	$21.6 \times 21.6 \times 7.6$	24.1	0.1	65.8
			100.0	$70.2 \simeq 2\nu/3$
	$24.8 \times 24.8 \times 7.6$	27.3	0.1	51.4
			100.0	$54.0 \simeq \nu/2$

5.5 Summary

In this chapter, three simulation studies were given in Zemax for harvesting 1 W – typical required power for a SC – by a 100 m IR wireless link in darkness. Zemax is a well known optical design software used for the design and analysis of imaging and non-imaging systems. The propagation of light through an optical system is modelled by ray tracing. The use of Zemax for the simulation of complex physical effects – diffraction, aberrations and scattering – and optical components – mirrors, lenses and diffusers – is the first step before the implementation of a practical system. Thus, a 785 nm wireless link was designed considering 42 LDs with collimation lenses and a mono-c-Si cell. The simulation and analytical models were in close agreement showing that the transfer of 7 W up to 30 m with geometrical losses of only 2% was feasible. Therefore, the minimum required efficiency of the solar cell was only 13.9%, while an efficiency of 13.3% was measured in the experiments of Chapter 4 for an input optical power of 134.4 mW. However, a beam enclosure was required due to eye safety restrictions for Class 3B systems, and this was the main limitation.

A significant increase in the transmitter's dimensions was applied to the second design to affirm eye safety from a Class 1 system. In particular, a 975 nm LD of an efficiency of 53% was used to transmit 10 W to the mono-c-Si cell. Uniform illumination is desired for a maximum electrical performance of a solar receiver. Hence, a transformation of the elliptical Gaussian beam to a beam of uniform intensity was attained using Powell lenses at the transmitter. Two large mirrors were used at the transmitter and receiver for beam collimation and reception, respectively. However, the uniformity of beam irradiance was modified by the collimation

mirror due to the astigmatism induced by the lenses. Therefore, a second case was considered neglecting the use of Powell lenses. The MPE of the extended $975\,\text{nm}$ source was shown to decrease along the wireless link with a minimum value of $8.9\,\text{mW/cm}^2$ at $100\,\text{m}$. Despite this fact, harvesting at least $1\,\text{W}$ at $100\,\text{m}$ was shown to be feasible meeting the eye safety requirements for Class 1 systems. However, the order of m^3 for the mirror dimensions was the main disadvantage for a practical application of power supply to SCs. Nevertheless, the use of $975\,\text{nm}$ laser sources along with LPCs could create power transfer links of end-to-end efficiency of the order of 30% and could be considered in near field applications such as wireless charging of electrical vehicles.

In the third study, a $1550\,\text{nm}$ LD was selected because its large MPE of $100\,\text{mW/cm}^2$ allows for a significant decrease in the mirror dimensions. The use of a III-IV semiconductor solar cell – designed for monochromatic illumination at $1550\,\text{nm}$ with a maximum efficiency of 45% – was considered. The designed link was highly directive with an average beam convergence of $11.9\,\mu\text{rad}$ defined by the full width at 36.8% of peak intensity. Harvesting $1.2\,\text{W}$ of electrical power from an estimated number of 47 LPCs was shown to be attainable at $100\,\text{m}$. The area of each cell was only $5 \times 5\,\text{mm}^2$; therefore, the size of an array of 47 LPCs is calculated to be $11.75\,\text{cm}^2$, which is suitable for practical applications of OWPT. Most importantly, the mirror dimensions were shown to be $17.8 \times 17.8 \times 7.6\,\text{cm}^3$ and $24.8 \times 24.8 \times 7.6\,\text{cm}^3$ for a link operation at 102% and 54% of the MPE, respectively. Thus, the requirement for a Class 1 laser system was met. These dimensions are considered to be acceptable for a practical application of wireless energy transfer to SCs. Overall, the designed $1550\,\text{nm}$ laser link had low complexity because of the small number of optical components; was considered to be eye safe with a classification of Class 1; was capable of transferring $1.2\,\text{W}$ of electrical power at $100\,\text{m}$; and comprised optics of acceptable dimensions for practical applications. It is hoped that these results could form the basis for further investigations of OWPT not only for SCs but also for other applications such as the solar power satellite and unmanned aerial vehicles or drones.

Chapter 6
Hybrid solar/laser based energy harvesting systems with electrochemical storage

6.1 Introduction

The worst case light conditions for small cell (SC) energy harvesting (EH) correspond to power transfer only from dedicated optical sources in darkness. These conditions have already been considered in Chapters 3, 4 and 5. However, the unique potential of harvesting power not only from optical sources but also from sunlight remains unexplored. Hence, as a first step, the concept of outdoor SC EH from sunlight at daytime is studied experimentally in this chapter. The objective is to determine the generated power levels with a desired value of 1 W and assess if additional power from optical sources is required.

In particular, two solar panels are used with the ability to harvest maximum power of 5 W and 10 W under standard test conditions (STC), respectively. The 5 W solar panel is used under sunny weather conditions. The 10 W panel is used while partly cloudy conditions are prevailing. An average electrical power of 3.7 W is measured using the 5 W panel for one hour. Also, average power and peak power of 4.1 W and 9 W, respectively, are generated by the 10 W panel within a two-hour period. Harvesting at least 1 W of electrical power is shown to be feasible for periods in the order of hours during the day even under partly cloudy weather conditions. The variability of weather conditions is shown to affect the harvested power causing fluctuations with minimum values in the order of mW. Therefore, the use of a battery is required to balance the generated electrical power. In addition to electrochemical storage, hybrid EH from sources of light amplification by stimulated emission of radiation (laser) and sunlight is shown to be required for SCs in the presence of dense clouds, since the harvested power decreases to levels of mW.

As a next step, a simulation study is given for the determination of the battery size required for an autonomous year-round SC operation based on solar EH. Hence, the use of the 5 W and 10 W

solar panels from the experiments is considered. The results show the feasibility of autonomous SC operation for a year, but the dimensions and weight of the batteries are not suitable for a practical application of SC EH. Thus, the design of a hybrid EH system is proposed based on solar EH using the 10 W panel and the 1550 nm laser based wireless power transfer (WPT) link from Chapter 5. The feasibility of the provision of the SC with 1 W is shown even without electrochemical storage. However, a battery with suitable dimensions is shown to be useful as a back-up solution during adverse weather conditions, which cause reduction in the transmitted optical power.

The rest of the chapter is organised as follows. The experiments for the harvested power from sunlight are given in Section 6.2. The simulation study with the addition of a battery for year-round SC operation is provided in 6.3. Finally, a summary of this chapter is given in Section 6.4.

6.2 Experiments: Harvested power from sunlight

The system components and power measurements using the 5 W and the 10 W solar panels are given below. Different resistance values are used in the experiments to observe how the mismatch losses of the load affect the harvested power.

6.2.1 System components

The data sheet parameters of the two multi-crystalline silicon (multi-c-Si) solar panels are given in Table 6.1. The STC maximum power is used to distinguish solar panel #1 from solar panel #2.

Table 6.1: *Data sheet parameters of solar panels used for EH from sunlight*

Multi-crystalline silicon (multi-c-Si) solar panel #1			Multi-crystalline silicon solar panel #2		
Parameter	Unit	Value	Parameter	Unit	Value
Number of cells connected in series, N_c	-	36	N_c	-	36
Effective area, S_{eff}	[cm^2]	365.0	S_{eff}	[cm^2]	673.9
Maximum electrical harvested power, P_m	[W]	5.0†	P_m	[W]	10.0†
Power conversion efficiency, η_{sr}	(%)	13.7†	η_{sr}	(%)	14.8†
Characteristic resistance, R_{ch}	[Ω]	56.7†	R_{ch}	[Ω]	28.8†

†Standard test conditions (STC) values.

The same physical location is used for the two experimental scenarios. The measurements are taken under approximately line-of-sight (LoS) and non-LoS conditions. Since an inexpensive large scale SC deployment requires an uncomplicated base station structure, the use of a tracking system for tilt or axis displacement with respect to the sun is avoided. The inclination, ω, is defined as the angle between z- axis and the rectangular level of the solar receiver, as shown in Figures 6.1 and 6.4. The heading is defined as the angle of orientation of the measurement device (compass application of a smart phone) and north (N). In the experiments, both of the solar panels have a heading of $18°$ and a N-northeast orientation. An Arduino device is used for real time measurements of the harvested power with practical resistor loads, R_{L}, of $25\,\Omega$, $50\,\Omega$ and $75\,\Omega$ connected to the output of the receivers.

6.2.2 Scenario I: 5 W solar panel

The $5\,\mathrm{W}$ multi-c-Si solar panel is used in Scenario I. The measurements of power, P_{L}, are conducted on 6 September 2015 under sunny conditions. The setup of Scenario I is given in Figure 6.1. The inclination of the solar panel is measured to be $59.2°$ using the compass application of a smart phone.

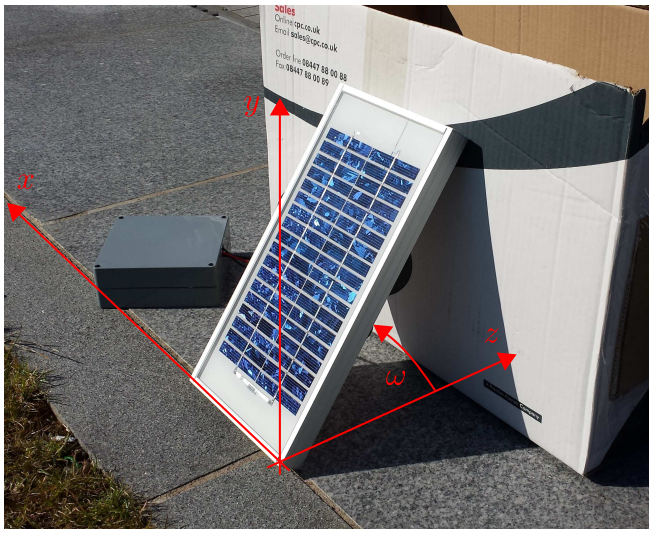

Figure 6.1: *Scenario I: Experimental setup for EH from a five Watt solar panel under sunny conditions.*

The measured data of Scenario I are given in Figure 6.2 for a load resistance of $25\,\Omega$ from 13:00 to 14:00. A deep fade of the power is observed between 13:02 and 13:05 induced by the appearance of clouds. The minimum and maximum power samples are measured to be

119.2 mW and 3.3 W, respectively. Overall, an average harvested power of 3.1 W is calculated from the collected data. In other words, the targeted value of 1 W is shown to be exceeded by 3.1 times on average.

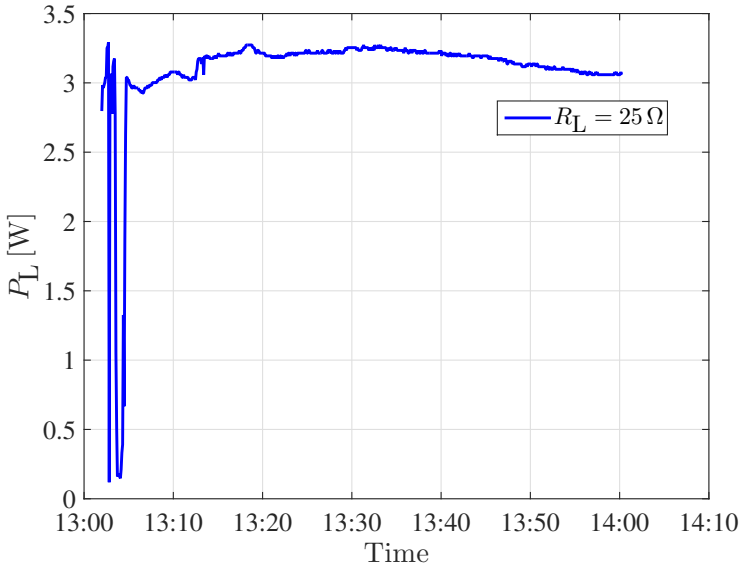

Figure 6.2: *Scenario I: Harvested electrical power between 1 post meridiem (pm) and 2 pm.*

The experimental data of the power harvested by the 5 W solar panel between 15:07 and 16:05 are given in Figure 6.3. In this case, the load resistance is $R_{\mathrm{L}} = 50\,\Omega$, and the average electrical power is calculated to be 3.7 W. The generated power remains above 2.97 W during the whole period of the observed time. As times passes, the harvested power decreases because of earth's rotation. The increase in R_{L} from $25\,\Omega$ to $50\,\Omega$ results in better load matching, since $R_{\mathrm{ch}} = 56.7\,\Omega$. Therefore, an increase in the average electrical power by 1.2 times is shown to be attained. Small scale rapid fluctuations of the harvested power are observed within periods of minutes, and these can be attributed to the effect of scintillation or atmospheric turbulence [55].

6.2.3 Scenario II: 10 W solar panel

In Scenario II, the 10 W solar panel is used for electrical power generation from sunlight. The setup of Scenario II is given in Figure 6.4. Partly cloudy conditions prevail during the measurements. The measurements last from 12:03 to 14:08 and from 16:35 to 18:45 on 11 September 2015. The experiment is continued from 11:35 to 14:05 on 16 September 2015. Parameter ω is

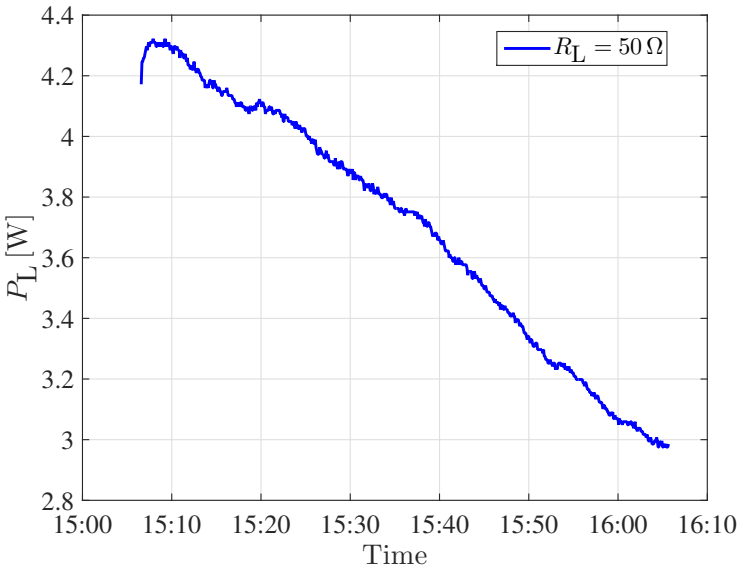

Figure 6.3: *Scenario I: Harvested electrical power between 3:07 pm and 4:05 pm.*

measured to be $40.8°$ using the compass application of a smart phone.

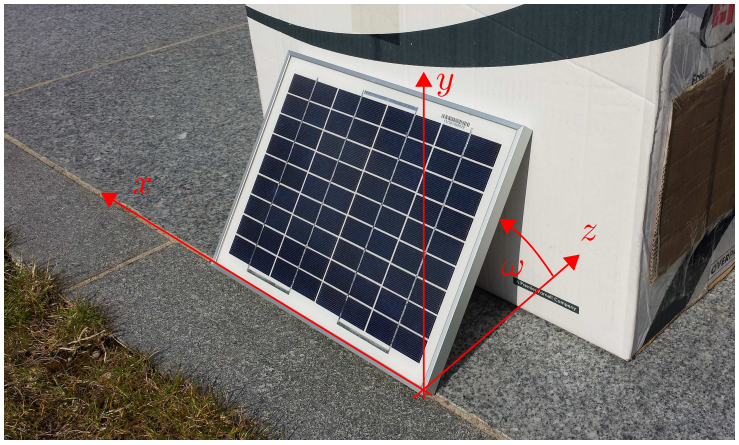

Figure 6.4: *Scenario II: Experimental setup for EH from a ten Watt solar panel under partly cloudy conditions.*

The harvested electrical power of the $10\,\mathrm{W}$ multi-c-Si panel is given for the time period of 12:03 and 14:08 in Figure 6.5. A resistor value of $75\,\Omega$ is used in this time period. The existence of a large number of fades in the graph is attributed to the high density of clouds, which reflect and scatter sunlight rays. Despite the occurrence of partly cloudy weather conditions, the harvested power is falling below the required amount of $1\,\mathrm{W}$ for only five minutes. Also, the minimum

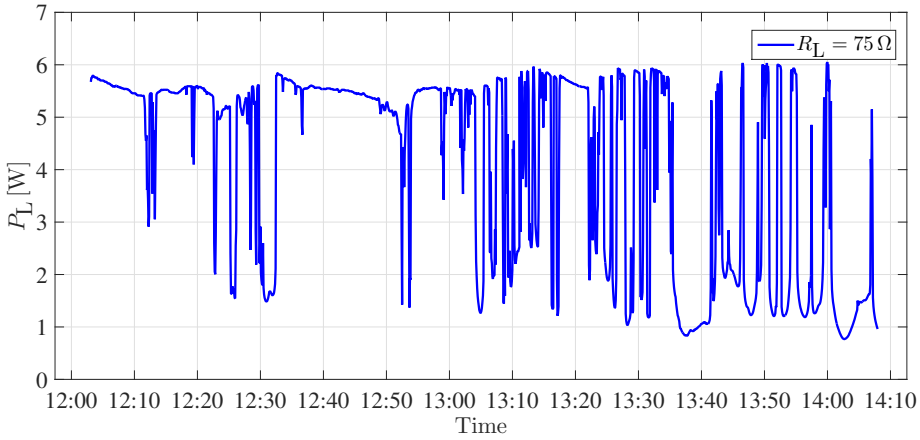

Figure 6.5: *Scenario II: Harvested electrical power between 12:03 pm and 2:08 pm.*

power is measured to be 769 mW at 14:02, that is only 231 mW below the targeted value of 1 W. The maximum electrical power is measured to be 6.05 W at 13:59. The average electrical power over the period of two hours and three minutes is calculated to be 4.1 W. Therefore, the target of harvesting 1 W is again overachieved by 4.1 times on average within two hours.

The measured data of power harvested by the 10 W solar panel from 16:35 to 18:45 are given in Figure 6.6. The load resistance has a value of 75 Ω. The harvested electrical power remains

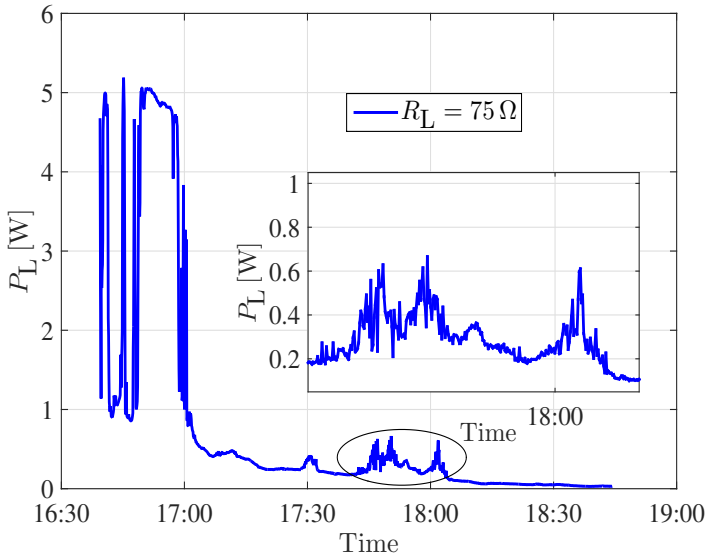

Figure 6.6: *Scenario II: Harvested electrical power between 4:35 pm and 6:45 pm.*

above the level of 857 mW until 17:02. The power levels remain in the order of mW after

17:02. Attenuated power seems to be harvested between 17:40 and 18:05 with minimum and maximum values of $100\,\text{mW}$ and $665.8\,\text{mW}$, respectively. The fluctuations of power during this period can be explained by shadowing effects. The harvested power attenuates steadily after 18:05 with a minimum value of $29\,\text{mW}$. The average harvested power is calculated to be $748.6\,\text{mW}$ during the whole period of measurements.

The measured electrical power using the $10\,\text{W}$ multi-c-Si solar panel with a load of $50\,\Omega$ from 11:35 to 14:05 is shown in Figure 6.7. The maximum power is shown to be achieved at the

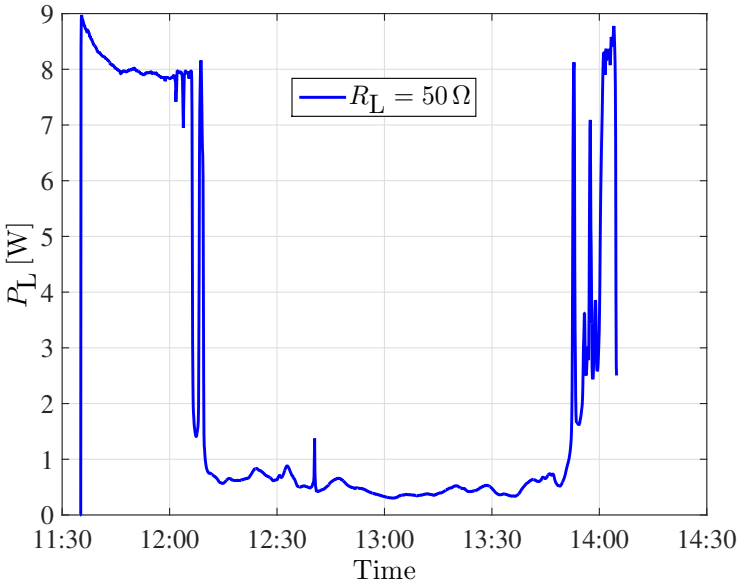

Figure 6.7: *Scenario II: Harvested electrical power between 11:35 ante meridiem (am) and 2:05 pm.*

beginning of the measurements with a value of $8.97\,\text{W}$. This large value corresponds to 89.7% of the maximum harvested power of the multi-c-Si panel under STC. An intense 'slow' fade of the power is observed from 12:09 to 13:52 with an average value of $529.4\,\text{mW}$. The received power is significantly attenuated because of clouds. Note that even during the presence of weather conditions of high-density clouds, the average power is larger than $0.5\,\text{W}$. The harvested power from the $50\,\Omega$ load increases gradually after 13:52 with some 'fast' fluctuations reaching a maximum value of $8.78\,\text{W}$. The average harvested power during the entire observed period of time is calculated to be $2.53\,\text{W}$. The decrease in load resistance from $75\,\Omega$ to $50\,\Omega$ that is closer to $R_\text{ch} = 28.8\,\Omega$ results in larger harvested amounts of power from the photovoltaic (PV) panel due to the decrease in mismatch losses of the load. This is observed by a comparison of the P_L values in Figure 6.5 and Figure 6.6 with the respective ones in Figure 6.7.

6.3 Battery addition for autonomous year-round SC operation

As a next step, the simulation software Homer Legacy [107] is used to determine the required size of the battery for the solar EH system to supply the SC with 1 W for each hour of the year. Three scenarios of SC EH are investigated assuming the use of the 5 W PV panel and the 10 W PV panel from the experiments. The feasibility of an autonomous SC operation is studied based on exclusively solar EH in the two first scenarios; and solar EH during daytime with complementary laser based WPT in the third scenario. The simulation parameters and the three scenarios are given below.

6.3.1 Simulation parameters

The simulation parameters of the solar EH system are summarised in Table 6.2. The seasonal

Table 6.2: *Simulation parameters*

Parameters	Units	Values
Day-to-day variability factor	(%)	20.0
Time-step-to-time-step variability factor	(%)	15.0
Slope, ω	[°]	40.8
Azimuth	[°]	18.0
De-rating factor	(%)	80.0
Ground reflectance	(%)	20.0
Temperature coefficient of power	[%/°C]	-0.5
Nominal operating cell temperature	[°C]	25.0

profile of the direct current electrical load is given in Figure 6.8. Two random variability factors are used for the load: the day-to-day and time-step-to-time-step factor. The day-to-day coefficient denotes the standard deviation in the sequence of daily averages, i.e. a daily noise input. The factor of time step to time step represents the standard deviation in the difference of hourly data and the average daily profile, i.e. an hourly noise input. An array of 8760 hourly values of load data of 1 W is created for the whole year in Homer from the specified daily profiles. Each hourly value is then multiplied by a factor $\alpha = 1 + \delta_d + \delta_h$, where δ_d and δ_h denote the daily and hourly perturbation factors, respectively. The daily perturbation factor is randomly selected once per day from a normal distribution with a mean of zero and a standard deviation equal to the daily noise input. Similarly, the hourly perturbation factor is randomly selected every hour from a normal distribution with a mean of zero and a standard deviation equal to the hourly noise input.

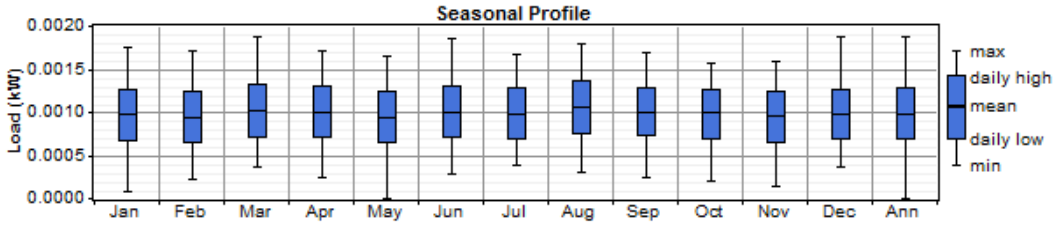

Figure 6.8: *Monthly and annual profile of electrical load in kW [107].*

The location coordinates of $55°\ 55'$ N and $3°\ 10'$ west are used for the latitude and the longitude of the PV panels, respectively. The data of solar radiation, i.e. energy per square metre, per day and the clearness index for each month are given in Figure 6.9. The clearness index is a

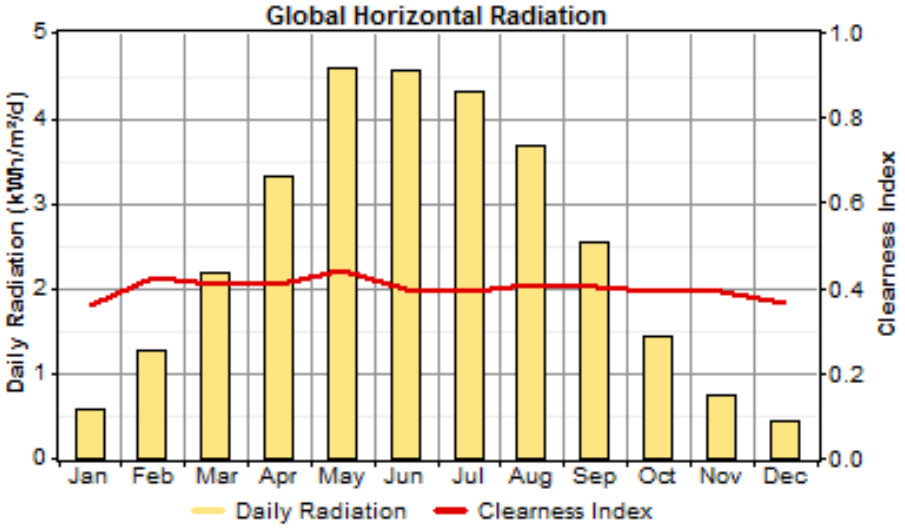

Figure 6.9: *Daily solar energy in kWh per square metre and clearness index over each month of 2001 in Edinburgh [107].*

measure of the clearness of the atmosphere and is defined by the ratio of the radiation on the horizontal surface of the earth over the extraterrestrial horizontal radiation. The daily average of solar radiation is calculated to be $2.47\,\mathrm{kWh/m^2}$. Note that the solar data are obtained on-line through the software and refer to 2001. To the best of the author's knowledge, there is no availability of solar data for Edinburgh after 2001. Hence, the measured data of Section 6.2 cannot be compared with hourly values of generated power from on-line sources.

The slope is defined by the angle at which the solar panels are mounted relative to the horizontal and is identical to the inclination ω. The azimuth is the direction towards which the PV panels are tilted and is equal to the heading of the panels. South is considered to have an azimuth of

$0°$, while N has an azimuth of $180°$. The de-rating factor of the solar devices accounts for losses due to soiling, wiring, shading, snow cover and ageing under real-world operating conditions.

Temperature is an important factor that affects the efficiency of solar cells and is modelled in the simulation. The average monthly values of ambient temperature from [108] are used for Edinburgh. The temperature coefficient of power indicates how the maximum harvested power varies with the temperature of the cells. Also, the efficiency values of Table 6.1 are used for the two solar panels.

6.3.2 Solar EH using the 5 W panel

A Hoppecke 16 OPzS 2000 battery is added to the solar EH system. Note that this is a typical example of a battery with nominal energy content of $4\,\text{kWh}$. This value is the product of the nominal voltage and capacity of the storage device which are $2\,\text{V}$ and $2\,\text{kAh}$, respectively. Zero to five such vented lead-acid batteries are assumed in the optimization process. The simulation results show that two batteries are required. Also, the state of charge (SoC) is defined by the capacity that can be discharged from a battery at a certain moment [109]. The monthly SoC of the batteries is given in Figure 6.10. The batteries are shown to be discharged constantly

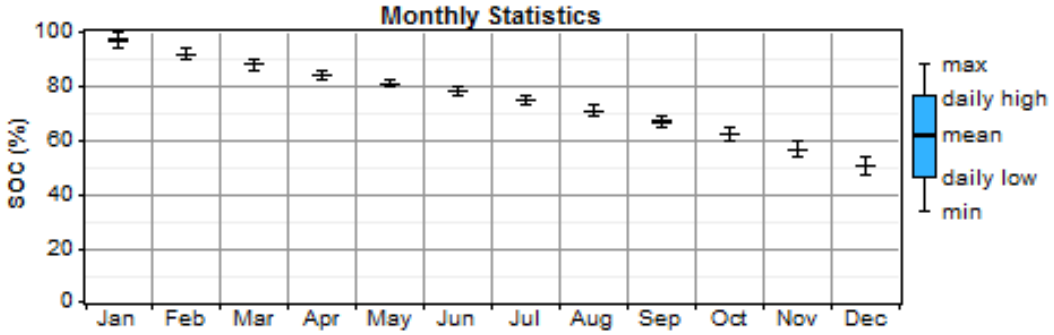

Figure 6.10: *Monthly SoC of the batteries used with the* 5 *W solar panel.*

over the year reaching their lowest mean SoC of 50% in December that is 20% over their minimum SoC. This means that the load requirement will not be possibly met in the next years without recharging the batteries. In addition, the total maximum weight and dimensions of two $4\,\text{kWh}$ storage devices such as the Hoppecke 16 OPzS 2000 are $302\,\text{kg}$ and $43 \times 80 \times 163\,\text{cm}^3$, respectively [110]. Therefore, the weight and dimensions of these batteries are not suitable for a practical application of SC EH.

6.3.3 Solar EH using the 10 W panel

In this simulation scenario, the battery type Hoppecke 8 OPzS 800 is used with a nominal voltage of 2 V and a nominal capacity of 800 Ah. Thus, the nominal energy content of the battery is 1.6 kWh. Again, zero to five such batteries are considered in the optimization method. The results show the feasibility of providing the SC with 1 W per hour using one Hoppecke 8 OPzS 800 battery. The monthly average electrical production of the 10 W PV panel is given in Figure 6.11. It is observed that the electrical demand of 1 W is not met in January, February,

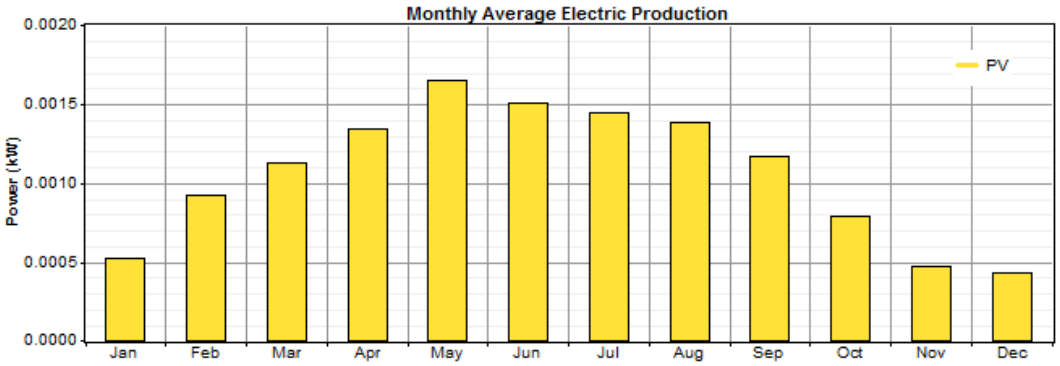

Figure 6.11: *Average harvested electrical power of the* 10 *W solar panel in kW over each month.*

October, November and December. Thus, the additional required power during these months is provided by the battery. Also, the monthly SoC of the battery is given in Figure 6.12. The

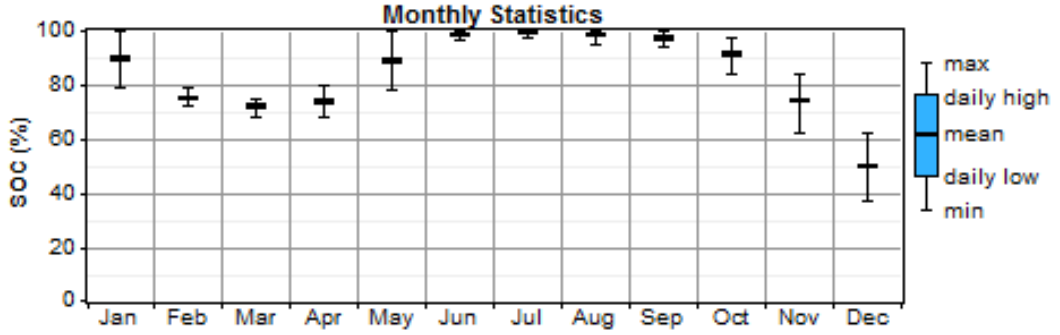

Figure 6.12: *Monthly SoC of the battery used with the* 10 *W solar panel.*

battery is shown to be discharged from January to March to satisfy the load demand, and is charged until July with the highest mean SoC of 99.3%. Also, it remains highly charged until September, since at least 1 W is produced, as shown in Figure 6.11. However, the generated power falls below 0.5 W in November and in December, and the battery SoC decreases ac-

cordingly. The lowest average SoC is observed in December with a value of 50.1%. Since the minimum SoC of this battery is 30%, it might not be able to provide the load with 1 W in the next years. Finally, the maximum weight and dimensions of this battery are 63.1 kg and $21.5 \times 19.3 \times 71$ cm^3, respectively, which are still not practical for SC power supply [110].

6.3.4 Hybrid solar/IR EH

To decrease the dimensions and energy content of the battery required for an autonomous SC operation, a hybrid solar/infrared (IR) EH solution is proposed. In particular, the operation of a 100 m WPT link is considered using the 1550 nm laser diode and the laser power converter (LPC) of Chapter 5.

The 'generator' component is used to model the laser system in Homer. The sizes of 1 W and 2 W are considered in the optimization process. These values refer to the maximum power provided to the load; therefore they denote the maximum harvested electrical power of the LPC. Also, a lifetime of $15{,}000$ h and a minimum load ratio of 1% are used in the simulation. The minimum load ratio is the minimum allowable load on the generator, expressed as a percentage of its rated capacity. This prevents the generator from operating at a very low load. The laser system is forced to be 'on' during the whole year. The battery with the lowest energy content in Homer is used for simulation. This is a Vision CP6100D battery with a nominal voltage of 6 V and a nominal capacity of 10 Ah. The volume and the weight of this battery are $15 \times 5.1 \times 9.4$ cm^3 and 1.67 kg, respectively, which are considered to be suitable for practical SC power supply. Zero and one devices are considered for optimization.

The simulation results show the feasibility of meeting the load demand using the 10 W panel, a 2 W laser system and either one battery or none. In other words, the proposed EH system is able to operate autonomously without a battery. However, a storage device is important to be used as a back-up solution in case of unfavourable weather conditions, which attenuate the levels of power transferred without wires to the SC. The monthly average electrical power generated by the hybrid EH system using the 10 W solar panel and the 1550 nm LPC is given in Figure 6.13. A complementary behaviour is observed in the monthly power generation of the hybrid system. Solar EH is favourable mostly during the summer months, which have the longest daylight periods of the year. Therefore, the IR laser based WPT system needs to provide the largest amounts of power in winter, during which the longest nighttime periods of the year occur. More importantly, the highest value of average electrical production from the

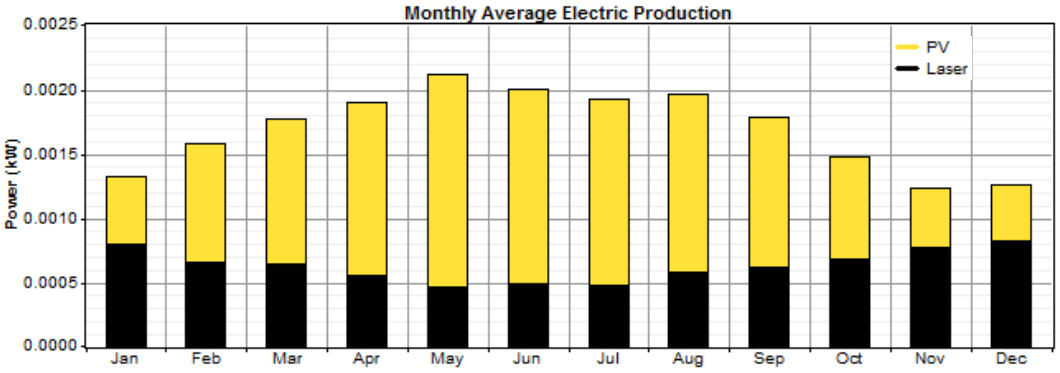

Figure 6.13: *Average generated electrical power in kW over each month of the hybrid solar/laser EH system.*

laser system is 824 mW in December, and harvesting 1.2 W from the 1550 nm LPC under clear weather conditions has been shown to be feasible through simulations in Chapter 5. The total annual average generated power is measured to be 1.69 W per hour. This value consists of 1.06 W produced by the 10 W panel and 0.63 W generated by the IR laser system.

Despite the fact that the daily levels of solar radiation are almost the same in May and in June (see Figure 6.9), the electrical power generated by the PV panel is shown to be higher in May with a peak value of 1.65 W. This is attributed to the lower values of cell temperature observed in May compared with these in June, as shown in Figure 6.14. In particular, the average ambient temperature is 10.8 °C and 13.4 °C in May and in June, respectively. Thus, the hourly average cell temperature is calculated to be 11.6 °C in May and 14.2 °C in June. Since a linear model is used for the maximum harvested power and the cell temperature in Homer, the solar panel efficiency scales linearly with the cell temperature. Also, the efficiency decreases with an increase in cell temperature. Therefore, the 10 W PV panel has higher efficiency in May compared with June with the calculated values 21.5% and 20.2%, respectively.

In Figure 6.14, the electrical power per hour generated by the PV panel and the laser system in May and in June is also given. It can be observed that the laser system contributes to the produced power mostly during nighttime while solar EH is zero. Since an autonomous operation of the hybrid EH system without electrochemical storage is feasible, the battery remains fully charged during the whole year, i.e. the SoC is constantly 100%.

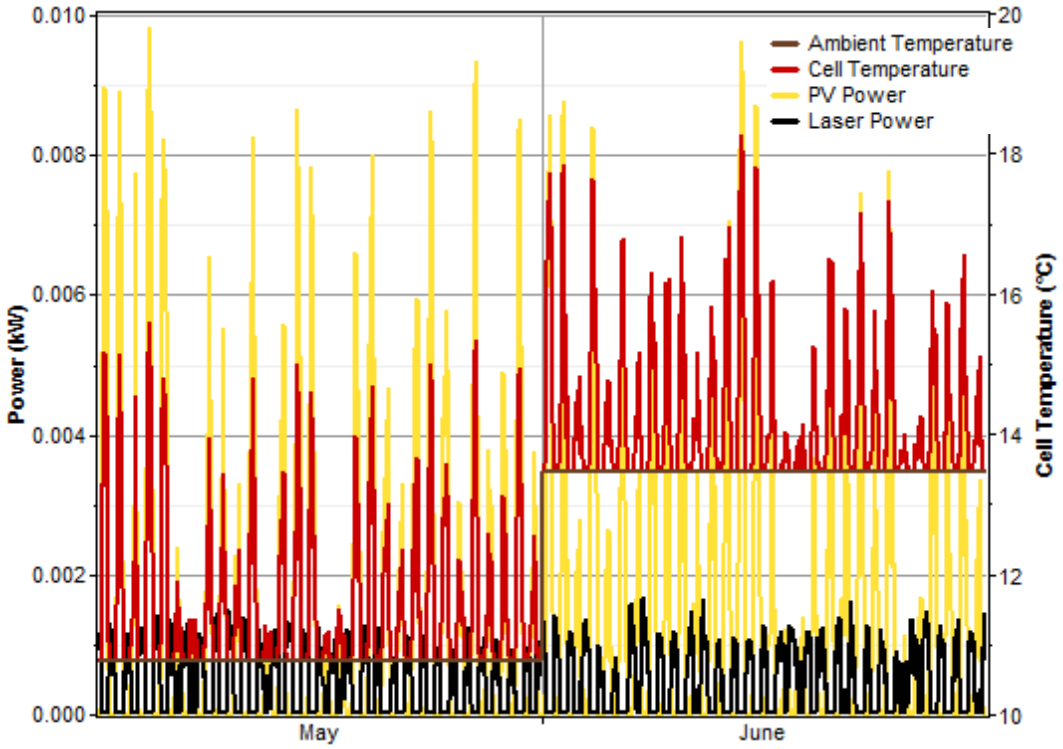

Figure 6.14: *Hourly generated electrical power, ambient temperature and cell temperature of the hybrid solar/IR system in May and in June.*

6.4 Summary

In this chapter, two experimental setups were created for power harvesting from sunlight in an outdoor environment. Two multi-c-Si solar panels were used with the capability of generating 5 W and 10 W under STC, respectively. Sunny weather conditions prevailed when the 5 W solar receiver was used. The 10 W solar receiver was used under partly cloudy conditions. An average harvested power of 3.7 W was measured, when the 5 W solar panel was used with a 50 Ω load for one hour. Despite the frequent occurrence of clouds, the average power was measured to be 4.1 W for a two-hour period using the 10 W PV panel. Also, the power levels were shown to be decreasing below 1 W only for five minutes. An average harvested power of 0.53 W was determined under strong fading conditions of two hours induced by high-density clouds, and a peak power of 9 W was measured. Overall, harvesting at least 1 W of electrical power for SCs was shown to be feasible for periods in the order of hours. More importantly, the power of 1 W was shown to be overachieved by up to 4.1 times even in the partial presence of clouds. However, the variability of weather conditions was shown to cause fluctuations in the harvested power decreasing it to levels in the order of mW. Therefore, in order to balance

the generation of electrical energy, the use of a battery for electrochemical storage of the solar energy was required. In the presence of clouds, additional power from optical sources was shown to be needed as the generated power from sunlight was in the order of mW.

A follow-up simulation study was given in order to determine the required battery size for supplying 1 W to a SC on an annual basis in Edinburgh. The feasibility of autonomous solar EH was investigated using the 5 W panel and the 10 W panel with one or two batteries. While these systems were shown to be able to operate for one year, the dimensions and weight of the storage devices were unsuitable for practical SC EH. Hence, a hybrid system was proposed using the 10 W PV panel for solar EH and the 1.55 μm laser based WPT link from Chapter 5. The hybrid solar/IR EH system was able to provide an autonomous SC operation without the use of a device for electrochemical storage. The annual total electrical production was 1.69 W per hour. The complementary power from the IR laser system was 0.63 W; this is below 1 W, which was achieved in Chapter 5. More importantly, the SoC of the battery was shown to be constantly 100% during the whole year. The dimensions of the storage device were shown to be practical for SC EH, and its energy content was only 60 Wh. Therefore, the use of such a battery serves as a practical back-up solution in the presence of unfavourable – foggy/rainy – weather conditions, which could cause significant attenuation in the optical and, thus, the harvested electrical power of the laser link.

The design of a solar EH system depends highly on the solar radiation levels of the geographical area considered. One of the places on earth with the highest global horizontal radiation – best case scenario – is the Antofagasta region in Chile; the values of long term average of daily sum are shown to be more than 7.5 kWh/m^2 in the solar world map for 2016 [111]. According to the same solar map, Edinburgh is shown to have a long term average of daily sum of global horizontal radiation of less than 2.5 kWh/m^2 – it is very close to areas of the world with the lowest radiation levels, i.e. worst case scenario. Therefore, a SC implemented in Antofagasta is expected to be able to operate autonomously on a year-round basis exclusively through solar EH. Also, the required size of the solar panel for harvesting 1 W is expected to decrease compared with the 10 W PV receiver of this study. One scenario of SC EH with average values of global horizontal radiation could be realised in Athens, Greece; the long term average of daily sum is shown to be 5 kWh/m^2 [111]. In this case, the additional use of laser sources would again be required mostly over nighttime. Thus, the required power levels from laser are not expected to change significantly in Athens compared with the reported ones in this

chapter. However, the lifetime of the battery in Athens would be extended compared with the same one in Edinburgh due to the more infrequent supply of power to the load.

Chapter 7
Summary, conclusions and future work

In this thesis, the general objective was to investigate the concept of optical wireless power transfer (OWPT) through light sources carrying high speed data for communication. However, research was focused on the topic of optical energy harvesting (EH) using off-the-shelf electronic light sources and photovoltaic (PV) devices. Thus, the data communication part was not subject to this thesis. In particular, two areas were researched – the OWPT to small cells (SCs) during darkness hours; and outdoor solar EH during daytime for SCs. The electrical power required for an autonomous operation of a radio frequency (RF) SC was determined to be 1 W. As a first step, dedicated optical sources, such as a light-emitting diode (LED) and diodes of light amplification by stimulated emission of radiation (laser), were used to transmit power to a solar receiver, and this was the worst case scenario in terms of ambient light conditions. The conditions of darkness were selected, because the system must be able to harvest power when there is no ambient light. Also, the best conditions for SC EH occur during daytime because electrical power can be harvested from sunlight and radiation of optical sources simultaneously. Hence, the principle of SC EH from sunlight was investigated during daytime to determine the generated power and the required size of a battery and to assess if the use of optical sources was needed.

7.1 Summary and conclusions

In Chapter 2, a literature review of the research areas of this thesis was given. An analytical background was provided for the concept of wireless power transfer (WPT) considering the use of a laser diode (LD), a collimation lens and a PV receiver that was either a cell or a panel. More importantly, this analytical framework was developed to model for the first time a complete optical link for power transfer using artificial optical sources with solar cells. Well established physical models, such as the elliptical Gaussian beam, $ABCD$ matrices and the single diode based physical equivalent circuit, were analysed, as they were used to support the

simulation and experimental results of the next chapters. The presented link model is hoped to form the basis for further investigations in the area of OWPT for more practical applications, such as the solar power satellite (SPS) and wireless charging of electrical vehicles.

In Chapter 3, the application limits of OWPT were investigated for the first time for an indoor white light-emitting diode (WLED) based scenario during darkness hours. A novel analytical model was developed considering OWPT exclusively from artificial radiation sources such as WLEDs to PV panels. In particular, the Lambertian source was used to model a WLED of high luminous flux of $2200\,\mathrm{lm}$ and the brightness theorem was used to determine the parameters of semi-angle of half power, which were modified by the optics. This theoretical link model was combined with uncomplicated electrical measurements in order to extract the – k parameters – ratio of optical-to-electrical power efficiency over the fill factor (FF) of the solar panel for different scenarios of light collimation. Thus, these k parameters could be verified and used for future large scale experiments carried out at longer link distances and with larger components.

Three experimental studies were conducted using precise optics for efficient light collimation at the transmitter. An amorphous silicon (a-Si) solar panel was used at the receiver. The parabolic mirror (PM) provided the best solution for light collimation and OWPT. This fact was attributed to the large paraboloid surface that was able to collect and collimate the light rays of the WLED better than the lens and the reflector. However, even in this case, the harvested electrical power and the efficiency of the entire link were significantly low with values of $18.3\,\mathrm{mW}$ and 0.1%, respectively. This finding was attributed to both the Lambertian radiation pattern of the WLED and the considerably low energy efficiency of the a-Si solar panel. The low harvested power and end-to-end power efficiency could be improved by the use of WLEDs with higher output power levels and a large PM at the solar panel to increase the receiver gain. The main disadvantage, though, would be a further increase in the dimensions of the receiver. Therefore, according to the experiments and theory, it can be concluded that WLED based visible light communication systems will be unable to provide power to a RF SC, which typically requires $1\,\mathrm{W}$. Future work was determined to consider a design based on high power laser arrays due to the high directivity and the compact dimensions they provide. The use of new solar cell technologies of higher power efficiency would also be studied.

Thus, a follow-up study was presented in Chapter 4 for an indoor laser based scenario for EH during nighttime. In particular, an experimental study was undertaken to determine the maximum link efficiency, maximum harvested power and optical receiver efficiency. The optical

sources were up to five red continuous wave LDs combined with the use of aspheric lenses for beam collimation. The optical receivers were two solar panels and a solar cell based on the technology of multi-crystalline silicon (multi-c-Si) and mono-crystalline silicon (mono-c-Si), respectively. The first solar panel consisted of 36 cells, and the second solar panel had eight cells. The link distance was 5.2 m. A high energy efficiency with a FF of 69% and a harvested electrical power of 30.6 mW was attained by the eight cell solar panel. The best value of maximum link efficiency of 3.2% was achieved by two optical transmitters and the solar cell. This relatively low value was justified by the contribution of the low measured average efficiency of the two LDs of 26.8% and the solar cell efficiency of 13.3%. For the same link, the geometrical losses of optical power were estimated to be only 10.6%. This fact was sufficient to characterise the optical link as highly efficient with OWPT showing great potential at longer distances. It was explained that this low value of link efficiency was not the absolute maximum using today's components, but it could be increased by a respective increase in the components efficiency. This could be achieved using infrared (IR) LDs of high conversion efficiency, e.g. 54% at 975 nm, along with monochromatic laser power converters (LPCs), as shown in Chapter 5. However, the analytical calculation of the maximum permissible exposure (MPE) and nominal ocular hazard distance for eye safety resulted in the need for a beam enclosure of up to 3.6 m.

Most importantly, a comparison was made for the same optical wireless link with a state-of-the-art inductive power transfer system with optimally shaped dipole coils. As a result, a performance improvement in terms of total power efficiency by 2.7 times was achieved by the link consisting of two LDs and a solar cell. Therefore, the concept of indoor OWPT was concluded to have an acceptable efficiency of comparable levels with RF based EH systems. The additional harvested power from sunlight is expected to offer performance superiority to OWPT systems compared with RF based WPT systems. This is because solar devices are able to harvest power simultaneously from man-made optical sources, such as lasers, and a natural resource, i.e. sunlight, while typical rectennas or induction coils lack this advantage in the RF domain. In addition, the required number of red LDs for harvesting 1 W was estimated according to the single diode physical equivalent circuit of the solar panel; 61 red transmitters were calculated assuming the use of the mono-c-Si cell. This value was achieved for a particular set of parameters of the components and will be modified if a slight change of the input parameters such as the output power per diode and beam divergence occurs.

In Chapter 4, another experimental study was undertaken for the determination of the laser beam divergence. A targeted value of 1 mrad was considered because the beam diameter is only 10 cm at 100 m, assuming a laser point source. In particular, an optical transmitter was created by the use of the red LD and a spherical lens. Also, the analytical model developed for the prediction of the elliptical Gaussian beam propagation in Chapter 2 was applied to the experimental data for curve fitting and estimation of its unknown parameters. As a result, the divergence of full width at 36.8% of peak intensity was determined to be 3 mrad and 5.75 mrad along the 'slow' and 'fast' axes of the laser beam, respectively. Moreover, the beam divergence determined by the diameter of the circular image was measured to be only 2.1 mrad. Therefore, the beam diameter will be 21 cm at 100 m, assuming a laser point source. Despite the fact that the obtained values of beam divergence were at least twice the targeted 1 mrad, the additional optical losses could be counterbalanced by the use of a large collection mirror or a large solar panel at the receiver. Thus, this single optical link was concluded to be characterised by high directivity enabling the application of OWPT to longer distances.

In Chapter 5, three designs of a 100 m IR laser based wireless link were simulated in Zemax for harvesting 1 W. The transition from the wavelength of 660 nm to the IR region of the spectrum was made to explore the possibilities of designing an eye-safe transmitter with practical dimensions. The required number of red LDs for harvesting 1 W from the mono-c-Si PV cell was estimated to be 61 in Chapter 4. Also, the best maximum link efficiency measured in the experiments was 3.2%. These facts provided the basis for the first design of an array of 42 LDs and collimation lenses operating at 785 nm. The transmission power of the laser array was 7.2 W. An average full width at half maximum beam divergence of 1.4 mrad was calculated. The feasibility of harvesting an electrical power of 1 W up to 30 m was shown, since at least 7 W of optical power were received. However, the use of a shielding tube of up to 54.3 m would be required for eye safety of this Class 3B system.

Thus, in the second design, a transmitter of 10 W was created by a 975 nm LD with a high typical efficiency of 53% and a collimation mirror of dimensions in the order of m^3. The receiver was modelled by a collection mirror of the same dimensions and the mono-c-Si cell. The IR beam, transmitted to free space, was highly collimated with an estimated convergence and divergence in the order of μrad. The objective of harvesting 1 W was shown to be feasible up to 100 m including meeting the requirements for Class 1 eye safety, but the mirror dimensions were unsuitable for the application of wireless power supply to SCs. In addition, the MPE of

the $975\,\text{nm}$ transmitter was shown to decrease along the wireless channel achieving its lowest value of only $8.9\,\text{mW/cm}^2$ at $100\,\text{m}$. Nevertheless, the use of $975\,\text{nm}$ laser sources along with LPCs could create power transfer links with end-to-end efficiencies of the order of 30% and could also be considered in near field applications such as wireless charging of electrical vehicles.

Therefore, in the third design, a LD operating at $1550\,\text{nm}$ and at $4\,\text{W}$ was used due to its large MPE of $100\,\text{mW/cm}^2$ for Class 1 systems. A LPC was considered at the receiver with a maximum reported efficiency of 45% for harvesting $1\,\text{W}$. The mirror dimensions were in the order of cm^3 for a wireless link operation at 54% of the MPE. In addition to these suitable mirror dimensions, an optical power of $2.8\,\text{W}$ was transferred to the LPC at $100\,\text{m}$. One LPC of $5 \times 5\,\text{mm}^2$ was reported to achieve the efficiency of 42% for the irradiance of $237.5\,\text{mW/cm}^2$. Thus, the required number of such devices – connected in series – to ensure the same efficiency was 47. The size of an array of 47 LPCs was calculated to be $11.75\,\text{cm}^2$, which is suitable for practical applications of OWPT. Overall, the designed $1550\,\text{nm}$ laser link was characterised by low complexity because of the small number of optical components; was considered to be eye safe with a classification of Class 1; was capable of transferring $1.2\,\text{W}$ of electrical power at $100\,\text{m}$; and comprised optics of acceptable dimensions for practical applications. It is hoped that these results will form the basis for further investigations of OWPT not only for SCs but also for other applications such as the SPS and unmanned aerial vehicles or drones.

In Chapter 6, two experimental setups were created for EH from sunlight in an outdoor environment. In particular, a multi-c-Si solar panel with a maximum power of $5\,\text{W}$, rated at standard test conditions (STC), was used under sunny weather conditions. An average electrical power of $3.1\,\text{W}$ was measured with a resistor load of $25\,\Omega$ for a two hour period. Also, this parameter increased to $3.7\,\text{W}$ for an one hour period with a resistance of $50\,\Omega$ due to better load matching. Another multi-c-Si PV panel with a STC maximum power of $10\,\text{W}$ was used under partly cloudy weather conditions. Despite the presence of high density clouds, the required amount of $1\,\text{W}$ was shown to be affirmed for a two hour period with a $75\,\Omega$ load. In this case, the average harvested power was calculated to be $4.1\,\text{W}$. When the load resistance decreased to $50\,\Omega$ that is closer to the characteristic resistance of the panel, the highest peak power of $9\,\text{W}$ was achieved. The presence of clouds resulted in a significant attenuation of the harvested power for one hour and 43 minutes with an average value of $0.53\,\text{W}$. Overall, the constant power supply of at least $1\,\text{W}$ to SCs was shown to be feasible for periods in the order of hours. However, the variability

of weather conditions resulted in an instability of the harvested power with values in the order of mW for short periods of time.

Thus, a follow-up simulation study was given for the determination of the required battery size for a year-round autonomous operation of a SC in Edinburgh. The feasibility of energy autonomy was shown through solar EH for one year considering the $5\,\mathrm{W}$ and the $10\,\mathrm{W}$ panels used in the experiments. However, the weight and dimensions of the batteries were not suitable for a practical application of power supply to SCs. Therefore, a hybrid EH system was proposed assuming the use of the $10\,\mathrm{W}$ panel for solar EH and the $1550\,\mathrm{nm}$ laser based link from Chapter 5. The simulation results showed that supplying $1\,\mathrm{W}$ to outdoor SCs was achievable during the whole year with an annual average electrical production of $0.63\,\mathrm{W}$ from the laser link. A harvested electrical power of at least $1\,\mathrm{W}$ was shown to be feasible in Chapter 5 using the $1550\,\mathrm{nm}$ laser link. Therefore, the load demand could be met using the same laser system in the hybrid design. In addition, no electrochemical storage was shown to be required for the hybrid solar/IR EH system. However, the use of a battery with energy content of only $60\,\mathrm{Ah}$ would be suitable as a back-up solution in case of degradation or failure of the power transfer link due to adverse weather conditions, such as fog, rain and snow.

The geographical area under investigation was mentioned to be one of the most important parameters that affects the design of a solar EH system. Edinburgh was shown to have an average daily global horizontal radiation of less than $2.5\,\mathrm{kWh/m^2}$ – this was very close to the lowest radiation levels in the world, i.e. worst case scenario. One of the places on earth with the highest global horizontal radiation – best case scenario – was the Antofagasta region in Chile; the average daily values were shown to be more than $7.5\,\mathrm{kWh/m^2}$. Therefore, a SC implemented in Antofagasta was expected to be able to operate autonomously on a year-round basis exclusively through solar EH. Also, the required size of the solar panel for harvesting $1\,\mathrm{W}$ would decrease compared with the $10\,\mathrm{W}$ PV receiver of this study. One scenario of SC EH with average values of global horizontal radiation could be realised in Athens, Greece; the daily value was shown to be $5\,\mathrm{kWh/m^2}$. In this case, the additional use of lasers would be required, but with lower transferred power levels compared with the reported ones in Chapter 6. The average generated power by the laser system was $0.63\,\mathrm{W}$ per hour in Edinburgh achieved with solar radiation that was half the respective value in Athens. Therefore, it was concluded that the average generated power per hour by the laser system would be in the order of $0.32\,\mathrm{W}$ in Athens.

7.2 Limitations and future work

A major limitation in the design of an OWPT link for SC power harvesting of 1 W was shown to be the eye safety requirement. Despite the fact that the white light beam transmitted by the PM in Chapter 3 was divergent, the eye safety regulations need to be considered according to the British standard BS EN 62471:2008 [112]. The use of 660 nm LDs and lenses for power transmission at 5 m in Chapter 4 resulted in the requirement of a multi-beam enclosure of up to 3.6 m that is 72% of the link distance. Also, the 100 m WPT system consisting of 785 nm LDs and lenses in Chapter 5 was shown to need multi-beam shielding of up to 54.3 m, i.e. 54.3% of the link distance. A simple way to resolve this issue is to increase the size of the collimation lenses and to enclose the area between the LDs and the lenses. However, the resulting dimensions of the transmitter and the receiver could be unsuitable for the practical application of wireless power supply to SCs, such as these of the 975 nm laser transmitter in Chapter 5. Therefore, the feasibility of creating a laser based WPT system for SCs depends highly on the trade-off between the MPE and the maximum allowable transmitter-receiver dimensions. An interesting solution was provided designing a laser link with off-axis PMs that operates at 1550 nm in Chapter 5. Future work will consider an experimental implementation of this laser link with relative measurements of the optical power to determine the beam divergence and to affirm the restrictions of a Class 1 system.

Another major limitation of this work is that the research was very specific – as it was problem oriented – and, thus, general results could not be produced. This means that a slight variation of the input parameters of the system will potentially result in the need for a new set of experiments. One of the reasons is that visible LDs have stricter eye safety requirements compared with IR LDs; thus, the MPE decreases for visible laser sources accordingly. Also, the power conversion efficiency of laser sources even of the same wavelength depends highly on the output power; therefore, different power efficiencies are achieved for different amounts of input power. The use of LDs of different beam divergence potentially requires collimation optics of different dimensions. One of the reasons that a laser based analytical model was developed in Chapter 2 was to estimate the required number of laser sources for harvesting 1 W. Particular assumptions were made for the responsivity of the PV receiver based on the experiments of Chapter 4. However, the system parameters of responsivity and solar panel efficiency are expected to change for optical power regions of the order of W compared with the mW levels of the experiments. Therefore, it would be more valuable to implement first a laser system that

harvests at least 1 W and then measure parameters of the model that cannot be theoretically predicted in advance. Although harvesting 1 W during nighttime was not demonstrated in this thesis, the indoor implementation of the 1550 nm laser link of Chapter 5 will be considered in order to verify the simulation results.

Since the technology of solar cells constitutes another important physical constraint in power efficiency, the use of one or multiple 1.55 μm LPCs with potential efficiencies from 35% to 45% will be of major importance [15, 113]. The increased LPC efficiency is expected to increase the total efficiency of the OWPT links, which was currently shown to be in the order of only 3%. Note that the absence of commercial availability of high power single junction and multi-junction solar cells was another limitation for the experimental work of this thesis. Outdoor experiments will also be conducted to determine a realistic link budget, which includes optical losses induced by adverse weather conditions. So long as the wavelength of 1550 nm was shown to offer a high MPE, new components will be explored in the mid-IR region for the creation of WPT systems of suitable dimensions for SCs.

The research study of solar/laser based EH for SCs in Chapter 6 was also limited to the area of Edinburgh. Thus, more places on earth will be investigated as a next step according to the solar global horizontal radiation levels. Data from solar maps will be used along with relevant mathematical analysis of PV EH. This will contribute to the generation of a general model able to determine the power requirements from sunlight, lasers and batteries for an autonomous SC operation in any place on earth. The 10 W multi-c-Si PV panel and the array of 1550 nm cells could be used for outdoor EH from sunlight and laser sources, respectively, for a proof of concept. Another important future direction is the investigation of free space optical (FSO) back-haul communication for SCs. As a first step, the achievable data rates of the communication link will be explored using a laser source for power transfer. The transmission possibility of a 2.5 GHz RF signal with a double sided communication bandwidth of 10 MHz will be explored. Thus, the use of optical sources with 3-dB bandwidth in the order of GHz, such as the vertical-cavity surface-emitting lasers [114], will be considered. The separation of the downlink and uplink communication paths between the SC and the central unit will be investigated for the selection of the actual link components. Single carrier modulation techniques, such as on-off keying or pulse position modulation, could be considered to maintain the complexity of the SC low. Finally, the use of optical orthogonal frequency division multiplexing will be explored to increase the data rate of the FSO link to the region of Gb/s.

Appendix A

Mathematical derivation of (2.12), (2.43), (2.44) and (2.61)

The total optical power of the beam is expressed as the double integral over the transverse x-y plane by:

$$\begin{aligned} P_{\text{Tx,o}} &= \int_{-\infty}^{\infty}\int_{-\infty}^{\infty} G(x,y,z)\mathrm{d}x\mathrm{d}y \\ &\overset{(2.11)}{=} G_0 \frac{W_{0\text{x}}W_{0\text{y}}}{W_{\text{x}}(z)W_{\text{y}}(z)} \int_{-\infty}^{\infty} \exp\left[\frac{-2x^2}{W_{\text{x}}^2(z)}\right]\mathrm{d}x \int_{-\infty}^{\infty} \exp\left[\frac{-2y^2}{W_{\text{y}}^2(z)}\right]\mathrm{d}y \\ &= G_0 \frac{W_{0\text{x}}W_{0\text{y}}}{W_{\text{x}}(z)W_{\text{y}}(z)} \int_{0}^{\infty} 2\exp\left[\frac{-2x^2}{W_{\text{x}}^2(z)}\right]\mathrm{d}x \int_{0}^{\infty} 2\exp\left[\frac{-2y^2}{W_{\text{y}}^2(z)}\right]\mathrm{d}y. \end{aligned} \tag{A.1}$$

The two exponential integrals of the second part of (A.1) yield the following result [115]:

$$\begin{aligned} P_{\text{Tx,o}} &= G_0 \frac{W_{0\text{x}}W_{0\text{y}}}{W_{\text{x}}(z)W_{\text{y}}(z)} W_{\text{x}}(z)\sqrt{\frac{\pi}{2}} W_{\text{y}}(z)\sqrt{\frac{\pi}{2}} \\ &= \frac{\pi}{2} G_0 W_{0\text{x}}W_{0\text{y}} \cdot \blacksquare \end{aligned}$$

The inverse of q- parameter along the x- axis of the Gaussian beam at the input plane of the solar receiver is computed by:

$$\frac{1}{q_{4\text{x}}} = \frac{C'q_{0\text{x}} + D'}{A'q_{0\text{x}} + B'}. \tag{A.2}$$

The substitution of $q_{0\text{x}} = j\pi W_{0\text{x}}^2/\lambda_0$ to (A.2) yields:

$$\begin{aligned} \frac{1}{q_{4\text{x}}} &= \frac{jC'\frac{\pi W_{0\text{x}}^2}{\lambda_0} + D'}{jA'\frac{\pi W_{0\text{x}}^2}{\lambda_0} + B'} = \frac{\left(jC'\frac{\pi W_{0\text{x}}^2}{\lambda_0} + D'\right)\left(-jA'\frac{\pi W_{0\text{x}}^2}{\lambda_0} + B'\right)}{\left(jA'\frac{\pi W_{0\text{x}}^2}{\lambda_0} + B'\right)\left(-jA'\frac{\pi W_{0\text{x}}^2}{\lambda_0} + B'\right)} \\ &= \frac{A'C'\left(\frac{\pi W_{0\text{x}}^2}{\lambda_0}\right)^2 + jB'C'\frac{\pi W_{0\text{x}}^2}{\lambda_0} - jA'D'\frac{\pi W_{0\text{x}}^2}{\lambda_0} + B'D'}{\left(A'\frac{\pi W_{0\text{x}}^2}{\lambda_0}\right)^2 + B'^2}, \end{aligned}$$

which can finally be expressed as a complex number by:

$$\frac{1}{q_{4\mathrm{x}}} = \frac{A'C'\left(\frac{\pi W_{0\mathrm{x}}^2}{\lambda_0}\right)^2 + B'D'}{\left(A'\frac{\pi W_{0\mathrm{x}}^2}{\lambda_0}\right)^2 + B'^2} - j\frac{(A'D' - B'C')\frac{\pi W_{0\mathrm{x}}^2}{\lambda_0}}{\left(A'\frac{\pi W_{0\mathrm{x}}^2}{\lambda_0}\right)^2 + B'^2}. \tag{A.3}$$

Note that the term $A'D' - B'C' = \det[\mathbf{M}]$ in (A.3), where $\det[.]$ represents the determinant of a matrix. It can be shown that $\det[\mathbf{M}] = \det[\mathbf{M}_2\mathbf{M}_{\text{lens}}\mathbf{M}_1] = \det[\mathbf{M}_2]\det[\mathbf{M}_{\text{lens}}]\det[\mathbf{M}_1] = 1$, since $\det[\mathbf{M}_2] = \det[\mathbf{M}_{\text{lens}}] = \det[\mathbf{M}_1] = 1$. Therefore, (A.3) can be expressed as:

$$\frac{1}{q_{4\mathrm{x}}} = \frac{A'C'\left(\frac{\pi W_{0\mathrm{x}}^2}{\lambda_0}\right)^2 + B'D'}{\left(A'\frac{\pi W_{0\mathrm{x}}^2}{\lambda_0}\right)^2 + B'^2} - j\frac{\frac{\pi W_{0\mathrm{x}}^2}{\lambda_0}}{\left(A'\frac{\pi W_{0\mathrm{x}}^2}{\lambda_0}\right)^2 + B'^2} \cdot \blacksquare$$

Similarly, the inverse of q- parameter along the y- axis of the Gaussian beam at the input plane of the solar receiver is given by:

$$\frac{1}{q_{4\mathrm{y}}} = \frac{A'C'\left(\frac{\pi W_{0\mathrm{y}}^2}{\lambda_0}\right)^2 + B'D'}{\left(A'\frac{\pi W_{0\mathrm{y}}^2}{\lambda_0}\right)^2 + B'^2} - j\frac{\frac{\pi W_{0\mathrm{y}}^2}{\lambda_0}}{\left(A'\frac{\pi W_{0\mathrm{y}}^2}{\lambda_0}\right)^2 + B'^2} \cdot \blacksquare$$

The ratio of the optical power collected by a rectangular optical receiver with the dimensions of $2x_0 \times 2y_0$ at a distance $z \geq d_0 + t_\mathrm{c}$ over the total optical power can be expressed by:

$$\begin{aligned}
\eta_\mathrm{c}(z) &= \frac{1}{(1-r)P_{\text{Tx,o}}}\int_{-x_0}^{x_0}\int_{-y_0}^{y_0} G'(x,y,z)\mathrm{d}x\mathrm{d}y \\
&\overset{(2.33)}{=} \frac{2}{\pi W'_\mathrm{x}(z')W'_\mathrm{y}(z'')}\int_{-x_0}^{x_0}\exp\left[\frac{-2x^2}{W'^2_\mathrm{x}(z')}\right]\mathrm{d}x\int_{-y_0}^{y_0}\exp\left[\frac{-2y^2}{W'^2_\mathrm{y}(z'')}\right]\mathrm{d}y \\
&= \frac{2}{\pi W'_\mathrm{x}(z')W'_\mathrm{y}(z'')}\int_{0}^{x_0} 2\exp\left[\frac{-2x^2}{W'^2_\mathrm{x}(z')}\right]\mathrm{d}x\int_{0}^{y_0} 2\exp\left[\frac{-2y^2}{W'^2_\mathrm{y}(z'')}\right]\mathrm{d}y.
\end{aligned} \tag{A.4}$$

Again, the two exponential integrals of the second part of (A.4) result in [115]:

$$\begin{aligned}
\eta_\mathrm{c}(z) &= \frac{2}{\pi W'_\mathrm{x}(z')W'_\mathrm{y}(z'')}W'_\mathrm{x}(z')\frac{\pi}{2}\mathrm{erf}\left[\frac{\sqrt{2}x_0}{W'_\mathrm{x}(z')}\right]W'_\mathrm{y}(z'')\mathrm{erf}\left[\frac{\sqrt{2}y_0}{W'_\mathrm{y}(z'')}\right] \\
&= \mathrm{erf}\left[\frac{\sqrt{2}x_0}{W'_\mathrm{x}(z')}\right]\mathrm{erf}\left[\frac{\sqrt{2}y_0}{W'_\mathrm{y}(z'')}\right] \cdot \blacksquare
\end{aligned}$$

Appendix B
Classification of the red laser system

B.1 Single LD

The maximum output optical power of the red laser diode (LD) is $P_{\text{Tx,o,m}} = 130\,\text{mW}$ [63]. The beam diameter is defined in BS EN 60825-1:2014 [46] as the smallest circle that contains 63% of the total laser power, i.e. $1/e$ beam width. Also, the beam divergence is defined as the far field plane angle of the cone created by the beam diameter. So long as the LD has a Gaussian elliptical profile, the beam divergences are defined along the x- and y- axes as $\varphi_{\text{x}} = 2\vartheta_{\text{x}}$ and $\varphi_{\text{y}} = 2\vartheta_{\text{y}}$, respectively. In particular, they are calculated to be $\varphi_{\text{x}} = 12.5^\circ \simeq 0.22\,\text{rad}$ and $\varphi_{\text{y}} = 21.2^\circ \simeq 0.37\,\text{rad}$ from [63]. According to (2.1) and (2.2) the beam diameters along the x- and y- axes can be calculated up to the $1/e \simeq 0.37$ points of the intensity pattern. In particular, the application of $\lambda_0 = 0.66\,\mu\text{m}$, $\vartheta_{\text{x}} = 6.25^\circ$ and $\vartheta_{\text{y}} = 10.6^\circ$ to (2.1) and (2.2) results in $W_{0\text{x}} = 1.92\,\mu\text{m}$ and $W_{0\text{y}} = 1.12\,\mu\text{m}$, respectively. Therefore, the beam diameters along the x- and y- directions are calculated to be $D_{0\text{x}} = 2W_{0\text{x}} = 3.84\,\mu\text{m}$ and $D_{0\text{y}} = 2W_{0\text{y}} = 2.24\,\mu\text{m}$, respectively.

Condition 3 of Table 10 [46] can be applied to the selected optical emitter. The measurement of accessible emission limit (AEL) needs to be made by the use of a circular aperture stop with a diameter of $D_{\text{ap}} = 7\,\text{mm}$ at a distance $d_{\text{m}} = 10\,\text{cm}$ from the optical source. The specific LD is divergent and the elliptical beam has larger dimensions than the circular area of the aperture stop. Therefore, the AEL must be expressed in terms of irradiance (in mW/cm^2) rather than optical power (in mW). The angular subtenses along the x- and y- axes can be found from:

$$\alpha_{\text{x}} = 2\tan^{-1}\left(\frac{D_{0\text{x}}}{2d_{\text{m}}}\right) \approx \frac{D_{0\text{x}}}{d_{\text{m}}} \tag{B.1}$$

and

$$\alpha_{\text{y}} = 2\tan^{-1}\left(\frac{D_{0\text{y}}}{2d_{\text{m}}}\right) \approx \frac{D_{0\text{y}}}{d_{\text{m}}}. \tag{B.2}$$

In particular, applying the values of $D_{0\text{x}} = 3.84\,\mu\text{m}$, $D_{0\text{y}} = 2.24\,\mu\text{m}$ and $d_{\text{m}} = 10^5\,\mu\text{m}$ to (B.1) and (B.2), the angular subtenses are calculated to be $\alpha_{\text{x}} = 38.4\,\mu\text{rad} < \alpha_{\text{min}} = 1.5\,\text{mrad}$ and

$\alpha_{\mathrm{y}} = 22.4\,\mu\mathrm{rad} < \alpha_{\mathrm{min}}$, respectively. Note that the classification principle 4.3 d) of [46] states that the angular subtense of a rectangular source is computed by the arithmetic mean value of the two angular dimensions of the source. Also, any value of the angular subtense smaller than α_{min} or bigger than $\alpha_{\mathrm{max}} = 100\,\mathrm{mrad}$ needs to be limited to α_{min} or α_{max}, respectively, before the calculation of mean value. Therefore, $\alpha = (1.5+1.5)/2 = 1.5\,\mathrm{mrad}$ and the LD is assumed to be a point source.

Assume that the LD can be classified as Class 3R and select a time base of $0.25\,\mathrm{s}$ according to the classification principle 4.3 e) of [46]. Then, the correction factor, C_6, is equal to 1 according to Table 9 [46]. Therefore, the AEL is determined to be $\kappa = 5\,\mathrm{mW}$ based on Table 6 [46]. The AEL expressed as irradiance is computed by:

$$G_{\mathrm{AEL}} = \frac{\kappa}{\pi(D_{\mathrm{ap}}/2)^2}. \tag{B.3}$$

The application of $\kappa = 5\,\mathrm{mW}$ and $D_{\mathrm{ap}} = 0.7\,\mathrm{cm}$ to (B.3) results in $G_{\mathrm{AEL}} \simeq 13\,\mathrm{mW/cm^2}$.

Now, the beam irradiance must be determined at $d_{\mathrm{m}} = 10\,\mathrm{cm}$ from the LD chip and be compared with G_{AEL}. For this reason, the beam diameter along the x- and y-axes is calculated by the use of (2.3) and (2.4), respectively. The application of $z = d_{\mathrm{m}} = 10\,\mathrm{cm}$, $W_{0\mathrm{x}} = 1.92\,\mu\mathrm{m}$ and $\lambda_0 = 0.66\,\mu\mathrm{m}$ to (2.3) yields $W_{\mathrm{x}}(10\,\mathrm{cm}) = 10.94\,\mathrm{mm}$. Also, the values of $z = d_{\mathrm{m}} = 10\,\mathrm{cm}$, $W_{0\mathrm{y}} = 1.12\,\mu\mathrm{m}$ and $\lambda_0 = 0.66\,\mu\mathrm{m}$ are applied to (2.4) and they result in $W_{\mathrm{y}}(10\,\mathrm{cm}) = 18.76\,\mathrm{mm}$. Therefore, the beam diameters at $d_{\mathrm{m}} = 10\,\mathrm{cm}$ are $D_{\mathrm{x}}(10\,\mathrm{cm}) = 2W_{\mathrm{x}}(10\,\mathrm{cm}) = 21.88\,\mathrm{mm}$ and $D_{\mathrm{y}}(10\,\mathrm{cm}) = 2W_{\mathrm{y}}(10\,\mathrm{cm}) = 37.52\,\mathrm{mm}$. The geometry of the circular aperture is approximated by that of a square aperture with side length equal to the diameter of the circular aperture, i.e. $2x_0 = 2y_0 = 7\,\mathrm{mm}$. In this case, the collection efficiency can be expressed based on (2.61) by:

$$\eta_{\mathrm{c}}(z) = \mathrm{erf}\left[\frac{\sqrt{2}x_0}{W_{\mathrm{x}}(z)}\right]\mathrm{erf}\left[\frac{\sqrt{2}y_0}{W_{\mathrm{y}}(z)}\right], \tag{B.4}$$

where $W_{\mathrm{x}}(z)$ and $W_{\mathrm{y}}(z)$ are given by (2.3) and (2.4), respectively. The values of $z = d_{\mathrm{m}} = 10\,\mathrm{cm}$, $x_0 = y_0 = 3.5\,\mathrm{mm}$, $W_{\mathrm{x}}(10\,\mathrm{cm}) = 10.94\,\mathrm{mm}$ and $W_{\mathrm{y}}(10\,\mathrm{cm}) = 18.76\,\mathrm{mm}$ are applied to (B.4) resulting in $\eta_{\mathrm{c}}(10\,\mathrm{cm}) = 0.139$. Therefore, the received optical power is $P_{\mathrm{Rx,o}}(10\,\mathrm{cm}) = \eta_{\mathrm{c}}(10\,\mathrm{cm})P_{\mathrm{Tx,o,m}} = 0.139 \times 130 = 18.07\,\mathrm{mW}$. Finally, the received beam

irradiance from a square aperture of side length $2x_0$ is given by:

$$G_{\mathrm{Rx}}(z) = \frac{P_{\mathrm{Rx,o}}(z)}{(2x_0)^2}. \tag{B.5}$$

The application of $z = d_0 = 10\,\mathrm{cm}$, $P_{\mathrm{Rx,o}}(10\,\mathrm{cm}) = 18.07\,\mathrm{mW}$ and $2x_0 = 0.7\,\mathrm{cm}$ to (B.5) results in $G_{\mathrm{Rx}}(10\,\mathrm{cm}) = 36.88\,\mathrm{mW/cm^2}$. This value is larger than G_{AEL}. Consequently, the LD cannot be classified as Class 3R.

Now, the LD is considered to belong to Class 3B, and a time base of $100\,\mathrm{s}$ is selected according to the classification principle 4.3 e). The received optical power, i.e. $P_{\mathrm{Rx,o}}(10\,\mathrm{cm}) = 18.07\,\mathrm{mW}$, is less than the AEL, i.e. $\kappa = 0.5\,\mathrm{W}$, derived from Table 8. As a result, the optical source is classified as Class 3B.

B.2 Laser diode and collimation lens

In this case, the laser consists of the direct current power supply, the LD and the aspheric lens used in Scenario III of Experiment II. So long as the area between the LD and the lens is shielded by an aluminium tube, the total optical device is considered to be an extended optical source. Note that Condition 1 of Table 10 [46] is applicable to collimated beams, but the most restrictive condition must be used for classification and, again, this is Condition 3 of Table 10 [46]. Thus, the measurement of AEL needs to be made by the use of a circular aperture stop with a diameter of $D_{\mathrm{ap}} = 7\,\mathrm{mm}$ at a distance of $d_{\mathrm{m}} = 10\,\mathrm{cm}$ from the new beam waist according to Table 11 [46]. As a first step, the new beam waists must be determined. The application of the values of parameters presented in Table 4.1 to (2.1)–(2.10) and (2.14)–(2.30) results in $W_{3\mathrm{x}} = 34.93\,\mu\mathrm{m}$ and $W_{3\mathrm{y}} = 20.39\,\mu\mathrm{m}$. Therefore, the substitution of $z' = d_{\mathrm{m}} = 10\,\mathrm{cm}$, $W_{3\mathrm{x}} = 34.93\,\mu\mathrm{m}$ and $\lambda_0 = 660\,\mathrm{nm}$ to (2.31) gives $W'_{\mathrm{x}}(10\,\mathrm{cm}) = 602.46\,\mu\mathrm{m}$. Also, the values of $z'' = d_{\mathrm{m}} = 10\,\mathrm{cm}$, $W_{3\mathrm{y}} = 20.39\,\mu\mathrm{m}$ and $\lambda_0 = 660\,\mathrm{nm}$ are applied to (2.32) and yield $W'_{\mathrm{y}}(10\,\mathrm{cm}) = 1.03\,\mathrm{mm}$. So long as the beam diameters at $10\,\mathrm{cm}$ from the beam waists are smaller than the diameter of the circular stop aperture, the AEL can be expressed as power and not as irradiance. The angular subtenses along the x- and y- axes are given by:

$$\alpha_{\mathrm{x}} = 2\tan^{-1}\left[\frac{W'_{\mathrm{x}}(d_{\mathrm{m}})}{d_{\mathrm{m}}}\right] \approx \frac{2W'_{\mathrm{x}}(d_{\mathrm{m}})}{d_{\mathrm{m}}} \tag{B.6}$$

and

$$\alpha_{\mathrm{y}} = 2\tan^{-1}\left[\frac{W'_{\mathrm{y}}(d_{\mathrm{m}})}{d_{\mathrm{m}}}\right] \approx \frac{2W'_{\mathrm{y}}(d_{\mathrm{m}})}{d_{\mathrm{m}}}. \tag{B.7}$$

The application of $W'_{\mathrm{x}}(10\,\mathrm{cm}) = 602.46\,\mu\mathrm{m}$, $W'_{\mathrm{y}}(10\,\mathrm{cm}) = 1.03\,\mathrm{mm}$ and $d_{\mathrm{m}} = 10\,\mathrm{cm}$ to (B.6) and (B.7) results in $\alpha_{\mathrm{x}} = 12\,\mathrm{mrad}$ and $\alpha_{\mathrm{y}} = 20.6\,\mathrm{mrad}$, respectively. Therefore, $\alpha = (\alpha_{\mathrm{x}} + \alpha_{\mathrm{y}})/2 = 16.3\,\mathrm{mrad}$.

Assume that the optical transmitter can be classified as Class 3R, and select a time base of $0.25\,\mathrm{s}$ according to the classification principle 4.3 e) of [46]. Then, the correction factor C_6 is equal to $\alpha/\alpha_{\mathrm{min}} = 10.867$ according to Table 9 [46]. Therefore, the AEL is determined to be $\kappa = 5C_6$ [mW] based on Table 7 [46] and, finally, $\kappa = 54.34\,\mathrm{mW}$.

Now, the laser beam power needs to be calculated at $10\,\mathrm{cm}$ from the beam waists in order to be compared with the AEL of Class 3R. So long as $d_{1\mathrm{x}} \simeq d_{1\mathrm{y}}$ according to Table 4.1, the collection efficiency of the rectangular receiver is calculated at $z' \simeq z'' = 10\,\mathrm{cm}$. The application of $x_0 = y_0 = 3.5\,\mathrm{mm}$, $W'_{\mathrm{x}}(10\,\mathrm{cm}) = 602.46\,\mu\mathrm{m}$ and $W'_{\mathrm{y}}(10\,\mathrm{cm}) = 1.03\,\mathrm{mm}$ to (2.61) gives a collection efficiency value of $\eta_{\mathrm{c}}(10\,\mathrm{cm}) = 1$, as expected. So, the received optical power is $P_{\mathrm{Rx,o}}(10\,\mathrm{cm}) = P_{\mathrm{Tx,o,m}} = 130\,\mathrm{mW}$ that is larger than $\kappa = 54.34\,\mathrm{mW}$. Therefore, again this optical transmitter is not classified as Class 3R, but as Class 3B. This is because the AEL of Class 3B is $\kappa = 500\,\mathrm{mW}$.

Appendix C
Selected publications

C.1 Conference papers

J. Fakidis, M. Ijaz, S. Kucera, H. Claussen, and H. Haas, "On the Design of an Optical Wireless Link for Small Cell Backhaul Communication and Energy Harvesting," in *Proc. IEEE 25th Annu. Int. Symp. Personal Indoor Mobile Radio Commun.*, Washington, DC, USA, Sep. 2014, pp. 58–62.

J. Fakidis, S. Kucera, H. Claussen, and H. Haas, "On the Design of a Free Space Optical Link for Small Cell Backhaul Communication and Power Supply," in *Proc. IEEE Int. Conf. Commun. Workshop*, London, U.K., Jun. 2015, pp. 1428–1433.

C.2 Journal paper

J. Fakidis, S. Videv, S. Kucera, H. Claussen, and H. Haas, "Indoor Optical Wireless Power Transfer to Small Cells at Nighttime," *IEEE J. Lightw. Technol.*, vol. 34, no. 13, pp. 3236–3258, Jul. 2016.

2014 IEEE 25th International Symposium on Personal, Indoor and Mobile Radio Communications

On the Design of an Optical Wireless Link for Small Cell Backhaul Communication and Energy Harvesting

John Fakidis*, Muhammad Ijaz*, Stepan Kucera†, Holger Claussen†, and Harald Haas*

*Institute for Digital Communications
Li-Fi R&D Centre
The University of Edinburgh
Edinburgh, EH9 3JL, UK
Email: {j.fakidis, m.ijaz, h.haas}@ed.ac.uk

†Bell Laboratories, Alcatel-Lucent
Blanchardstown Business & Technology Park
Dublin 15, Ireland
Email: {stepan.kucera,
holger.claussen}@alcatel-lucent.com

***Abstract*—The outdoor deployment of small cells (SCs) in heterogeneous cellular networks for mobile communications is advantageous from both the capacity and the power consumption point of view. In practice, however, the network operators are limited by the high costs associated with the provisioning of backhaul communication and power supply to the SCs. This paper addresses these operational challenges by using optical links at the same time for high-capacity backhaul and wireless power supply. In particular, we present an experimental design of an optical wireless link for energy harvesting (EH). Our system consists of (i) a high-brightness white light-emitting diode (WLED) with an output luminous flux of $2200\,$lm, and (ii) an amorphous silicon (a-Si) solar panel. The distance of the experimental link ranges from $0.5\,$m to $5\,$m. The visible-light EH from the solar panel is negatively affected by the Lambertian radiation pattern of the WLED. In order to increase the collimation of the source light, we use three optical elements - a spherical lens, a reflector, and a parabolic mirror. The latter is shown to achieve a gain of $28.4\,$dB in EH over a distance of $5\,$m compared to the non-collimated case.**

I. Introduction

The deployment of outdoor small cells (SCs) in wireless cellular networks is widely accepted as a solution to the exponential traffic growth of mobile data communications [1]. SCs substantially increase the overall network capacity [2] and also reduce the total power consumption of the network [3]. In practical terms, however, with a large-scale SC deployment the installation of SC power supply and backhaul communication between the SCs and their network gateways represents a major cost factor. One type of SCs in radio frequency (RF) cellular networks are *femtocells* [4], [5]. They are small, plug and play base stations (BSs) characterized by low levels of transmit power and low cost. However, in heterogeneous networks the backhaul communication between the SCs and the central units (CUs) has insufficient capacity [5]. Also, a mains power supply is required, and the energy demands levels are high, due to the signal-processing functionalities.

Light-emitting diodes (LEDs) provide high-speed communication in addition to room illumination [6]. One particular area of optical wireless technology is visible-light communication (VLC) [7]. VLC systems have attracted significant research interest due to their unique advantages. They can handle a large amount of data, offer secure communication, avoid electro-magnetic interference (EMI) and use almost limitless licence-free spectrum. The concept of SCs can be successfully implemented in high-speed VLC networks defined as optical *attocells* [8]. Optical attocell effectively constitutes a next level of SC in heterogeneous wireless networks. In [9], it is shown that an optical attocell network, based on off-the-shelf white LEDs (WLEDs), can provide improved area spectral efficiency of the order of two to three in heterogeneous networks. Also, optical attocells do not interfere with RF communication links.

The feasibility of a $3\,$Gb/s VLC link is demonstrated in [10]. The energy harvesting (EH) potentials of VLC are shown in [11]. Therefore, in this study we investigate the use of VLC to provide high-speed data and power to SC RF femtocells. In particular, we focus our research on the remote power supply of a simple energy-autonomous SC comprising a compact solar panel. The visible-light link is created by a high-luminance WLED. An analytical study is validated by a set of experiments.

The Lambertian radiation pattern of a LED source is identified as the major bottleneck in efficient energy transfer because it complicates the collimation of the LED light. In this context, three different optical elements for light collimation are investigated: a spherical plano-convex (PCX) lens, a reflector, and a parabolic mirror (PM). The photovoltaic (PV) panel of the SC used is based on an amorphous silicon (a-Si) material. The main reason is that a-Si solar cells present the best responsivity in the visible range of $[380, 720]\,$nm compared to the technologies of crystaline silicon (c-Si), cadmium telluride (CdTe), and copper indium gallium selenide (CIGS) [12].

The rest of the paper is organized as follows: Section II offers an approximate analytical formulation of the investigated system. In Sections III and IV, the experimental setup and conducted studies are described, respectively. In Section V, the results are summarized and discussed. Section VI offers concluding remarks.

978-1-4799-4912-0/14/$31.00 ©2014 IEEE

II. Analytical Framework

The general analytical models of the devices comprising the EH system are given below. In this paper, the model of the PM is not presented. Hereafter, the term "extended source" is used to describe the combined use of the optical source, *i.e.*, WLED, with optics.

A. Optical Source

The electrical power supply of an electronic WLED-driver is $P_{\text{elec}}^{\text{in}} = V_{\text{in}} I_{\text{in}}$ [W], where V_{in} [V] and I_{in} [A] denote the input voltage and current, respectively. The power efficiency of the driver can be defined as: $\eta_{\text{d}} = P_{\text{elec}}^{\text{LED}} / P_{\text{elec}}^{\text{in}}$, where $P_{\text{elec}}^{\text{LED}}$ is the input electrical power of the WLED. The operating point of the WLED ranges from its minimum to the maximum value in the dynamic range. The photometric unit of luminous flux, Φ [lm], for a WLED can be expressed as [13]:

$$\Phi = 683 \frac{\text{lm}}{\text{W}} \int_{380\text{nm}}^{720\text{nm}} \text{p}(\lambda)\text{V}(\lambda)\text{d}\lambda, \tag{1}$$

where λ [nm] is the variable wavelength in the visible-light spectrum, $\text{p}(\lambda)$ [W/nm] denotes the power spectral distribution (PSD) of the source and $\text{V}(\lambda)$ represents the eye-sensitivity function. The luminous efficiency, known also as luminous efficacy of the source, $\eta_{\text{LED}} = \Phi / P_{\text{elec}}^{\text{LED}}$ [lm/W], connects the electrical power with the luminous flux [13]. The data sheet of the WLED used provides the relative PSD [14]. For this reason, (1) is manipulated as:

$$\Phi = 683 \frac{\text{lm}}{\text{W}} P_{\text{opt},\lambda_0}^{\text{max}} \int_{380\text{nm}}^{720\text{nm}} \text{b}(\lambda)\text{V}(\lambda)\text{d}\lambda, \tag{2}$$

where $P_{\text{opt},\lambda_0}^{\text{max}}$ denotes the maximum optical power at a specific wavelength λ_0. The fraction $\text{b}(\lambda) = \text{p}(\lambda) / P_{\text{opt},\lambda_0}^{\text{max}}$ represents the relative PSD of the light source. The total optical power of the WLED, $P_{\text{opt}}^{\text{T,LED}}$, can be determined as follows [13]:

$$P_{\text{opt}}^{\text{T,LED}} = P_{\text{opt},\lambda_0}^{\text{max}} \int_{380\text{nm}}^{720\text{nm}} \text{b}(\lambda)\text{d}\lambda. \tag{3}$$

We combine the solution of (2) for $P_{\text{opt},\lambda_0}^{\text{max}}$ and (3). We also take into account the aforementioned relationships of the driver efficiency as well as the WLED efficacy. The resulting formula expresses the total optical power of the source:

$$P_{\text{opt}}^{\text{T,LED}} = \frac{\eta_{\text{LED}} \eta_{\text{d}} \int_{380\text{nm}}^{720\text{nm}} \text{b}(\lambda)\text{d}\lambda}{683 \frac{\text{lm}}{\text{W}} \int_{380\text{nm}}^{720\text{nm}} \text{b}(\lambda)\text{V}(\lambda)\text{d}\lambda} P_{\text{elec}}^{\text{in}}. \tag{4}$$

All of the parameters of the second part of (4) can now be obtained from the data sheet of the WLED [14]. The measured value of η_{d} is provided in Section III. The values of $\text{V}(\lambda)$ can be acquired from [13].

B. Optical Wireless Channel

Line-of-sight (LOS) conditions are considered for the optical wireless channel. In this work, the planes of the optical source and the solar panel are considered to be parallel. It is also assumed that perfect alignment of the optical axes among the WLED, the respective collimation optics and the solar panel is attained. The direct-current (DC) gain of the channel is calculated by [15]:

$$H_{\text{LOS}} = \frac{(m+1)A_R}{2\pi d^2}, \tag{5}$$

where m denotes the Lambertian order of the (extended) source, A_{R} [m^2] is the effective area of the receiver and d [m] is the link distance. The Lambertian order is computed by $m = -\ln(2)/\ln[\cos(\phi_{1/2})]$, where $\phi_{1/2}$ [rad] is the semi-angle of half-power of the (extended) source radiation pattern [15].

C. Receiver

The receiver includes a PV panel as well as a variable resistor. The optical power at the receiver input, $P_{\text{opt}}^{\text{R}}$, can be calculated by:

$$P_{\text{opt}}^{\text{R}} = H_{\text{LOS}} P_{\text{opt}}^{\text{T}}, \tag{6}$$

where $P_{\text{opt}}^{\text{T}}$ describes the optical transmit power either from the WLED or the extended source. The ideal harvested electrical power from the PV panel can be defined as $P_{\text{elec}}^{\text{ideal}} = V_{\text{oc}} I_{\text{sc}}$, where V_{oc} is the open-circuit voltage and I_{sc} denotes the short-circuit current. The power efficiency, η_{sp}, of the solar panel is defined as [12]:

$$\eta_{\text{sp}} = \frac{P_{\text{elec}}^{\text{max}}}{P_{\text{opt}}^{\text{R}}}, \tag{7}$$

where $P_{\text{elec}}^{\text{max}}$ represents the maximum harvested electrical power. The above symbol is defined as $P_{\text{elec}}^{\text{max}} = V_{\text{mp}} I_{\text{mp}}$, where V_{mp} and I_{mp} denote the voltage and current at the maximum-power point of the panel, respectively. The fill-factor, FF, of a solar panel can be used as a metric of approximation of the ideal operation [12]. The fill-factor is defined as:

$$\text{FF} = \frac{P_{\text{elec}}^{\text{max}}}{P_{\text{elec}}^{\text{ideal}}}. \tag{8}$$

We combine the solution of (7) for $P_{\text{elec}}^{\text{max}}$ with the solution of (8) for $P_{\text{elec}}^{\text{ideal}}$. Therefore, the following relationship is obtained:

$$P_{\text{elec}}^{\text{ideal}} = k P_{\text{opt}}^{\text{R}}, \tag{9}$$

where $k = \eta_{\text{sp}}/\text{FF}$ is defined as the ratio of the power efficiency over the fill-factor of the solar panel. The values of η_{sp} and FF are highly dependent on the received optical power, *i.e.*, $P_{\text{opt}}^{\text{R}}$, and temperature of the PV module. The total maximum efficiency of the link that connects the input and maximum output electrical power is defined as: $\eta_{\text{max}} = P_{\text{elec}}^{\text{max}} / P_{\text{elec}}^{\text{in}}$.

D. Optics

The use of optical elements in the CU affects not only the optical power but also the radiation pattern of the WLED.

1) PCX Lens: The received optical power, $P_{\text{opt}}^{\text{R,lens}}$, at the input (front) circular plane of the lens can be calculated using (5) and (6). In particular, we obtain:

$$P_{\text{opt}}^{\text{R,lens}} = \frac{(m_{\text{LED}}+1) D_{\text{lens}}^2}{8 d'^2} P_{\text{opt}}^{\text{T,LED}}, \tag{10}$$

where m_{LED} denotes the Lambertian order of the WLED, D_{lens} [mm] is the lens diameter and d' [mm] is the distance

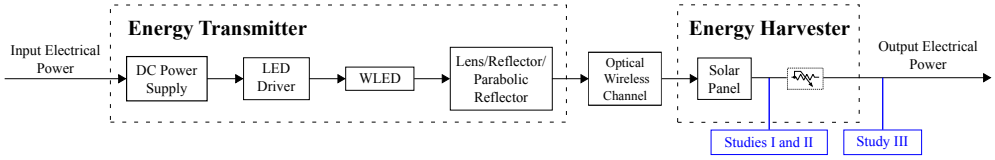

Fig. 1. Block diagram of the experimental EH system.

between the WLED and the lens. The output optical power of the lens can be expressed as:

$$P_{\text{opt}}^{\text{T,lens}} = T_{\text{lens}} P_{\text{opt}}^{\text{R,lens}}, \tag{11}$$

where T_{lens} denotes the average transmittance of the lens over the visible-light spectrum. The modified semi-angle of half-power can be approximated by [16]:

$$\phi_{1/2}^{\text{lens}} = \frac{D_{\text{s}}}{2d'}, \tag{12}$$

where D_{s} [mm] is the diameter of the optical source.

2) Reflector: The transmitted optical power of the reflector is calculated by:

$$P_{\text{opt}}^{\text{T,refl}} = T_{\text{refl}} P_{\text{opt}}^{\text{T,LED}}, \tag{13}$$

where T_{refl} denotes the transmittance of the reflector. According to the "etendue" conservation law, we can find a lower bound of the semi-angle of half-power using the following relationship [17]:

$$\phi_{1/2}^{\text{refl}} \geq \frac{D_{\text{s}} \phi_{1/2}^{\text{LED}}}{D_{\text{refl}}}, \tag{14}$$

where D_{refl} [cm] is the external diameter of the reflector. We can apply the respective data sheet values introduced in Section III to (14) and assume that $\phi_{1/2}^{\text{refl}} = 9.5°$.

III. Experimental Set-up

The block diagram of the experimental set-up is given in Fig. 1. The measured power efficiency of the driver is 88%. The WLED used is a high-brightness BXRA-40E2200-B-00 Bridgelux array of 24 chips [14]. The diameter of the light-emitting surface (LES) is 16 mm. The typical luminous flux and the semi-angle of half-power are 2200 lm and 60° ($m_{\text{LED}} = 1$), respectively.

The features of the three utilized optics are described below. First, an Edmund optics spherical PCX lens with a magnesium fluoride (MgF_2) anti-reflection (AR) coating is used with a 75 mm- diameter and focal length. The average transmittance of the thick lens over the visible region of wavelengths is 98.6%. Secondly, a spot-light CN12159 LENA-S-DL LEDiL reflector is used. The external diameter and the height of the reflector are 11.1 cm and 8.62 cm, respectively. The transmittance of the reflector is 78%. Finally, an Edmund optics large parabolic reflector is investigated. The diameter of the PM is 60.96 cm and the effective focal length is 15.24 cm. The paraboloid reflector has a semi-angle of half-power equal to 3°. The center hole of the mirror has a diameter of 3.81 cm.

TABLE I
PV Panel Data Sheet Parameters

V_{oc} [V]	I_{sc} [mA]	V_{mp} [V]	I_{mp} [mA]	$P_{\text{elec}}^{\text{max}}$ [W]
17.6	356	15.6	330	5.15

The main component of the receiver is an a-Si A+ Life PA6-005 solar panel. The area of the solar panel is $30.4 \times 23.8\,\text{cm}^2$. Table I gives the electrical characteristics provided by the PV panel manufacturer, and these refer to standard test conditions (STC) [12].

It is ensured that ambient light is negligible and does not contribute to the collected optical power from the solar panel.

IV. Experimental Studies

A series of three experimental studies was conducted. The basic criterion of the system performance is the maximization of the measured $P_{\text{elec}}^{\text{ideal}}$ under the same electrical power dissipation at the transmitter. Our experimental studies are described below.

A. Study I

An initial study is conducted for five different experimental scenarios. The parameters V_{oc} and I_{sc} are measured for a distance range of $[0.5, 5]$ m using increments of 0.5 m in order to compute $P_{\text{elec}}^{\text{ideal}}$. The electrical power consumption at the CU, *i.e.*, $P_{\text{elec}}^{\text{in}}$, is kept constant and equal to 18.3 W.

In the first scenario, the WLED is used in the absence of optics at the CU. In the second experiment, the optical set-up of the transmitter includes the WLED as well as the PCX lens. The lens is placed at the focal point. In the third scenario, the optical system of the CU comprises the LED and the reflector. In the fourth experiment, the optical part of the transmitter consists of the WLED and the PCX lens. However, the lens is located such that $P_{\text{elec}}^{\text{ideal}}$ is maximized. In the fifth scenario, the CU includes the WLED and the large parabolic reflector or PM. The position of the PM is such that $P_{\text{elec}}^{\text{ideal}}$ is maximized. In particular, the parabolic reflector is placed at a distance of 16.8 cm from the LED. The last four experimental scenarios are shown in Fig. 2.

B. Study II

In this study, we select the three geometrical configurations of the optical transmitter that delivered the best performance in Study I. The link distance is fixed to 5 m. The experimental values of V_{oc} and I_{sc} are obtained as we change $P_{\text{elec}}^{\text{in}}$ from 3.25 W to 30.3 W. Finally, the values of $P_{\text{elec}}^{\text{ideal}}$ are calculated for the three experimental systems.

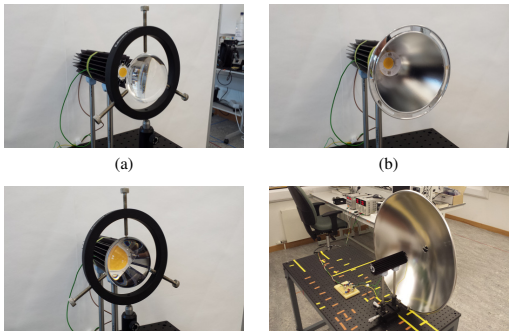

(a) (b) (c) (d)

Fig. 2. Transmitter part of four experimental scenarios: (a) Lens located at 7.5 cm from the WLED, (b) WLED and reflector, (c) Lens placed at 2.5 cm from the WLED, and (d) PM at 16.8 cm from the WLED.

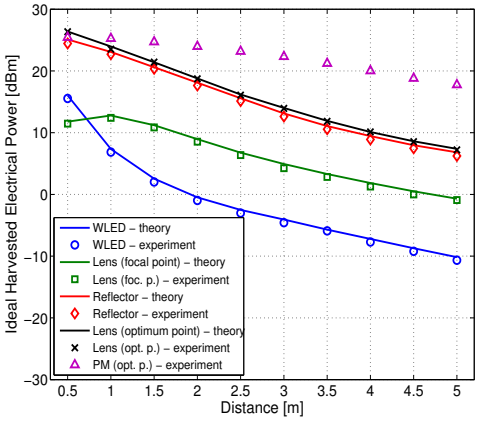

Fig. 3. $P_{\text{elec}}^{\text{ideal}}$ [dBm] vs. d [m] for an electrical power consumption of 18.3 W.

C. Study III

In this final study, we use the set-up of the transmitter that achieved the best performance in Study I and Study II. Different variable resistors are connected to the output of the solar cell. We modify the resistance, R_{L}, of each variable resistor in order to measure the current, I_{L}, and voltage, V_{L}, of the load. Finally, we calculate the actual harvested electrical power, $P_{\text{elec}}^{\text{L}}$, of the panel.

V. Results and Discussion

Fig. 3 presents the analytical and experimental results of Study I. The graphs labelled as "theory" are derived using (4)-(6) and (9)-(14). The system that uses the PCX lens located at its focal point exhibits an almost constant gain of 10 dB over the single-LED link for distances greater than 1.5 m. The spot-light reflector collects and transmits more rays from the WLED compared with the PCX lens due to its closed cone surface. The PCX lens placed at its focal point does not capture much light because of its small size and the wide semi-angle of half-power of the LED. To overcome the lens optical losses, the fourth experimental scenario of Study I was conducted. As a result, the light output of the lens increases, but the collimation or directivity of the beam decreases. A small gain of approximately 1.2 dB is achieved when the lens is located at its optimized position compared to the system with the reflector. The last scenario with the large PM attains the best performance. As the distance increases, the ideal harvested electrical power decreases with a lower rate of change compared to the other configurations. This is due to the increase in the effective surface area of the PM, *i.e.*, the paraboloid surface area that reflects the collected LED rays by the solar panel, that compensates the channel losses with increased distance. At a distance of 5 m the mirror exhibits a gain of 10.5 dB compared to the system with optimized lens positioning. Overall, at a distance of 5 m, the gain of the system with the PM is 28.4 dB compared to the single-LED link.

The results of Study II are illustrated in Fig. 4. The curve of the system using the parabolic reflector presents a greater rate of increase compared to the graphs of the other two systems. This means that the PM offers the greatest total maximum efficiency of all the EH systems. The scenario comprising the lens attains a gain of approximately 1.5 dB compared to the system with the reflector. The use of the large PM offers a performance superiority of about 10 dB and 11.5 dB in comparison with the other two systems.

Fig. 5 shows the experimental results and the fitted curves of Study III. Table II summarizes the measured values of the electrical parameters of Study III. Based on the measured data in Table II, we can calculate the values of $P_{\text{elec}}^{\text{in}}$, $P_{\text{elec}}^{\text{ideal}}$ and $P_{\text{elec}}^{\text{max}}$. In the low-power region of the LED, *i.e.*, $P_{\text{elec}}^{\text{in}} = 9.19$ W, we obtain $P_{\text{elec}}^{\text{ideal}} = 24.71$ mW and $P_{\text{elec}}^{\text{max}} = 7.69$ mW. The fill factor of the panel and the total maximum efficiency of the link are 31.12% and 0.084%, respectively. The resistor value at the maximum-power point of the panel is 1.43 kΩ. In addition, in the middle-power region of the WLED, *i.e.*, $P_{\text{elec}}^{\text{in}} = 18.3$ W, we find that $P_{\text{elec}}^{\text{ideal}} = 60.67$ mW and $P_{\text{elec}}^{\text{max}} = 18.32$ mW. It is also calculated that FF = 30.2% and $\eta_{\text{max}} = 0.1\%$. In this case, the measured load is $R_{\text{L}} = 2.07$ kΩ. A comparison of Tables I and II indicates that the measured values of the EH system with the PM are significantly lower than the respective data sheet electical characteristics of the solar panel. This can be explained by the fact that the spectral content of sun radiation is significantly wider than the visible spectrum of the WLED.

VI. Summary and Conclusions

The technology of VLC has been demonstrated to be able to provide high-speed data. While the communication capabilities have fairly well been investigated, a limited number of studies has been presented for the EH potential of

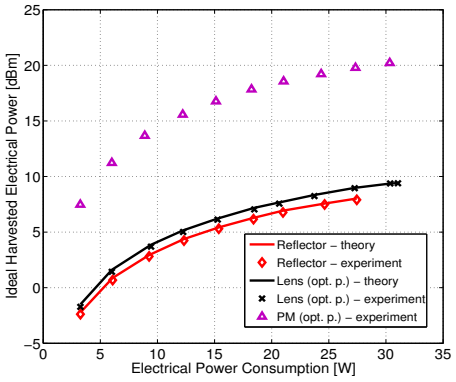

Fig. 4. $P_{\text{elec}}^{\text{ideal}}$ [dBm] vs. $P_{\text{elec}}^{\text{in}}$ [W] at a 5 m-distance.

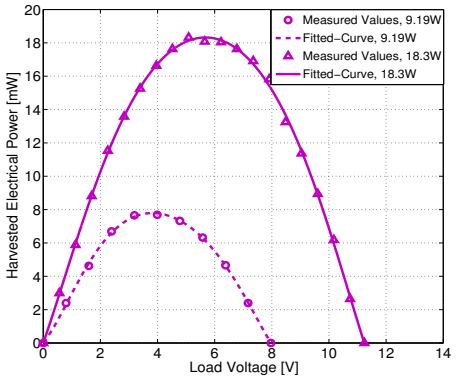

Fig. 5. $P_{\text{elec}}^{\text{L}}$ [mW] vs. V_{L} [V] using the PM at a 5 m-distance.

a VLC link. In this paper, we have, therefore, presented an analytical study accompanied by the respective experimental implementation of a visible-light link for EH. Three experimental studies were conducted using precise optics at the transmitter. An a-Si solar panel was used at the receiver. The PM provided the best solution for light collimation and EH. This fact was explained by the large paraboloid surface area that was able to collect and collimate the light rays of the WLED better than the lens and the reflector. However, even in this case, the harvested electrical power and the efficiency over the entire link were significantly low. This finding was attributed to both the Lambertian radiation pattern of the WLED and the considerably low energy efficiency of the a-Si solar panel. Future work will consider a design based on high-power lasers or laser arrays due to the high directivity and the compact dimensions they provide. Finally, the use of new solar-cell technologies of higher power efficiency will be studied.

TABLE II
MEASURED DATA OF STUDY III

V_{in} [V]	I_{in} [mA]	V_{oc} [V]	I_{sc} [mA]	V_{mp} [V]	I_{mp} [mA]
34.3	268	7.97	3.1	3.99	1.93
36.1	507	11.24	5.4	5.09	3.6

ACKNOWLEDGMENT

We acknowledge partial financial support by Bell Labs, Ireland. We would also like to thank Dr. Zixiong Wang for building the LED driver-circuit. Prof. Haas acknowledges support from the Engineering and Physical Sciences Research Council (EPSRC) under the Established Career Fellowship grant EP/K008757/1.

REFERENCES

[1] H. Claussen, L. T. Ho, and L. G. Samuel, "An Overview of the Femtocell Concept," *Bell Labs Tech. J.*, vol. 13, no. 1, pp. 221–245, 2008.
[2] W. Webb, *Wireless Communications: The Future*. John Wiley & Sons, 2007.
[3] R. Razavi and H. Claussen, "Urban Small Cell Deployments: Impact on the Network Energy Consumption," in *Proc. IEEE Wireless Commun. and Netw. Conf. Workshops (WCNCW)*, Paris, France, Apr. 1 2012, pp. 47–52.
[4] J. Andrews, H. Claussen, M. Dohler, S. Rangan, and M. Reed, "Femtocells: Past, Present, and Future," *IEEE J. Sel. Areas Commun.*, vol. 30, no. 3, pp. 497–508, Apr. 2012.
[5] V. Chandrasekhar, J. Andrews, and A. Gatherer, "Femtocell Networks: A Survey," *IEEE Commun. Mag.*, vol. 46, no. 9, pp. 59–67, 2008.
[6] H. Elgala, R. Mesleh, and H. Haas, "Indoor Optical Wireless Communication: Potential and State-of-the-Art," *IEEE Commun. Mag.*, vol. 49, no. 9, pp. 56–62, Sep. 2011, ISSN: 0163-6804.
[7] T. Komine and M. Nakagawa, "Fundamental Analysis for Visible–Light Communication System using LED Lights," *IEEE Trans. Consum. Electron.*, vol. 50, no. 1, pp. 100–107, Feb. 2004.
[8] D. Tsonev, S. Videv, and H. Haas, "Light Fidelity (Li-Fi): Towards All-Optical Networking," in *Proc. SPIE, Broadband Access Commun. Technol. VIII*, vol. 9007, Dec. 18 2013. [Online]. Available: http://dx.doi.org/10.1117/12.2044649
[9] I. Stefan, H. Burchardt, and H. Haas, "Area Spectral Efficiency Performance Comparison between VLC and RF Femtocell Networks," in *Proc. IEEE Int. Conf. Commun. (ICC)*, Budapest, Hungary, Jun. 9–13 2013, pp. 1–5.
[10] D. Tsonev, H. Chun, S. Rajbhandari, J. J. D. McKendry, S. Videv, E. Gu, M. Haji, S. Watson, A. E. Kelly, G. Faulkner, M. D. Dawson, H. Haas and D. O'Brien, "A 3-Gb/s Single-LED OFDM-based Wireless VLC Link Using a Gallium Nitride μLED," *IEEE Photon. Technol. Lett.*, vol. 26, no. 7, pp. 637–640, Apr. 2014.
[11] Z. Wang, D. Tsonev, S. Videv, and H. Haas, "Towards Self-Powered Solar Panel Receiver for Optical Wireless Communication," in *Proc. IEEE Int. Conf. Commun. (ICC)*, Sydney, Australia, Jun. 10–14 2014, pp. 1–6.
[12] A. Luque and S. Hegedus, Eds., *Handbook of Photovoltaic Science and Engineering*, 2nd ed. John Wiley & Sons, Mar. 2011.
[13] E. Schubert, *Light-Emitting Diodes*, 1st ed. Cambridge University Press, 2003, ISBN 0 521 82330 7.
[14] Bridgelux, "Bridgelux ES Rectangle Array Series Product Datasheet DS24," Retrieved Dec. 04, 2013 from http://www.farnell.com/datasheets/1504249.pdf, Nov. 2011.
[15] J. M. Kahn and J. R. Barry, "Wireless Infrared Communications," *Proc. IEEE*, vol. 85, no. 2, pp. 265–298, Feb. 1997.
[16] E. Diaz and M. Knobl, "Prototyping Illumination Systems with Stock Optical Components," Photonik International, 2012.
[17] E. Hecht, *Optics*, 3rd ed., ser. World student series edition. Addison-Wesley, 1998.

IEEE ICC 2015 - Workshop on Visible Light Communications and Networking (VLCN)

On the Design of a Free Space Optical Link for Small Cell Backhaul Communication and Power Supply

John Fakidis*, Stepan Kucera†, Holger Claussen† and Harald Haas*

*Institute for Digital Communications
Li-Fi Research and Development Centre
The University of Edinburgh
Edinburgh, EH9 3JL, UK
Email: {j.fakidis, h.haas}@ed.ac.uk

†Bell Laboratories, Alcatel-Lucent
Blanchardstown Business & Technology Park
Dublin 15, Ireland
Email: {stepan.kucera,
holger.claussen}@alcatel-lucent.com

***Abstract*—The concept of small cells (SCs) is widely acknowledged for its significant benefits in energy efficiency and capacity of heterogeneous cellular networks. However, a large scale outdoor installation of SCs is limited by cost factors. Therefore, wireless backhaul communication and wireless power supply to SCs could significantly reduce deployment costs. The focus of this paper is on the investigation of the use of free space optical (FSO) links for power transfer to SCs in an indoor environment. In particular, an experimental design of a red light link for wireless power transmission (WPT) and energy harvesting (EH) is presented in the absence of ambient light. The transmitter includes up to five laser diodes (LDs) with a typical output optical power of 50 mW per LD. Light collimation is achieved by the use of aspheric lenses. The receiver comprises a crystalline silicon (c-Si) solar panel placed at 5.2 m from the optical transmitter. The use of five pairs of LDs and lenses results in a maximum harvested power of 10.4 mW. This study shows that the number of optical transmitters required for the generation of an electrical power of 1 W (demanded for the operation of a SC) from the solar panel is estimated to be 110.**

I. Introduction

The technology of small cells (SCs) is widely accepted as one of the most promising solutions to the exponential increase in capacity demand in wireless cellular networks [1]. Although a large scale outdoor deployment of SCs is beneficial in terms of network capacity and power consumption [2], the high cost represents the main restrictive factor. Wireless backhaul communication and alternative sources of power supply can make the installation of SCs more cost effective.

A potential power supply source for SCs is based on the concept of wireless power transmission (WPT). Wireless power transmission for long distance links is attainable only by radio frequency (RF) or microwave and laser-based systems [3]. In the RF region, receivers for energy harvesting (EH) are typically diode-based circuits termed 'rectennas' [4]. In the visible light (VL) spectrum, the widely available and low cost receivers for EH are solar panels. Every photovoltaic (PV) panel comprises a number of solar cells. In an outdoor scenario with SCs, a natural resource, i.e., sunlight, can significantly contribute to the harvested power in VL-based EH, whereas only 'dedicated' RF antennas can be used for RF-based WPT. However, the variability of weather conditions significantly affects the amount of harvested power. Therefore, the worst-case scenario of WPT from a 'dedicated' laser-based source or RF antenna is considered to be a complementary and reliable solution.

The emerging field of visible light communications (VLC) has been proposed as a complementary technology to RF systems, and as a candidate solution to the exponential increase in demand in wireless data transmission [5]. The great potential of VLC links created by off-the-shelf light-emitting diodes (LEDs) has been shown by the feasible transmission data rates of up to 3 Gb/s [6]. The capabilities of a solar panel receiver for both high speed data communication and EH were investigated in [7]. Therefore, the main objective of this research is the design of VLC or free space optical (FSO) links able to provide backhaul communication and power to SCs.

An optical wireless link formed by a high brightness white LED (WLED) and a parabolic mirror was investigated as a potential solution for SC EH in [8]. However, the amount of electrical power (18.3 mW) harvested from an amorphous silicon (a-Si) solar panel was too low for the required power of a SC of about 1 W. Also, the maximum link efficiency was significantly low (0.1%). This research is a follow-up study of [8]. This paper focuses on the aspects of exclusive laser-based WPT and solar panel-based EH at a distance of 5.2 m in an indoor environment. In particular here, a high power red light laser diode (LD) is used as an optical source. The selected wavelength of 660 nm allows for a visible and therefore practically uncomplicated alignment of the link components. Also, the spectral responsivity of typical crystalline silicon (c-Si) solar cells takes larger values close to the red region of the VL spectrum [9]. The use of two different lenses is examined for best light collimation. A multi-crystalline silicon (mc-Si) PV panel is used at the receiver. An analytical model of the system is presented for identifying the best lens and the optimum distance from the LD for efficient WPT. A set of two experimental studies is conducted. The number of optical transmitters, i.e., pairs of LD-lens, scales from one to five. An estimation of the required number of optical transmitters is made for the achievement of 1 W of electrical power harvested from the receiver. The main contribution of this paper is the

978-1-4673-6305-1/15/$31.00 ©2015 IEEE

IEEE ICC 2015 - Workshop on Visible Light Communications and Networking (VLCN)

increase in the experimental maximum link efficiency by a significant factor of 7.4 for a $5.2\,\mathrm{m}$ link distance compared to the best result of our previous work [8].

The rest of the paper is organized as follows: Section II gives a physical system model. In Section III, the experimental set-up and studies are explained. In Section IV the results are summarized and discussed. Finally, Section V gives concluding remarks.

II. Analytical Model

The main components of the system implemented are LDs, lenses and a solar panel. The respective general analytical models for these are given in Sections II-A, II-B and II-C. Four important factors for the link efficiency are defined in Section II-D. The term 'far field' refers to the region further than the Rayleigh range introduced in Section II-A.

A. Single Laser Diode

In the far field, the relative optical intensity (or irradiance) versus the parallel and perpendicular to the junction angular divergence can be approximated by Gaussian curves of different widths [10]. Also, the selected LD operates at the fundamental transverse electrical (TE) mode. Therefore, an elliptical Gaussian beam propagation model is considered for the generated laser beam.

The Gaussian beam radii along the x- and y-direction are given by [11]:

$$W_{\mathrm{x}}(z) = W_{0\mathrm{x}}\sqrt{1+\left(\frac{z}{z_{0\mathrm{x}}}\right)^2}, \tag{1}$$

and:

$$W_{\mathrm{y}}(z) = W_{0\mathrm{y}}\sqrt{1+\left(\frac{z}{z_{0\mathrm{y}}}\right)^2}, \tag{2}$$

where $W_{0\mathrm{x}}$ is the beam waist radius along the x-axis; and $W_{0\mathrm{y}}$ is the beam waist radius along the y-axis. The values of $z_{0\mathrm{x}} = \pi W_{0\mathrm{x}}^2/\lambda_{\mathrm{p}}$ and $z_{0\mathrm{y}} = \pi W_{0\mathrm{y}}^2/\lambda_{\mathrm{p}}$ represent the Rayleigh range on the x- and y-axes, respectively. Quantity λ_{p} denotes the LD operating wavelength. At $z = z_{0\mathrm{x}}$ and $z = z_{0\mathrm{y}}$, the beam radius (or width) in the two transverse axes becomes $\sqrt{2}W_{0\mathrm{x}}$ and $\sqrt{2}W_{0\mathrm{y}}$, respectively. When $z \gg z_{0\mathrm{x}}$ and $z \gg z_{0\mathrm{y}}$, (1) and (2) can be transformed to:

$$W_{\mathrm{x}}(z) \simeq \frac{W_{0\mathrm{x}}}{z_{0\mathrm{x}}}z = \frac{\lambda_{\mathrm{p}}}{\pi W_{0\mathrm{x}}}z, \tag{3}$$

and:

$$W_{\mathrm{y}}(z) \simeq \frac{W_{0\mathrm{y}}}{z_{0\mathrm{y}}}z = \frac{\lambda_{\mathrm{p}}}{\pi W_{0\mathrm{y}}}z. \tag{4}$$

In the far field, the beam radii increase approximately linearly with z defining an elliptical cone of half angles:

$$\theta_{\mathrm{x}} = \tan^{-1}\left[\frac{W_{\mathrm{x}}(z)}{z}\right] \overset{(3)}{=} \tan^{-1}\left(\frac{\lambda_{\mathrm{p}}}{\pi W_{0\mathrm{x}}}\right), \tag{5}$$

and:

$$\theta_{\mathrm{y}} = \tan^{-1}\left[\frac{W_{\mathrm{y}}(z)}{z}\right] \overset{(4)}{=} \tan^{-1}\left(\frac{\lambda_{\mathrm{p}}}{\pi W_{0\mathrm{y}}}\right). \tag{6}$$

The defined half angles θ_{x} and θ_{y} are termed beam divergences in the x- and y-direction, respectively.

The q-parameters of the Gaussian beam in the x- and y-directions are described by [11]:

$$\frac{1}{q_{\mathrm{x}}(z)} = \frac{1}{R_{\mathrm{x}}(z)} - j\frac{\lambda_p}{\pi W_{\mathrm{x}}^2(z)}, \tag{7}$$

and:

$$\frac{1}{q_{\mathrm{y}}(z)} = \frac{1}{R_{\mathrm{y}}(z)} - j\frac{\lambda_p}{\pi W_{\mathrm{y}}^2(z)}, \tag{8}$$

where $R_{\mathrm{x}}(z)$ and $R_{\mathrm{y}}(z)$ denote the radii of curvature in the axes of the transverse plane. Radii of curvature are described by the relationships:

$$R_{\mathrm{x}}(z) = z\left[1+\left(\frac{z_{0\mathrm{x}}}{z}\right)^2\right], \tag{9}$$

and:

$$R_{\mathrm{y}}(z) = z\left[1+\left(\frac{z_{0\mathrm{y}}}{z}\right)^2\right]. \tag{10}$$

B. Free Space and Aspheric Lens

A convenient method to relate the input and output of an optical system is the use of ray transfer or $ABCD$ matrices [11]. The method of $ABCD$ matrices is also widely used in microwave communications [12]. In matrix optics, a simple 2×2 matrix connects the position and angle of paraxial rays at the input and output plane of an optical system through linear algebraic equations. Note that the application of $ABCD$ law to a Gaussian beam connects the q-parameters of the beam.

The $ABCD$ matrix of free space between the LD and the lens placed at a distance d_0 is:

$$\mathbf{M}_1 = \begin{bmatrix} 1 & d_0 \\ 0 & 1 \end{bmatrix}. \tag{11}$$

If a collimating lens is placed at its focal point as specified in the respective data sheet, the distance between the emission point of the source and input lens surface is termed back focal distance (BFD), and is given by [13]:

$$\beta = f\left[1-\frac{t_{\mathrm{c}}(n-1)}{nR_1}\right], \tag{12}$$

where quantity f denotes the effective focal length (EFL); t_{c} represents the thickness; and n is the refractive index of the lens material. Parameter R_1 denotes the radius of curvature of the input side of the lens.

The back surface of the aspheric lens is considered to be spherical. This assumption provides a worst-case scenario for the lens model. The elements of the $ABCD$ matrix for a thick lens, $\mathbf{M}_{\mathrm{lens}}$, with two spherical surfaces of different radii of curvature are given below [13]:

$$A' = 1-\frac{t_{\mathrm{c}}(n-1)}{nR_1}, \tag{13}$$

$$B' = \frac{t_{\mathrm{c}}}{n}, \tag{14}$$

$$C' = -(n-1)\left(\frac{1}{R_1}-\frac{1}{R_2}\right) - \frac{t_{\mathrm{c}}(n-1)^2}{nR_1R_2}, \tag{15}$$

$$D' = 1+\frac{t_{\mathrm{c}}(n-1)}{nR_2}. \tag{16}$$

The value of R_2 denotes the radius of curvature of the output side of the lens.

Finally, the $ABCD$ matrix of free space between the output of the lens and the incidence plane to the solar panel is calculated by:

$$\mathbf{M}_2 = \begin{bmatrix} 1 & d-(d_0+t_c) \\ 0 & 1 \end{bmatrix}, \tag{17}$$

where d is the distance between the LD emission point and the solar panel. Therefore, the system $ABCD$ matrix can be written as the product of ray transfer matrices of individual components:

$$\mathbf{M} = \mathbf{M}_2\mathbf{M}_{\text{lens}}\mathbf{M}_1. \tag{18}$$

The general $ABCD$ matrix, $\mathbf{M}$, is applied to the elliptical Gaussian beam using the transformation [11]:

$$q_{\text{out}} = \frac{Aq_{\text{in}} + B}{Cq_{\text{in}} + D}, \tag{19}$$

where q_{in} and q_{out} denote the q-parameters of the Gaussian beam at the LD emission point ($z = 0$) and the input plane of the panel, respectively, either on the x- or y-axis.

C. Solar Panel

The selected solar panel consists of N_{C} cells connected in series. An effective single solar cell equivalent circuit for two or more cells connected in series is proposed in [14]. Also, a variable resistor, R_{L}, is connected to the output of the panel. A transcendental relationship between the load current, I_{L}, and voltage, V_{L}, describes the electrical behavior of the panel as given in [14]:

$$I_{0,\text{eff}}\left\{\exp\left[\frac{q}{A_{\text{eff}}k_{\text{B}}T}\left(V_{\text{L}} - R_{\text{S,eff}}I_{\text{L}}\right)\right] - 1\right\} + \\ + \frac{V_{\text{L}} - R_{\text{S,eff}}I_{\text{L}}}{R_{\text{P,eff}}} - I_{\text{Ph, eff}} - I_{\text{L}} = 0. \tag{20}$$

The physical constants $q = 1.602\times10^{-19}\,\text{C}$ and $k_{\text{B}} = 8.617\times10^{-5}\,\text{eV/K}$ represent the electron charge and Boltzmann constant, respectively. The temperature of the panel, T, is assumed to be $298\,\text{K}$. This model includes five unknown parameters, i.e., $I_{0,\text{eff}}$, $R_{\text{S,eff}}$, A_{eff}, $R_{\text{P,eff}}$ and $I_{\text{Ph,eff}}$. These parameters are strongly dependent on the values of optical power received from the panel. The value of $I_{0,\text{eff}}$ represents the effective dark saturation current of the diode. Parameters $R_{\text{S,eff}}$ and $R_{\text{P,eff}}$ denote the effective series and parallel resistance, respectively. The resistance R_{L} is considered to be part of $R_{\text{S,eff}}$. The size $I_{\text{Ph,eff}}$ is the effective generated photocurrent. The electrical power, P_{L}, harvested from the load resistor is given by $P_{\text{L}} = V_{\text{L}}I_{\text{L}}$. A simple 'exhaustive' search algorithm with discrete search space is implemented in order to estimate the five unknown parameters of the solar panel. The first part of (20) is the objective function of the problem, and is minimized. Then, the five identified parameters are applied to the model for curve fitting of the experimental data. The experimental measurements of I_{L} and V_{L} are used for finding a local solution to the non-linear curve-fitting problem.

TABLE I
FEATURES OF THE LASER DIODE

P_{typ} [mW]	λ_{p} [nm]	$\vartheta_{\parallel}$ [mrad]	$\vartheta_{\perp}$ [mrad]
50	660	174.5 (10°)	296.7 (17°)

D. Link Efficiency

An important aspect of the technology of WPT and EH is the total efficiency of a link. The external power efficiency of a LD can be defined as:

$$\eta_{\text{LD}} = \frac{P_{\text{Tx,o}}}{P_{\text{in}}} \times 100\%, \tag{21}$$

where $P_{\text{Tx,o}}$ denotes the output optical power of the LD and P_{in} is the direct current (DC) input electrical power. The fill factor (FF) of a solar panel shows how well the circuit approximates the ideal behaviour of a current source. The FF of a PV panel is given by [9]:

$$\text{FF} = \frac{V_{\text{m}}I_{\text{m}}}{V_{\text{oc}}I_{\text{sc}}} \times 100\%, \tag{22}$$

where V_{oc} and I_{sc} denote the open-circuit voltage and short-circuit current, respectively. Also, V_{m} and I_{m} represent the voltage and current at the maximum-power point (MPP) of the panel, respectively. The optical-to-electrical conversion efficiency or responsivity of the panel can be defined as:

$$\rho = \frac{I_{\text{Ph,eff}}}{P_{\text{Rx,o}}}, \tag{23}$$

where $P_{\text{Rx,o}}$ denotes the received optical power from the PV panel. Finally, the maximum link efficiency is computed by:

$$\eta_{\text{max}} = \frac{P_{\text{m}}}{P_{\text{in}}} \times 100\%, \tag{24}$$

where P_{m} denotes the maximum electrical power, and is given by: $P_{\text{m}} = V_{\text{m}}I_{\text{m}}$.

III. EXPERIMENTAL MODEL

Physical dimensions, and the electrical and optical characteristics of the components used are given in Section III-A. The objectives of each experimental study and the system set-up are explained in Section III-B.

A. System Components

A single mode Opnext HL6544FM high power LD with a multi-quantum well (MQW) structure is used as an optical source for WPT [10]. The semiconductor material of the LD is aluminium gallium indium phosphide (AlGaInP). Table I gives the data sheet values of the main features for this light source. Size P_{typ} denotes the typical value of output optical power. Angles $\vartheta_{\parallel}$ and $\vartheta_{\perp}$ refer to the full width at half maximum (FWHM) intensity in parallel and perpendicular plane to the junction, respectively.

The relatively large angular divergence of the optical source requires the use of a precise lens for light collimation. Although lenses with spherical surfaces are low cost and are relatively uncomplicated to manufacture, they have spherical aberrations [13]. This inherent defect of spherical lenses prevents

IEEE ICC 2015 - Workshop on Visible Light Communications and Networking (VLCN)

TABLE II
CHARACTERISTICS OF THE ASPHERIC LENSES

Part Number	R_1 [mm]	R_2 [mm]	t_c [mm]	f [mm]	r (%)
ACL12708U-A	15.65	−4.753	7.5	8.02	0.25
ACL4532	130	−18.281	18.5	32	10

efficient light collimation. In contrast, the complex geometry of aspheres allows for correction of spherical aberration and creates collimated beams of better quality [13]. Therefore, two aspheric condenser lenses are used in the experiments. The first condenser lens is an ACL12708U-A with anti-reflection (AR) coating and a diameter of 1.3 cm. The second lens is a 4.5 cm uncoated ACL4532. Table II gives the main features of both aspheres extracted from their respective data sheets [15], [16]. Quantities R_1, R_2, t_c and f have already been defined in Section II-B. The value of r (%) represents the reflectance of lens. The refractive index of the lens material is 1.52.

Finally, a SX 305 PV panel is used as the optical receiver for EH [17]. This solar panel comprises 36 mc-Si cells with silicon nitride (Si_3N_4) AR coating. The cells are placed in the form of a 4×9 matrix and are connected in series. The total effective area of the panel is $17.1 \times 22.8\,\text{cm}^2$. A maximum possible efficiency of 11.54% can be assumed from [17].

B. Experimental Studies

A series of two experimental studies is conducted in order to determine the maximum possible electrical power harvested from the solar panel. Load resistance is modified for the measurement of 21 pairs of (V_L, I_L) for every experimental scenario. Load voltage and current have values in the range of $[0, V_{oc}]$ and $[0, I_{sc}]$, respectively. The link distance is 5.2 m. Note that ambient light coming from the room luminaires contributes to the harvested power in the first study, and is ensured to be negligible in the second one.

1) Study I: Two experimental scenarios are implemented in the first study. A single pair of LD-lens is used in these scenarios. Also, the PV panel area is 'overfilled' with the red laser beam (the elliptical beam illuminates the total area of the rectangular panel and a small region around it). Note that the LD-lens distance (d_0) is set to be the optimum one to maximize the output power of the panel. The transmitter comprises the 4.5 cm lens placed at 2.6 cm from the LD in the first scenario. The second scenario is realized by the use of the 1.3 cm lens at 3.75 mm from the LD. An illustration of this scenario is given in Fig. 1(a).

2) Study II: This study consists of six different experimental scenarios. A lens with a diameter of 1.3 cm is used in all of these scenarios. From each of the first to fifth scenarios, the number of LD-lens pairs, N_{Tx}, scales from one to five, respectively. Laser diodes are connected in parallel. Distance d_0 for all of the LD-lens pairs is equal to 3.8 mm with a tolerance of ± 0.2 mm. Different laser beams 'overfill' the same total area of the panel. The fifth scenario implemented is shown in Fig. 1(b). The sixth scenario is realized by the use of five pairs of LD-lens. The only difference with the fifth scenario is that the optical transmitters point the laser beams at different regions of the solar panel. Therefore, different cells are illuminated by the five optical sources in this case.

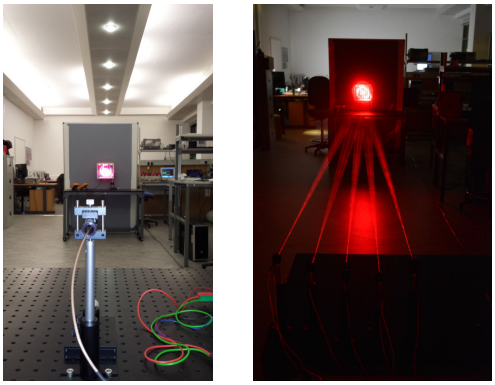

(a) Second scenario of Study I. (b) Fifth scenario of Study II.

Fig. 1. Experimental red light laser links for WPT to a mc-Si-based panel at a distance of 5.2 m (a) with ambient light, and (b) without ambient light.

IV. RESULTS AND DISCUSSION

Essential parameters for the LD are calculated in Section IV-A. Analytical results are given in Section IV-B. The experimental results of the two studies are presented in Section IV-C. Finally, an estimation of the number of required LDs for harvesting 1 W of electrical power from the panel is presented in Section IV-D according to the physical model.

A. Calculation of the Laser Diode Parameters

In the far field pattern diagram from [10], the parallel and perpendicular to the junction beam divergences corresponding to the full width at 0^{th} intensity point are $2\theta_x = 40° = 698.13$ mrad and $2\theta_y = 80° = 1.4$ rad, respectively. The elliptical cone defined from these values of angular divergence contains 100% of the optical power. Solving (5) and (6) for W_{0x} and W_{0y}, respectively, results in: $W_{0x} = \lambda_p/[\pi \tan(\theta_x)] = 660/[\pi \tan(20°)] = 577.2$ nm, and $W_{0y} = \lambda_p/[\pi \tan(\theta_y)] = 660/[\pi \tan(40°)] = 250.37$ nm. Therefore, the rectangular cross section of the MQW laser source has the dimensions of $w = 2W_{0x} = 1.15\,\mu$m, and $l = 2W_{0y} = 500.74\,\text{nm} \simeq 0.5\,\mu$m. The Rayleigh range in the x- and y- axis is calculated to be: $z_{0x} = \pi(577.2^2 \times 10^{-9})/660 = 1.586\,\mu$m, and $z_{0y} = \pi(250.37^2 \times 10^{-9})/660 = 0.298\,\mu$m, respectively. An output optical power $P_{Tx,o} = 62.6$ mW of the LD can be computed for a forward current of 120 mA from [10]. Therefore, for a DC input power $P_{in} = 282$ mW, the external power efficiency of the LD is $\eta_{LD} = 22.2\%$.

B. Analytical Results

An illustration of the Gaussian beam radii in the axes of x and y as a function of distance for five theoretical scenarios is shown in Fig. 2. These curves are derived using (3), (4) and (7)-(19). The system performance criterion is the collection of 100% of optical power from the solar panel.

Light collimation is improved in both axes by the addition of any of the two (1.3 cm or 4.5 cm) lenses compared to the non-collimated scenario (single LD). In the cases of setting the lenses at their focal points (pairs of orange and magenta

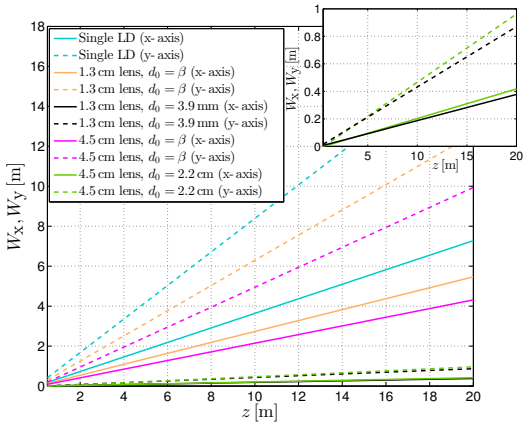

Fig. 2. Theoretical illustration of W_x, W_y [m] vs. z [m].

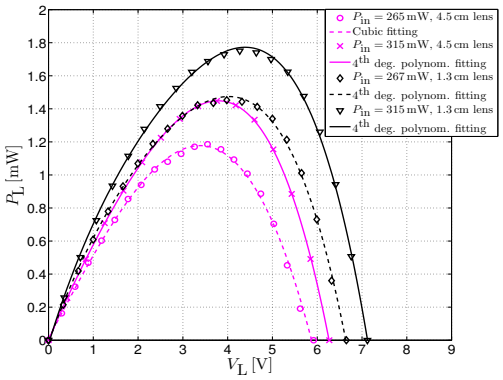

Fig. 3. Experimental V-P curves of Study I.

lines), the scenario of the 4.5 cm lens achieves better light transmission than that of the 1.3 cm one. This effect can be attributed to the longer radii of curvature of ACL4532 (see Table II) resulting in larger beam waists and Rayleigh ranges. A similar performance is attained for the lens-based scenarios (pairs of black and green lines), when the lenses are placed at the distances of 3.9 mm and 2.2 cm from the LD, respectively. Most importantly, it is observed that light collimation is further improved when either of the two aspheric lens is placed out of its focus and much closer to the LD. This is because the laser beam uses a smaller lens surface and the marginal rays are better collimated when focusing at larger distances. This theoretical effect indicates that in the experimental links the LD-lens distances should be set close to the theoretical values of 3.9 mm and 2.2 cm.

C. Experimental Results and Curve Fitting

The experimental data of (V_L, P_L) for Study I are shown in Fig. 3. Basic polynomial curve fitting is applied to each set of measurements. In terms of maximum harvested power, a gain factor of 1.2 is attained by the last scenario (black solid line) compared to the first one (magenta solid line) when the dissipated power at the transmitter is 315 mW. This finding is explained by the fact that the uncoated 4.5 cm lens attenuates the transmitted optical power to the solar panel more than the AR-coated 1.3 cm lens. This difference is also noticeable in the reflectance values of lenses, as presented in Table II.

The experimental results of Study II are given in Fig. 4. The curves labelled as 'physical model' are derived using (20). The values of FF and η_{max} measured for all of the six experimental scenarios are shown in Table III. Generally, the values of FF denote a low energy efficiency of the panel. This is attributed to both the low irradiance levels received as well as mismatch losses of the cells. As long as the irradiance distribution of the laser beam is elliptical and Gaussian, the cells placed at the edges of the PV panel are illuminated with lower optical power compared with the centrally-placed cells. Power generated by

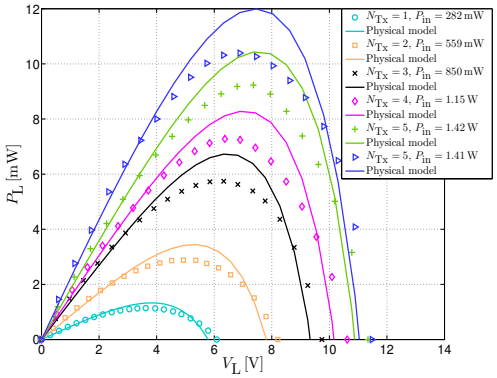

Fig. 4. Experimental V-P curves of Study II.

cells with higher illumination levels can be dissipated by cells with lower irradiance levels instead of the load. Therefore, the electrical output of the entire panel is determined by the cells with the lowest performance. The increase in η_{max} with the number of LDs used is due to a respective increase in the solar panel efficiency. However, this trend is not confirmed by scenarios 4 and 5. This can be explained by imperfections induced from the implementation of the optical transmitters. Although the best measured value of $\eta_{max} = 0.74\%$ is very low, note that the maximum possible is 2.56% for the components used ($22.2\% \times 11.54\% = 2.56\%$). This theoretical upper bound can be approximated by increasing N_{Tx}. The estimated values of the five solar panel unknown parameters for the six scenarios are given in Table IV. These five parameters scale with an increase in $P_{Rx,o}$ due to a respective increase in N_{Tx}, and this is in agreement with [18].

TABLE III
MEASURED FILL FACTOR AND MAXIMUM LINK EFFICIENCY

Scenario	1	2	3	4	5	6
FF(%)	34.4	34.7	37	39.3	38.7	36.2
$\eta_{\max}$ (%)	0.4	0.52	0.67	0.63	0.65	0.74

TABLE IV
ESTIMATED UNKNOWN PARAMETERS OF THE SOLAR PANEL

Scenario	$I_{0,\text{eff}}$ [µA]	$R_{\text{S,eff}}$ [Ω]	A_{eff}	$R_{\text{P,eff}}$ [kΩ]	$I_{\text{Ph, eff}}$ [mA]
1	117.3	1500	120	32	0.47
2	103.9	950	125	35.5	0.86
3	115.8	850	135	38	1.4
4	111.8	750	140	40.5	1.5
5	116.9	650	145	41.5	1.8
6	229.2	600	175	42	2.2

D. Estimation of the Number of Optical Transmitters

Let $N_{\text{Tx,req}}$ be the required number of pairs of LDs and lenses for $P_{\text{m}} = 1\,\text{W}$ at $d = 5.2\,\text{m}$. In scenario 6 (five optical transmitters), a value of $V_{\text{m}} = 6.89\,\text{V}$ is achieved with $P_{\text{m}} = 10.39\,\text{mW}$. Therefore, a maximum possible value of $V_{\text{m}} = 16.5\,\text{V}$ can be assumed for the solar panel at high illumination levels for attaining $P_{\text{m}} = 1\,\text{W}$ according to [17]. The load current at MPP is calculated to be $I_{\text{m}} = 1/16.5 = 60.6\,\text{mA}$. The values of $16.5\,\text{V}$ and $60.6\,\text{mA}$ are substituted for V_{L} and I_{L}, respectively, in (20). Then, the application of the 'exhaustive' search algorithm to (20) results in the following set of parameters: $(1.1\,\text{mA}, 0.1\,\Omega, 290, 90\,\text{k}\Omega, 69.1\,\text{mA})$. The responsivity of the solar panel is assumed to be $\rho = 0.01\,\text{mA/mW}$. Solving (23) for $P_{\text{Rx,o}}$ results in: $P_{\text{Rx,o}} = I_{\text{Ph,eff}}/\rho = 69.1/0.01 = 6.91\,\text{W}$. The total amount of optical power is considered to be received from the panel, i.e., $P_{\text{Rx,o}} = N_{\text{Tx,req}} P_{\text{Tx,o}}$. Therefore, the required number of optical transmitters is calculated to be: $N_{\text{Tx,req}} = P_{\text{Rx,o}}/P_{\text{Tx,o}} = 6.91/(62.6 \times 10^{-3}) \approx 110$.

V. SUMMARY AND CONCLUSIONS

The great potential of high speed data transmission for VLC systems has been extensively researched and demonstrated. However, the two-fold objective of simultaneous data communication and WPT in the optical domain remains an unexplored research area. Therefore, the capabilities of a red light laser-based link for WPT and EH from an off-the-shelf mc-Si solar panel were investigated in this study. In particular, the performance of two aspheric lenses was experimentally compared for best light collimation. Also, an analytical model was used to identify the optimum distance between light source and lens. A second experimental study was conducted using one to five pairs of LD and lens, i.e., optical transmitters, in an indoor environment in the absence of ambient light. The maximum link efficiency attained from five optical transmitters was $0.74\,\%$, and the respective maximum harvested power was $10.4\,\text{mW}$ for a link distance of $5.2\,\text{m}$. These values were too low for the required power of a SC of $1\,\text{W}$. This effect was explained by the low levels of optical power received and also mismatch losses among cells of the panel. An estimated number of 110 optical transmitters was required for harvesting $1\,\text{W}$ from the panel. While currently the overall link efficiency and harvested power are in the order of 1% and a few mW, respectively, the contribution of power from ambient light remains unexploited in this context. Future work will consider a larger number of LDs with higher power efficiency in order to increase the solar panel efficiency and the maximum link efficiency.

ACKNOWLEDGMENT

We acknowledge partial financial support by Bell Labs, Alcatel-Lucent Ireland. Professor Haas acknowledges support from the Engineering and Physical Sciences Research Council (EPSRC) under the Established Career Fellowship grant EP/K008757/1.

REFERENCES

[1] H. Claussen, L. T. Ho, and L. G. Samuel, "An Overview of the Femtocell Concept," *Bell Labs Tech. J.*, vol. 13, no. 1, pp. 221–245, 2008.
[2] R. Razavi and H. Claussen, "Urban Small Cell Deployments: Impact on the Network Energy Consumption," in *Proc. IEEE Wireless Commun. and Netw. Conf. Workshops (WCNCW)*, Paris, France, Apr. 1 2012, pp. 47–52.
[3] C. R. Valenta and G. D. Durgin, "Harvesting Wireless Power: Survey of Energy-Harvester Conversion Efficiency in Far-Field Wireless Power Transfer Systems," *IEEE Microw. Mag.*, vol. 15, no. 4, pp. 108–120, May 2014.
[4] U. Olgun, C.-C. Chen, and J. Volakis, "Investigation of Rectenna Array Configurations for Enhanced RF Power Harvesting," *IEEE Antennas Wireless Propag. Lett.*, vol. 10, pp. 262–265, Apr. 2011.
[5] H. Elgala, R. Mesleh, and H. Haas, "Indoor Optical Wireless Communication: Potential and State-of-the-Art," *IEEE Commun. Mag.*, vol. 49, no. 9, pp. 56–62, Sep. 2011.
[6] D. Tsonev, H. Chun, S. Rajbhandari, J. McKendry, S. Videv, E. Gu, M. Haji, S. Watson, A. Kelly, G. Faulkner, M. Dawson, H. Haas, and D. O'Brien, "A 3-Gb/s Single-LED OFDM-Based Wireless VLC Link Using a Gallium Nitride μLED," *IEEE Photon. Technol. Lett.*, vol. 26, no. 7, pp. 637–640, Apr. 2014.
[7] Z. Wang, D. Tsonev, S. Videv, and H. Haas, "On the Design of a Solar-Panel Receiver for Optical Wireless Communications with Simultaneous Energy Harvesting," *IEEE J. Sel. Areas Commun.*, vol. PP, no. 99, pp. 1–1, 2015.
[8] J. Fakidis, M. Ijaz, S. Kucera, H. Claussen, and H. Haas, "On the Design of an Optical Wireless Link for Small Cell Backhaul Communication and Energy Harvesting," in *Proc. IEEE 25th Int. Symp. Pers. Indoor and Mobile Radio Commun. (PIMRC)*, Washington, DC USA, Sep. 2–5 2014, pp. 32–36.
[9] A. Luque and S. Hegedus, Eds., *Handbook of Photovoltaic Science and Engineering*, 2nd ed. John Wiley & Sons, Mar. 2011.
[10] Opnext, "HL6544FM Visible High Power Laser Diodes," Retrieved May 19, 2014 from http://www.thorlabs.de/thorcat/21700/HL6544FM-MFGSpec.pdf, Mar. 2009.
[11] B. E. A. Saleh and M. C. Teich, *Fundamentals of Photonics*, 1st ed., ser. Wiley Series in Pure and Applied Optics. John Wiley & Sons, Inc., Jan. 1991.
[12] D. M. Pozar, *Microwave Engineering*, 4th ed., A. Melhorn, Ed. John Wiley & Sons, Dec. 2011.
[13] E. Hecht, *Optics*, 4th ed., A. Black, Ed. Addison-Wesley, 2002.
[14] A. Bauer, J. Hanisch, and E. Ahlswede, "An Effective Single Solar Cell Equivalent Circuit Model for Two or More Solar Cells Connected in Series," *IEEE J. Photovolt.*, vol. 4, no. 1, pp. 340–347, Jan. 2014.
[15] Thorlabs, "ACL12708U-A - Aspheric Condenser Lens, AR-Coated 350-700 nm, 1/2", f=8 mm," Retrieved May 22, 2014 from http://www.thorlabs.de/thorcat/CTN/ACL12708U-A-AutoCADPDF.pdf, Nov. 2013.
[16] ——, "ACL4532 - Aspheric Condenser Lens, 45 mm, f=32 mm, NA=0.612, Uncoated," Retrieved May 30, 2014 from http://www.thorlabs.de/thorcat/19000/ACL4532-AutoCADPDF.pdf, Sep. 2009.
[17] BP Solar, "BP Solar SX 305 5W PV Module," Retrieved June 4, 2014 from http://www.omniinstruments.co.uk/images/downloads/3353.pdf, Jul. 2007.
[18] A. Ortiz-Conde, D. Lugo-Munoz, and F. J. Garcia-Sanchez, "An Explicit Multiexponential Model as an Alternative to Traditional Solar Cell Models with Series and Shunt Resistances," *IEEE J. Photovolt.*, vol. 2, no. 3, pp. 261–268, Jul. 2012.

3236 JOURNAL OF LIGHTWAVE TECHNOLOGY, VOL. 34, NO. 13, JULY 1, 2016

Indoor Optical Wireless Power Transfer to Small Cells at Nighttime

John Fakidis, *Student Member, IEEE*, Stefan Videv, Stepan Kucera, *Senior Member, IEEE*, Holger Claussen, *Senior Member, IEEE*, and Harald Haas, *Member, IEEE*

***Abstract*—The application of wireless backhaul communication and power transfer to outdoor small cells (SCs) could significantly decrease their installation cost. In this paper, the concept of indoor optical wireless power transfer to SCs is investigated in the absence of ambient light, i.e., during darkness hours. An experimental study is conducted by the use of up to four red laser diodes (LDs), a crystalline silicon solar panel and cell placed at 5.2 m. A value of 69% is measured for the fill factor of the solar panel. Also, a total power efficiency of 3.2% is measured for an optical wireless (OW) link with an average efficiency of two LDs of 26.8%, a solar cell efficiency of 13.3% and only 10.6% of geometrical losses. A comparison of this link with a state-of-the-art inductive power transfer system shows an improvement of the total power efficiency by 2.7 times. Another OW link is implemented with a divergence of full width at 36.8% of the peak intensity of 3 and 5.75 mrad along the small and large axes of the beam, respectively. The experimental levels of harvested power are in the order of mW, whereas approximately 1 W is required for the operation of a SC. Therefore, a 42 laser-based transmitter is designed both analytically and by the use of the simulation tool Zemax. The respective results show the feasibility of delivering 7.2 W of optical power to a solar cell of up to 30 m distance with geometrical losses of only 2%, but a beam enclosure is also required due to eye safety restrictions.**

***Index Terms*—Diode lasers, energy efficiency, energy harvesting (EH), laser beams, optical wireless power transfer (OWPT), quantum well lasers, radio frequency (RF), rectennas, small cells (SCs), solar energy.**

I. Introduction

THE principle of small cells (SCs) is widely accepted as one of the solutions with most potential to the exponential increase in capacity demand of heterogeneous mobile networks [1]. Despite the fact that a large scale outdoor deployment of SCs offers advantages such as high network capacity [2] and reduced power consumption [3], the high installation cost is the most restrictive factor. The technology of optical fibers is considered to be one of the potential solutions to the provision of high speed backhaul communication to SCs [4]. However, the main disadvantages are the installation cost and the requirement for a mains power supply. Therefore, alternative sources of power supply and wireless backhaul communication can make the deployment of SCs more cost effective.

The concept of energy harvesting (EH) or power harvesting (PH) from natural resources, such as sun and wind, [5] as an alternative source of power supply has the main disadvantage of the variability of weather conditions. Therefore, the technology of wireless power transfer (WPT) from artificial electromagnetic (EM) sources has been proposed as a complementary and reliable solution. The concept of WPT was inspired and demonstrated for the first time by Nikola Tesla in the late 19th century using a radio frequency (RF) resonant transformer, termed a Tesla coil [6]. The application of WPT is also feasible using devices operating at the visible light (VL) and infrared part of the EM spectrum, such as laser diodes (LDs) or light-emitting diodes (LEDs) and solar cells. The concept in the optical domain is termed optical wireless power transfer (OWPT).

The research field of optical wireless communications (OWC) has been proposed as a complementary technology to RF data communication and as a potential solution to the exponential increase in demand for wireless data transmission [7]. The broad research field of OWC can be separated into two parts: free space optical (FSO) communications and visible light communications (VLC). Free space optical systems mostly comprise coherent data transmission using lasers at the transmitter and photodiodes (PDs) at the receiver. Also, FSO systems are usually deployed outdoors covering distances of several kilometers. Visible light communications facilitate the use of LEDs and PDs and are mainly applied to indoor public places such as offices, conference venues, museums, hotels and hospitals.

The objective is to investigate the simultaneous application of OWPT for the provision of 1 W and high speed FSO backhaul communication to outdoor SCs. However, as a first step, in this comprehensive study, research is focused on the indoor OWPT to SCs at nighttime. The conditions of darkness are selected because the system should also work when there is no ambient light to harvest. A set of three studies is reported in this paper. In Study I, a small number of LDs is used for optical power transmission in the order of mW to observe how the solar receiver efficiency scales with the input optical power. According to that result and a physical model, an estimation of the number of LDs required to achieve 1 W of harvested power is made. However, since the experimental distance in Study I

Manuscript received December 11, 2015; revised March 07, 2016; accepted April 05, 2016. Date of publication April 20, 2016; date of current version June 22, 2016. This work was supported in part by the Bell Labs, Nokia Ireland. The work of H. Haas was supported by the Engineering and Physical Sciences Research Council under the Established Career Fellowship Grant EP/K008757/1. Part of the material in this paper was presented at the IEEE International Conference on Communication Workshops, London, U.K., Jun. 8, 2015.

J. Fakidis, S. Videv, and H. Haas are with the Li-Fi Research and Development Centre, Institute for Digital Communications, School of Engineering, University of Edinburgh, Edinburgh EH9 3JL, U.K. (e-mail: j.fakidis@ed.ac.uk; s.videv@ed.ac.uk; h.haas@ed.ac.uk).

S. Kucera and H. Claussen are with the Bell Laboratories, Nokia, Blanchardstown Business & Technology Park, Dublin 15, Ireland (e-mail: stepan.kucera@nokia.com; holger.claussen@nokia.com).

Color versions of one or more of the figures in this paper are available online at http://ieeexplore.ieee.org.

Digital Object Identifier 10.1109/JLT.2016.2555883

is only 5.2 m and the concept of power supply to SCs refers to practical link distances of 100 m−300 m, we need to affirm that the optical wireless (OW) link operates at longer distances. For this reason, Study II is undertaken for the determination of laser beam divergence. A targeted beam divergence of 1 mrad is considered because the beam diameter is only 10 cm at 100 m, assuming the LD to be a point source. Therefore, the geometrical losses of such a laser link could be compensated by the use of a receiver with a large aperture. The estimated number of LDs required for harvesting 1 W is 61, as shown in Study I. Therefore, in Study III a multiple laser transmitter is designed to transfer wirelessly 7.2 W of optical power to the solar cell that achieved the highest efficiency in Study I. However, in Study III a number of 42 LDs with collimation lenses are simulated, since they transmit higher levels of power than the LDs considered in Study I.

A. Study I: Total Link and Components Efficiency

The implemented OWPT links operate at a distance of 5.2 m in order to compare metrics of electrical performance (such as total power efficiency and harvested power) with the respective parameters measured in [8]–[10]. A solar panel and a single solar cell are used in the experiments. Also, a physical model is developed for the propagation of an elliptical Gaussian beam through a lens to free space and is used to obtain the laser classification and to determine the irradiance limits for eye safety [11]. An effective single diode physical model of the solar panel [12] is presented and applied to the experimental data for curve fitting. Most importantly, the analytical models are used to estimate the number of optical transmitters required to achieve 1 W of harvested power. Since the total link efficiency is a function of the efficiency of the components, the efficiency of the LDs and solar cell is measured to determine the geometrical losses. The performance of this link in terms of total efficiency is fairly compared with a state-of-the-art inductive power transfer system (IPTS) with optimally shaped dipole coils [10]; this shows an improvement by 2.7 times. The maximum harvested power is measured to be only 25.7 mW; and an estimated number of 61 LDs and lenses is shown to be required for harvesting 1 W.

B. Study II: Laser Beam Collimation

In Study II, a single LD is used with a large lens for light collimation. Also, the physical model of the Gaussian beam propagation developed in Study I is applied to the experimental measured points of irradiance. Thus, divergence values of full width at 36.8% of the peak intensity of 3 mrad and 5.75 mrad are reported along the small and large axes of the beam, respectively. Therefore, it can be concluded that the developed OW link is capable of transmitting power efficiently at long distances, such as 100 m−300 m.

C. Study III: Harvested Power With a Targeted Value of 1 W

In Study III, the feasibility of harvesting 1 W is investigated using a simulation framework in Zemax and the respective analytical model of multiple elliptical Gaussian beams developed in Study I. Although 61 LDs with a typical output power of 50 mW for each diode are shown to be required for harvesting 1 W in Study I, LDs with typical output power of 171 mW for each diode are considered in Study III. In particular, an array of 42 LDs and lenses is created with the capability of transmitting 7.2 W to the solar cell that achieved the highest efficiency in Study I up to 30 m. The geometrical losses of this multiple link are calculated to be only 2% based on the simulation and analytical model, and both are in close agreement. However, enclosure of the laser beams is required due to eye safety restrictions.

The rest of the paper is organized as follows: in Section II, a literature review is given. In Section III, the study of total link and components efficiency is provided. In Section IV, the study of laser beam collimation is given. In Section V, the study of harvesting 1 W is provided. Finally, concluding comments are given in Section VI.

II. Previous Work

Tesla's pioneering work has attracted research interest mostly in the RF and more specifically in the microwave (μw) region of the EM spectrum [13], [14]. The basic methods of WPT are near field magnetic resonance coupling [15], [16]; inductive coupling [10], [17]; far field RF or far field RF or power transfer [18], [19]; and power transmission from laser sources [20], [21].

A. Radio Frequency Based WPT

In [15], a strongly coupled magnetic resonance system was implemented and had the capability of transferring the amount of 60 W up to a distance of 2 m with an overall wall-to-load efficiency of 15%. Also, in [17], the transfer of 105 W at a distance of 30 cm was demonstrated by the use of an IPTS with a direct current (dc)-to-load efficiency of 77%. However, so long as the outdoor installation of SCs requires a harvested amount of electrical power of 1 W at relatively long link distances in the order of 100 m−300 m, the only potential solutions are considered to be the techniques of wireless power transmission from RF or μw antennas and laser sources [13].

The EH functionality of RF or μw radiation is executed by a diode-based circuit, termed as rectenna [13], [22]. The rectenna consists of a rectifying circuit and a receiving antenna for the conversion of the input RF or μw power to dc power. In [13], an overview of the state-of-the-art measured values of rectenna efficiency ranging from 1.2% to 90.6% was presented. However, the results of total link efficiency and distance were not reported. Note that rectennas are exclusively designed to harvest either ambient RF power in the order of a few μW [23] or RF power from 'dedicated' antennas [24]. Thus, they do not have the ability to harvest power from a natural resource.

B. Optical Wireless Power Transfer and EH From Sunlight

The concept of OWPT based on laser sources was first introduced for the application of solar power satellite [20], [25]. Current research developments in the technology of high power LDs report levels of output optical power greater than 10 W with a respective conversion efficiency more than 65% in the wavelength region of 940 nm−980 nm [26]. Also, the use of passive optical elements for light collimation, such

as lenses, creates uncomplicated laser systems of very high directivity. In addition to this important characteristic, the wide availability of outdoor solar panels presents the unique potential of PH both from ambient light, where sunlight is included, and from 'dedicated' laser sources establishing the principle of OWPT. Moreover, high levels of irradiance of 100 mW/cm^2 are received from sunlight under standard test conditions (STC) [27].

In [28], consolidated tables with reported efficiency values of solar cells and modules measured at STC are given. In particular, the modules of amorphous silicon (a-Si) have an efficiency of 12.3%. Also, the inexpensive technologies of mono-crystalline silicon (mono-c-Si) cells and multi-crystalline silicon (multi-c-Si) modules have an efficiency in the order of 25.6% and 18.5%, respectively. The best efficiency values are reported for the technology of concentrator photovoltaics that is based on multi-junction cells [29]. A maximum efficiency of 45.7% of a multi-junction cell with a concentrator is reported in [28].

The exclusive indoor application of OWPT was studied in [8] and [9]. In these studies, ambient light was ensured to be negligible and therefore the concept of OWPT to SCs was investigated for dark conditions. In [8], an OW link was created by the use of a high brightness white LED, a large parabolic mirror for light collimation and an a-Si solar panel placed at 5 m. The maximum measured link efficiency and harvested power were only 0.1% and 18.3 mW, respectively. This fact was attributed to significant geometrical optical losses and very low energy efficiency of the a-Si technology of the panel. The serious geometrical losses of optical power stemmed from the Lambertian radiation pattern of the LED which was the major obstacle for efficient light collimation. Consequently, the next step was the use of highly directive laser sources and a different type of solar panel.

In the follow-up study [9], the OW link was implemented with 1 to 5 red LDs with respective collimation lenses and a multi-c-Si solar panel located at 5.2 m. The maximum measured link efficiency and harvested power using 5 LDs with lenses were only 0.74% and 10.4 mW, respectively. The low levels of link efficiency were attributed to the low LD efficiency and low solar panel efficiency. Also, the low amount of harvested power was explained by the low transmitted optical power and the effect of mismatch losses among cells of the same panel.

C. Simultaneous Wireless Communication and Power Transfer

The practical feasibility of simultaneous EH and data communication by a rectenna was demonstrated in [30] and [31]. In [30], an axial ratio bandwidth of 12.1% and a rectenna efficiency of 57.3% were reported for a link distance of only 35 cm. In [31], a rectenna efficiency of 63% was measured with an input power of 25 mW operating at 5.78 GHz for a link distance of 80 cm.

The data transfer using VLC systems has been investigated broadly [32], [33] and the feasibility of a data rate of 3 Gb/s by a LED source was demonstrated in [34]. Most importantly, the simultaneous use of a solar panel both for PH in the order of mW and high speed OWC with a data rate of 12 Mb/s was demonstrated in [35] for link distances of up to 95 cm. Also, the same concept was realized in [36], but with the use of a small solar cell capable of harvesting 1 mW of power and receiving data with a rate of only 3 kb/s.

Since the research objective is to achieve high speed FSO backhaul communication and power transfer to outdoor SCs, a review of the constraints imposed by an atmospheric channel and the potential solutions is given below.

1) Challenges Induced by an Atmospheric Channel: Laser beam propagation through an atmospheric channel is constrained by factors such as atmospheric attenuation, scintillation, misalignment and ambient light noise [37]. Atmospheric attenuation causes power reduction of the optical waves. It is presented in the form of absorption by gas molecules and Rayleigh and Mie scattering by gas molecules or aerosol particles that are suspended in the air and exist in fog, rain, clouds, smoke and dust [38]. The term scintillation, also known as atmospheric turbulence, is used to describe the random changes in light intensity caused by variations in the refractive index of the atmosphere [38]. Since highly directive laser beams are applied in FSO systems, precise alignment between the transmitter and receiver is required for the maximum possible collection of optical power by the detector. Finally, ambient light, where sunlight is included, can affect the signal-to-noise ratio at the receiver, as it is detected in the form of shot noise.

2) Potential Solutions to the Atmospheric Channel's Constraints: Atmospheric losses under clear weather conditions are considered to be negligible and, in this case, only geometrical losses are dominant [39]. Note that a FSO link may become unavailable under heavy fog conditions, but these conditions occur rarely and depend on the local topography and wind conditions. In addition, even under such worst-case weather conditions, multiple FSO links can be created by a number of transmitters and receivers applying the maximal ratio combining technique for the selection of the best channel. The scintillation effect results in fading, i.e. temporal and spatial fluctuations of the optical and therefore electrical power of the received signal. The negative effects of scintillation can be alleviated using the method of aperture averaging [40]. Also, the use of a multi-element receiver, such as a solar panel, and relatively large optical devices, such as mirrors, for light collimation and reception are the most efficient ways to address misalignment problems. Therefore, the use of a large aperture at the receiver is considered to be an effective mitigation technique of the effects of scintillation and misalignment. In data communication, while a typical photodetector can be driven to saturation from excessive amounts of ambient light, a solar receiver is more resilient to large amounts of received optical power. Also, since ambient light presents slow variations in time, it can be totally removed either by the use of optical filters or other advanced detection techniques. Finally, the presence of ambient light is an important advantage for EH, as the solar receiver is able to harvest energy not only from 'dedicated' laser sources, but also from the natural resource, i.e. sunlight.

III. Study I: Total Link and Components Efficiency

The objectives, methods, setups, applied analytical models and results of Experiments I–III of Study I are summarized in Table I.

TABLE I
SUMMARY OF EXPERIMENTS IN STUDY I

Study I		Total link and components efficiency			
Experiment		I		II	III
Objective		Determination of maximum fill factor, link efficiency and harvested power		Determination of each laser diode efficiency	Determination of solar receiver efficiency
Method		Measurement of 21 values pairs of load voltage and current		Measurement of output power for 22 values of input power	Measurement of 25 values of received optical power
Scenario		I	II	–	–
Setup	Optical source	1–4 Laser diodes	1–3 Laser diodes	Single laser diode	2 Laser diodes
	Optics	1–4 Aspheric lenses	1–3 Aspheric lenses	–	2 Aspheric lenses
	Receiver	Solar panel	Solar cell	Optical power sensor	Solar cell
	Measurement device	Multimeters		Optical power sensor	Optical power sensor
	Link distance	5.2 m		1.5 mm	5.2 m
Analytical model		(33)–(41)		Quadratic curve fitting*	–
Results		$f_{sr} = 69\%$ $\eta_{\rm m} = 2.7\%$ $P_{\rm m} = 30.6$ mW	$f_{sr} = 54.2\%$ $\eta_{\rm m} = 3.2\%$ $P_{\rm m} = 25.7$ mW	$\eta_{\rm LD}^{**} = \{28.1\%, 30.2\%, 32.2\%, 32.9\%\}$	$\eta_{sr} = 13.3\%$

*No physical model is applied to the experimental data, but two mathematical quadratic polynomials are used.
**Maximum values.

A. Objective

The objective of Study I is to increase the experimental energy efficiency of the 5 m OW link created in [8] and [9]. This is achieved by a decrease in the dimensions, number of cells and a different technology use of the solar receiver in [8] and [9]. An increased maximum link efficiency reduces the number of optical transmitters (i.e. LDs and collimation lenses) required to achieve a harvested electrical power of 1 W. Since each component contributes to the total link efficiency, the efficiency of every single component is determined.

B. Analytical Model

The analytical models of the generated laser beam from the diode, thick lens, reshaped beam from the lens, solar panel and efficiency of total link and components are given below.

An elliptical Gaussian model is considered for the laser beam generated from the diode and the reasoning for this is given in Appendix A. A geometrical illustration of a Gaussian beam is shown in Fig. 1 on the x-z and y-z planes, respectively. When a Gaussian beam passes through any circularly symmetric optical component aligned with the optical beam axis, the Gaussian beam remains Gaussian so long as the paraxial approximation holds for the system [41]. Paraxial approximation is defined in Appendix A. The geometrical parameters and the intensity characteristics of the Gaussian beam emitted from the LD are modified by the geometrical and optical properties of the lens. Therefore, the beam parameters are calculated at four different transverse planes, namely, the emission rectangular area of the LD; the vertices of the input and output surfaces of the aspheric lens; and the positions of the new beam waists along the x- and y-axes, respectively.

1) Generated Beam From the Laser Diode: The LDs used in this study have a multi-quantum well (MQW) structure. The emission rectangular layers of the junction placed inside the packages of the LDs have an area of $(2W_{0x}) \times (2W_{0y})$ [42]. Parameters W_{0x} and W_{0y} denote the beam waists along the x- and y-axes, respectively. They are calculated from the far field relative intensity patterns as a function of the angular divergences [43], [44]. In particular, the beam waists generated from the LD ($z = 0$) are given by [41]:

$$W_{0x} = \frac{\lambda_0}{\pi \tan(\vartheta_x)} \approx \frac{\lambda_0}{\pi \vartheta_x} \tag{1}$$

and

$$W_{0y} = \frac{\lambda_0}{\pi \tan(\vartheta_y)} \approx \frac{\lambda_0}{\pi \vartheta_y}. \tag{2}$$

The symbol λ_0 denotes the LD operating wavelength, and ϑ_x [rad] and ϑ_y [rad] represent the perpendicular and parallel to the junction beam divergences. The values of ϑ_x and ϑ_y correspond to the half width at half maximum (HWHM) intensity points of the Gaussian graphs [43], [44]. The selection of the HWHM beam divergence values is made for the applicability of the paraxial approximation. However, note that the beam divergence of a Gaussian beam can also be defined according to the $1/e \simeq 0.368$ and $1/e^2 \simeq 0.135$ of peak intensity points [37], [45]. It is considered that the optical beam passes from the package aperture of the LD without any optical losses. Also, it is assumed that the protective glass window placed at the front surface of the LD package does not affect the intensity characteristics of the optical beam generated from the MQW source [43], [44]. Therefore, diffraction effects from the circular aperture of the LD are not considered here. This is explained by the Gaussian form of beam intensity shown in the respective LD data sheets [43], [44] instead of the form of a Bessel beam characterized by side lobes [41].

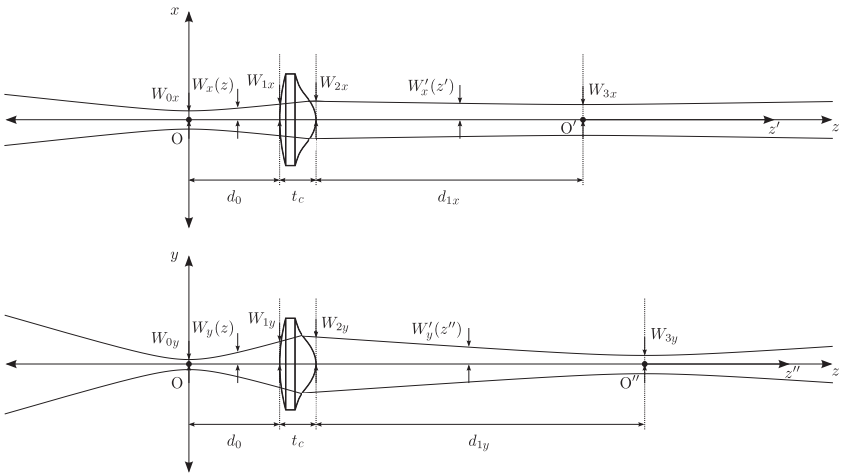

Fig. 1. Geometrical representation of the elliptical Gaussian beam transmitted through an aspheric lens along the x- and y-axes.

The beam radii along the x- and y-axes can be expressed as a function of distance from the emission area of the LD by [41]:

$$W_x(z) = W_{0x}\sqrt{1+\left(\frac{z}{z_{0x}}\right)^2} \tag{3}$$

and

$$W_y(z) = W_{0y}\sqrt{1+\left(\frac{z}{z_{0y}}\right)^2}, \tag{4}$$

where $0 \le z \le d_0$; and d_0 denotes the distance between the cross section of the emission source and the tangent plane to the input surface of the lens. Also, z_{0x} and z_{0y} represent the Rayleigh range of the LD beam along the x- and y-directions, respectively. The Rayleigh range is defined as the axial distance between the beam waist and the point where the beam radius is increased by a multiplication factor of $\sqrt{2}$ from its minimum value. These parameters are given by $z_{0x} = \pi W_{0x}^2/\lambda_0$ and $z_{0y} = \pi W_{0y}^2/\lambda_0$ [41].

The beam radii at the tangent plane to the input surface of the lens ($z = d_0$) along the x- and y-axes are calculated by:

$$W_{1x} = W_x(d_0) \overset{(3)}{=} W_{0x}\sqrt{1+\left(\frac{d_0}{z_{0x}}\right)^2} \tag{5}$$

and

$$W_{1y} = W_y(d_0) \overset{(4)}{=} W_{0y}\sqrt{1+\left(\frac{d_0}{z_{0y}}\right)^2}. \tag{6}$$

The radii of curvature of the Gaussian beam generated from the LD along the x- and y-axes at $z = d_0$ are given by [41]:

$$R_{1x} = d_0\left[1+\left(\frac{z_{0x}}{d_0}\right)^2\right] \tag{7}$$

and

$$R_{1y} = d_0\left[1+\left(\frac{z_{0y}}{d_0}\right)^2\right]. \tag{8}$$

The q-parameters of the Gaussian beam at $z = d_0$ in the x- and y-directions are described by [41]:

$$\frac{1}{q_{1x}} = \frac{1}{R_{1x}} - j\frac{\lambda_0}{\pi W_{1x}^2} \tag{9}$$

and

$$\frac{1}{q_{1y}} = \frac{1}{R_{1y}} - j\frac{\lambda_0}{\pi W_{1y}^2}, \tag{10}$$

where $j = \sqrt{-1}$ is the imaginary unit.

The optical intensity or irradiance, G, of the generated elliptical Gaussian beam in the Cartesian coordinate system, (x, y, z), is expressed as follows [41]:

$$G(x,y,z) = G_0\frac{W_{0x}W_{0y}}{W_x(z)W_y(z)} \times \exp\left\{-2\left[\frac{x^2}{W_x^2(z)}+\frac{y^2}{W_y^2(z)}\right]\right\}, \tag{11}$$

where $0 \le z \le d_0$; and $G_0 = G(0,0,0)$ is the overall peak intensity.

The total optical power, $P_{\mathrm{Tx,o}}$, of the generated beam is computed at a distance of $0 \le z \le d_0$ by [41]:

$$P_{\mathrm{Tx,o}} = \frac{\pi}{2}G_0 W_{0x}W_{0y}. \tag{12}$$

The proof of (12) is presented in Appendix B. Combining (11) and (12), the laser beam intensity can be described as a function

of $P_{\mathrm{Tx,o}}$ by:

$$G(x,y,z) = \frac{2P_{\mathrm{Tx,o}}}{\pi W_x(z) W_y(z)} \times \exp\left\{-2\left[\frac{x^2}{W_x^2(z)} + \frac{y^2}{W_y^2(z)}\right]\right\}. \quad (13)$$

2) Thick Lens: A method to relate the input and output of an optical system is the use of ray transfer or $ABCD$ matrices [46]. The method of $ABCD$ matrices is also widely used in μw communications [47]. In matrix optics, a simple 2×2 matrix connects the position and angle of paraxial rays at the input and output plane of an optical system through linear algebraic equations. Note that the application of the $ABCD$ law to a Gaussian beam connects the q-parameters of the beam [41]. The diameter of the lens is represented by Δ to avoid any confusion with D, the last element of an $ABCD$ matrix.

The rear surface of the aspheric lens is considered to be spherical. This assumption provides a worst-case scenario for the lens model in terms of light collimation. The elements of an $ABCD$ matrix for a thick lens with two spherical surfaces of different radii of curvature are [48]:

$$A = 1 - \frac{t_c(n-1)}{nR_1}, \quad (14)$$

$$B = \frac{t_c}{n}, \quad (15)$$

$$C = -(n-1)\left(\frac{1}{R_1} - \frac{1}{R_2}\right) - \frac{t_c(n-1)^2}{nR_1R_2}, \quad (16)$$

$$D = 1 + \frac{t_c(n-1)}{nR_2}. \quad (17)$$

The parameters t_c and n represent the thickness and the refractive index of the lens, respectively. Also, R_1 and R_2 are the radii of the input and output surface of the lens, respectively. The q-parameters of the beam for the x- and y-axes at $z = d_0$ and $z = d_0 + t_c$ are connected through the relationships [41]:

$$q_{2x} = \frac{Aq_{1x} + B}{Cq_{1x} + D} \quad (18)$$

and

$$q_{2y} = \frac{Aq_{1y} + B}{Cq_{1y} + D}. \quad (19)$$

Also, the q-parameters of the beam at $z = d_0 + t_c$ are given by:

$$\frac{1}{q_{2x}} = \frac{1}{R_{2x}} - j\frac{\lambda_0}{\pi W_{2x}^2} \quad (20)$$

and

$$\frac{1}{q_{2y}} = \frac{1}{R_{2y}} - j\frac{\lambda_0}{\pi W_{2y}^2}. \quad (21)$$

Parameters W_{2x} and W_{2y} represent the beam radii along the x- and y-axes at the tangent plane to the output surface of the lens ($z = d_0 + t_c$). Also, R_{2x} and R_{2y} denote the radii of curvature of the reshaped Gaussian beam from the lens at $z = d_0 + t_c$. Then, all of these quantities can be calculated from:

$$R_{2x} = \frac{1}{\mathrm{Re}\{1/q_{2x}\}}, \quad (22)$$

$$R_{2y} = \frac{1}{\mathrm{Re}\{1/q_{2y}\}}, \quad (23)$$

$$W_{2x} = \sqrt{-\frac{\lambda_0}{\pi \mathrm{Im}\{1/q_{2x}\}}} \quad (24)$$

and

$$W_{2y} = \sqrt{-\frac{\lambda_0}{\pi \mathrm{Im}\{1/q_{2y}\}}}. \quad (25)$$

Operators $\mathrm{Re}\{.\}$ and $\mathrm{Im}\{.\}$ represent the real and imaginary parts of $1/q_{2x}$ and $1/q_{2y}$, and are calculated by (18) and (19), respectively.

3) Reshaped Beam From the Lens: The distance between the reshaped beam waists and the tangent plane to the output surface of the lens in the x- and y-direction are d_{1x} and d_{1y}, respectively. These values of distance can be computed by [41]:

$$d_{1x} = -\frac{R_{2x}}{1 + \left[\lambda_0 R_{2x}/\left(\pi W_{2x}^2\right)\right]^2} \quad (26)$$

and

$$d_{1y} = -\frac{R_{2y}}{1 + \left[\lambda_0 R_{2y}/\left(\pi W_{2y}^2\right)\right]^2}. \quad (27)$$

Also, the waists of the reshaped Gaussian beam, W_{3x} and W_{3y}, are given by [41]:

$$W_{3x} = \frac{W_{2x}}{\sqrt{1 + \left[\pi W_{2x}^2/\left(\lambda_0 R_{2x}\right)\right]^2}} \quad (28)$$

and

$$W_{3y} = \frac{W_{2y}}{\sqrt{1 + \left[\pi W_{2y}^2/\left(\lambda_0 R_{2y}\right)\right]^2}}, \quad (29)$$

along the x- and y-axis, respectively.

Now, the reshaped beam radius along the x-axis can be expressed as a function of distance from the vertex of output surface of the lens by:

$$W_x'(z') = W_{3x}\sqrt{1 + \left(\frac{z'}{z_{3x}}\right)^2}, \quad (30)$$

where $z' = z - d_0 - t_c - d_{1x} \geq -d_{1x}$ is a substituted variable for distance, and $z_{3x} = \pi W_{3x}^2/\lambda_0$ is the Rayleigh range along the x-axis. Similarly, the reshaped beam radius along the y-direction is given as a function of distance from the vertex of output surface of the lens by:

$$W_y'(z'') = W_{3y}\sqrt{1 + \left(\frac{z''}{z_{3y}}\right)^2}, \quad (31)$$

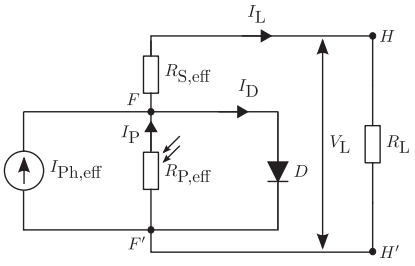

Fig. 2. Physical equivalent circuit of the solar panel to an effective single solar cell model [12].

where $z'' = z - d_0 - t_c - d_{1y} \geq -d_{1y}$ is another substituted variable for distance, and $z_{3y} = \pi W_{3y}^2/\lambda_0$ is the Rayleigh range along the y-axis.

The reshaped Gaussian beam intensity can be computed according to (13) by:

$$G'(x,y,z) = \frac{2(1-r)P_{\rm Tx,o}}{\pi W_x'(z')W_y'(z'')} \times \exp\left\{-2\left[\frac{x^2}{W_x'^2(z')} + \frac{y^2}{W_y'^2(z'')}\right]\right\}, \quad (32)$$

where $z \geq d_0 + t_c$ and r denotes the reflectance of the lens.

4) Physical Model of Solar Panel and Curve Fitting: In [12], a single diode-based physical model of a solar panel consisting of $N_{\rm c}$ cells connected in series was proposed. The physical equivalent circuit of that model is shown in Fig. 2. A variable resistor, $R_{\rm L}$, is also connected to the output branch, HH', of the solar receiver. Parasitic resistance effects of this photovoltaic (PV) panel are modeled by an effective series resistance, $R_{\rm S,eff}$, and an effective shunt resistance, $R_{\rm P,eff}$. The main factors that contribute to the series resistance generation are the current flow across the p-n junction of the cells; the contact resistance between the metallic grid and the semiconductor; and the resistance between the top and rear metallic contacts. The shunt resistance is caused mainly by manufacturing imperfections rather than a flawed design of solar cells.

The application of Kirchhoff's current law to the circuit node F in Fig. 2 gives:

$$I_{\rm D} - I_{\rm P} - I_{\rm Ph,eff} + I_{\rm L} = 0, \quad (33)$$

where $I_{\rm D}$ is the forward current of the diode; $I_{\rm P}$ is the parallel current to the source flowing through the branch $F'F$; $I_{\rm Ph,eff}$ is the effective generated photocurrent; and $I_{\rm L}$ denotes the load current. The current $I_{\rm D}$ is given by the Shockley diode equation [12]:

$$I_{\rm D} = I_{0,\rm eff}\left\{\exp\left[\frac{q}{A_{\rm eff}k_{\rm B}T}\left(V_{\rm L} - R_{\rm S,eff}I_{\rm L}\right)\right] - 1\right\}. \quad (34)$$

The value of $I_{0,\rm eff}$ represents the effective dark saturation current of the diode. The physical constants $q = 1.602 \times 10^{-19}$ C and $k_{\rm B} = 8.617 \times 10^{-5}$ eV/K denote the electron charge and Boltzmann constant, respectively. The temperature of the PV panel is assumed to be $T = 298$ K. The quantities $A_{\rm eff}$ and $V_{\rm L}$ represent the effective ideality factor of the diode and the load voltage, respectively. According to Kirchhoff's voltage law, the current $I_{\rm P}$ is computed by:

$$I_{\rm P} = \frac{V_{\rm L} - R_{\rm S,eff}I_{\rm L}}{R_{\rm P,eff}}. \quad (35)$$

A transcendental relationship connects the load current and load voltage. This is observed by the substitution of $I_{\rm D}$ for the second part of (34) and $I_{\rm P}$ for the second part of (35) in (33). Transcendental equations have only approximate numerical solutions and do not have closed form solutions. The electrical power, $P_{\rm L}$, harvested from the load resistor is given by $P_{\rm L} = V_{\rm L}I_{\rm L}$.

This particular model has two measurable parameters, $I_{\rm L}$ and $V_{\rm L}$, and five unknown parameters, $I_{0,\rm eff}$, $R_{\rm S,eff}$, $A_{\rm eff}$, $R_{\rm P,eff}$ and $I_{\rm Ph,eff}$. These parameters are strongly dependent on the values of optical power incident on the panel. An estimation method of the five unknown parameters is followed by the application of a simple exhaustive search algorithm with discrete search space. The optimization problem that is solved can be expressed based on [49] as follows:

$$\min_{\substack{I_{0,\rm eff},R_{\rm S,eff},A_{\rm eff}\\ R_{\rm P,eff},I_{\rm Ph,eff}}} \sum_{i=1}^{21}\left|I_{0,\rm eff}\left\{\exp\left\{\frac{q\left[V_{\rm L}(i) - R_{\rm S,eff}I_{\rm L}(i)\right]}{A_{\rm eff}k_{\rm B}T}\right\} - 1\right\} - \frac{V_{\rm L}(i) - R_{\rm S,eff}I_{\rm L}(i)}{R_{\rm P,eff}} - I_{\rm Ph,eff} + I_{\rm L}(i)\right| \quad (36)$$

$$\text{subject to :} \quad I_{0,\rm eff,min} \leq I_{0,\rm eff} \leq I_{0,\rm eff,max} \quad (37)$$

$$R_{\rm S,eff,min} \leq R_{\rm S,eff} \leq R_{\rm S,eff,max} \quad (38)$$

$$A_{\rm eff,min} \leq A_{\rm eff} \leq A_{\rm eff,max} \quad (39)$$

$$R_{\rm P,eff,min} \leq R_{\rm P,eff} \leq R_{\rm P,eff,max} \quad (40)$$

$$I_{\rm Ph,eff,min} \leq I_{\rm Ph,eff} \leq I_{\rm Ph,eff,max}. \quad (41)$$

Twenty one measurements are conducted for every V-P curve of the WPT systems implemented in Experiment I. The subscripts 'min' and 'max' of each of the five unknown parameters of (37)–(41) denote the real positive minimum and maximum value of the finite search space, respectively. The five identified parameters are first refined by the application of 'fsolve' in Matlab and the resulting values are applied to (33)–(35) for curve fitting of the experimental data. Note that the experimental measurements of $I_{\rm L}$ and $V_{\rm L}$ are also used for the determination of a local solution to this non-linear curve-fitting problem [50].

5) Total Link and Components Efficiency: An important aspect of the technology of WPT is the total efficiency of a link that is a function of the components efficiency. The external power efficiency of a LD can be defined as:

$$\eta_{\rm LD} = \frac{P_{\rm Tx,o}}{P_{\rm in}} \times 100\%, \quad (42)$$

where $P_{\rm in}$ is the dc input electrical power to the optical source.

Line of sight (LoS) conditions are assumed for the OW channel. So long as the experiments are conducted in an indoor environment, no atmospheric attenuation of the laser beam due to absorption from molecules and scattering effects (Mie or Rayleigh) with aerosol particles is considered [37], [51]. Therefore, only geometrical losses of the transmitted optical power are assumed due to the laser beam divergence over distance.

In practice, the typical geometry of an optical receiver (solar cell or panel) is rectangular with an effective area of $S_{\rm eff} = 2x_0 \times 2y_0$, where x_0 is the half length and y_0 is the half width. The ratio of the optical power collected by the rectangular solar receiver, $P_{\rm Rx,o}(z)$, at a distance of $z \geq d_0 + t_c$ over the total transmitted optical power can be defined as the collection efficiency, $\eta_{\rm ceff}(z)$. This factor can be calculated in the case of a single optical link by:

$$\eta_{\rm ceff}(z) = \frac{P_{\rm Rx,o}(z)}{(1-r)P_{\rm Tx,o}} \times 100\% = {\rm erf}\left[\frac{\sqrt{2}x_0}{W'_x(z')}\right]{\rm erf}\left[\frac{\sqrt{2}y_0}{W'_y(z'')}\right] \times 100\%, \quad (43)$$

where ${\rm erf}\,[.]$ denotes the error function. Quantities $W'_x(z')$ and $W'_y(z'')$ are given by (30) and (31), respectively. An analytical derivation of (43) is provided in Appendix B. This very useful parameter provides information about the geometrical losses of the optical link. In fact, the geometrical losses are determined by the efficiency of collimation of the optical source. As the beam divergence decreases, the geometrical losses decrease, accordingly, for a solar panel of constant dimensions. Therefore, the laser beam can propagate more efficiently at longer distances.

The most important metric of the energy efficiency of a solar panel or cell is the optical-to-electrical conversion efficiency. This factor is computed by [27]:

$$\eta_{\rm sr}(z) = \frac{P_{\rm m}}{P_{\rm Rx,o}(z)} \times 100\%, \quad (44)$$

where $P_{\rm m}$ denotes the maximum electrical power and is given by $P_{\rm m} = V_{\rm m} I_{\rm m}$. Also, $V_{\rm m}$ and $I_{\rm m}$ represent the voltage and current at the maximum power point (MPP) of the panel, respectively. The fill factor (FF) of a solar panel shows how well the circuit approximates the ideal behavior of a current source. The FF of a PV panel is given by [27]:

$$f_{\rm sr} = \frac{V_{\rm m} I_{\rm m}}{V_{\rm oc} I_{\rm sc}} \times 100\%, \quad (45)$$

where $V_{\rm oc}$ and $I_{\rm sc}$ denote the open-circuit voltage and short-circuit current, respectively. The responsivity of the solar receiver can be defined as:

$$\rho(z) = \frac{I_{\rm Ph,eff}}{P_{\rm Rx,o}(z)}. \quad (46)$$

However, a common assumption of $I_{\rm Ph,eff} \simeq I_{\rm sc}$ is made practically [52]. This is explained by the low series resistance and high parallel resistance of the solar panel. In this case, the responsivity becomes a purely measurable quantity as both the short-circuit current and the received optical power can be measured.

Finally, the maximum link efficiency is computed by:

$$\eta_{\rm m} = \frac{P_{\rm m}}{P_{\rm in}} \times 100\%. \quad (47)$$

The combination of (42)–(47) forms an expression of the maximum link efficiency as a function of the LD, lens, collection and solar receiver efficiency given by:

$$\eta_{\rm m} = \eta_{\rm LD}(1-r)\eta_{\rm ceff}(z)\eta_{\rm sr}(z) \times 100\% = \eta_{\rm LD}(1-r)\eta_{\rm ceff}(z) f_{\rm sr}\rho(z) V_{\rm oc} \times 100\%, \quad (48)$$

where the assumption of $I_{\rm Ph,eff} \simeq I_{\rm sc}$ is made.

C. Eye Safety Regulations

Important parameters for eye safety are given below for the LD used in all of the experiments and the LD and collimation lens used in Scenario II of Experiment I according to the British Standard BS EN 60825-1:2014 [11]. The classification process is shown analytically in Appendices C and D.

1) Single Laser Diode: The LD used in the experiments (i.e. HL6544FM) has not been classified by the manufacturer [43]. For this reason, a methodology for its classification is presented in Appendix C, based on [11]. This methodology leads to the conclusion that the LD is classified as Class 3B. Laser products of Class 3B are normally hazardous when there is intrabeam ocular exposure, i.e. within the nominal ocular hazard distance (NOHD), $d_{\rm NOHD}$, according to [11]. Also, the viewing of diffuse reflections is normally safe. The accessible emission limit (AEL), κ, of Class 3B is $\kappa = 500$ mW according to Table 8 of [11]. The maximum permissible exposure (MPE), ν, is determined from Table A.1 [11] to be $\nu = 10$ W/m^2 $= 1$ mW/cm^2. The LD irradiance measured from a square aperture stop with side length $2x_0$ at a distance z is computed by:

$$G_{\rm Rx}(z) = \frac{{\rm erf}\left[\frac{\sqrt{2}x_0}{W_x(z)}\right]{\rm erf}\left[\frac{\sqrt{2}x_0}{W_y(z)}\right]P_{\rm Tx,o,m}}{(2x_0)^2}, \quad (49)$$

where $P_{\rm Tx,o,m}$ denotes the maximum output optical power of the LD; and $W_x(z)$ and $W_y(z)$ are given by (3) and (4), respectively. In order to determine the NOHD, the inequality $G_{\rm Rx}(d_{\rm NOHD}) \leq \nu = 1$ mW/cm^2 needs to be solved. The graphical solution of this inequality, i.e. the intersection point of the two curves representing $G_{\rm Rx}(z)$ and ν, for the applied values of λ_0 to x_0 given in Table II, to (3), (4) and (49) results in $d_{\rm NOHD} = 63$ cm. Therefore, a safe setup requires proper enclosure of the beam inside a tube with a length of 63 cm from the LD. This is because visual access to the laser beam and its specular reflections inside the NOHD must be prevented.

2) Laser Diode and Collimation Lens: When the optical beam of a LD is collimated by the use of a lens, its optical and geometrical characteristics are modified compared with the use case of a single LD. Therefore, reclassification of the laser is required. This process is analyzed in Appendix D. Even in this case, the laser system is classified as Class 3B. Again, the AEL is 500 mW. However, the MPE is given in Table A.2 of [11] by $\nu = 18C_6T_2^{-0.25}$ [W/m^2] for $t > T_2$, where C_6 is a correction factor computed in Appendix D to be 10.867. Parameter T_2 is determined from Table 9 of [11]

TABLE II
ANALYTICAL PARAMETERS FOR THE DETERMINATION OF d_{NOHD}

Parameter	Unit	Value	Parameter	Unit	Value
λ_0	[nm]	660	A	–	0.836
$P_{\mathrm{Tx,o,m}}$	[mW]	130	B	[mm]	4.93
W_{0x}	[μm]	1.92	C	[cm^{-1}]	−1.247
W_{0y}	[μm]	1.12	D	–	0.46
x_0	[mm]	3.5	R_{2x}	[cm]	13.93
d_0	[mm]	3.25	R_{2y}	[cm]	13.93
W_{1x}	[μm]	355.62	W_{2x}	[μm]	837.21
W_{1y}	[μm]	609.62	W_{2y}	[mm]	1.44
R_{1x}	[mm]	3.25	d_{1x}	[cm]	−13.91
R_{1y}	[mm]	3.25	d_{1y}	[cm]	−13.93

to be $T_2 = 10 \times 10^{[(\alpha-\alpha_{\min})/98.5]} = 10 \times 10^{[(16.3-1.5)/98.5]} = 14.13$ s, where α and $\alpha_{\min}$ are defined and determined in Appendices C and D. Therefore, the value of MPE is calculated to be $\nu = 18 \times 10.867 \times 14.13^{-0.25} = 100.89$ W/m^2 $= 10.09$ mW/cm^2. Here, the irradiance of the optical transmitter measured from a square aperture stop with side length $2x_0$ at a distance z is given by:

$$G'_{\mathrm{Rx}}(z) = \frac{\mathrm{erf}\left[\frac{\sqrt{2}x_0}{W'_x(z')}\right]\mathrm{erf}\left[\frac{\sqrt{2}x_0}{W'_y(z'')}\right]P_{\mathrm{Tx,o,m}}}{(2x_0)^2}, \qquad (50)$$

where the assumption of $(1-r) \simeq 1$ is made and $W'_x(z')$ and $W'_y(z'')$ are given by (30) and (31), respectively. Again, the inequality $G'_{\mathrm{Rx}}(d_{\mathrm{NOHD}}) \leq \nu = 10.09$ mW/cm^2 needs to be solved for the determination of d_{NOHD}. This inequality is solved graphically by the application of the values of Table II to (1)–(10), (14)–(31) and, finally, (50). The resulting value of NOHD is $d_{\mathrm{NOHD}} = 3.6$ m and this means that the laser beam must be enclosed into a shielding tube of length of 3.6 m from the output surface of the lens for eye safety. For a safer practical setup with a smaller NOHD, either the distance between the LD and the lens should be modified so that the beam becomes more divergent inducing more geometrical losses to the link, or the transmission power should decrease according to the MPE level.

D. Experimental System and Results

The selected components, objectives, methods, setups, applied analytical models and results of Experiments I–III are given below.

1) System Components: The values of components' parameters from their respective data sheets [43], [54]–[56] are summarized in Table III. A single mode Opnext HL6544FM high power LD with a MQW structure is used as an optical source for power transmission [43]. This laser is a continuous wave (CW) source. The semiconductor material of this LD is aluminium gallium indium phosphide. Angles $\vartheta_{\parallel}$ and $\vartheta_{\perp}$ refer to the full width at half maximum (FWHM) intensity along the parallel and perpendicular plane to the junction, respectively. The selected wavelength of 660 nm favors a visible and, therefore, uncomplicated alignment of the components. Also, the spectral responsivity of silicon (Si)-based receivers has large values in the red region of the VL spectrum [57]. The long wavelength of 1550 nm, widely used in FSO communications [37], is not considered because of the respective very low spectral responsivity of typical Si cells or panels [27].

The relatively large angular divergence of the optical source along both transverse x- and y-axes requires the use of a precise lens for light collimation. Lenses with spherical surfaces are low cost and are relatively uncomplicated to manufacture, but they have spherical aberrations [48]. In contrast, the complex geometry of aspheres allows for correction of spherical aberration and creates collimated beams of better quality [48]. In this study, an ACL12708U-A aspheric lens made of B270 optical crown glass with anti-reflection coating (ARC) is used in Experiments I and III [54].

The off-the-shelf optical receivers used for PH are a multi-c-Si solar panel and a mono-c-Si solar cell. In general, mono-c-Si cells have larger efficiency and are more expensive than multi-c-Si-based cells. More specifically, a MC-SP0.8-NF-GCS multi-c-Si-based panel with eight cells connected in series is used in Scenario I of Experiment I [55]. The dimensions of this panel are 8.8×7.8 cm^2. Also, the mono-c-Si cell has dimensions of 12.5×12.5 cm^2 and is used in Scenario II of Experiment I [56].

2) Experiment I—Objective, Method, Setup and Applied Analytical Model: The objective of Study I, to increase the experimental energy efficiency of the 5 m OW link created in [8] and [9], is undertaken in this experiment. The system block diagram created for WPT is shown in Fig. 3. The term 'optical transmitter' is defined as a single pair of a LD and an aspheric lens. First, an amount of electrical power, P_{in}, is supplied to a number, N_{Tx}, of optical transmitters. The LDs are connected in parallel. The optical power generated from either a single LD or multiple LDs, $P_{\mathrm{Tx,o}}$, is passed through a single lens or multiple lenses for beam collimation. The distance between each LD and the respective input lens surface is adjusted so that the product of V_{oc} and I_{sc} is maximized at the solar receiver. The output optical power of a single lens or multiple lenses, $(1-r)P_{\mathrm{Tx,o}}$, is transmitted through an indoor LoS wireless channel that induces mostly geometrical and misalignment losses. The optical power collected from the solar receiver (panel or cell) is $P_{\mathrm{Rx,o}}$. A final amount of electrical power, P_{L}, is harvested from a variable resistor that represents the load of the PV panel or cell.

In Experiment I, the parameters of f_{sr}, η_{m} and P_{m} are determined. For this reason, the variable resistor is modified for the measurement of 21 pairs of $(V_{\mathrm{L}}, I_{\mathrm{L}})$ by the use of two multimeters. Also, the respective values of R_{L} are measured. The values of V_{L} and I_{L} are in the range $[0, V_{\mathrm{oc}}]$ and $[0, I_{\mathrm{sc}}]$, respectively. The link distance measured from the output surface of the lens to the input plane of the receiver is 5.2 m. The experimental data are fit by the application of (33)–(41) of the solar receiver physical model.

This experiment includes two different scenarios. In Scenario I, the number of N_{Tx} scales from 1 to 4, and the multi-c-Si panel is used. In Fig. 4, the pattern of two optical transmitters on the PV panel is illustrated. In Scenario II, the number of N_{Tx} increases from 1 to 3, and the mono-c-Si cell is used. In Fig. 5, the laser beam pattern on the solar cell for $N_{\mathrm{Tx}} = 3$ and the measured voltage and current of the load are shown.

TABLE III
STUDY I: DATA SHEET PARAMETERS OF COMPONENTS

Laser diode			Aspheric lens			Multi-crystalline silicon solar panel			Mono-crystalline silicon solar cell		
Parameter	Unit	Value	Parameter	Unit	Value	Parameter	Unit	Value	Parameter	Unit	Value
λ_0	[nm]	660	Δ	[cm]	1.27	N_c	–	8	N_c	–	1
$\vartheta_{\parallel}$	[mrad]	174.5*	R_1	[mm]	15.65	$S_{\rm eff}$	[cm^2]	68.64	$S_{\rm eff}$	[cm^2]	156.25
	[deg]	10*	R_2	[mm]	−4.75	$P_{\rm m}$	[W]	0.8†	$P_{\rm m}$	[W]	2.91†
$\vartheta_{\perp}$	[mrad]	296.7*	t_c	[mm]	7.5	$\eta_{\rm sr}$	(%)	11.66†	$\eta_{\rm sr}$	(%)	18.62†
	[deg]	17*	f	[mm]	8.02	$f_{\rm sr}$	(%)	72.46†	$f_{\rm sr}$	(%)	78.53†
$P_{\rm Tx,o}$	[mW]	50**	n	–	1.52						
$\eta_{\rm LD}$	(%)	22.2**	r	(%)	0.25						

*Full width at half maximum (FWHM) values.
**Typical values.
†Standard test conditions (STC) values [53].

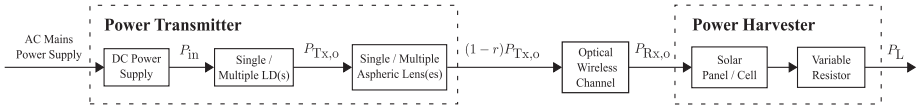

Fig. 3. System block diagram in Experiment I.

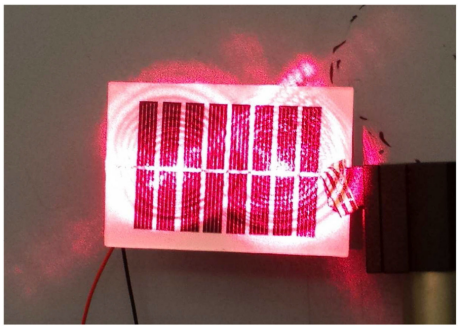

Fig. 4. Scenario I: Beam pattern formed by two optical transmitters on the solar panel.

Fig. 5. Scenario II: Beam pattern of three laser sources and measurement of $P_{\rm m}$.

The experimental measurements of $P_{\rm L}$ over $V_{\rm L}$ for Scenarios I and II are shown in Fig. 6(a) and (b), respectively. The curves labeled as 'Physical Model' are generated by a local solution of (36). The measured parameters are presented in Table IV and the respective parameters of [8] and [9] are given for comparison reasons. Also, the five estimated parameters of the model of solar receiver are given in Table V.

Note that a peak harvested power is observed for each V-P curve in Scenarios I and II of Fig. 6. The peak electrical power harvested from a solar receiver is feasible under the conditions of perfect load matching. In this case, the characteristic resistance of the solar receiver (i.e. the output resistance at the MPP) is equal to the resistance of the load [58]. Thus, the maximum possible amount of electrical power is transferred to the load connected to the output of the solar cell or panel.

3) Scenario I—Results and Discussion: In Scenario I, the values of $f_{\rm sr}$, $\eta_{\rm m}$ and $P_{\rm m}$ are quite low when one optical transmitter is used. In this case, the laser beam illuminates the whole rectangular area of the solar panel. Cells placed at the edges of the panel receive less optical power compared with the centrally placed ones due to the elliptical and Gaussian beam profile. Therefore, power generated by cells with higher received irradiance levels is dissipated by cells with lower irradiance levels. This effect induces mismatch losses among different cells of the panel. As a result, the total electrical output of the PV panel is determined by cells with the lowest performance.

A significant increase in the values of $f_{\rm sr}$, $\eta_{\rm m}$ and $P_{\rm m}$ by at least 1.5, 2.9 and 5.6 times, respectively, is observed when $N_{\rm Tx} > 1$ compared with the case of $N_{\rm Tx} = 1$. When the number of optical transmitters is larger than 1, the laser beams cover smaller circular and elliptical areas mainly inside the panel area illuminating different cells as shown in Fig. 4 for $N_{\rm Tx} = 2$. Thus, a more uniformly illuminated pattern is formed and the effect of mismatch losses becomes less significant. As $N_{\rm Tx}$ increases from 2 to 4, the values of $f_{\rm sr}$, $\eta_{\rm m}$ and $P_{\rm m}$ increase gently, as expected due to the respective increase in $P_{\rm Rx,o}$ and, therefore, $\eta_{\rm sr}$. The multi-c-Si solar panel presents a significantly

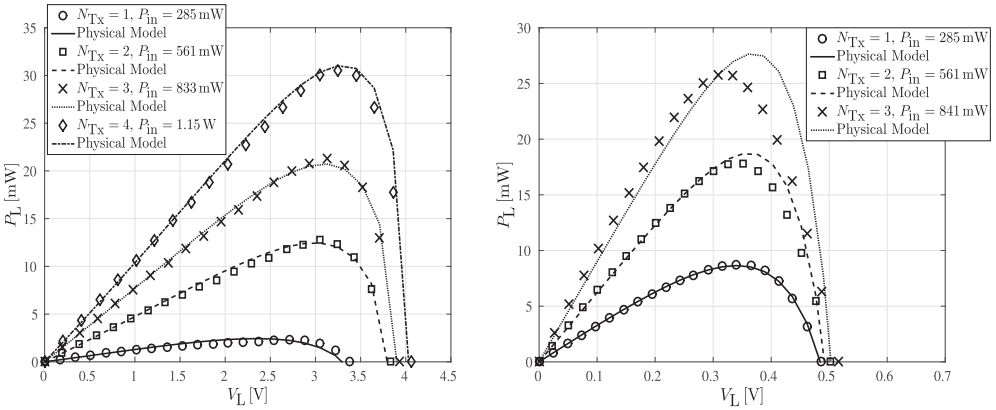

Fig. 6. Experiment I: Measured data of harvested electrical power versus load voltage of (a) Scenario I and (b) Scenario II supported by the physical model curves.

TABLE IV
MEASURED PARAMETERS OF EXPERIMENT I AND AUTHORS' PREVIOUS RESEARCH

Scenario I						Scenario II					
N_{Tx}	d_0 [mm]	f_{sr} (%)	η_{m} (%)	P_{m} [mW]	$R_{\mathrm{L}}^{\dagger}$ [Ω]	N_{Tx}	d_0 [mm]	f_{sr} (%)	η_{m} (%)	P_{m} [mW]	$R_{\mathrm{L}}^{\dagger}$ [Ω]
1	7.0*	45.08	0.80	2.3	3200	1	3.25**	53.35	3.06	8.7	13.5
2	6.0*	66.89	2.28	12.8	731	2	3.25***	54.20	3.17	17.8	7.3
3	5.5*	68.55	2.56	21.3	460	3		49.39	3.06	25.7	4.0
4	5.0*	69.03	2.66	30.6	344						
Measured Parameters in [8]						Measured Parameters in [9]					
N_{Tx}	d_0 [cm]	f_{sr} (%)	η_{m} (%)	P_{m} [mW]	$R_{\mathrm{L}}^{\dagger}$ [kΩ]	N_{Tx}	d_0 [mm]	f_{sr} (%)	η_{m} (%)	P_{m} [mW]	$R_{\mathrm{L}}^{\dagger}$ [kΩ]
1	16.8	31.12	0.08	7.69	1.43	1		34.41	0.40	1.1	11.51
		30.20	0.10	18.32	2.07	2		34.69	0.52	2.9	8.45
						3	3.8***	36.98	0.67	5.7	6.98
						4		39.27	0.63	7.3	5.57
						5		38.75	0.65	9.2	5.87
								36.20	0.74	10.4	4.56

Tolerance of * ±0.5 mm, ** ±0.75 mm and *** ±0.25 mm.
†Measured at the maximum power point (MPP).

TABLE V
ESTIMATED PARAMETERS OF SOLAR RECEIVER MODEL FOR EXPERIMENT I

Scenario I						Scenario II					
N_{Tx}	$I_{0,\mathrm{eff}}$ [μA]	$R_{\mathrm{S},\mathrm{eff}}$ [Ω]	A_{eff}	$R_{\mathrm{P},\mathrm{eff}}$ [kΩ]	$I_{\mathrm{Ph},\mathrm{eff}}$ [mA]	N_{Tx}	$I_{0,\mathrm{eff}}$ [μA]	$R_{\mathrm{S},\mathrm{eff}}$ [Ω]	A_{eff}	$R_{\mathrm{P},\mathrm{eff}}$ [kΩ]	$I_{\mathrm{Ph},\mathrm{eff}}$ [mA]
1	312.83	500	65	5.0	1.3	1	675.57	1.04	4.82	26.3	33.3
2	54.69	110	32	4.0	4.7	2	107.89	0.08	3.02	27.0	62.6
3	52.96	70	30	4.5	7.7	3	144.29	0.03	3.05	90.0	90.5
4	21.85	50	25	3.0	10.2						

large f_{sr} value of 69% in the case of $N_{\mathrm{Tx}} = 4$. Therefore, this receiver has a very high energy efficiency, very close to its STC value of 72.46%.

The values of f_{sr}, η_{m} and P_{m} for $N_{\mathrm{Tx}} = 4$ are increased by the multiplication factors of 2, 26.6 and 1.7, respectively, compared with the values of the same parameters in our first experimental study [8]. This significantly improved performance, especially for η_{m}, is attributed to the large restriction of geometrical losses by the use of the more directive optical sources of LDs compared with LEDs, and to the higher energy efficiency of multi-c-Si than that of a-Si technology of solar panels. Also, f_{sr}, η_{m} and P_{m} for $N_{\mathrm{Tx}} = 4$ are increased by the

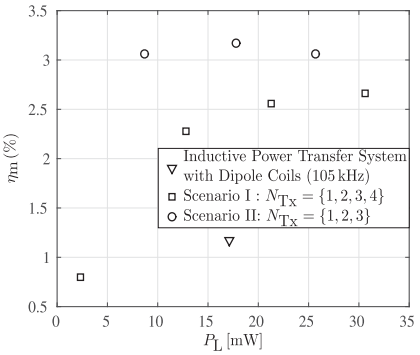

Fig. 7. Experimental maximum link efficiency versus the maximum harvested electrical power.

factors of 1.8, 4.2 and 4.2, respectively, compared with the same parameters obtained in [9]. These improved values are obtained due to the decrease in dimensions and number of cells of the solar panel that allows for the concentration of more optical power uniformly distributed on the cells. Thus, the effect of mismatch losses is less significant than that in [9].

The resistance load values measured at the MPP decrease from 3.2 kΩ to 344 Ω, while the received optical power increases. For a practical $R_{\rm L}$ value of 50 Ω, better load matching can be achieved either by an increase in $N_{\rm Tx}$ and therefore $P_{\rm Rx,o}$, or by the use of a dc-to-dc converter for maximum power point tracking [59].

4) Scenario II—Results and Discussion: In Scenario II, the values of $f_{\rm sr}$ and $\eta_{\rm m}$ are expected to increase as the number of optical transmitters increases. However, this expectation is not confirmed in the case of $N_{\rm Tx} = 3$. This is explained by the significantly low decrease in effective series resistance value from 80 mΩ ($N_{\rm Tx} = 2$) to 30 mΩ ($N_{\rm Tx} = 3$) compared with the transition from 1.04 Ω ($N_{\rm Tx} = 1$) to 80 mΩ ($N_{\rm Tx} = 2$), as shown in Table V. Therefore, more power is dissipated in the series resistance and, finally, the FF and efficiency of the solar cell decrease. The series resistance of the cell decreases, when the incident optical power increases. This is attributed to the increase in the conductivity of the active layer [60]. Also, note that the curve of maximum link efficiency as a function of harvested power in Scenario II shown in Fig. 7 is in close agreement with the curve of solar cell efficiency versus incident optical power in [61].

Comparing the two scenarios, the best value of $\eta_{\rm m} = 3.17\%$ is achieved in the case of $N_{\rm Tx} = 2$ for Scenario II. Note that this value of maximum link efficiency is low because of the low values of $\eta_{\rm LD}$ and $\eta_{\rm sr}$(5.2 m) as shown in Section III-D7.

A comparison of the values of $f_{\rm sr}$ and $\eta_{\rm m}$ for $N_{\rm Tx} = 2$ with the values of the same parameters in [8] shows an increase of 1.6 and 32 times, respectively. The same comparison with the results of [9] presents an increase by 1.6 and 6.2 times, respectively. Also, quantity $P_{\rm m}$ for $N_{\rm Tx} = 3$ is increased by the factors of 1.4 and 4.4 compared with [8] and [9], respectively. A slightly better performance in terms of $\eta_{\rm m}$ of Scenario II compared with Scenario I is observed. This is attributed to the larger optical-to-electrical conversion efficiency of mono-c-Si cell than that of multi-c-Si panel as expected by observing Table III. Also, the larger area of 2.3 times of the PV cell compared with the solar panel allows for the reception of a larger amount of $P_{\rm Rx,o}$ reducing the geometrical losses.

Finally, the values of measured $R_{\rm L}$ at the MPP are quite low due to the low values of $V_{\rm L}$. Therefore, matching of the output of the cell with a practical load of 50 Ω can be achieved either by a dc-to-dc converter or by the connection of a large number of cells in series.

5) Comparison of Scenarios I and II with an IPTS: In [10], a state-of-the-art experimental study is presented by the implementation of an IPTS with dipole coils able to deliver amounts of power in the order of hundreds of W. In Fig. 16 of [10], the power efficiency measured from the input of the inverter to the load resistor is plotted as a function of the power harvested from the load for different values of distance of 2 m, 3 m, 4 m and 5 m. The operating frequency of the system is 105 kHz [10]. A comparison of the OW systems implemented in the two Scenarios of Experiment I and the IPTS is shown in Fig. 7 in terms of link efficiency at a distance of 5 m. When Scenario II is applied, the maximum link efficiency is improved from a value of 1.17% to 3.17% that represents a significant increase of 2.7 times. Therefore, taking into account the fact that IPTSs are designed to operate at short distances of a few cm [14] or m [10], the developed OW link with two sources has an acceptable value of $\eta_{\rm m}$ and the link distance can be further extended.

6) Experiment II—Objective, Method, Setup, Applied Analytical Model and Results: The objective of Experiment II is to determine the efficiency values of each of the four LDs as a function of their input power. Therefore, the output optical power of each LD is measured for 22 different values of input electrical power. A Thorlabs S121B Si sensor with a square area of 1×1 cm^2 is placed at 1.5 mm from each LD in order to collect and measure the total amount of optical power of each laser beam. The mean values of experimental data are fit by two simple quadratic curves applied to the two operation regions of the device. These two regions are characterized by spontaneous and stimulated emission, respectively.

The external power efficiency of the four LDs is shown in Fig. 8 as a function of $P_{\rm in}$. The maximum efficiency values of the four LDs shown as #1, #2, #3 and #4 are measured to be 28.1%, 30.2%, 32.2% and 32.9%, respectively. In the first region of the theoretical curve, the output optical power remains at very low levels of up to 94.6 μW, as $P_{\rm in}$ increases from 0 to 95.4 mW. Also, for the same values of $P_{\rm in}$, the mean value of power efficiency of the four LDs ranges from 0.05% to 0.1%. This region of applied $P_{\rm in}$ causes spontaneous emission to the LD, one of the basic forms of interaction between atoms and photons in quantum physics [62]. In spontaneous emission, an atom transits from an upper energy level, E_2, to a lower energy level, E_1, releasing a photon, and this is a random process. In the second region of the theoretical curve, $P_{\rm Tx,o}$ increases significantly up to 86.1 mW with a respective efficiency of 29.1%, while $P_{\rm in}$ scales from 95.4 mW to 320 mW. This region

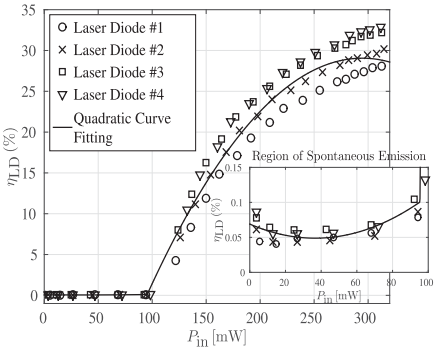

Fig. 8. Experiment II: Laser diodes efficiency versus input electrical power.

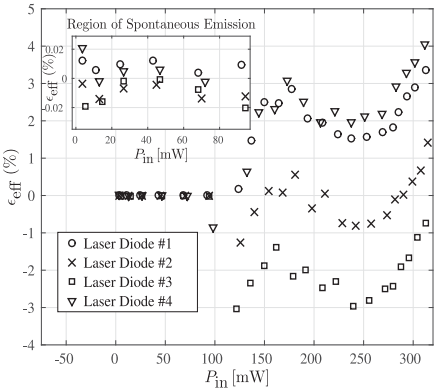

Fig. 9. Experiment II: Efficiency error as a function of input electrical power for four laser diodes.

of P_{in} induces stimulated emission to the optical source [62]. In stimulated emission, a photon of energy $E_2 - E_1$ interacts with an atom placed at an upper energy level. This atom transits to a lower energy level emitting a second photon of similar characteristics with the first one.

In order to compare the variation between the four LDs, the error in efficiency, ϵ_{eff} (%), is used and is defined as the difference in theoretical efficiency by the experimental efficiency data for each LD. Fig. 9 shows how the error in efficiency of the four LDs scales with the input electrical power of each LD. The mean squared error in power efficiency of each of the LDs is calculated to be $3.46 \cdot 10^{-4}$, $3.13 \cdot 10^{-5}$, $3.52 \cdot 10^{-4}$ and $4.89 \cdot 10^{-4}$. This means that the LD shown as #2 in Figs. 8 and 9 best approximates the efficiency values of the theoretical curve. In the case of a large number of LDs, such as the 42-based laser transmitter designed in Section V, the variation of LDs is expected to affect the harvested power. Therefore, to affirm 1 W with high confidence, the required number of optical sources should be estimated based on the LD with the lowest efficiency.

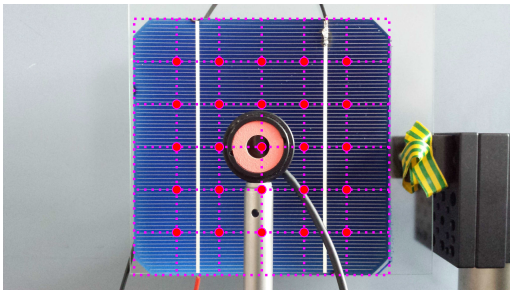

Fig. 10. Experiment III: Measurement points of irradiance for the calculation of $P_{\mathrm{Rx,o}}$ in front of the solar cell.

7) Experiment III—Objective, Method, Setup and Results: Experiment III is undertaken for the determination of the solar cell efficiency. Two LDs with aspheric lenses are transmitting power to the mono-c-Si cell placed at a distance of 5.2 m. The electrical input power is 561.3 mW. The S121B sensor is used for the measurement of 25 values of power, P_{s}, at a distance of 3.4 cm from the solar cell. The measurement points are located on a square grid as shown in Fig. 10. The distance between two consecutive points is 2.08 cm. The average irradiance of the 25 measured points is computed and is multiplied by S_{eff}. Therefore, the value of $P_{\mathrm{Rx,o}}(5.2\,\mathrm{m})$ is calculated, and the parameters of $\eta_{\mathrm{sr}}(5.2\,\mathrm{m})$, $\rho(5.2\,\mathrm{m})$ and $\eta_{\mathrm{ceff}}(5.2\ \mathrm{m})$ are determined from (44), (46) and (48), respectively.

The 25 measured data of P_{s} are shown in Fig. 11 versus the x- and y-dimensions of the solar cell. The power of each of the two optical transmitters measured at the (x, y, z) points of $(0, 0, 3.7\ \mathrm{cm})$ and $(0, 0, 3.2\ \mathrm{cm})$ is 74.58 mW and 72.8 mW, respectively. These values are significantly attenuated at a distance of 5.2 m from the transmitters. In particular, the maximum optical power measured at the (x, y, z) point of $(0, 2.08\ \mathrm{cm}, 5.2\ \mathrm{m})$ is 3.12 mW. The average irradiance value of these 25 measurements is $0.86\ \mathrm{mW}/(1\ \mathrm{cm}^2) = 0.86\ \mathrm{mW/cm}^2$. Therefore, the received optical power of the cell is calculated to be $P_{\mathrm{Rx,o}}(5.2\ \mathrm{m}) = 0.86 \times 12.5^2 = 134.38$ mW.

The application of $P_{\mathrm{in}} = 17.8$ mW and $P_{\mathrm{Rx,o}} = 134.38$ mW to (44) results in $\eta_{\mathrm{sr}}(5.2\ \mathrm{m}) = 13.25\%$ in the case of $N_{\mathrm{Tx}} = 2$. This value of solar receiver efficiency is 5.37% lower than the respective one at STC (see Table III) and therefore the cell is able to accommodate more optical power. For this reason, the specific mono-c-Si cell is selected to be the receiver in the simulation model developed for the objective of harvesting 1 W in Study III. Moreover, the maximum power that this cell can generate under STC is 2.91 W according to Table III that is larger than the required amount of 1 W.

So long as the experimental value of $\eta_{\mathrm{sr}}(5.2\ \mathrm{m})$ is now known, an estimation of the collection efficiency can be made using (48). The term $(1 - r)$ of (48) is assumed to be negligible because $r = 0.0025 \ll 1$. The input electrical power of 561 mW is equally supplied to the two optical transmitters. Thus, the electrical-to-optical efficiency of two optical

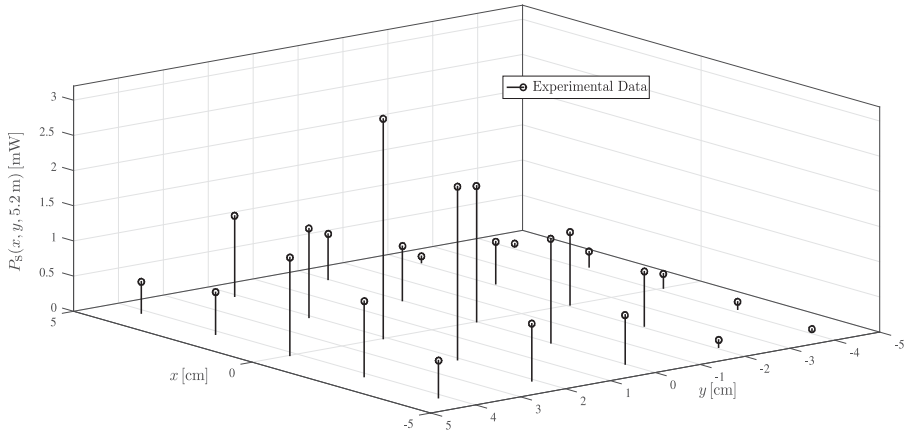

Fig. 11. Experiment III: Optical power measured by a sensor on the x-y transverse plane of the solar cell.

transmitters for $P_{\rm in} = 561$ mW is the same as $\eta_{\rm LD}$ of $N_{\rm Tx} = 1$ for $P_{\rm in} = 280.5$ mW. Also, a mean value of $\eta_{\rm LD} = 26.76\%$ is calculated for $P_{\rm in} = 280.5$ mW based on the quadratic curve fitting of Fig. 8. Therefore, the application of $\eta_{\rm m} = 0.0317$, $\eta_{\rm LD} = 0.2676$ and $\eta_{\rm sr}(5.2\ {\rm m}) = 0.1325$ to (48) results in the collection efficiency value of $\eta_{\rm ceff}(5.2\ {\rm m}) = 89.4\%$. This very high value allows for the characterization of the link with two LDs as highly directive so that it effectively delivers 134.38 mW to a solar cell area of $12.5 \times 12.5\ {\rm cm}^2$ placed at 5.2 m with only 10.6% of optical losses.

Finally, the application of $I_{\rm Ph,eff} = 62.6$ mA and $P_{\rm Rx,o}(5.2\ {\rm m}) = 134.38$ mW to (46) gives an estimated responsivity of $\rho(5.2\ {\rm m}) = 0.47$ mA/mW. An experimental value of responsivity of $\rho(5.2\ {\rm m}) = 0.49$ mA/mW is obtained under the assumption of $I_{\rm Ph,eff} \simeq I_{\rm sc} = 65.4$ mA.

8) Estimation of the Number of Optical Transmitters: Let $N_{\rm Tx,req}$ be the required number of pairs of LDs and lenses for harvesting 1 W at a 5.2 m link distance. In Scenario II of Experiment I, a value of $V_{\rm m} = 351$ mV is achieved with $P_{\rm m} = 17.8$ mW for $N_{\rm Tx} = 2$. Therefore, a required voltage $V'_{\rm m} = 537$ mV is assumed for the solar cell at high illumination levels for attaining $P'_{\rm m} = 1$ W according to [56]. The load current at MPP is calculated to be $I'_{\rm m} = 1/0.537 = 1.86$ A. The values of 537 mV and 1.86 A are substituted for $V_{\rm L}$ and $I_{\rm L}$, respectively, in the 'exhaustive' search algorithm (36). This results in the following set of parameters: $(I_{0,\rm eff}, R_{\rm S,eff}, A_{\rm eff}, R_{\rm P,eff}, I_{\rm Ph,eff}) = (83.9\ {\rm pA},\ 0.5\ {\rm m\Omega},\ 1,\ 500\ {\rm k\Omega},\ 1.96\ {\rm A})$. The responsivity of the solar panel is considered to be $\rho = 0.49$ A/W, as measured in Experiment III. Solving (46) for $P_{\rm Rx,o}$ results in: $P_{\rm Rx,o} = I_{\rm Ph,eff}/\rho = 1.96/0.49 = 4$ W. An assumption of 10.6% of geometrical optical losses is made, as measured in Experiment III. Thus, the transmitted optical power is calculated to be $P_{\rm Tx,o} = P_{\rm Rx,o}/\eta_{\rm ceff} = 4/0.894 = 4.47$ W. Therefore, the required number of optical transmitters is calculated to be: $N_{\rm Tx,req} = 4.47/(73.69 \times 10^{-3}) \approx 61$, where 73.69 mW is the average output optical power of the two LDs measured in Experiment III.

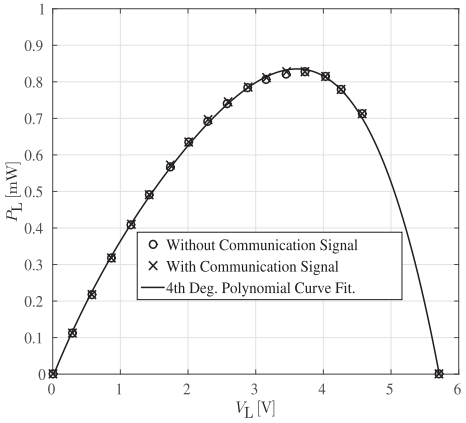

Fig. 12. V-P curve of resistor load with and without the application of a communication signal.

9) Variation of Harvested Power and Link Efficiency Induced by the Application of Data Communication: In order to investigate the variation of PH and link efficiency induced by the reception of an information signal, an experiment with the solar receiver designed in [35] is undertaken. In particular, a single optical transmitter transfers power and data simultaneously to the solar panel placed at a link distance of 5.2 m. Also, an orthogonal frequency division multiplexing (OFDM) signal with adaptive bit and energy loading is applied for communication [35]. The OFDM signal has a single sided communication bandwidth of 5 MHz. An average data rate of 16.6 Mb/s is achieved at the receiver with a respective average bit error rate of $1.52 \cdot 10^{-3}$. Fig. 12 shows how the harvested power of the load scales with voltage, with and without the reception of the alternating current (ac) communication signal. A fourth degree polynomial is

TABLE VI
SUMMARY OF EXPERIMENT IN STUDY II

Study II		Laser beam collimation	
Experiment		IV	
Objective		Determination of beam divergence with a target of 1 mrad	
Method		Measurement of diameter of circular laser beam images and 23 values of received optical power	
Setup	Optical source	Single laser diode	
	Optics	Spherical lens	
	Receiver	Optical power sensor	
	Measurement device	Optical power sensor	
	Link distance	4 m and 8 m	
Analytical model		(1)–(10) and (14)–(32)	
Results		Definition I	Definition II
		$\psi = 2.1$ mrad	$\psi_x = 3$ mrad
			$\psi_y = 5.8$ mrad

TABLE VII
STUDY II: DATA SHEET PARAMETERS OF LENS

Parameter	Δ	R_1	R_2	t_c	f	n	r
Unit	[cm]	[mm]	[mm]	[mm]	[cm]	–	(%)
Value	7.5	∞	-38.76	32.68	7.5	1.52	1.5

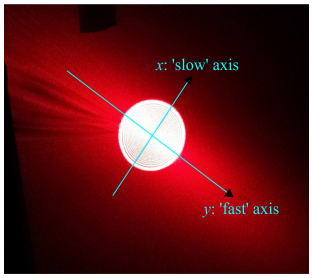

Fig. 13. Experiment IV: Beam pattern and vertical axes for the determination of beam divergence.

applied to the experimental data for curve fitting. The harvested power of the load remains the same, even when an OFDM signal is received. So long as the time domain OFDM signal has a zero mean value, the dc biased optical OFDM signal has the mean value of the dc bias. The receiver circuit comprises one branch for EH and a second branch for data communication with an inductor and a capacitor, respectively. Therefore, the EH branch captures the dc component, whereas the communication branch captures the ac signal. Finally, since the input electrical power to the transmitter is constant, the link efficiency also remains unaffected by the communication signal received.

IV. STUDY II: LASER BEAM COLLIMATION

The objective, method, setup, applied analytical model and results of Experiment IV of Study II are summarized in Table VI.

A. Objective

The objective of Study II is the creation of an OW link able to transmit power efficiently at long distances, such as 100 m−300 m. Thus, Experiment IV is undertaken for the determination of beam divergence with a targeted value of 1 mrad. For this reason, the collimation capability of a large diameter lens is investigated. The motivation of using a relatively large optical element in front of the LD is two-fold. First, the etendue law, also known as brightness theorem, states that the product of source area and the solid angle subtended by the system's entrance pupil as seen by the source remains constant in an optical system with passive components [63], [64]. This means that decreased beam divergence and, therefore, efficient beam collimation can be achieved by a respective increase in dimensions of the lens. Also, a lens with large diameter is able to spread the optical power received from the LD decreasing the irradiance values along any of its transverse planes. Therefore, eye safety is improved, and the product of LD-lens can be classified as a lower Class [11].

B. Experimental System and Results

1) Experiment IV—Method, Setup and Applied Analytical Model: The characteristics of the red LD used in this experiment are given in Table III. Also, a 45-368 plano-convex (PCX) spherical lens made of borosilicate glass Schott BK7 with magnesium fluoride (MgF_2) ARC is used [65]. The features of the lens are given in Table VII.

In Experiment IV, the beam generated from the LD is collimated by the PCX spherical lens placed at $d_0 = 5.15$ cm from the LD with a tolerance of ± 0.5 mm. The optical power emitted from the LD is measured to be 4.76 mW. The pattern of circular and elliptical image of the lens and LD, respectively, at 4 m from the output surface of the lens are shown in Fig. 13. The beam divergence is defined and determined in two different ways. First, the beam divergence is defined as the plane angle of the truncated cone created by the circular image that is measured at two different link distances, d_1 and d_2. In particular, the diameter of the circular image, D_{im}, is measured at $d_1 = 4$ m and $d_2 = 8$ m, respectively. In this case, the beam divergence is calculated by:

$$\psi = 2\tan^{-1}\left[\frac{D_{\mathrm{im}}(d_2) - D_{\mathrm{im}}(d_1)}{2(d_2 - d_1)}\right]. \tag{51}$$

Also, note that the new beam waist is located before the distance of 4 m so that the images at 4 m and 8 m belong entirely to a diverging cone.

So long as the first definition does not include any information of the beam intensity, a second definition is used. In particular, the half width of the beam is estimated at the two points where the irradiance is decreased by $1/e$ times or 36.8% of the peak irradiance. For this reason, appropriate curve fitting with the

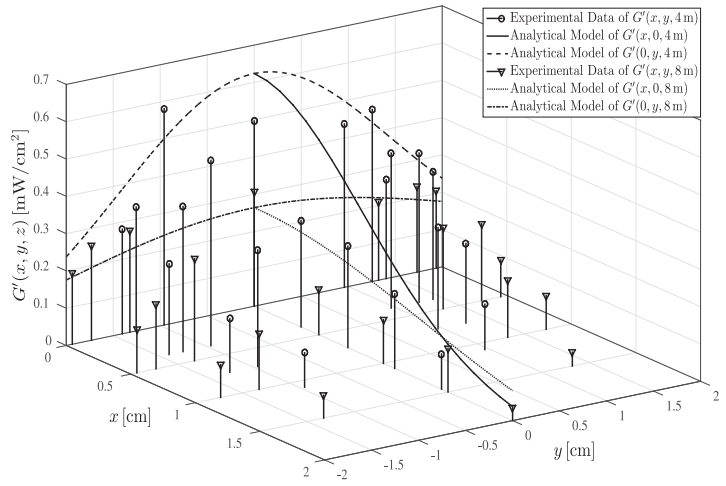

Fig. 14. Experiment IV: Data of irradiance on the x–y transverse plane of the laser beam at 4 m and 8 m accompanied by the respective analytical model curves.

TABLE VIII
ANALYTICAL PARAMETERS FOR CURVE FITTING OF DATA IN EXPERIMENT IV

Parameter	Unit	Value	Parameter	Unit	Value
$P_{\mathrm{Tx,o}}$	[mW]	4.76	A	–	1
λ_0	[nm]	660	B	[mm]	21.5
ϑ_x	[deg]	6.25	C	[m^{-1}]	-13.42
ϑ_y	[deg]	10.6	D	–	0.712
W_{0x}	[μm]	1.92	W_{2x}	[mm]	7.99
W_{0y}	[μm]	1.12	W_{2y}	[mm]	13.66
G_0	[kW/cm^2]	140.7	R_{2x}	[m]	3.54
d_0	[cm]	5.15	R_{2y}	[m]	3.54
W_{1x}	[mm]	5.64	d_{1x}	[m]	-3.54
W_{1y}	[mm]	9.64	d_{1y}	[m]	-3.54
R_{1x}	[mm]	51.5	W_{3x}	[μm]	92.93
R_{1y}	[mm]	51.5	W_{3y}	[μm]	54.39

analytical model presented in Section III-B1, III-B2 and III-B3 is applied to the data measured along the 'slow' x- and 'fast' y-axes, respectively. A number of 23 irradiance measurements is conducted at the distances of 4 m and 8 m inside the semi circle of the image. Also, the illumination symmetry around both axes enables the calculation of the received optical power inside the circular image. Here, the beam divergence along the x- and y-axis is calculated by:

$$\psi_x = 2\tan^{-1}\left[\frac{W'_x(d_2) - W'_x(d_1)}{d_2 - d_1}\right] \tag{52}$$

and

$$\psi_y = 2\tan^{-1}\left[\frac{W'_y(d_2) - W'_y(d_1)}{d_2 - d_1}\right], \tag{53}$$

respectively. The values of $W'_x(z)$ and $W'_y(z)$ denote the beam radii up to the $1/e$ points of peak irradiance along the x- and y-direction and have already been defined in (30) and (31), respectively.

2) Experiment IV—Results and Discussion: The diameters of the circular images at 4 m and 8 m are measured to be 2.9 cm and 3.75 cm, respectively. Thus, the application of $d_1 = 4$ m, $d_2 = 8$ m, $D_{\mathrm{im}}(4\ \mathrm{m}) = 2.9$ cm and $D_{\mathrm{im}}(8\ \mathrm{m}) = 3.75$ cm to (51) results in a measured beam divergence of $\psi = 2.12$ mrad. This value is very close to the objective of 1 mrad that is achievable by the use of a lens with even larger diameter than that of the spherical one. Also, the optical power contained in the circular image is measured to be 1.94 mW and 1.87 mW at $d_1 = 4$ m and $d_2 = 8$ m, respectively. Therefore, 40.8% and 39.3% of the transmitted optical power of $P_{\mathrm{Tx,o}} = 4.76$ mW is included in the circular image at 4 m and 8 m, respectively. This means that the lens placed at 5.15 cm from the LD fails to collect and collimate the whole optical power of the source inducing geometrical losses. Finally, the elliptical image (see Fig. 13) includes the remaining amount of optical power.

The experimental data of intensity at 4 m and 8 m fitted by the respective curves of analytical model are shown in Fig. 14. The curves labeled as 'Analytical Model' are derived by the use of (1)–(10) and (14)–(32). The analytical parameters used for curve fitting of the experimental data are shown in Table VIII. The slight deviation of some measured data points from the elliptical Gaussian fitting is explained by the existence of the diffraction effect [66]. This effect occurs when an optical wave passes through an aperture and is strongly dependent on the distance between the aperture and the observation plane, the wavelength and the aperture dimensions. In particular, here the diffraction effect stems from the transmission of the laser beam through the circular aperture of the lens mount to free space. The small black rings observed in the circular image of Fig. 13 and in Fig. 4 are translated to deep 'dips' of the irradiance. Also, even slight misalignment between the optical source and the lens can significantly affect the beam irradiance pattern observed at the far field. The application of the physical model

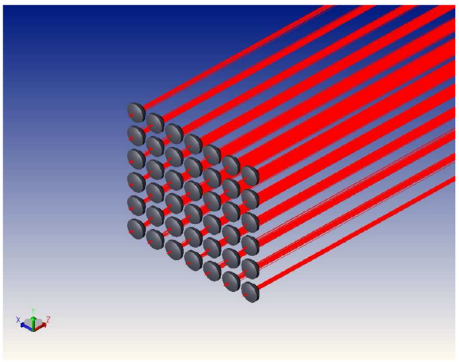

Fig. 15. Non-sequential components shaded model of the array of 7×6 laser diodes and lenses.

of the elliptical Gaussian beam for curve fitting results in the values of $W'_x(4\text{ m}) = 1.2$ cm and $W'_x(8\text{ m}) = 1.8$ cm. Therefore, the application of these values to (52) yields $\psi_x = 3$ mrad. Similarly, the beam radius along the y-axis is calculated to be $W'_y(4\,\text{m}) = 2\,\text{cm}$ and $W'_y(8\,\text{m}) = 3.15\,\text{cm}$. Therefore, the beam divergence of the 'fast' axis is computed to be $\psi_y = 5.75$ mrad by (53).

V. Study III: Harvested Power with a Targeted Value of 1 W

A. Motivation and Objective

In Study I, the number of red LDs required to harvest 1 W using a mono-c-Si cell was estimated to be 61. Also, the experimental levels of the transmitted power were in the order of mW. As a next step, here an array of 42 LDs is designed for the transmission of an amount of optical power able to be converted to 1 W by the mono-c-Si cell. The number of 42 LDs operating at 785 nm is selected because of their ability to transmit larger amounts of power with higher efficiency than the red LDs used in Study I. In order to achieve a maximum harvested power of 1 W, a minimum efficiency of 13.89% is required from the solar cell.

B. Approach

The transmitter of 7.2 W of total optical power is designed in Zemax comprising 42 LDs and collimation lenses. Also, the elliptical Gaussian propagation model presented in Section III is used to support the simulation results given in Section V-E.

C. Simulation Model

The optical design consists of the following objects: source diode, even asphere lens, array and detector rectangle created in the non-sequential components mode. Laser diodes and respective aspheric lenses are placed in a rectangular array with perfectly aligned optical axes, as shown in Fig. 15.

TABLE IX
Simulation Parameters of 785 nm Laser Diode

	Parameter	N_{lr}	N_{anr}	$P_{\text{Tx,o}}$	a_x	a_y
	Unit	–	–	[mW]	[deg]	[deg]
Source	Value	10^3	10^7	171.1	6.37	12.74
diode	Parameter	S_x, S_y	N_x	N_y	Δx	Δy
	Unit	–	–	–	[mm]	[mm]
	Value	1	7	6	15.2	16.77

The object source diode is used for the simulation of a Panasonic LNCT22PK01WW CW LD. This LD has a typical efficiency of 27.4% and FWHM beam divergences of $\vartheta_{\parallel} = 7.5°$ and $\vartheta_{\perp} = 15°$. According to the model of the source diode, the intensity of the beam generated from a rectangular source is given by:

$$G_{\text{s}}(\theta_x, \theta_y) = G_{\text{s},0} \times \exp\left\{-2\left[\left(\frac{\theta_x}{a_x}\right)^{2S_x} + \left(\frac{\theta_y}{a_y}\right)^{2S_y}\right]\right\}, \quad (54)$$

where $G_{\text{s},0}$ denotes the overall peak intensity, note that the manufacturers of LDs give the relative instead of the absolute value of intensity; θ_x and θ_y are the angles in degrees along the x- and y-directions, respectively; and a_x and a_y are the angular divergences in degrees on the x-z and y-z planes, respectively. The FWHM angular divergences are given by $a_x = \vartheta_{\parallel}/\sqrt{2\ln(2)}$ and $a_y = \vartheta_{\perp}/\sqrt{2\ln(2)}$.

Also, the values of S_x and S_y are the super-Gaussian factors along the x- and y-axes, respectively and range from 0.01 to 50. The special case of $S_x = S_y = 1$ corresponds to a typical elliptical Gaussian beam. The simulation parameters of the object source diode are given in Table IX. Parameters N_{lr} and N_{anr} denote the number of layout rays and analysis rays, respectively. The term $P_{\text{Tx,o}}$ is used for the output optical power of each LD. Also, N_x and N_y represent the number of LDs placed along the x- and y-axis, respectively. Finally, Δx and Δy are the distances between the centers of two LDs and lenses placed consecutively along the x- and y-direction, respectively.

The even asphere lens is used for the simulation of a Thorlabs ACL12708U-B lens with an ARC for the wavelength range of 650 nm−1050 nm [67]. The aspheric coefficients of lens are given in [67]. The array object is used for the creation of a rectangular array consisting of 7×6 identical aspheric lenses. An orthogonal descent optimizer is used for the determination of d_0 which denotes the distance between each LD and the input surface of its respective collimation lens. The performance criteria are the maximization of total flux and spatial uniformity. Finally, the value of d_0 is refined by the use of a Hammer optimizer yielding $d_0 = 3.737$ mm. A $12.5 \times 12.5\,\text{cm}^2$ rectangular detector modeling the mono-c-Si solar cell is used to measure the received optical power for a distance range of [1, 100] m using increments of 1 m. The material of the detector rectangle is selected to be absorb and the number of pixels along the x- and y-dimension is 150×150.

TABLE X
ANALYTICAL PARAMETERS

Parameter	Unit	Value	Parameter	Unit	Value
$P_{\mathrm{Tx,o}}$	[mW]	171.1	R_{1x}	[mm]	3.74
λ_0	[nm]	785	R_{1y}	[mm]	3.74
ϑ_x	[deg]	3.75	A	–	0.836
ϑ_y	[deg]	7.5	B	[mm]	4.93
N_x	–	7	C	[cm^{-1}]	1.247
N_y	–	6	D	–	0.46
Δx	[mm]	15.2	W_{2x}	[μm]	528.19
Δy	[mm]	16.77	W_{2y}	[mm]	1.06
W_{0x}	[μm]	3.81	R_{2x}	[m]	−1.38
W_{0y}	[μm]	1.9	R_{2y}	[m]	−1.39
G_0	[MW/cm^2]	1.51	d_{1x}	[cm]	54.63
d_0	[mm]	3.737	d_{1y}	[m]	1.27
W_{1x}	[μm]	244.97	W_{3x}	[μm]	410.15
W_{1y}	[μm]	491.99	W_{3y}	[μm]	311.92

D. Eye Safety Regulations

1) Single Laser Diode: The LD considered in the simulation model is also classified as Class 3B according to the manufacturer [44]. The MPE in terms of irradiance is calculated to be $\nu = 1.5$ mW/cm^2 similar to the methodology presented in Appendix C. Also, the NOHD is determined to be $d_{\mathrm{NOHD}} = 75$ cm and, therefore, the near infrared beam radiation requires enclosure with a length of 75 cm.

2) Laser Diode and Collimation Lens: The optical transmitter consisting of the LD and lens considered in the simulation model is classified as Class 3B, similar to the methodology presented in Appendix D. The MPE is calculated to be $\nu = 6.66$ mW/cm^2 and the NOHD is $d_{\mathrm{NOHD}} = 54.3$ m. Therefore, a shielding tube with a length of 54.3 m is required which is not suitable for practical applications. In order to restrict the NOHD, either the beam diameter should increase by the use of a lens with a larger diameter or the output power of the LD should decrease based on the MPE value.

E. Results and Discussion

The parameters of the analytical model presented in Section III-B1, III-B2 and III-B3 are used to verify the simulation model and are summarized in Table X. The analytical curves of $\pm W'_x(z)$ and $\pm W'_y(z)$ of a single optical link are shown in Fig. 16(a) and (b) for distances up to 5 m and up to 100 m, respectively. These curves are derived by the use of (1)–(10) and (14)–(31). Note that the reference point $z = 0$ denotes the tangent plane to the output surface of the lens and the beam widths refer to the FWHM intensity points. In Fig. 16(a), it is observed that the laser beam along the y-axis focuses on a smaller beam waist at a longer distance and then diverges more than the laser beam along x-axis. The theoretical values of beam divergence expressed at FWHM intensity are calculated to be $\psi_x = 1.22$ mrad and $\psi_y = 1.6$ mrad according to Fig. 16(b). Also, the beam diameters along the x- and y-directions are 12.1 cm and 15.8 cm, respectively, at the link distance of 100 m.

Finally, the received optical power of the 42 laser link is shown as a function of distance in Fig. 17 based on the analytical and simulation model. The two curves are in close agreement, and a maximum gap of 1 dB is observed at the distance of 100 m. According to the analytical model, a value of optical power of 7.15 W is delivered effectively to 20 m. Also, a simulation-based value of 7.13 W is able to be transferred to 10 m. After the distance of 20 m, the analytical curve falls with a larger rate compared with the simulation curve (see Fig. 17). This effect is attributed to the term of $W'_x(z')W'_y(z'')$ that exists in the denominator of (32) in the theoretical model. This term attenuates the irradiance and therefore the optical power faster

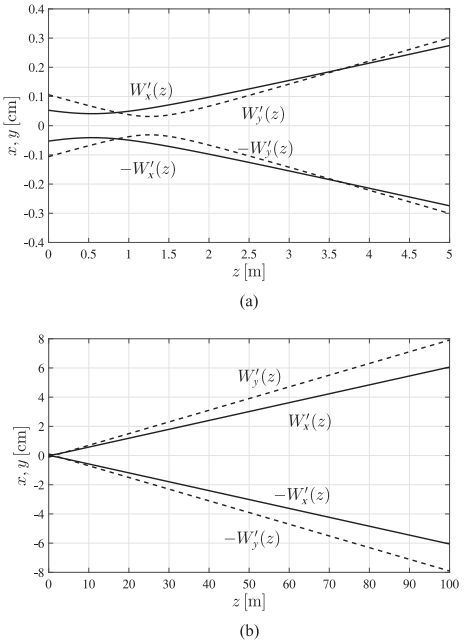

Fig. 16. Theoretical full width at half maximum (FWHM) intensity of the single laser beam versus distance up to (a) 5 m and (b) 100 m along x- and y-axes.

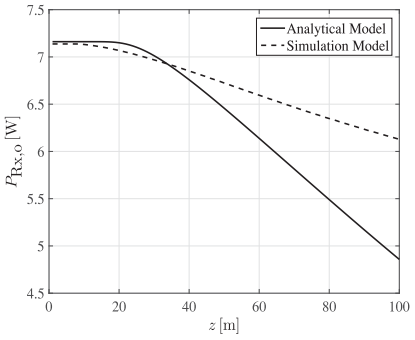

Fig. 17. Received optical power versus distance for two different models.

than the respective irradiance of (54) of the simulation model. Also, the rear surface of the aspheric lens is modeled as spherical in Section III-B2 and this geometrical assumption makes light collimation less efficient. The geometrical losses of optical power are 0.09 dB and 0.1 dB at the link distance of 30 m for the analytical and simulation model, respectively. This means that the particular multiple laser-based link presents a very large collection efficiency of 97.9% and 97.7% at 30 m according to theory and simulation, respectively. The optical-to-electrical efficiency of the particular cell is measured to be 13.25% for an input optical power of 134.38 mW in Experiment III. A received optical power of about 7 W is expected to increase the power conversion efficiency. At the same time the increase in the temperature of the cell is expected to reduce the value of η_{sr} slightly. Overall, the targeted value of 1 W is expected to be achieved in practice by this large amount of received optical power for link distance values of up to 30 m.

VI. Summary and Conclusion

In this comprehensive study, the application of the principle of OWPT to SCs was investigated for the first time for an indoor scenario during darkness hours, i.e. in the absence of ambient light.

In particular, an experimental study was undertaken to determine the maximum link efficiency, maximum harvested power and optical receiver efficiency. The optical sources were up to four red CW LDs combined with the use of aspheric lenses for beam collimation. The optical receivers were a solar panel and a solar cell based on the technology of multi-c-Si and mono-c-Si, respectively. The link distance was 5.2 m. A high energy efficiency with a FF of 69% and a harvested electrical power of 30.6 mW was attained by the solar panel. The best value of maximum link efficiency of 3.2% was achieved by two optical transmitters and the solar cell. This relatively low value was explained by the contribution of the low measured average efficiency of the two LDs of 26.8% and the solar cell efficiency of 13.3%. For the same link, the geometrical losses of optical power were estimated to be only 10.6% and this fact was sufficient to characterize the optical link as highly efficient with OWPT showing great potential at longer distances. However, the analytical calculation of the MPE and NOHD for eye safety resulted in the need for a beam enclosure of up to 3.6 m. Also, a comparison was made for the same OW link with a state-of-the-art IPTS with optimally shaped dipole coils. As a result, a performance improvement in terms of total power efficiency by 2.7 times was achieved by the link consisting of two LDs and a solar cell. Therefore, the applicability of indoor OWPT to SCs was demonstrated with an acceptable link efficiency and the possibility of extending the distance of 5.2 m.

Another experimental study was undertaken for the determination of the laser beam divergence with a targeted value of 1 mrad. In particular, an optical transmitter was created by the use of the red LD and a spherical lens. Also, an analytical model was developed for the prediction of the elliptical Gaussian beam propagation and was applied to the experimental data for curve fitting and estimation of its unknown parameters. As a result, the divergence of full width at 36.8% of peak intensity was determined to be 3 mrad and 5.75 mrad along the 'slow' and 'fast' axes of the laser beam, respectively. Moreover, the beam divergence determined by the diameter of the circular image was measured to be only 2.1 mrad. Thus, this single optical link was characterized by high directivity enabling the application of OWPT to longer distances.

The best maximum harvested power measured in the experiments was 30.6 mW. This provided the basis for the determination of the number of LDs needed to achieve the target of 1 W which is required for the operation of small RF cells. This led to a 42 laser-based transmitter of 7.2 W that transfers power to the mono-c-Si cell placed up to 100 m. The system was designed by the use of the simulation tool Zemax and the respective theoretical model of Gaussian beam propagation. The beam divergence defined by the FWHM intensity was analytically determined to be 1.2 mrad and 1.6 mrad along the 'slow' and 'fast' axes, respectively. In addition to this large directivity, the simulation and analytical models were in close agreement showing that the transfer of 7.2 W up to 30 m with geometrical losses of only 2% was feasible. Therefore, the minimum required efficiency of the solar cell was only 13.9%, while an efficiency of 13.3% was measured in the experiments for an input optical power of 134.4 mW. However, a beam enclosure was required due to eye safety restrictions.

Finally, in a practical outdoor scenario of power supply to a SC, the great potential of harvesting sunlight power in addition to WPT from 'dedicated' laser sources remains unresearched. This important advantage of solar cells over rectennas, harvesting additional power from a natural source as well as from human-made EM sources, gives the opportunity for a wide application of the principle of OWPT.

Appendix A
Motivation for a Gaussian Beam Model and Paraxial Approximation

The manufacturers' data sheets for LDs give a graph of the far field relative intensity versus the parallel and perpendicular to the junction angular divergence of the beam. These angular divergence graphs can be approximated by Gaussian curves of different widths for the LDs considered in this research [43], [44]. Also, the selected LDs operate at the fundamental transverse electrical mode. Therefore, an elliptical Gaussian beam propagation model is considered for the generated laser beam [41].

Ray optics, also known as geometrical optics, is the simplest theory that describes light propagation [46]. According to this theory, light consists of optical rays traveling from one medium to another under defined geometrical rules. Optical rays are described by their position in space and inclination. In paraxial optics, a subset of ray optics, rays propagate at small angles from an optical axis, which the optical components are aligned with. Also, in wave optics, waves with wavefront normals forming small angles with the propagation z-axis are called paraxial. These waves satisfy the paraxial Helmholtz equation [68]. A well known and useful solution of this equation is the

Gaussian beam. Paraxial optics is used in first-order ray tracing and Gaussian optics. In particular, the paraxial approximation is used and is described by the properties: $\sin(\vartheta) \approx \vartheta, \tan(\vartheta) \approx \vartheta$ and $\cos(\vartheta) \approx 1$, where ϑ [rad] is the angle between the optical axis and the ray.

APPENDIX B
MATHEMATICAL DERIVATION OF (12) AND (43)

The total optical power of the beam is expressed as the double integral over the transverse x-y plane by:

$$\begin{aligned} P_{\mathrm{Tx,o}} &= \int_{-\infty}^{\infty}\int_{-\infty}^{\infty} G(x,y,z)\mathrm{d}x\mathrm{d}y \\ &= G_0 \frac{W_{0x}W_{0y}}{W_x(z)W_y(z)} \int_{-\infty}^{\infty} \exp\left[\frac{-2x^2}{W_x^2(z)}\right]\mathrm{d}x \\ &\quad \times \int_{-\infty}^{\infty} \exp\left[\frac{-2y^2}{W_y^2(z)}\right]\mathrm{d}y \\ &= G_0 \frac{W_{0x}W_{0y}}{W_x(z)W_y(z)} \int_{0}^{\infty} 2\exp\left[\frac{-2x^2}{W_x^2(z)}\right]\mathrm{d}x \\ &\quad \times \int_{0}^{\infty} 2\exp\left[\frac{-2y^2}{W_y^2(z)}\right]\mathrm{d}y. \end{aligned} \tag{55}$$

The two exponential integrals of the second part of (55) yield the following result [69]:

$$\begin{aligned} P_{\mathrm{Tx,o}} &= G_0 \frac{W_{0x}W_{0y}}{W_x(z)W_y(z)} W_x(z)\sqrt{\frac{\pi}{2}} W_y(z)\sqrt{\frac{\pi}{2}} \\ &= \frac{\pi}{2} G_0 W_{0x}W_{0y}. \end{aligned} \tag{56}$$

The ratio of the optical power collected by a rectangular optical receiver with the dimensions of $2x_0 \times 2y_0$ at a distance $z \geq d_0 + t_c$ over the total optical power can be expressed by:

$$\begin{aligned} \eta_{\mathrm{ceff}}(z) &= \frac{1}{(1-r)P_{\mathrm{Tx,o}}} \int_{-x_0}^{x_0}\int_{-y_0}^{y_0} G'(x,y,z)\mathrm{d}x\mathrm{d}y \\ &\overset{(32)}{=} \frac{2}{\pi W_x'(z')W_y'(z'')} \int_{-x_0}^{x_0} \exp\left[\frac{-2x^2}{W_x'^2(z')}\right]\mathrm{d}x \\ &\quad \times \int_{-y_0}^{y_0} \exp\left[\frac{-2y^2}{W_y'^2(z'')}\right]\mathrm{d}y \\ &= \frac{2}{\pi W_x'(z')W_y'(z'')} \int_{0}^{x_0} 2\exp\left[\frac{-2x^2}{W_x'^2(z')}\right]\mathrm{d}x \\ &\quad \times \int_{0}^{y_0} 2\exp\left[\frac{-2y^2}{W_y'^2(z'')}\right]\mathrm{d}y. \end{aligned} \tag{57}$$

Again, the two exponential integrals of the second part of (57) result in [69]:

$$\begin{aligned} \eta_{\mathrm{ceff}}(z) &= \frac{2}{\pi W_x'(z')W_y'(z'')} W_x'(z')\frac{\pi}{2}\mathrm{erf}\left[\frac{\sqrt{2}x_0}{W_x'(z')}\right] \\ &\quad \times W_y'(z'')\mathrm{erf}\left[\frac{\sqrt{2}y_0}{W_y'(z'')}\right] \\ &= \mathrm{erf}\left[\frac{\sqrt{2}x_0}{W_x'(z')}\right]\mathrm{erf}\left[\frac{\sqrt{2}y_0}{W_y'(z'')}\right]. \end{aligned} \tag{58}$$

APPENDIX C
CLASSIFICATION OF THE SINGLE LASER DIODE

The maximum output optical power of the LD is $P_{\mathrm{Tx,o,m}} = 130$ mW [43]. The beam diameter is defined in BS EN 60825-1:2014 [11] as the smallest circle that contains 63% of the total laser power, i.e. $1/e$ beam width. Also, the beam divergence is defined as the far field plane angle of the cone created by the beam diameter. So long as the LD has a Gaussian elliptical profile, the beam divergences are defined along the x- and y-axes as $\varphi_x = 2\vartheta_x$ and $\varphi_y = 2\vartheta_y$, respectively. In particular, they are calculated to be $\varphi_x = 12.5^\circ \simeq 0.22$ rad and $\varphi_y = 21.2^\circ \simeq 0.37$ rad from [43]. According to (1) and (2) the beam diameters along the x- and y-axes can be calculated up to the $1/e \simeq 0.37$ points of the intensity pattern. In particular, the application of $\lambda_0 = 0.66$ μm, $\vartheta_x = 6.25^\circ$ and $\vartheta_y = 10.6^\circ$ to (1) and (2) results in $W_{0x} = 1.92$ μm and $W_{0y} = 1.12$ μm, respectively. Therefore, the beam diameters along the x- and y-directions are calculated to be $D_{0x} = 2W_{0x} = 3.84$ μm and $D_{0y} = 2W_{0y} = 2.24$ μm, respectively.

Condition 3 of Table 10 [11] can be applied to the selected optical emitter. The measurement of AEL needs to be made by the use of a circular aperture stop with a diameter of $D_{\mathrm{ap}} = 7$ mm at a distance $d_{\mathrm{m}} = 10$ cm from the optical source. The specific LD is divergent and the elliptical beam has larger dimensions than the circular area of the aperture stop. Therefore, the AEL must be expressed in terms of irradiance (in mW/cm^2) rather than optical power (in mW). The angular subtenses along the x- and y-axes can be found from:

$$\alpha_x = 2\tan^{-1}\left(\frac{D_{0x}}{2d_{\mathrm{m}}}\right) \approx \frac{D_{0x}}{d_{\mathrm{m}}} \tag{59}$$

and

$$\alpha_y = 2\tan^{-1}\left(\frac{D_{0y}}{2d_{\mathrm{m}}}\right) \approx \frac{D_{0y}}{d_{\mathrm{m}}}. \tag{60}$$

In particular, applying the values of $D_{0x} = 3.84$ μm, $D_{0y} = 2.24$ μm and $d_{\max} = 10^5$ μm to (59) and (60), the angular subtenses are calculated to be $\alpha_x = 38.4$ μrad $< \alpha_{\min} = 1.5$ mrad and $\alpha_y = 22.4$ μrad $< \alpha_{\min}$, respectively. Note that the classification principle 4.3 d) of [11] states that the angular subtense of a rectangular source is computed by the arithmetic mean value of the two angular dimensions of the source. Also, any value of the angular subtense smaller than $\alpha_{\min}$ or bigger than $\alpha_{\max} = 100$ mrad needs to be limited to $\alpha_{\min}$ or $\alpha_{\max}$, respectively, before the calculation of mean value. Therefore, $\alpha = (1.5 + 1.5)/2 = 1.5$ mrad and the LD is assumed to be a point source.

Assume that the LD can be classified as Class 3R and select a time base of 0.25 s according to the classification principle 4.3 e) of [11]. Then, the correction factor, C_6, is equal to 1 according to Table 9 [11]. Therefore, the AEL is determined to be $\kappa = 5$ mW based on Table 6 [11]. The AEL expressed as irradiance is computed by:

$$G_{\mathrm{AEL}} = \frac{\kappa}{\pi(D_{\mathrm{ap}}/2)^2}. \tag{61}$$

The application of $\kappa = 5$ mW and $D_{\mathrm{ap}} = 0.7$ cm to (61) results in $G_{\mathrm{AEL}} \simeq 13$ mW/cm^2.

Now, the beam irradiance must be determined at $d_{\rm m} = 10$ cm from the LD chip and be compared with $G_{\rm AEL}$. For this reason, the beam diameter along the x- and y-axes is calculated by the use of (3) and (4), respectively. The application of $z = d_{\rm m} = 10$ cm, $W_{0x} = 1.92$ μm and $\lambda_0 = 0.66$ μm to (3) yields $W_x(10\,{\rm cm}) = 10.94$ mm. Also, the values of $z = d_{\rm m} = 10$ cm, $W_{0y} = 1.12$ μm and $\lambda_0 = 0.66$ μm are applied to (4) and they result in $W_y(10\,{\rm cm}) = 18.76$ mm. Therefore, the beam diameters at $d_{\rm m} = 10$ cm are $D_x(10\,{\rm cm}) = 2W_x(10\,{\rm cm}) = 21.88$ mm and $D_y(10\,{\rm cm}) = 2W_y(10\,{\rm cm}) = 37.52$ mm. The geometry of the circular aperture is approximated by that of a square aperture with side length equal to the diameter of the circular aperture, i.e. $2x_0 = 2y_0 = 7$ mm. In this case, the collection efficiency can be expressed based on (43) by:

$$\eta_{\rm ceff}(z) = {\rm erf}\left[\frac{\sqrt{2}x_0}{W_x(z)}\right]{\rm erf}\left[\frac{\sqrt{2}y_0}{W_y(z)}\right], \tag{62}$$

where $W_x(z)$ and $W_y(z)$ are given by (3) and (4), respectively. The values of $z = d_{\rm m} = 10$ cm, $x_0 = y_0 = 3.5$ mm, $W_x(10\ {\rm cm}) = 10.94$ mm and $W_y(10\ {\rm cm}) = 18.76$ mm are applied to (62) resulting in $\eta_{\rm ceff}(10\ {\rm cm}) = 0.139$. Therefore, the received optical power is $P_{\rm Rx,o}(10\ {\rm cm}) = \eta_{\rm ceff}(10\ {\rm cm})P_{\rm Tx,o,m} = 0.139 \times 130 = 18.07$ mW. Finally, the received beam irradiance from a square aperture of side length $2x_0$ is given by:

$$G_{\rm Rx}(z) = \frac{P_{\rm Rx,o}(z)}{(2x_0)^2}. \tag{63}$$

The application of $z = d_0 = 10$ cm, $P_{\rm Rx,o}(10\ {\rm cm}) = 18.07$ mW and $2x_0 = 0.7$ cm to (63) results in $G_{\rm Rx}(10\ {\rm cm}) = 36.88$ mW/cm^2. This value is larger than $G_{\rm AEL}$. Consequently, the LD cannot be classified as Class 3R.

Now, the LD is considered to belong to Class 3B, and a time base of 100 s is selected according to the classification principle 4.3 e). The received optical power, i.e. $P_{\rm Rx,o}(10\ {\rm cm}) = 18.07$ mW, is less than the AEL, i.e. $\kappa = 0.5$ W, derived from Table VIII. As a result, the optical source is classified as Class 3B.

Appendix D
Classification of the Laser Diode Used with Collimation Lens

In this case, the laser consists of the dc power supply, the LD and the aspheric lens used in Scenario II of Experiment II. So long as the area between the LD and the lens is shielded by an aluminum tube, the total optical device is considered to be an extended optical source. Note that Condition 1 of Table 10 [11] is applicable to collimated beams, but the most restrictive condition must be used for classification and, again, this is Condition 3 of Table 10 [11]. Thus, the measurement of AEL needs to be made by the use of a circular aperture stop with a diameter of $D_{\rm ap} = 7$ mm at a distance of $d_{\rm m} = 10$ cm from the new beam waist according to Table 11 [11]. As a first step, the new beam waists must be determined. The application of the values of parameters presented in Table II to (1)–(10) and (14)–(29) results in $W_{3x} = 34.93\,{\rm \mu m}$ and $W_{3y} = 20.39\,{\rm \mu m}$. Therefore, the substitution of $z' = d_{\rm m} = 10$ cm, $W_{3x} = 34.93$ μm and $\lambda_0 = 660$ nm to (30) gives $W'_x(10\ {\rm cm}) = 602.46$ μm. Also, the values of $z'' = d_{\rm m} = 10$ cm, $W_{3y} = 20.39$ μm and $\lambda_0 = 660$ nm are applied to (31) and yield $W'_y(10\ {\rm cm}) = 1.03$ mm. So long as the beam diameters at 10 cm from the beam waists are smaller than the diameter of the circular stop aperture, the AEL can be expressed as power and not as irradiance. The angular subtenses along the x- and y-axes are given by:

$$\alpha_x = 2\tan^{-1}\left[\frac{W'_x(d_{\rm m})}{d_{\rm m}}\right] \approx \frac{2W'_x(d_{\rm m})}{d_{\rm m}} \tag{64}$$

and

$$\alpha_y = 2\tan^{-1}\left[\frac{W'_y(d_{\rm m})}{d_{\rm m}}\right] \approx \frac{2W'_y(d_{\rm m})}{d_{\rm m}}. \tag{65}$$

The application of $W'_x(10\ {\rm cm}) = 602.46$ μm, $W'_y(10\ {\rm cm}) = 1.03$ mm and $d_{\rm m} = 10$ cm to (64) and (65) results in $\alpha_x = 12$ mrad and $\alpha_y = 20.6$ mrad, respectively. Therefore, $\alpha = (\alpha_x + \alpha_y)/2 = 16.3$ mrad.

Assume that the optical transmitter can be classified as Class 3R, and select a time base of 0.25 s according to the classification principle 4.3 e) of [11]. Then, the correction factor C_6 is equal to $\alpha/\alpha_{\rm min} = 10.867$ according to Table 9 [11]. Therefore, the AEL is determined to be $\kappa = 5C_6$ [mW] based on Table 7 [11] and, finally, $\kappa = 54.34$ mW.

Now, the laser beam power needs to be calculated at 10 cm from the beam waists in order to be compared with the AEL of Class 3R. So long as $d_{1x} \simeq d_{1y}$ according to Table II, the collection efficiency of the rectangular receiver is calculated at $z' \simeq z'' = 10$ cm. The application of $x_0 = y_0 = 3.5$ mm, $W'_x(10\ {\rm cm}) = 602.46$ μm and $W'_y(10\ {\rm cm}) = 1.03$ mm to (43) gives a collection efficiency value of $\eta_{\rm ceff}(10\ {\rm cm}) = 1$, as expected. So, the received optical power is $P_{\rm Rx,o}(10\ {\rm cm}) = P_{\rm Tx,o,m} = 130$ mW that is larger than $\kappa = 54.34$ mW. Therefore, again this optical transmitter is not classified as Class 3R, but as Class 3B. This is because the AEL of Class 3B is $\kappa = 500$ mW.

References

[1] H. Claussen, L. T. Ho, and L. G. Samuel, "An overview of the femtocell concept," *Bell Labs Tech. J.*, vol. 13, no. 1, pp. 221–245, Spring 2008.

[2] W. Webb, *Wireless Communications: The Future*. New York, NY, USA: Wiley, 2007.

[3] R. Razavi and H. Claussen, "Urban small cell deployments: Impact on the network energy consumption," in *Proc. IEEE Wireless Commun. Netw. Conf. Workshops*, Paris, France, Apr. 2012, pp. 47–52.

[4] C. Ranaweera *et al.*, "Design and optimization of fiber optic small-cell backhaul based on an existing fiber-to-the-node residential access network," *IEEE Commun. Mag.*, vol. 51, no. 9, pp. 62–69, Sep. 2013.

[5] Y. Mao, Y. Luo, J. Zhang, and K. Letaief, "Energy harvesting small cell networks: Feasibility, deployment, and operation," *IEEE Commun. Mag.*, vol. 53, no. 6, pp. 94–101, Jun. 2015.

[6] N. Tesla, "The transmission of electrical energy without wires as a means for furthering peace," *Elect. World Eng.*, pp. 21–24, Jan. 1905.

[7] H. Elgala, R. Mesleh, and H. Haas, "Indoor optical wireless communication: Potential and state-of-the-art," *IEEE Commun. Mag.*, vol. 49, no. 9, pp. 56–62, Sep. 2011.

[8] J. Fakidis, M. Ijaz, S. Kucera, H. Claussen, and H. Haas, "On the design of an optical wireless link for small cell backhaul communication and energy harvesting," in *Proc. IEEE 25th Annu. Int. Symp. Personal Indoor Mobile Radio Commun.*, Washington, DC, USA, Sep. 2014, pp. 58–62.

[9] J. Fakidis, S. Kucera, H. Claussen, and H. Haas, "On the design of a free space optical link for small cell backhaul communication and power

supply," in *Proc. IEEE Int. Conf. Commun. Workshop*, London, U.K., Jun. 2015, pp. 1428–1433.
[10] C. Park, S. Lee, G.-H. Cho, and C. Rim, "Innovative 5-m-off-distance inductive power transfer systems with optimally shaped dipole coils," *IEEE Trans. Power Electron.*, vol. 30, no. 2, pp. 817–827, Feb. 2015.
[11] *Safety of Laser Products. Equipment Classification and Requirements*, British Standards Institution (BSI) Std. BS EN 60 825-1:2014, Aug. 2014.
[12] A. Bauer, J. Hanisch, and E. Ahlswede, "An effective single solar cell equivalent circuit model for two or more solar cells connected in series," *IEEE J. Photovolt.*, vol. 4, no. 1, pp. 340–347, Jan. 2014.
[13] C. R. Valenta and G. D. Durgin, "Harvesting wireless power: Survey of energy-harvester conversion efficiency in far-field wireless power transfer systems," *IEEE Microw. Mag.*, vol. 15, no. 4, pp. 108–120, May 2014.
[14] X. Lu, P. Wang, D. Niyato, D. I. Kim, and Z. Han, "Wireless networks with RF energy harvesting: A contemporary survey," *IEEE Commun. Surveys Tuts.*, vol. 17, no. 2, pp. 757–789, Apr.–Jun. 2015.
[15] A. Kurs, A. Karalis, R. Moffatt, J. D. Joannopoulos, P. Fisher, and M. Soljacic, "Wireless power transfer via strongly coupled magnetic resonances," *Science*, vol. 317, no. 5834, pp. 83–86, Jul. 2007.
[16] B. Choi, E. Lee, J. Huh, and C. Rim, "Lumped impedance transformers for compact and robust coupled magnetic resonance systems," *IEEE Trans. Power Electron.*, vol. 30, no. 11, pp. 6046–6056, Nov. 2015.
[17] M. Pinuela, D. Yates, S. Lucyszyn, and P. Mitcheson, "Maximizing DC-to-load efficiency for inductive power transfer," *IEEE Trans. Power Electron.*, vol. 28, no. 5, pp. 2437–2447, May 2013.
[18] T. Le, K. Mayaram, and T. Fiez, "Efficient far-field radio frequency energy harvesting for passively powered sensor networks," *IEEE J. Solid-State Circuits*, vol. 43, no. 5, pp. 1287–1302, May 2008.
[19] R. Dickinson, "Power in the sky: Requirements for microwave wireless power beamers for powering high-altitude platforms," *IEEE Microw. Mag.*, vol. 14, no. 2, pp. 36–47, Mar. 2013.
[20] L. Summerer and O. Purcell, "Concepts for wireless energy trasmission via laser," presented at the 1st Int. Conf. Space Optical Syst. Appl., Tokyo, Japan, Feb. 2009.
[21] A. Sahai and D. Graham, "Optical wireless power transmission at long wavelengths," in *Proc. IEEE Int. Conf. Space Opt. Syst. Appl.*, Santa Monica, CA, USA, May 2011, pp. 164–170.
[22] W. C. Brown, "The history of power transmission by radio waves," *IEEE Trans. Microw. Theory Techn.*, vol. 32, no. 9, pp. 1230–1242, Sep. 1984.
[23] M. Pinuela, P. Mitcheson, and S. Lucyszyn, "Ambient RF energy harvesting in urban and semi-urban environments," *IEEE Trans. Microw. Theory Techn.*, vol. 61, no. 7, pp. 2715–2726, Jul. 2013.
[24] V. Marian, B. Allard, C. Vollaire, and J. Verdier, "Strategy for microwave energy harvesting from ambient field or a feeding source," *IEEE Trans. Power Electron.*, vol. 27, no. 11, pp. 4481–4491, Nov. 2012.
[25] P. E. Glaser, "Power from the sun: Its future," *Science*, vol. 162, no. 3856, pp. 857–861, Nov. 1968.
[26] P. Crump *et al.*, "Efficient high-power laser diodes," *IEEE J. Sel. Topics Quantum Electron.*, vol. 19, no. 4, pp. 1501211–1501211, Jul. 2013.
[27] J. L. Gray, "The physics of the solar cell," in *Handbook of Photovoltaic Science and Engineering*. 2nd ed. New York, NY, USA: Wiley, Jun. 2011, pp. 82–129.
[28] M. A. Green, K. Emery, Y. Hishikawa, W. Warta, and E. D. Dunlop, "Solar cell efficiency tables (Version 46)," *Progress Photovolt., Res. Appl.*, vol. 23, no. 7, pp. 805–812, Jul. 2015.
[29] G. Kinsey, A. Nayak, M. Liu, and V. Garboushian, "Increasing power and energy in amonix CPV solar power plants," *IEEE J. Photovolt.*, vol. 1, no. 2, pp. 213–218, Oct. 2011.
[30] M. Ali, G. Yang, and R. Dougal, "A new circularly polarized rectenna for wireless power transmission and data communication," *IEEE Antennas Wireless Propag. Lett.*, vol. 4, pp. 205–208, Aug. 2005.
[31] X.-X. Yang, C. Jiang, A. Elsherbeni, F. Yang, and Y.-Q. Wang, "A novel compact printed rectenna for data communication systems," *IEEE Trans. Antennas Propag.*, vol. 61, no. 5, pp. 2532–2539, May 2013.
[32] S. Dimitrov and H. Haas, "Information rate of OFDM-based optical wireless communication systems with nonlinear distortion," *IEEE J. Lightw. Technol.*, vol. 31, no. 6, pp. 918–929, Mar. 2013.
[33] A. Hussein and J. Elmirghani, "Mobile multi-gigabit visible light communication system in realistic indoor environment," *IEEE J. Lightw. Technol.*, vol. 33, no. 15, pp. 3293–3307, Aug. 2015.
[34] D. Tsonev *et al.*, "A 3-Gb/s single-LED OFDM-based wireless VLC link using a gallium nitride μLED," *IEEE Photon. Technol. Lett.*, vol. 26, no. 7, pp. 637–640, Apr. 2014.
[35] Z. Wang, D. Tsonev, S. Videv, and H. Haas, "On the design of a solar-panel receiver for optical wireless communications with simultaneous energy harvesting," *IEEE J. Sel. Areas Commun.*, vol. 33, no. 8, pp. 1612–1623, Aug. 2015.
[36] S.-M. Kim and J.-S. Won, "Simultaneous reception of visible light communication and optical energy using a solar cell receiver," in *Proc. IEEE Int. Conf. Converg.*, Jeju Island, South Korea, Oct. 2013, pp. 896–897.
[37] S. Bloom, E. Korevaar, J. Schuster, and H. Willebrand, "Understanding the performance of free-space optics [Invited]," *OSA J. Opt. Netw.*, vol. 2, no. 6, pp. 178–200, Jun. 2003.
[38] D. K. Killinger, J. H. Churnside, and L. S. Rothman, "Atmospheric optics," in *Handbook of Optics: Volume V—Atmospheric Optics, Modulators, Fiber Optics, X-Ray and Neutron Optics*. 3rd ed. New York, NY, USA: McGraw-Hill, 2010, pp. 1–50.
[39] A. Mostafa and S. Hranilovic, "Channel measurement and Markov modeling of an urban free-space optical link," *IEEE/OSA J. Opt. Commun. Netw.*, vol. 4, no. 10, pp. 836–846, Oct. 2012.
[40] F. S. Vetelino, C. Young, L. Andrews, and J. Recolons, "Aperture averaging effects on the probability density of irradiance fluctuations in moderate-to-strong turbulence," *OSA J. Appl. Opt.*, vol. 46, no. 11, pp. 2099–2108, Apr. 2007.
[41] B. E. A. Saleh and M. C. Teich, "Beam optics," in *Fundamentals of Photonics* (Wiley Series in Pure and Applied Optics). 1st ed. New York, NY, USA: Wiley, Jan. 1991, pp. 80–107.
[42] B. E. A. Saleh and M. C. Teich, "Semiconductor photon sources," in *Fundamentals of Photonics*. (Wiley Series in Pure and Applied Optics). 1st ed. New York, NY, USA: Wiley, Jan. 1991, pp. 592–643.
[43] Opnext, "HL6544FM visible high power laser diodes," Mar. 2009. [Online]. Available: http://www.thorlabs.de/thorcat/21700/HL6544FM-MFGSpec.pdf
[44] Panasonic, "Laser diode LNCT22PK01WW," Sep. 2013. [Online]. Available: http://docs-europe.electrocomponents.com/webdocs/1305/0900766b81305a62.pdf
[45] J. Alda, "Laser and Gaussian beam propagation and transformation," *Encyclopedia Opt. Eng.*, pp. 999–1013, 2003.
[46] B. E. A. Saleh and M. C. Teich, "Ray optics," in *Fundamentals of Photonics*. (Wiley Series in Pure and Applied Optics). 1st ed., New York, NY, USA: Wiley, Jan. 1991, pp. 1–40.
[47] D. M. Pozar, *Microwave Engineering*. 4th ed., A. Melhorn, Ed., New York, NY, USA: Wiley, Dec. 2011.
[48] E. Hecht, *Optics*. 4th ed., A. Black, Ed., Reading, MA, USA: Addison-Wesley, 2002.
[49] S. Boyd and L. Vandenberghe, *Convex Optimization*. Cambridge, U.K.: Cambridge Univ. Press, 2004.
[50] A. Sellami and M. Bouaicha, "Application of the Genetic algorithms for identifying the electrical parameters of pv solar generators," in *Solar Cells—Silicon Wafer-Based Technologies*. West Palm Beach, FL, USA: InTech, 2011, pp. 349–364.
[51] D. Killinger, "Free space optics for laser communication through the air," *Opt. Photon. News*, vol. 13, no. 3, pp. 36–42, Oct. 2002.
[52] M. Villalva, J. Gazoli, and E. Filho, "Comprehensive approach to modeling and simulation of photovoltaic arrays," *IEEE Trans. Power Electron.*, vol. 24, no. 5, pp. 1198–1208, May 2009.
[53] I. Tobias, C. del Canizo, and J. Alonso, "Crystalline silicon solar cells and modules, " in *Handbook of Photovoltaic Science and Engineering*. 2nd ed. New York, NY, USA: Wiley, Jun. 2011, pp. 265–308.
[54] Thorlabs, "ACL12708U-A—Aspheric Condenser Lens, AR-Coated 350-700 nm, Diameter = 1.27 cm, f = 8 mm," Nov. 2013. [Online]. Available: http://www.thorlabs.de/thorcat/CTN/ACL12708U-A-AutoCADPDF.pdf
[55] Multicomp, "MC-SP0.8-NF-GCS Solar Panel, 0.8W, 4V, No Frame," Dec. 2010. [Online]. Available: http://www.farnell.com/datasheets/1671797.pdf
[56] "125×125 mm^2 Monocrystalline Solar Cells 2.91 W Mono 5×5," Dec. 2014. [Online]. Available: http://www.ebay.co.uk/itm/125x125-Monocrystalline-Solar-Cells-2-91-Watt-Mono -5x5-/221545517144?item=221545517144&ssPageName=ADME:L:OC:GB:3160
[57] S. Chander, A. Purohit, A. Nehra, S. P. Nehra, and M. S. Dhaka, "A study on spectral response and external quantum efficiency of mono-crystalline silicon solar cell," *Int. J. Renewable Energy Res.*, vol. 5, no. 1, pp. 41–44, 2015.
[58] Y. Baghzouz, "Basic photovoltaic theory," in *Handbook of Clean Energy Systems*. 1st ed. New York, NY, USA: Wiley, Jun. 2015, pp. 283–296.
[59] H. Schmidt, B. Burger, and J. Schmid, "Power conditioning for photovoltaic power systems," in *Handbook of Photovoltaic Science and Engineering*. 2nd ed. New York, NY, USA: Wiley, Jun. 2011, pp. 954–983.
[60] J. D. Arora, A. V. Verma, and M. Bhatnagar, "Variation of series resistance with temperature and illumination level in diffused junction poly- and

single-crystalline silicon solar cells," *J. Mater. Sci. Lett.*, vol. 5, no. 12, pp. 1210–1212, Dec. 1986.
[61] F. Khan, S. N. Singh, and M. Husain, "Effect of illumination intensity on cell parameters of a silicon solar cell," *J. Solar Energy Mater. Solar Cells*, vol. 94, no. 9, pp. 1473–1476, Sep. 2010.
[62] B. E. A. Saleh and M. C. Teich, "Photons and atoms," in *Fundamentals of Photonics* (Wiley Series in Pure and Applied Optics). 1st ed. New York, NY, USA: Wiley, Jan. 1991, pp. 423–459.
[63] R. W. Boyd, *Radiometry and the Detection of Optical Radiation* (Wiley Series in Pure and Applied Optics). New York, NY, USA: Wiley, Jun. 1983.
[64] R. S. Quimby, "Appendix A: Solid angle and the brightness theorem," in *Photonics and Lasers: An Introduction*. New York, NY, USA: Wiley, 2006, pp. 495–498.
[65] Edmund Optics, "Lens PCX 75 mm diam $\times$ 75 mm FL MgF_2," 2014. [Online]. Available: http://www.edmundoptics.com/optics/optical-lenses/plano-convex-pcx-spherical-singlet-lenses/mgf2-coated-plano-convex-pcx-lenses/45368/
[66] B. E. A. Saleh and M. C. Teich, "Fourier optics," in *Fundamentals of Photonics* (Wiley Series in Pure and Applied Optics). 1st ed. New York, NY, USA: Wiley, Jan. 1991, pp. 108–156.
[67] Thorlabs, "ACL12708U-B—Aspheric Condenser Lens, AR-Coated 650–1050 nm, $D = 1.27$ cm and $f = 8$ mm," Nov. 2013. [Online]. Available: https://www.thorlabs.de/thorcat/CTN/ACL12708U-B-AutoCADPDF.pdf
[68] B. E. A. Saleh and M. C. Teich, "Wave Optics," in *Fundamentals of Photonics* (Wiley Series in Pure and Applied Optics). 1st ed. New York, NY, USA: Wiley, Jan. 1991, pp. 41–79.
[69] I. S. Gradshteyn and I. M. Ryzhik, *Table of Integrals, Series, and Products*. 7th ed., A. Jeffrey and D. Zwillinger, Eds. New York, NY, USA: Academic, Mar. 2007.

John Fakidis (S'14) was awarded the Diploma Degree (5 years) in electrical and computer engineering from the Aristotle University of Thessaloniki, Thessaloniki, Greece in 2011, with specialization in Telecommunications. Since 2012, he has been a Ph.D. candidate at the Institute for Digital Communications, University of Edinburgh, Edinburgh, U.K. His research areas are multiple access schemes for optical wireless communications and optical wireless power transfer systems for small cells. Also, he works collaboratively with the industry partner Bell Laboratories, Nokia in Ireland.

Stefan Videv received the B.Sc. degree in electrical engineering and computer science from Jacobs University Bremen, Bremen, Germany, in 2007, and the M.Sc. degree in communications, systems, and electronics in 2009 from the same university. He received the Ph.D. degree for his thesis titled Techniques for Green Radio Cellular Communications from the University of Edinburgh, Edinburgh, U.K. He is currently working as an Experimental Officer at the Li-Fi R&D Center, University of Edinburgh and working in the field of visible light communications. His research interests include quick prototyping of communication systems, smart resource allocation, and energy efficient communications.

Stepan Kucera (S'14–M'06) received the M.Sc. degree from Czech Technical University in Prague, Prague, Czech Republic, in 2003, and the Ph.D. degree in Informatics from the Graduate School of Informatics, Kyoto University, Kyoto, Japan, in 2008. He is a Research Scientist at Nokia Bell Laboratories in Ireland since 2011. Between 2008 and 2011, he was with the New Generation Wireless Communications Research Center, Keihanna Research Laboratories, NICT, Japan. He filed more than 40 patents and published more than 30 book chapters, transactions, and conference papers in peer-reviewed IEEE venues.

His expertise lies mainly in the area of wireless and IP networking technology, including both proprietary solutions and 3GPP/IEEE/IETF standards. His current work focuses on the development of novel next-generation technologies, networks, and services as well as their standardization and deployment. He is also the (co)-recipient of four professional awards (the Irish Laboratory of the Year Award and the Irish Commercial Laboratory of the Year Award in 2014, the IEEE Kansai Student Researcher Encouragement Award in 2007, the Best Student Paper Award at IEEE Vehicular Technology Conference Fall 2006) as well as was nominated for the Ericsson Young Scientist Award in 2010 and the IEICE Young Researcher Encouragement Award in 2009.

He actively serves on technical boards of major IEEE journals and conferences.

Holger Claussen (M'01–SM'10) received the Ph.D. degree in signal processing for digital communications from the University of Edinburgh, U.K., in 2004. He is the Leader of Small Cells Research Department at Bell Labs, Nokia with a team in Ireland and the U.S. In this role, he and his team are innovating in all areas related to future evolution, deployment, and operation of small cell networks to enable exponential growth in mobile data traffic. His research in this domain has been commercialized in Nokia's (formerly Alcatel-Lucent's) Small Cell product portfolio and continues to have significant impact. He received the 2014 World Technology Award in the individual category Communications Technologies for innovative work of the greatest likely long-term significance. Prior to this, he was the Head of the Autonomous Networks and Systems Research Department, Bell Labs, Ireland, where he directed research in the area of self-managing networks to enable the first large scale femtocell deployments from 2009 onwards. He joined the Bell Labs in 2004, where he began his research in the areas of network optimization, cellular architectures, and improving energy efficiency of networks. He is the author of more than 90 publications and 110 filed patent applications. He is a Fellow of the World Technology Network, Senior Member of the IEEE, and Member of the IET.

Harald Haas (S'98–A'00–M'03) received the Ph.D. degree from the University of Edinburgh, Edinburgh, U.K., in 2001. He currently holds the Chair of Mobile Communications at the University of Edinburgh, and is a Co-founder and the Chief Scientific Officer of pureLiFi Ltd as well as the Director of the LiFi Research and Development Center at the University of Edinburgh. His main research interests include optical wireless communications, hybrid optical wireless and RF communications, spatial modulation, and interference coordination in wireless networks. He first introduced and coined spatial modulation and LiFi. LiFi was listed among the 50 best inventions in TIME Magazine 2011. He was an Invited Speaker at TED Global 2011, and his talk: "Wireless Data from Every Light Bulb" has been watched online more than 2.2 million times. He gave a second TED Global lecture in 2015 on the use of solar cells as LiFi data detectors and energy harvesters. This has been viewed online more than 1 million times. He holds 31 patents and has more than 30 pending patent applications. He has published 300 conferences and journal papers including a paper in science. He co-authors a book entitled: *"Principles of LED Light Communications Towards Networked Li-Fi"*(Cambridge University Press, 2015). He is the Editor of IEEE TRANSACTIONS ON COMMUNICATIONS and IEEE JOURNAL OF LIGHTWAVE TECHNOLOGIES. He was a Co-recipient of recent best paper awards at the IEEE Vehicular Technology Conference (VTC-Fall) in Las Vegas in 2013, and VTC-Spring in Glasgow in 2015. He was a Co-recipient of the EURASIP Best Paper Award for the *Journal on Wireless Communications and Networking* in 2015, and a Co-recipient of the Jack Neubauer Memorial Award of the IEEE Vehicular Technology Society. In 2012, he received prestigious Established Career Fellowship from the EPSRC (Engineering and Physical Sciences Research Council) within the Information and Communications Technology in the U.K. He received the Tam Dalyell Prize 2013 awarded by the University of Edinburgh for excellence in engaging the public with science. In 2014, he was selected by EPSRC as one of ten RISE (Recognising Inspirational Scientists and Engineers) Leaders in the U.K.

Bibliography

[1] H. Elgala, R. Mesleh, and H. Haas, "Indoor Optical Wireless Communication: Potential and State-of-the-Art," *IEEE Commun. Mag.*, vol. 49, no. 9, pp. 56–62, Sep. 2011.

[2] H. Claussen, L. T. Ho, and L. G. Samuel, "An Overview of the Femtocell Concept," *Bell Labs Tech. J.*, vol. 13, no. 1, pp. 221–245, Spring 2008.

[3] W. Webb, *Wireless Communications: The Future*. New York, NY, USA: Wiley, Jan. 2007.

[4] R. Razavi and H. Claussen, "Urban Small Cell Deployments: Impact on the Network Energy Consumption," in *Proc. IEEE Wireless Commun. Netw. Conf. Workshops*, Paris, France, Apr. 2012, pp. 47–52.

[5] C. Ranaweera *et al.*, "Design and Optimization of Fiber Optic Small-Cell Backhaul Based on an Existing Fiber-to-the-Node Residential Access Network," *IEEE Commun. Mag.*, vol. 51, no. 9, pp. 62–69, Sep. 2013.

[6] D. Gunduz, K. Stamatiou, N. Michelusi, and M. Zorzi, "Designing Intelligent Energy Harvesting Communication Systems," *IEEE Commun. Mag.*, vol. 52, no. 1, pp. 210–216, Jan. 2014.

[7] Y. Mao, Y. Luo, J. Zhang, and K. Letaief, "Energy Harvesting Small Cell Networks: Feasibility, Deployment, and Operation," *IEEE Commun. Mag.*, vol. 53, no. 6, pp. 94–101, Jun. 2015.

[8] N. Tesla, "The Transmission of Electrical Energy without Wires as a Means for Furthering Peace," *Elect. World Eng.*, pp. 21–24, Jan. 1905.

[9] A. R. Ekti, M. Z. Shakir, E. Serpedin, and K. A. Qaraqe, "End-to-End Downlink Power Consumption of Heterogeneous Small-Cell Networks Based on the Probabilistic Traffic Model," in *Proc. IEEE Wireless Commun. Netw. Conf.*, Istanbul, Turkey, Apr. 2014, pp. 1138–1142.

[10] G. Auer *et al.*, "How Much Energy is Needed to Run a Wireless Network?" *IEEE Wireless Commun.*, vol. 18, no. 5, pp. 40–49, Oct. 2011.

[11] S. Shahramian, Y. Baeyens, N. Kaneda, and Y. K. Chen, "A 70–100 GHz Direct-Conversion Transmitter and Receiver Phased Array Chipset Demonstrating 10 Gb/s Wireless Link," *IEEE J. Solid-State Circuits*, vol. 48, no. 5, pp. 1113–1125, May 2013.

[12] Z. Wang, D. Tsonev, S. Videv, and H. Haas, "On the Design of a Solar-Panel Receiver for Optical Wireless Communications with Simultaneous Energy Harvesting," *IEEE J. Sel. Areas Commun.*, vol. 33, no. 8, pp. 1612–1623, Aug. 2015.

[13] J. D. Arora, A. V. Verma, and M. Bhatnagar, "Variation of Series Resistance with Temperature and Illumination Level in Diffused Junction Poly- and Single-Crystalline Silicon Solar Cells," *J. Mater. Sci. Lett.*, vol. 5, no. 12, pp. 1210–1212, Dec. 1986.

[14] F. Khan, S. N. Singh, and M. Husain, "Effect of Illumination Intensity on Cell Parameters of a Silicon Solar Cell," *J. Solar Energy Mater. Solar Cells*, vol. 94, no. 9, pp. 1473–1476, Sep. 2010.

[15] S. D. Jarvis, J. Mukherjee, M. Perren, and S. J. Sweeney, "Development and Characterisation of Laser Power Converters for Optical Power Transfer Applications," *Optoelectron.*, vol. 8, no. 2, pp. 64–70, Apr. 2014.

[16] C. R. Valenta and G. D. Durgin, "Harvesting Wireless Power: Survey of Energy-Harvester Conversion Efficiency in Far-Field Wireless Power Transfer Systems," *IEEE Microw. Mag.*, vol. 15, no. 4, pp. 108–120, May 2014.

[17] X. Lu, P. Wang, D. Niyato, D. I. Kim, and Z. Han, "Wireless Networks with RF Energy Harvesting: A Contemporary Survey," *IEEE Commun. Surveys Tuts.*, vol. 17, no. 2, pp. 757–789, Apr.–Jun. 2015.

[18] A. Kurs *et al.*, "Wireless Power Transfer via Strongly Coupled Magnetic Resonances," *Sci.*, vol. 317, no. 5834, pp. 83–86, Jul. 2007.

[19] B. Choi, E. Lee, J. Huh, and C. Rim, "Lumped Impedance Transformers for Compact and Robust Coupled Magnetic Resonance Systems," *IEEE Trans. Power Electron.*, vol. 30, no. 11, pp. 6046–6056, Nov. 2015.

[20] M. Pinuela, D. Yates, S. Lucyszyn, and P. Mitcheson, "Maximizing DC-to-Load Efficiency for Inductive Power Transfer," *IEEE Trans. Power Electron.*, vol. 28, no. 5, pp. 2437–2447, May 2013.

[21] C. Park, S. Lee, G.-H. Cho, and C. Rim, "Innovative 5-m-Off-Distance Inductive Power Transfer Systems with Optimally Shaped Dipole Coils," *IEEE Trans. Power Electron.*, vol. 30, no. 2, pp. 817–827, Feb. 2015.

[22] T. Le, K. Mayaram, and T. Fiez, "Efficient Far-Field Radio Frequency Energy Harvesting for Passively Powered Sensor Networks," *IEEE J. Solid-State Circuits*, vol. 43, no. 5, pp. 1287–1302, May 2008.

[23] R. Dickinson, "Power in the Sky: Requirements for Microwave Wireless Power Beamers for Powering High-Altitude Platforms," *IEEE Microw. Mag.*, vol. 14, no. 2, pp. 36–47, Mar. 2013.

[24] L. Summerer and O. Purcell, "Concepts for Wireless Energy Trasmission via Laser," presented at the 1st Int. Conf. Space Opt. Syst. Appl., Tokyo, Japan, Feb. 2009.

[25] A. Sahai and D. Graham, "Optical Wireless Power Transmission at Long Wavelengths," in *Proc. IEEE Int. Conf. Space Opt. Syst. Appl.*, Santa Monica, CA, USA, May 2011, pp. 164–170.

[26] W. C. Brown, "The History of Power Transmission by Radio Waves," *IEEE Trans. Microw. Theory Techn.*, vol. 32, no. 9, pp. 1230–1242, Sep. 1984.

[27] M. Pinuela, P. Mitcheson, and S. Lucyszyn, "Ambient RF Energy Harvesting in Urban and Semi-Urban Environments," *IEEE Trans. Microw. Theory Techn.*, vol. 61, no. 7, pp. 2715–2726, Jul. 2013.

[28] V. Marian, B. Allard, C. Vollaire, and J. Verdier, "Strategy for Microwave Energy Harvesting From Ambient Field or a Feeding Source," *IEEE Trans. Power Electron.*, vol. 27, no. 11, pp. 4481–4491, Nov. 2012.

[29] P. E. Glaser, "Power from the Sun: Its Future," *Sci.*, vol. 162, no. 3856, pp. 857–861, Nov. 1968.

[30] Advanced Concepts Team – European Space Agency (ESA), "Space-Based Solar Power." [Online]. Available: http://www.esa.int/gsp/ACT/nrg/projects/SPS.html. Accessed on: Jan. 11, 2017.

[31] N. Shinohara, "Wireless Power Transmission for Solar Power Satellite (SPS)," Kyoto Univ., Kyoto, Japan, Tech. Rep., 2008. [Online]. Available: http://www.sspi.gatech.edu/wptshinohara.pdf. Accessed on: Jan. 11, 2017.

[32] W. C. Brown, "History and Status of Beamed Power Technology and Applications at 2.45 Gigahertz," Raytheon Co., Waltham, MA, USA, Tech. Rep. 90N10150, Jul. 1989. [Online]. Available: https://ntrs.nasa.gov/archive/nasa/casi.ntrs.nasa.gov/19900000834.pdf. Accessed on: Jan. 12, 2017.

[33] P. Crump *et al.*, "Efficient High-Power Laser Diodes," *IEEE J. Sel. Topics Quantum Electron.*, vol. 19, no. 4, pp. 1 501 211–1 501 211, Jul. 2013.

[34] J. L. Gray, "The Physics of the Solar Cell," in *Handbook of Photovoltaic Science and Engineering*, 2nd ed. New York, NY, USA: Wiley, June 2011, pp. 82–129.

[35] M. A. Green, K. Emery, Y. Hishikawa, W. Warta, and E. D. Dunlop, "Solar Cell Efficiency Tables (Version 46)," *Progress Photovolt., Res. Appl.*, vol. 23, no. 7, pp. 805–812, Jul. 2015.

[36] G. Kinsey, A. Nayak, M. Liu, and V. Garboushian, "Increasing Power and Energy in Amonix CPV Solar Power Plants," *IEEE J. Photovolt.*, vol. 1, no. 2, pp. 213–218, Oct. 2011.

[37] D. J. Friedman, J. M. Olson, and S. Kurtz, "High-Efficiency III-V Multijunction Solar Cells," in *Handbook of Photovoltaic Science and Engineering*, 2nd ed. New York, NY, USA: Wiley, Jun. 2011, pp. 314–364.

[38] R. Ramabadran and B. Mathur, "Effect of Shading on Series and Parallel Connected Solar PV Modules," *Modern Appl. Sci.*, vol. 3, no. 10, pp. 32–41, Oct. 2009.

[39] Y. Baghzouz, "Basic Photovoltaic Theory," in *Handbook of Clean Energy Systems*, 1st ed. New York, NY, USA: Wiley, Jun. 2015, pp. 283–296.

[40] A. Schonecker and K. Bucher, "Influence of Non-Uniform Illumination on Spectral Response and Efficiency Measurements of Large Area Solar Cells," in *Proc. IEEE Rec. 22nd Photovolt. Specialists Conf.*, Las Vegas, NV, USA, Oct. 1991, pp. 203–208.

[41] R. Jain, "Calculated Performance of Indium Phosphide Solar Cells under Monochromatic Illumination," *IEEE Trans. Electron Devices*, vol. 40, no. 10, pp. 1893–1895, Oct. 1993.

[42] J. Schubert *et al.*, "High-Voltage GaAs Photovoltaic Laser Power Converters," *IEEE Trans. Electron Devices*, vol. 56, no. 2, pp. 170–175, Feb. 2009.

[43] R. S. Quimby, "Lasers and Coherent Light," in *Photonics and Lasers: An Introduction*. New York, NY, USA: Wiley, 2006, pp. 281–291.

[44] ——, "Light Sources," in *Photonics and Lasers: An Introduction*. New York, NY, USA: Wiley, 2006, pp. 185–214.

[45] ——, "Optical Resonators," in *Photonics and Lasers: An Introduction*. New York, NY, USA: Wiley, 2006, pp. 293–306.

[46] *Safety of Laser Products. Equipment Classification and Requirements*, British Standards Institution (BSI) Std. BS EN 60 825-1:2014, Aug. 2014.

[47] *Safety of Laser Products. Equipment Classification and Requirements*, British Standards Institution (BSI) Std. BS EN 60 825-1:2007, Nov. 2007.

[48] S. Bloom, E. Korevaar, J. Schuster, and H. Willebrand, "Understanding the Performance of Free-Space Optics [Invited]," *OSA J. Opt. Netw.*, vol. 2, no. 6, pp. 178–200, Jun. 2003.

[49] Spectral Sciences Inc., "MODTRAN." [Online]. Available: http://modtran.spectral.com/modtran_index. Accessed on: 22 May, 2017.

[50] C. Honsberg and S. Bowden, "Solar Cell Operation – Spectral Response." [Online]. Available: http://www.pveducation.org/pvcdrom/solar-cell-operation/spectral-response. Accessed on: May 18, 2017.

[51] S. Dimitrov and H. Haas, "Information Rate of OFDM-Based Optical Wireless Communication Systems With Nonlinear Distortion," *IEEE J. Lightw. Technol.*, vol. 31, no. 6, pp. 918–929, Mar. 2013.

[52] A. Hussein and J. Elmirghani, "Mobile Multi-Gigabit Visible Light Communication System in Realistic Indoor Environment," *IEEE J. Lightw. Technol.*, vol. 33, no. 15, pp. 3293–3307, Aug. 2015.

[53] D. Tsonev *et al.*, "A 3-Gb/s Single-LED OFDM-based Wireless VLC Link Using a Gallium Nitride μLED," *IEEE Photon. Technol. Lett.*, vol. 26, no. 7, pp. 637–640, Apr. 2014.

[54] S.-M. Kim and J.-S. Won, "Simultaneous Reception of Visible Light Communication and Optical Energy Using a Solar Cell Receiver," in *Proc. IEEE Int. Conf. ICT Convergence*, Jeju Island, South Korea, Oct. 2013, pp. 896–897.

[55] D. K. Killinger, J. H. Churnside, and L. S. Rothman, "Atmospheric Optics," in *Handbook of Optics: Volume V – Atmospheric Optics, Modulators, Fiber Optics, X-Ray and Neutron Optics*, 3rd ed. New York, NY, USA: McGraw-Hill, 2010, pp. 1–50.

[56] M. A. Khalighi and M. Uysal, "Survey on Free Space Optical Communication: A Communication Theory Perspective," *IEEE Commun. Surveys Tuts.*, vol. 16, no. 4, pp. 2231–2258, Oct.–Dec. 2014.

[57] A. Mostafa and S. Hranilovic, "Channel Measurement and Markov Modeling of an Urban Free-Space Optical Link," *IEEE/OSA J. Opt. Commun. Netw.*, vol. 4, no. 10, pp. 836–846, Oct. 2012.

[58] F. S. Vetelino, C. Young, L. Andrews, and J. Recolons, "Aperture Averaging Effects on the Probability Density of Irradiance Fluctuations in Moderate-to-Strong Turbulence," *OSA J. Appl. Opt.*, vol. 46, no. 11, pp. 2099–2108, Apr. 2007.

[59] B. E. A. Saleh and M. C. Teich, "Beam Optics," in *Fundamentals of Photonics*, 1st ed., ser. Wiley in Pure and Applied Optics. New York, NY, USA: Wiley, Jan. 1991, pp. 80–107.

[60] ——, "Ray Optics," in *Fundamentals of Photonics*, 1st ed., ser. Wiley in Pure and Applied Optics. New York, NY, USA: Wiley, Jan. 1991, pp. 1–40.

[61] ——, "Wave Optics," in *Fundamentals of Photonics*, 1st ed., ser. Wiley in Pure and Applied Optics. New York, NY, USA: Wiley, Jan. 1991, pp. 41–79.

[62] ——, "Semiconductor Photon Sources," in *Fundamentals of Photonics*, 1st ed., ser. Wiley in Pure and Applied Optics. New York, NY, USA: Wiley, Jan. 1991, pp. 592–643.

[63] Opnext, "HL6544FM Visible High Power Laser Diodes," Mar. 2009. [Online]. Available: http://www.thorlabs.de/thorcat/21700/HL6544FM-MFGSpec.pdf. Accessed on: May 19, 2014.

[64] Panasonic, "Laser Diode LNCT22PK01WW," Sep. 2013. [Online]. Available: http://docs-europe.electrocomponents.com/webdocs/1305/0900766b81305a62.pdf. Accessed on: Feb. 27, 2015.

[65] J. Alda, "Laser and Gaussian Beam Propagation and Transformation," *Encyclopedia Opt. Eng.*, pp. 999–1013, 2003.

[66] R. J. Buist and P. G. Lau, "Thermoelectric Power Generator Design and Selection from TE Cooling Module Specifications," in *Proc. IEEE Int. Conf. Thermoelectr.*, Dresden, Germany, Aug. 1997, pp. 551–554.

[67] H. Sun, "Laser Diode Beam Basics," in *A Practical Guide to Handling Laser Diode Beams*, 2nd ed., ser. SpringerBriefs in Physics. Dordrecht, Netherlands: Springer, Feb. 2015, pp. 27–51.

[68] D. M. Pozar, *Microwave Engineering*, 4th ed., A. Melhorn, Ed. New York, NY, USA: Wiley, Dec. 2011.

[69] E. Hecht, *Optics*, 4th ed., A. Black, Ed. Reading, MA, USA: Addison-Wesley, 2002.

[70] A. Bauer, J. Hanisch, and E. Ahlswede, "An Effective Single Solar Cell Equivalent Circuit Model for Two or More Solar Cells Connected in Series," *IEEE J. Photovolt.*, vol. 4, no. 1, pp. 340–347, Jan. 2014.

[71] S. Boyd and L. Vandenberghe, *Convex Optimization*. Cambridge, U.K.: Cambridge Univ. Press, 2004.

[72] A. Sellami and M. Bouaicha, "Application of the Genetic Algorithms for Identifying the Electrical Parameters of PV Solar Generators," in *Solar Cells – Silicon Wafer-Based Technologies*. West Palm Beach, FL, USA: InTech, 2011, pp. 349–364.

[73] D. Killinger, "Free Space Optics for Laser Communication through the Air," *Opt. Photon. News*, vol. 13, no. 3, pp. 36–42, Oct. 2002.

[74] M. Villalva, J. Gazoli, and E. Filho, "Comprehensive Approach to Modeling and Simulation of Photovoltaic Arrays," *IEEE Trans. Power Electron.* , vol. 24, no. 5, pp. 1198–1208, May 2009.

[75] G. Notton, C. Cristofari, M. Mattei, and P. Poggi, "Modelling of a Double-Glass Photovoltaic Module Using Finite Differences," *Appl. Thermal Eng.*, vol. 25, no. 17–18, pp. 2854–2877, Dec. 2005.

[76] D. Tsonev, S. Videv, and H. Haas, "Towards a 100 Gb/s Visible Light Wireless Access Network," *Opt. Express*, vol. 23, no. 2, pp. 1627–1637, Jan. 2015. [Online]. Available: http://www.opticsexpress.org/abstract.cfm?URI=oe-23-2-1627

[77] R. W. Boyd, *Radiometry and the Detection of Optical Radiation*, ser. Wiley in Pure and Applied Optics. New York, NY, USA: Wiley, Jun. 1983.

[78] R. S. Quimby, "Appendix A: Solid Angle and the Brightness Theorem," in *Photonics and Lasers: An Introduction*. New York, NY, USA: Wiley, 2006, pp. 495–498.

[79] J. M. Kahn and J. R. Barry, "Wireless Infrared Communications," *Proc. IEEE*, vol. 85, no. 2, pp. 265–298, Feb. 1997.

[80] E. Schubert, *Light-Emitting Diodes*, 1st ed. Cambridge, U.K.: Cambridge Univ. Press, May 2003.

[81] Bridgelux, "Bridgelux ES Rectangle Array Series Product Datasheet DS24," Nov. 2011. [Online]. Available: http://www.farnell.com/datasheets/1504249.pdf. Accessed on: Dec. 4, 2013.

[82] F. R. Gfeller and U. Bapst, "Wireless In-House Data Communication Via Diffuse Infrared Radiation," *Proc. IEEE*, vol. 67, no. 11, pp. 1474–1486, Nov. 1979.

[83] E. Diaz and M. Knobl, "Prototyping Illumination Systems with Stock Optical Components," Photonik International, 2012.

[84] E. A. Schiff, S. Hegedus and X. Deng, "Amorphous Silicon-Based Solar Cells," in *Handbook of Photovoltaic Science and Engineering*, 2nd ed. New York, NY, USA: Wiley, Jun. 2011, pp. 487–545.

[85] H. Robertson, "Fundamentals of Photovoltaic Solar Technology for Battery Powered Applications," Jun. 2012. [Online]. Available: http://docplayer.net/12886325-Fundamentals-of-photovoltaic-solar-technology-for-battery-powered-applications.html. Accessed on: Dec. 14, 2013.

[86] Edmund Optics, "Lens PCX 75 mm diam. $\times$ 75 mm FL MgF_2," 2014. [Online]. Available: http://www.edmundoptics.com/optics/optical-lenses/plano-convex-pcx-spherical-singlet-lenses/mgf2-coated-plano-convex-pcx-lenses/45368/. Accessed on: Jun. 11, 2015.

[87] I. Tobias, C. del Canizo, and J. Alonso, "Crystalline Silicon Solar Cells and Modules," in *Handbook of Photovoltaic Science and Engineering*, 2nd ed. New York, NY, USA: Wiley, Jun. 2011, pp. 265–308.

[88] S. Chander, A. Purohit, A. Nehra, S. P. Nehra, and M. S. Dhaka, "A Study on Spectral Response and External Quantum Efficiency of Mono-Crystalline Silicon Solar Cell," *Int. J. Renewable Energy Res.*, vol. 5, no. 1, pp. 41–44, 2015.

[89] Thorlabs, "ACL12708U-A – Aspheric Condenser Lens, AR-Coated $350 - 700\,\mathrm{nm}$, $D = 1.27\,\mathrm{cm}$, $f = 8\,\mathrm{mm}$," Nov. 2013. [Online]. Available: http://www.thorlabs.de/thorcat/CTN/ACL12708U-A-AutoCADPDF.pdf. Accessed on: May 22, 2014.

[90] ——, "ACL4532 – Aspheric Condenser Lens, $D = 45\,\mathrm{mm}$, $f = 32\,\mathrm{mm}$, NA $= 0.612$, Uncoated," Sep. 2009. [Online]. Available: http://www.thorlabs.de/thorcat/19000/ACL4532-AutoCADPDF.pdf. Accessed on: May 30, 2014.

[91] BP Solar, "BP Solar SX 305 5 W PV Module," Jul. 2007. [Online]. Available: http://www.omniinstruments.co.uk/images/downloads/3353.pdf. Accessed on: Jun. 4, 2014.

[92] Multicomp, "MC-SP0.8-NF-GCS Solar Panel, 0.8 W, 4 V, No Frame," Dec. 2010. [Online]. Available: http://www.farnell.com/datasheets/1671797.pdf. Accessed on: Jun. 11, 2015.

[93] Ebay, "$125 \times 125\,\mathrm{mm}^2$ Monocrystalline Solar Cells $2.91\,\mathrm{W}$ Mono 5×5," Dec. 2014. [Online]. Available: http://www.ebay.co.uk/itm/125x125-Monocrystalline-Solar-Cells-2-91-Watt-Mono-5x5-/221545517144?item=221545517144&ssPageName=ADME:L:OC:GB:%20\\3160. Accessed on: Jun. 11, 2015.

[94] A. Ortiz-Conde, D. Lugo-Munoz, and F. J. Garcia-Sanchez, "An Explicit Multi-exponential Model as an Alternative to Traditional Solar Cell Models with Series and Shunt Resistances," *IEEE J. Photovolt.*, vol. 2, no. 3, pp. 261–268, Jul. 2012.

[95] H. Schmidt, B. Burger, and J. Schmid, "Power Conditioning for Photovoltaic Power Systems," in *Handbook of Photovoltaic Science and Engineering*, 2nd ed. New York, NY, USA: Wiley, Jun. 2011, pp. 954–983.

[96] B. E. A. Saleh and M. C. Teich, "Photons and Atoms," in *Fundamentals of Photonics*, 1st ed., ser. Wiley in Pure and Applied Optics. New York, NY, USA: Wiley, Jan. 1991, pp. 423–459.

[97] ——, "Fourier Optics," in *Fundamentals of Photonics*, 1st ed., ser. Wiley in Pure and Applied Optics. New York, NY, USA: Wiley, Jan. 1991, pp. 108–156.

[98] R. S. Quimby, "Review of Optics," in *Photonics and Lasers: An Introduction*. New York, NY, USA: Wiley, 2006, pp. 7–27.

[99] Zemax, "Getting Started with OpticStudio 15," May 2015. [Online]. Available: https://www.zemax.com/ZMXLLC/media/PDFLibrary/Brochures/OpticStudio_Getting Started.pdf?ext=.pdf. Accessed on: Jun. 17, 2015.

[100] Thorlabs, "ACL12708U-B – Aspheric Condenser Lens, AR-Coated $650 - 1050\,\mathrm{nm}$, $D = 1.27\,\mathrm{cm}$, $f = 8\,\mathrm{mm}$," Nov. 2013. [Online]. Available: https://www.thorlabs.de/thorcat/CTN/ACL12708U-B-AutoCADPDF.pdf. Accessed on: Apr. 1, 2015.

[101] I. Stamenov, I. Agurok, and J. E. Ford, "Optimization of High-Performance Monocentric Lenses," *OSA J. Appl. Opt.*, vol. 52, no. 34, pp. 8287–8304, Dec. 2013.

[102] Coherent, "Efficient Transformation of Gaussian Beams into Uniform, Rectangular Intensity Distributions." [Online]. Available: https://www.coherent.com/downloads/Transformation_GaussianBeams.pdf. Accessed on: Nov. 11, 2015.

[103] Sheaumann, "Product Specifications: $975\,\mathrm{nm}$ Multi-Mode Laser Diodes $400\,\mu\mathrm{m}$ Emitter ($8\,\mathrm{W}$–$10\,\mathrm{W}$)," Oct. 2015. [Online]. Available: https://www.lasercomponents.com/de/?embedded=1&file=fileadmin/user_upload/home/Datasheets/sheaumann/diodes/mm/975nm/975nm-mm-diodes-10w.pdf&no_cache=1. Accessed on: Dec. 4, 2015.

[104] Coherent, "Laser Diode Technical Note 1: Beam Circularization and Astigmatism-Correction," 1998. [Online]. Available: https://www.coherent.com/downloads/LaserDiodeTechNote1.pdf. Accessed on: Dec. 1, 2015.

[105] Laserline Optics Canada, "$45°$ Narrow Beam Powell Lens," Apr. 2012. [Online]. Available: http://www.laserlineoptics.com/pdfs/drawings/LOCP_8.9R45_drawings.pdf. Accessed on: Nov. 16, 2015.

[106] Edmund Optics, "Metallic Mirror Coatings." [Online]. Available: http://www.edmundoptics.co.uk/resources/application-notes/optics/metallic-mirror-coatings/. Accessed on: Oct. 18, 2016.

[107] Homer Energy, "Homer Legacy: The Original." [Online]. Available: http://www.homerenergy.com/HOMER_legacy.html. Accessed on: Oct. 27, 2016.

[108] Met Office, "Royal Botanic Garden Edinburgh Climate." [Online]. Available: http://www.metoffice.gov.uk/public/weather/climate/gcvwqum6h. Accessed on: Nov. 5, 2016.

[109] D. U. Sauer, "Electrochemical Storage for Photovoltaics," in *Handbook of Photovoltaic Science and Engineering*, 2nd ed. New York, NY, USA: Wiley, June 2011, pp. 896–953.

[110] Hoppecke, "OPzS Vented Lead-Acid Battery." [Online]. Available: https://www.hoppecke.com/fileadmin/Redakteur/Hoppecke-Main/Products/Downloads/OPzS_en.pdf. Accessed on: Nov. 14, 2016.

[111] SolarGIS, "Global Horizontal Irradiation," 2016. [Online]. Available: http://solargis.com/assets/graphic/free-map/GHI/Solargis-World-GHI-solar-resource-map-en.png. Accessed on: Jan. 12, 2017.

[112] *Photobiological Safety of Lamps and Lamp Systems*, British Standards Institution (BSI) Std. BS EN 62471:2008 Std., Sep. 2008.

[113] V. P. Khvostikov, S. V. Sorokina, F. Y. Soldatenkov, and N. K. Timoshina, "GaSb-based Photovoltaic Laser-Power Converter for the Wavelength $\lambda \approx 1550\,\mathrm{nm}$," *J. Semicond.*, vol. 49, no. 8, pp. 1079–1082, Aug. 2015.

[114] S. Spiga, A. Andrejew, G. Boehm, and M. C. Amann, "High-Speed 1.55-µm VCSELs for Datacom and Telecom Applications," in *Proc. IEEE 21st Optoelectron. Commun. Conf. and Int. Conf. Photon. Switching*, Niigata, Japan, Jul. 2016, pp. 1–3.

[115] I. S. Gradshteyn and I. M. Ryzhik, *Table of Integrals, Series, and Products*, 7th ed., A. Jeffrey and D. Zwillinger, Eds. New York, NY, USA: Academic, Mar. 2007.